IN-SERVICE PERFORMANCE EVALUATION OF FIRE AND IMPACT DAMAGED BRIDGES WITH CFRP LAMINATE STRENGTHENING

by

SANTOSH TIMILSINA

Presented to the Faculty of the Graduate School of

The University of Texas at Arlington in Partial Fulfillment

of the requirements

for the Degree of

DOCTOR OF PHILOSOPHY

THE UNIVERSITY OF TEXAS AT ARLINGTON

AUGUST 2018

Acknowledgments

First and Foremost, I would like to express my sincere appreciation to my advisor Dr. Nur Yazdani for his continuous support and guidance during my Ph.D. degree. His continuous mentorship with patience and enthusiasm and motivation helped me complete my research and dissertation in time. I am grateful to Dr. Ali Abolmaali, Dr. Mohsen Shahandashti, and Dr. Ashfaq Adnan for serving on my dissertation committee and for their encouragement and support during my study.

I would like to acknowledge the financial support from the Texas Department of Transportation (TxDOT). I also like to thank Walter Fisher III and Sunil Patel from TxDOT Dallas District for their valuable advice.

I am grateful to Mr. Lafe Sargent and Mr. Travis Kralicke from Southwest contractors and Mr. Michael Thomas from TxDOT for providing us with the aerial equipment and managing traffic control for the load tests. Their unceasing support and cooperation during the process was important to complete the tasks successfully.

I am thankful to my friend Dr. Eyosias Beneberu for his continuous help and guidance during the research work. Also, I would like to thank Dr. Mina Riad, Yazan Almomani, Natawut Chaiwino, Tariq Al Jaafreh, Towfiqul Quadir, Zaid Momani, Angie Uribe, Abel Mulenga, Kamal Sapkota, and Nicholas Salazar for all the help and hard work during the experiment.

I am deeply grateful to my parents and my family for their continuous support, motivation and for believing in me through the entirety of my research.

July 11, 2018

Abstract

IN-SERVICE PERFORMANCE EVALUATION OF FIRE AND IMPACT DAMAGED BRIDGES WITH CFRP LAMINATE STRENGTHENING

Santosh Timilsina, PhD

The University of Texas at Arlington, 2018

Supervising Professor: Nur Yazdani

Fire events and impact damage on bridges are few of the least understood of common extreme events. Bridge infrastructures that are subjected to hazards such as fire or impact from over height vehicle can catastrophically collapse or be heavily damaged. External wrapping of damaged concrete bridge components with Fiber Reinforced Polymer (FRP) laminates has been used as a strengthening technique for these bridges. Two such in-service bridges, one of which was fire damaged and the other impact damaged, both aged more than 50 years old in Irving, Texas, were selected for this study. The damaged beams of the concrete girders were subsequently repaired and strengthened with carbon FRP (CFRP) laminates. The girders were instrumented with strain gauges and displacement transducers, and a non-destructive live load test was carried out.

The results from the load test were used to evaluate the performance and determine the lateral flexural load distribution. The strengthened girder exhibited a lower midspan deflection and lower strain than a similar representative undamaged girder. FE models were prepared and calibrated using the experimental results. Fire model using a Fire Dynamics Simulator (FDS) and heat transfer analysis was used to accurately predict the post-fire material properties of concrete to calibrate the FE model for fire-damaged bridge. It was observed that

the modulus of elasticity of the fire damaged section of the bridge was reduced by 20% to 75% in different sections of the bridge. A calibrated FE model for the impact damaged bridge was also able to mirror the experimental performance of the bridge. Load distribution characteristics of the bridge were studied and compared with AASHTO LRFD distribution factors for moment.

Table of Contents

List of Figures

List of Tables

Chapter 1

Introduction

1.1 Background

There are currently 615,002 bridges in the United States and around 39% of the bridges are 50 years or older. The average age of bridges in the United States is 43 years old (ASCE 2017) which is one year higher than the reported value in the ASCE 2013 Report Card. The decades of the 1950s to 1970s saw a large number of bridges built in the United States as a result of development in infrastructure and the National Highway system. Most of these bridges are built for a design life of 50 years. It shows that a large number of bridges are reaching their 50-year design life period. As the number of bridges has been growing, so has the amount of traffic flowing in those bridges. The vehicle distance traveled has significantly increased from 2250 billion miles in 1993 to an astounding 3200 billion miles within over 20 years as shown in Figure 1-1 (FHWA, 2017).

Federal Highway Administration (FHWA) uses a rating factor called the condition rating to evaluate and code the condition of bridges. Condition ratings are used to describe the existing, in-place bridge as compared to its as-built condition. Condition ratings can provide a measure of how much deterioration a bridge has undergone through its life period. The rating criteria characterize the overall condition of the bridge including the materials, riding condition, condition of superstructure and substructures. Condition ratings range from 0 to 9 where 0 refers to a failed condition, and nine refers to Excellent Condition.

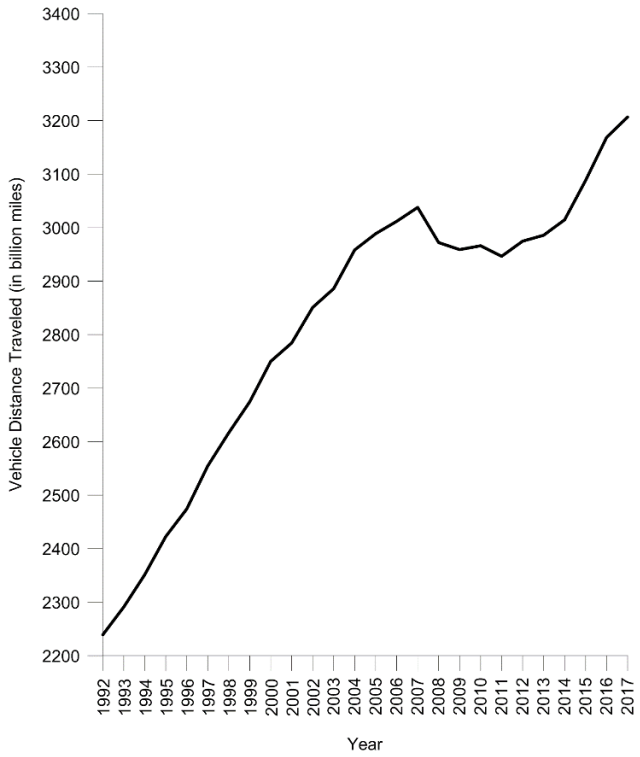

Figure 1-1 Vehicle distance traveled (FHWA, 2017)

FHWA identifies the bridges with condition rating 4 or less as structurally deficient bridges. A structurally deficient bridge is one for which either the substructure or the superstructure has a condition rating below 4. This does not mean that the bridge is in immediate danger or likely to collapse. However, continuous monitoring, inspection, and maintenance need to be carried out to maintain the bridge in service. Some bridges have to be restricted to light vehicles or completely closed to traffic. Although 'deficient' bridges do not pose an immediate safety risk, some bridges are not suitable for full American Association of State Highway and Transportation Officials (AASHTO) loads which requires load posting on bridges. Functionally obsolete bridges are those bridges which were built according to standards which are no longer in use. Inadequate lane widths, not enough vertical clearance or occasionally flooded bridges are some examples

which may be classified as functionally obsolete bridges. Although not inherently unsafe, these bridges need rehabilitation and maintenance for full proper usage.

According to FHWA, 9.1% of the nation's bridges were structurally deficient in 2016. 6.3% of the total bridge deck area belonged to structurally deficient bridges, and there were around 188 million trips across structurally deficient bridge each day (ASCE 2017). Texas alone has 53,869 bridges; which is the largest number of bridges by state. Texas Department of Transportation (TxDOT) maintains most of these bridges and continuously monitors and inspects the bridges for structural safety and integrity. The number of structurally deficient bridges in Texas is around 2%, and there are 17% functionally obsolete bridges. Currently, FHWA estimates a cost of $31 billion for the rehabilitation of bridges.

This asserts a concerted effort from all sectors for repair, rehabilitation, and strengthening of bridge structures. Deterioration in concrete bridges can occur in different ways including degradation of concrete through aging, corrosion of steel, loss of stiffness of bearing pads and diaphragms. There has been a concerted effort to reduce the number of structurally deficient bridges through repair, retrofit, and replacement over the past few decades. The focus in bridge and infrastructure has changed from new design and construction to repair and rehabilitation over the last couple of decades. The paradigm has shifted towards increasing the design life of the bridge rather than replacing them completely, which can be very expensive and time-consuming.

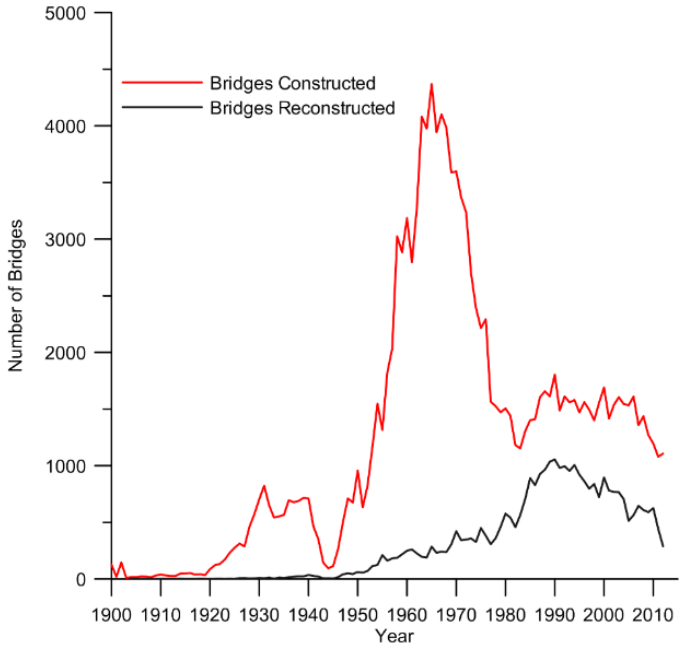

Figure 1-2 Construction and reconstruction of bridges over the years

There are different causes when concrete bridges can be structurally inadequate. One of the reasons may be due to a design or construction flaw. Natural hazards like fire and earthquake or accidental events like overheight vehicle, blast, arson or vandalism can also be the cause of damage to bridges. Also, governing design codes and guidelines can change to accommodate new advancements in the field of concrete which can often lead structures to be deficient. These deficient bridges need to be repaired, maintained or strengthened so that they can be safe to carry the current traffic load demand. Some of the common methods of strengthening of concrete bridges are externally bonded steel plates, steel or concrete jacketing, external post-tensioning and externally bonded fiber reinforced polymer (FRP). One of these strengthening techniques, widely accepted and used, is the external wrapping of damaged concrete bridge components with Fiber Reinforced Polymer (FRP) laminates. Carbon Fiber

Reinforced Polymer (CFRP) is widely used to strengthen concrete structural elements because of its several advantages. FRP materials are lightweight, noncorrosive, and exhibit high tensile strength. Cured FRP systems are often desirable in applications where aesthetics or access is a concern. FRP systems can also be used in areas with limited access where traditional techniques would be difficult to implement. (ACI 440.2R, 2008). Additional confinement of the concrete patch through CFRP wrapping is helpful to mitigate the possibility of a 'pop out' failure of the patch which can be catastrophic.

1.2 Problem Statement

The popularity of FRP laminate for strengthening purposes has been increasing over the last few decades. Currently, 24 highway departments in the United States are using strengthening by CFRP, and several others states are in the process of adopting it (Pallempati et al. 2016). External wrapping of CFRP has been found to increase the flexural strength of structural elements ranging from 10% to 160% (Meier and Kaiser, 1991; Ritchie et al., 1991; Sharif et al., 1994). External wrapping of CFRP laminate has been successfully used in bridge girders which have been significantly damaged or deteriorated. However, the long-term performance of such repair and strengthening technique has not been studied in detail. The performance of a bridge which was damaged and repaired and strengthened with CFRP can change significantly after a long period as a result of change in traffic conditions, seasonal and weather changes and aging of the structure.

The Federal Highway Administration (FHWA) requires that each bridge be inspected every two years (FHWA 2012). However, only visual inspection is being

carried out, and it depends on the individual's perception of the bridge. Moore et al. (2001) presented the variability between different visual inspections by comparing evaluations by 49 different inspectors. The condition rating for each structural element was found to vary significantly between different inspectors. This presents the difficulty in obtaining a uniform visual evaluation. It is recommended that supplementary methods like modeling and model calibration be employed in conjunction with visual inspection for load rating purposes (ASCE 2009).

Load tests and finite element modeling in conjunction with visual inspection is imperative for damaged and strengthened bridges as the performance of such bridges can be highly different than the undamaged bridges. Fire damage and lateral damage due to over-height vehicles are some of the most common causes of damage to bridge superstructure which require repair and strengthening. The material properties, stiffness, continuity of supports and composite action with the deck can change as a result of the damage which requires proper evaluation and advanced techniques to understand properly. Exposure to fire and high temperatures can cause spalling of concrete, microcracks, and loss of tensile strength of reinforcement. Also, the bearing pads, pier caps and substructure to be damaged which can adversely affect the behavior of the superstructure. In case of lateral impact damage due to overheight vehicle, there can be loss of concrete section and strands can be severed. Severed strands are occasionally spliced which is often known to have problems with size, geometry, amount of concrete cover or premature failure (Kasan, 2009). This can cause the bridge behavior to be non-uniform and unpredictable. Bridges, which do not collapse or girders which are not replaced, are often repaired with mortar and strengthened with CFRP

wrapping. However, along with the damage to the concrete and possible change in properties of the rebar and pre-stressing strands, there can be a change in the properties and bond between CFRP and concrete which can decrease the flexural capacity of the bridge girders. The bond between concrete and CFRP can deteriorate due to traffic-induced vibrations, ingress of water and chemicals within the bond surface which is why such bridges need to consistently tested and evaluated. Load tests and finite element modeling can provide the complete picture of the capacity of the bridge to carry AASHTO and state loads and help ascertain the overall system performance of the in-service bridge.

1.3 Scope and objectives of the study

The use of externally mounted CFRP strips to restore the flexural capacity of damaged girders is well documented (Scheibel et al. 2001, Klaiber et al. 2003, Aidoo et al. 2006, Reed and Peterman 2005). It has been found through these studies that the strengthening technique is effective to reduce deflection and recover the flexural capacities. The overall performance of such repaired and strengthened bridge after a certain period and the effectiveness of repair is a matter of study. Two bridges, one fire damaged and other, laterally damaged by an over-height vehicle, were selected for this study. Both these bridges were damaged which required repair and strengthening with CFRP strips on the bottom surface and U wraps around the beams. The objective of the study is to perform load tests on these bridges to obtain the response of the bridge and compare the performance of a CFRP strengthened beam with a similar undamaged beam. A finite element model was then created to simulate the properties and loading to obtain a calibrated model which can be used to perceive the overall performance of the bridge structure. Samples from the bridge were collected to predict the

present condition of the bridge accurately. Live-load distribution factors were then obtained using the calibrated model to fully understand the effectiveness of the strengthening procedure.

The objectives of the study are as follows:

1. Investigate the overall in-situ performance of a fire damaged, CFRP strengthened reinforced concrete bridge through instrumentation and static load testing.
2. Evaluate the performance of a prestressed concrete bridge with some impact-damaged, CFRP strengthened bridge girders through nondestructive load test.
3. Investigate and compare the performance of a CFRP strengthened beam with an undamaged beam to study and compare the strain, deflection and overall response under similar loading.
4. Prepare a realistic 3D finite element model of the whole bridge to simulate the geometrical properties, material properties, and the boundary conditions to understand the overall system behavior of the bridge.
5. Calibrate the 3D FEM model based on experimental load testing results and material samples collected, hence capturing the accurate behavior of the in-service bridge.
6. Calculate the live load distribution factors for the bridges, both through experimental results and calibrated model to compare and analyze the bridge performance.
7. Study the performance of the CFRP laminate system which has been in service for a certain period of time after strengthening.

1.4 Organization of the Dissertation

The dissertation is organized into six different chapters. The content of the chapters is described below.

Chapter 2- Literature Review

This chapter presents a review of previously carried out experimental work and nondestructive testing for condition assessment of bridges. Damage of concrete bridges and practice of CFRP repair is briefly touched in this section. A history and different methods of load tests are discussed further. Finite element modeling of bridges and model calibration through load tests is also mentioned.

Chapter 3- Experimental procedure

The instrumentation plan, method and different types of load tests are presented in this chapter. Bridge description and the history of damage and repair is talked about in detail.

Chapter 4- Finite Element modeling

Material properties, modeling techniques and analysis procedure for obtaining a full-scale baseline model of the bridge is presented in this chapter. Material testing, mesh refinement and steps to obtain a calibrated finite element model is detailed.

Chapter 5- Results and Discussion

The results obtained from the experimental load test is initially discussed and comparisons between a strengthened and undamaged beam are presented. Calibrated model results are also included in this chapter. A

comparison of the modeling and experimental results is presented through distribution factors for the beams.

Chapter 6- Summary, conclusions, and recommendations

The summary of the research conducted is presented. The conclusions drawn from the load test, calibrated finite element methods and material testing are presented. Recommendations for further research is finally made.

Chapter 2

Literature Review

2.1 Fire Hazard on bridges

Fire is one of the most severe hazards to any structure; buildings or bridges. Bridge fire incidents are commonly caused by crashing of vehicles, arson, tanker collapse, terrorist activities, or a vehicle catching fire. Fire on bridges is often not considered because of the low probability of occurrence. If the fire is severe, it can often lead to the collapse of the bridge. A survey by Battelle(2001) shows that the average number of annual highway vehicle fire incidents in the US is 376,000, which causes 570 civilian deaths and $1.28 billion of property losses. A voluntary survey of 18 highway departments showed that fire has caused more bridge collapse compared to earthquake (Wright et al., 2013; Alos-Moya et al. 2014). This shows that significant research needs to be carried out to understand the performance of bridge structures deteriorated by fire. Fire on bridges can cause significant economic losses which can come in the form of direct cost due to repair, retrofit or replacement of such structure. The indirect cost can arise from detour of traffic, time and cost involved with traffic congestion and its emergency nature (Gong et al. 2014). Damage of bridges in a busy metropolitan city with major highways can have adverse socio-economic impacts. Hydrocarbon fuel and hybrid batteries have become increasingly abundant which can be a major cause of highway fires during vehicle collisions (Quiel et al. 2015). Big tankers transporting a large amount of fuel or other flammable materials can catch fire and significantly damage a bridge structure.

The cases of highway bridge fire have been increasingly common and hydrocarbon fire is one of the major causes. A summary of fire incidents over the last 15 years is presented in Garlock et al. (2011) and reproduced here in Table 2-1. One such major fire incident occurred in Oakland, CA on the MacArthur Maze Bridge on April 29th, 2007 which led to the overpass collapse. A tanker carrying 8,600 gallons of gasoline traveling at a high speed overturned and caught fire on the I-80/880 interchange under I-580. Two I- 580 spans collapsed as a result of the fire. The bridge had six plate girders which supported a reinforced concrete deck. The spans collapsed (Figure 2-1) after 22 minutes as a result of the high-intensity fire. It was estimated that the fire caused an economic loss of $9 million to demolish, remove, and repair along with a cost of $2 million for traffic control (Bulwa and Fimrite,2010; Astaneh-Asl et al. 2009). It took 26 days for the replacement of the spans and reopening the bridge. The total economic loss to the San Francisco Bay area was estimated around $6 million per day (Chung et al. 2008).

Figure 2-1 Collapsed MacArthur Maze Bridge (New York Times 2007)

Table 2-1 Some major bridge fires in the last 20 years (Garlock et al. 2011)

Bridge/Location	Date	Cause of fire	Bridge material	Damage description
Bridge over I-75 near Hazel Park, MI, USA	July 15, 2009	A gasoline tanker struck an overpass on I-75	Composite deck (steel girders + reinforced concrete slab)	Complete collapse of the bridge, which fell on the freeway below
Big Four Bridge, Louisville, KY, USA	May 7, 2008	Electrical problem of the lighting system, took two and a half hours to control the fire	Steel truss bridge	Minor structural damage, resulting in large amount of debris on the bridge
Stop Thirty Road, State Route 386 Nashville, TN, USA	June 20, 2007	A fuel tanker truck rear-ended a loaded dump truck. The tanker erupted into flames beneath the bridge.	Concrete hollow box-beam bridge	The bridge sustained very little damage, and traffic was reopened after minor repairs
I-80/880 interchange in Oakland, CA, USA	April 29, 2007	A gasoline tanker crashed	Composite deck (steel girders + reinforced concrete slab) supported by reinforced concrete columns	A 160 m section of the interchange collapsed
Belle Isle Bridge in NW Expressway, Oklahoma City, OK, USA	January 28, 2006	A truck crashed into the bridge	Concrete deck (precast prestressed I-girders + cast in place reinforced concrete slab)	Concrete girders were slightly damaged by the fire The safety of the bridge was assessed, and the bridge was reopened to traffic
Bridge over the Norwalk River near Ridgefield, CT, USA	July 12, 2005	A tanker truck carrying 30.3 m^3 of gasoline overturned, caught fire and burned out on the bridge	Concrete deck (precast prestressed box girders + cast in place reinforced concrete slab)	The deck was replaced by a new one
I-95 Howard Avenue Overpass in Bridgeport, CT, USA	March 26, 2003	A car struck a truck carrying 30.3 m^3 of heating oil	Composite deck (steel girders + reinforced concrete slab)	Collapse of the southbound lanes and partial collapse of the Northbound lanes
I-20/I-59/I-65 interchange in Birmingham, AL, USA	January 5, 2002	A loaded gasoline tanker crashed	Steel girders	The main span sagged about 3 m (10 feet)
I-80W/I-580E ramp in Emeryville, CA, USA	February 5, 1995	A gasoline tanker crashed	Composite deck (steel girders + reinforced concrete slab)	Deck, guardrail, and some ancillary facilities were damaged

2.1.1 Fire Assessment and repair

A careful post-fire assessment for bridges is often required to evaluate the bridge damage induced due to the fire and determine the serviceability of the damaged bridge. Proper repair techniques can then be formulated based on the comprehensive assessment of bridge damage. Since the performance of fire exposed bridge is highly dependent on the material type used in the bridge, it is necessary to properly evaluate the strength properties of fire exposed concrete and steel.

Fire hazards, like any other hazards, are unpredictable and the response of the bridge during a fire can depend on several factors. The direction of wind, time of day, type of bridge, temperature and type of fire and fire-fighting technique can all affect the structure's response to fire. It can hence be difficult to properly assess and evaluate a fire exposed bridge. Standards and literature such as the NCHRP report 280 (Shanafelt 1985), PCI Manual 124 (PCI 2014), Fib Bulletin 46 can form the basis for post-fire assessment and repair strategies for concrete bridges. Visual inspection is the most effective and reliable means to assess the extent of fire damage (Tide 1998). Visual inspection consists of documenting concrete spalling, loss of concrete cover to reinforcement, concrete color, and excessive cracking (Garlock et al. 2011). The temperature-depth of the concrete can often be determined based on the color of the exposed aggregate as suggested in PCI Manual (PCI 2014) and shown in Table 2-2. As visual assessment is often subjective, it can be combined with optical microscopy with color image analysis (Short et al. 2001) and digital camera calorimetry (Colombo and Felicetti 2007).

Table 2-2 Probable correlation between fire exposed concrete color and Temperature (Gusta-ferro and Martin 1988)

Color	Probable maximum Temperature (˚C)
No Discoloration	<315
Pink	315-593
Whitish-Grey	>593
Buff (light tan)	>927

Other important indicators of temperature effect in concrete are cracking, spalling and loss of concrete cover. Transverse cracking can often be observed in the tensile region of the beam which can be an indicator of reduced stiffness and increased deflection. Guise et al. (1996) reported that the crack density decreases as compressive strength increases. Spalling can either be local spalling, sloughing off or explosive spalling based on the amount of temperature exposure (Garlock et al. 2011).

Impact rebound hammer can be used to perform hardness tests on the damage affected areas when calibration is performed on an unheated concrete (PCI Manual). Good correlation of impact rebound hammer with the color of concrete was obtained (Chew 1993; Stoddard 2004). Concrete cores are usually taken from the fire affected areas to be tested in the lab to obtain the compressive strength of concrete. Petrographic examination in accordance with ASTM standards (ASTM C856 2004) is often done to determine the extent of microcracking and property change due to paste alteration. Such damage can adversely affect the strength and durability of concrete and contribute to accelerated corrosion of the reinforcement and may shorten service life (Garlock et al. 2011). In addition to visual inspection and material testing, live load testing on the bridges affected by fire can be done to properly access the condition of the bridge.

Ballim and Silbernagl (2005) performed a non-destructive live load test in addition to visual inspection, material testing, and optical microscopy. The deflection response of the bridge girders for different truck positions was recorded and concluded that the load carrying capacity of the deck and the cantilever portion of the bridge was not compromised. Strain response from the bridge girders was not recorded and only a few girders were instrumented. A live load test on the fire-damaged bridge was also performed by Au (2016). A post-fire analysis of the bridge was done with a live load test. Six girders from the bridge were repaired and strengthened with CFRP and a proof load test was done to determine the load carrying capacity of the bridge. It was concluded that the bridge was performing in desired manner. The composite action of the bridge was found to be intact and safe to carry the design load. It has been found that load test is the most effective way to determine the in-service condition of a fire-damaged bridge (Au 2016; Ballim and Silbernagl 2005; Davis et al. 2006).

2.1.2 Material Properties at Elevated Temperature

Mechanical Properties of Concrete

The thermal and mechanical responses of reinforced or prestressed concrete member, subjected to a fire, depend on the properties of the constituent materials. The material properties can be highly variable and depend on the amount of temperature and heat exposure during the fire. The extent of strength loss and stiffness deterioration is determined by the inherent mechanical properties of the material. These properties include compressive and tensile strength, modulus of elasticity and stress-strain response of the material. Table 2-3 represents common changes in concrete during the heating phase based on Glasheen (2003) and PCI report (1988).

Table 2-3 Physical (appearance) changes in concrete during fire exposure

Temperature (°C)	Change
<100	Little or no concrete damage. Paste expands with loss of some free water, but few or no cracks and no color changes
250	Localized cracks. Paste is dehydrating with complete loss of free water causing ½% or more decrease in volume. Iron-bearing aggregates begin to acquire pink/red color
370	Cracks appear around aggregate due to differential thermal properties. Very rapid aggregate expansion of metamorphic and igneous rocks. Numerous microcracks present in cement paste observed in thin-sections. (Most normal weight concrete has lost half of its strength)
480-500	Concrete may begin to change to a purple grey color if enough iron and lime are present. Portlandite (calcium hydroxide), a major secondary hydration product, is altering to calcium carbonate. Paste has a patchy appearance in thin-sections
550	Serious cracking of paste and aggregates due to expansion. Purple-grey color may become more pronounced
800	Cement paste is completely dehydrated with severe shrinkage cracking and honeycombing. Concrete may begin to be friable and porous
1200	Some components of concrete begin to melt
1400	Concrete is completely vaporized

The thermal conductivity of concrete is affected by the amount of moisture and the type of aggregate. Specific heat is highly influenced by moisture content, aggregate type and density of concrete (Phan 1996; Harmathy et al. 1973; Kodur and Sultan 1998). Compressive strength of concrete decreases at higher temperatures. Figure 2-2 shows the variation of normalized compressive strength of Normal Strength Concrete (NSC) as a function of temperature. It can be seen that the compressive strength of concrete doesn't change much until a temperature of 400°C and rapidly decreases after that. This rapid decrease can be due to the onset of microcracks and change in microstructure of concrete and binder material.

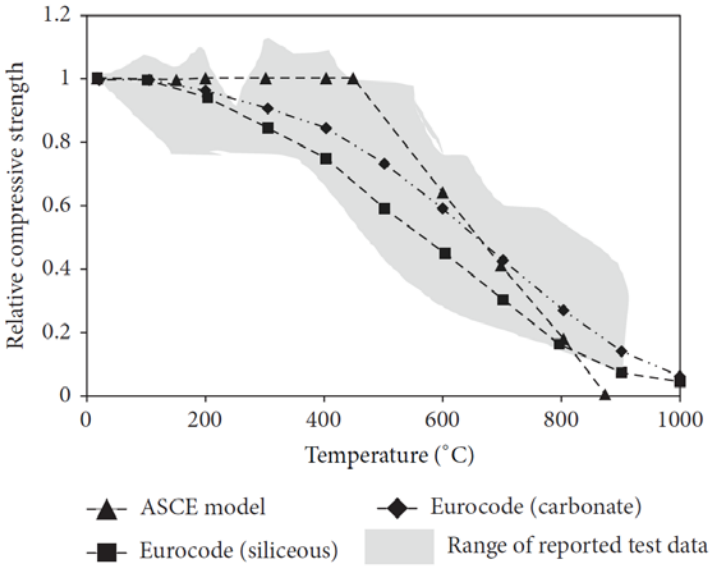

Figure 2-2 Variation of relative compressive strength of normal strength concrete as a function of temperature (Kodur 2014)

Figure 2-3 shows the variation of modulus of Elasticity of concrete with the change in temperature. It can be seen that the loss of stiffness of concrete at higher temperature is significant. It can be clearly illustrated from the stress-strain diagram at different temperatures for NSC as reported Kodur (2014) and seen in Figure 2-4. The temperature has a significant effect on the stress-strain response of concrete, as with the rate of rise in temperature. The strain corresponding to peak stress starts to increase, especially above 500^{o}C.This increase is significant and the strain at peak stress can reach four times the strain at room temperature (Kodur 2014).

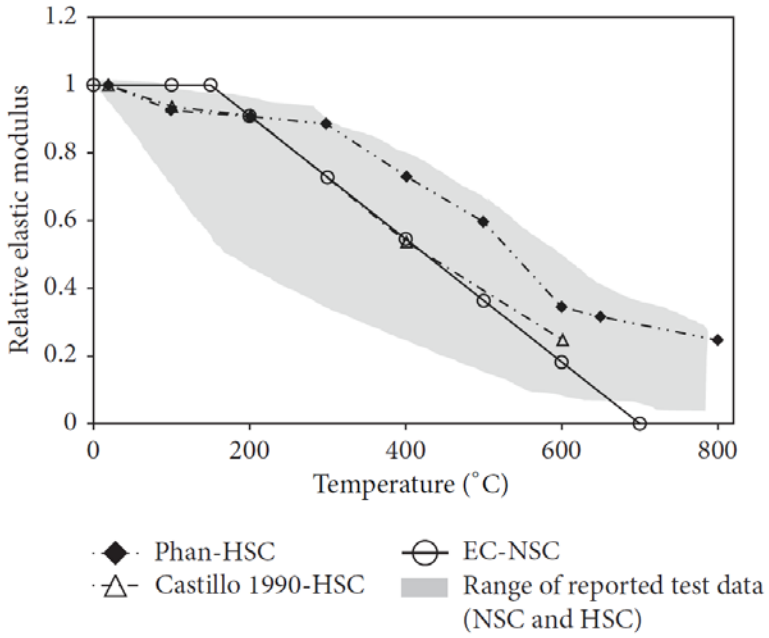

Figure 2-3 Variation in elastic modulus of concrete as a function of Temperature (Kodur 2014).

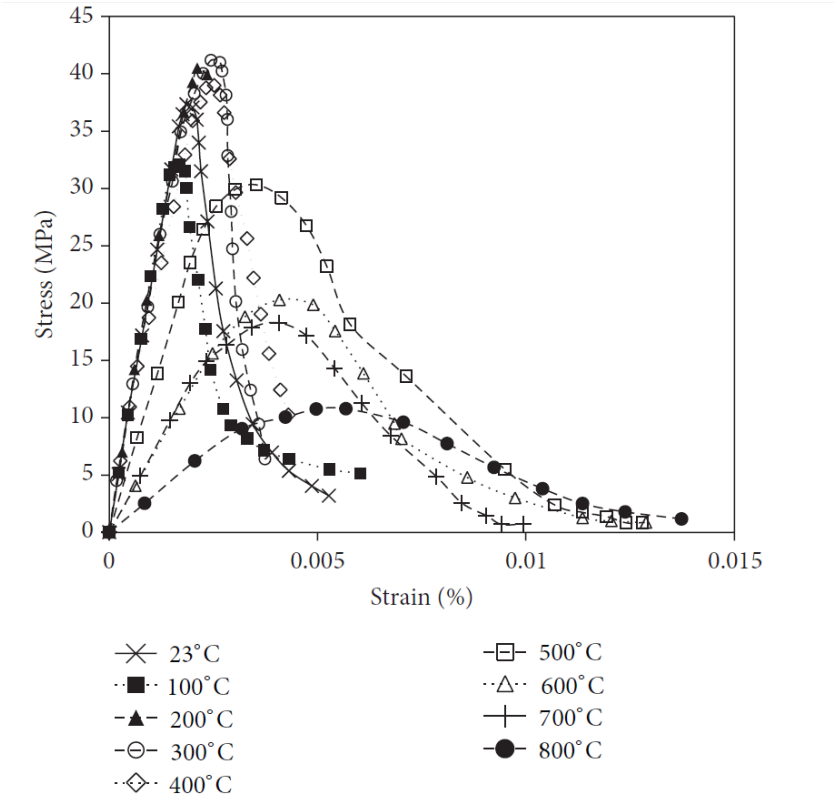

Figure 2-4 Stress-strain diagram of NSC at elevated temperatures (Kodur 2014).

Mechanical Properties of Mild Reinforcement

The thermal, mechanical and elongation properties of mild reinforcement can also change due to exposure to fire and high temperature. Mechanical properties of mild reinforcement can be characterized by the yield strength, ultimate strength, modulus of elasticity and stress-strain relationship. The stress-strain relationship of mild reinforcement at different temperatures, as suggested by Eurocode and ASCE is as shown in Figure 2-5. It can be seen that there is a significant decrease in yield stress and ultimate strength of mild reinforcement at higher temperatures. It is necessary to take into consideration this change, to accurately represent the behavior of mild reinforcement. According to Eurocode, prestressing steels begin to lose strength at 100°C, whereas mild reinforcements do at 400°C.

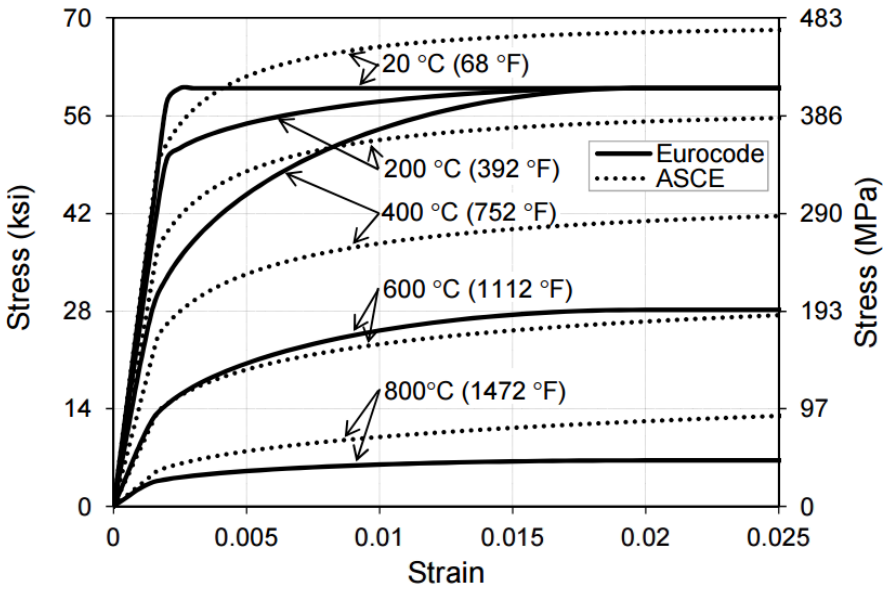

Figure 2-5 Variation of Stress-strain curves as a function of temperature for mild reinforcing steel (Eurocode 3, 2005)

The variation of the modulus of elasticity for mild reinforcement and prestressing strands from two different provisions, Eurocode-3 (2004) and ASCE

(1992) is presented in Figure 2-6. The modulus of elasticity for mild reinforcement decreases with increase in temperature. The decrease can be highly significant and exhibits S-shaped curve.

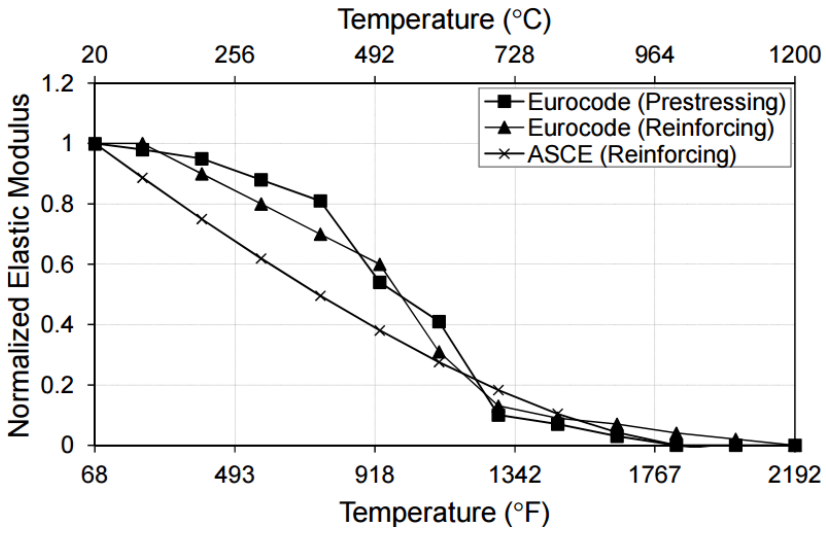

Figure 2-6 Variation of modulus of Elasticity for mild reinforcement and prestressing reinforcement at different temperatures (Eurocode 3, 2005; ASCE 1992)

Along with the change in elastic modulus, yield stress and stress-strain relationship, high temperature can induce permanent plastic deformation, often referred as creep strain. The effect of creep in mild reinforcement will not come into effect until the temperature is around 400°C to 500°C (Elghazouli et. al, 2009).

The thermal and mechanical properties of concrete and reinforcement can significantly affect the behavior of fire exposed bridges which need to be taken into consideration to accurately determine the performance of a fire exposed bridge and making an informed decision for repair and rehabilitation.

2.2 Impact damage of bridges

Accidental lateral damage of bridge girders by over-height vehicles is one of the major causes of damage in a bridge superstructure. Vehicle impact and deterioration are the major causes of damage in bridges (Kasan and Harries 2009). A nationwide survey shows that, on average, between twenty-five to thirty-five bridges are damaged by over-height vehicles every year (Fu et al. 2003). Most of these bridges are impacted multiple times because of inadequate vertical clearance as shown in Figure 2-7. NCHRP Project 12-21 (Shanafelt and Horn 1980) is one of the first publications on the topic. This document presents the state-of-the-art and the state-of-practice as of the date of publication. It is mainly focused on providing guidance for the assessment, inspection, and repair of damaged prestressed concrete bridge girders. A damage classification system to quantify the damage present, so that adequate repair technique can be incorporated, was proposed by the authors which were separated into three different categories as shown in Table 2-4.

Figure 2-7 Impact-damaged prestressed bridge girder (Kasan et al. 2013)

Table 2-4 Levels of damage in prestressed concrete girders (Shanafelt and Horn 1980)

Damage	Definition
Minor damage	Concrete with shallow spalls, nicks and cracks, scrapes and some efflorescence, rust or water stains. Damage at this level does not affect member capacity. Repairs are for aesthetic or preventative purposes.
Moderate damage	Larger cracks and sufficient spalling or loss of concrete to expose strands. Moderate damage does not affect member capacity. Repairs are intended to prevent further deterioration.
Severe damage	Any damage requiring structural repairs. Typical damage at this level includes significant cracking and spalling, corrosion and exposed and broken strands.

2.2.1 Damage Assessment and repair techniques

NCHRP Report 226 (Shanafelt and Horn 1980) gave some guidelines on the assessment, inspection, and repair of damaged prestressed concrete bridge girders. Suggestions were made for the repair and replacement of the damaged bridge girders based on the level of damage. A damage classification system which was proposed which can be used as a basis for preparing an adequate and efficient repair procedure. Major repair techniques suggested in Report 226 were external post-tensioning, metal sleeve splicing, strand splicing, a combination of above-mentioned methods, and replacement.

External post-tensioning is carried out on affected steel rods, strands or bars which are anchored by corbels or brackets that are cast or mounted onto the girder; typically on the girder's side. The steel rods, strands or bars are then tensioned by jacking against the bolster or preload. *Steel jacketing* is the use of steel plates to encase the girder to restore girder strength. With this repair technique, post-tensioning force can only be introduced by preloading. Generally, shear heads, studs

or through bars are attached to the steel jacketing to create a shear transfer between the steel jacket and substrate beam. Another repair technique, especially for prestressed strands, is *strand splices*. Strand splices can be done by restoring the prestressing force in the strand either by preloading, strand heating and torquing the splice, essentially making a turnbuckle of sorts.

NCHRP Report 226 provides the selection matrix, as shown in Table 2-5, for selecting repair methods for prestressed girders as reported by Kasan and Harries (2009). Although replacement of girder would seem like the best strategy for severely damaged girders, it may not be the most viable option due to other complexities like traffic closure, removal of roadway deck, disturbance to the deck rebar, and time for completion.

Table 2-5 Repair Selection Criteria (Shanafelt and Horn 1980).

Damage Assessment Factor	**Repair Method**			
	External PT	**Strand Splicing**	**Steel Jacket**	**Girder Replacement**
Behavior at Ultimate Load	Excellent	Excellent	Excellent	Excellent
Overload	Excellent	Excellent	Excellent	Excellent
Fatigue	Excellent	Limited	Excellent	Excellent
Adding Strength to Non-Damaged Girders	Excellent	N/A	Excellent	N/A
Combining Splice Methods	Excellent	Excellent	Excellent	N/A
Splicing Tendons or Bundled Strands	Limited	N/A	Excellent	Excellent
Number of Strands Spliced	Limited	Limited	Large	Unlimited
Preload Required	Perhaps	Yes	Probably	No
Restore Loss of Concrete	Excellent	Excellent	Excellent	Excellent
Speed of Repair	Good	Excellent	Good	Poor
Durability	Excellent	Excellent	Excellent	Excellent
Cost	Low	Very Low	Low	High
Aesthetics	Fair*	Excellent	Excellent	Excellent

N/A: not applicable
*can be improved to excellent by extending corbels on fascia girder

NCHRP Report 280 (Shanafelt and Horn 1985) was the second phase of NCHRP 12-21 where the guidelines and methods presented in the previous report were load tested and suggestions on implementation were made. A single girder was artificially damaged and repaired by one of the methods mentioned in the previous report. These repaired girders were then load tested. It should be noted that these tests were not up to failure. Ten different load tests were conducted on a single I-girder to measure the behavior of each repair (Kasan and Harries 2009):

1. Load girder up to 75% of the calculated ultimate load capacity;
2. Add concrete corbels and post-tension high-strength bars and load;
3. Disconnect high-strength bars and load (same as load test 1 but girder is now cracked);
4. Break out specified concrete to sever 4 strands (25% of the total 16 strands) and load;
5. Splice 4 strands with single strand splice and patch and load;
6. Reconnect post-tension high-strength bars (same test as test 5 but with external PT);
7. Disconnect bars, break out concrete and sever the four strands spliced in test 5 and load;
8. Patch the girder and tension the external bars;
9. Disconnect bars, break out patch, sever 2 more strands for a total of 6 and splice them with a steel jacket and load; and
10. Load the steel jacketed girder to 100% of the calculated ultimate moment capacity.

Since the load was applied incrementally and due to the lack of control specimen, proper conclusions cannot be drawn from the test. There has been a

significant number of research and tests carried out after the NCHRP Project 12-21 to validate different repair techniques on damaged prestressed girders.

Strand splicing is a technique of connecting severed strands to recover the prestress force in the damaged bridge girder. Different methods of strand splicing, torque wrench method, 'turn of the nut' method were studied by Labia et al. (1996) and found that the 'turn of the rut' method was successful in recovering the strength of the damaged girder. However, the location and size of the splicing and geometry of the girder have been found to be problematic. A strand-spliced test girder failed in tension at less than 82% of the original girder capacity (Olson et al. 1992). In any case, repairing more than 10-15% of the total number of strands within a single girder is not recommended (Zobel and Jirsa 1998). Various commercially available splices are often used for strand splicing lately.

2.2.2 CFRP Laminate Strengthening of damaged girders

One of the most popular methods of repair and strengthening of damaged prestressed girders is by the use of External bonded CFRP retrofit. The use of CFRP strips to restore the flexural capacity of damaged bridge girders have been well documented (Scheibel et al. 2001, Tumialan et al. 2001, Klaiber et al. 2003, Green et al. 2004, Reed and Peterman 2004, Wipf et al. 2004, Reed and Peterman 2005 and Reed et al. 2007). One or more than one layer of CFRP laminates is often attached to the tension side of the bridge girder to recover the flexural strength. CFRP strips are often provided transversely at a certain spacing to prevent the early debonding of the laminate. The increase in flexural capacity for the repaired girders has been reported in the range of 91% and 108% when compared with the undamaged, unrepaired control girder (Green et al. 2004). A 20% reduction in beam deflections was also observed (Klaiber et al. 2013). Along with the increased flexural capacity

and reduced deflection, CFRP also provides confinement to prevent any kind of popping out of concrete repair mortar.

CFRP may also be prestressed before application to utilize the tensile strength. It is initially prestressed before applying to the bottom surface. The benefits of stressing CFRP strips prior to application are similar to that of using a prestressed strand in a concrete beam. The four main advantages of using a stressed CFRP repair are: a) better utilization of the strengthening material; b) smaller and better-distributed cracks in concrete; c) unloading (stress relief) of the steel reinforcement; and d) higher steel yielding loads (Nordin and Taljsten 2006). Prestressing CFRP systems create an active load-carrying mechanism which ensures that a portion of the dead load is carried by the CFRP laminates. Other methods of repair and strengthening of damaged girders with CFRP are also tried and tested. Unbonded post-tensioned CFRP is one such method where CFRP strips are drawn into tension and post-tensioned by the use of mechanical anchors at girder ends. Near-surface mounted; where the CFRP strips are placed in the concrete cover; has also been effectively employed to increase the flexural capacity of damaged girder (Nordin et al. 2002 and Casadei et al. 2006). Kasan et al. (2014) presented a comparison between different repair techniques using CFRP, to evaluate the effectiveness of each repair method, in restoring the flexural capacity of damaged box girder.

Various repair techniques have been tried and tested in the laboratory environment. However, an actual field testing of impact-damaged bridge girder is limited. Kim et al. (2008) performed repair and CFRP strengthening on a 40-year-old four-span prestressed concrete girder. The repaired bridge indicates that the flexural strength of the damaged girder has been fully recovered to the undamaged state, and the serviceability has also been improved. A full-scale finite element analysis in

ANSYS was also performed to compare the flexural behavior of the bridge in the undamaged, damaged, and repaired states. The FEA model by Kim et al. (2008) was a linear Elastic model and no cracking behavior was included in the research. A stiffness comparison of the damaged and undamaged girder was performed based on the calibrated models. The FEA model showed that deflection of the exterior girder and strain in a typical internal prestressing strand after repair was reduced up to 5% compared to the damaged state as shown in Figure 2-8. The live loads were redistributed among the girders due to the prestressed CFRP sheets. A strength investigation of the girders was not performed. Kim et al. (2008b) also performed an analysis of the live load distribution factors (LLDF) of the bridge. It was found that the AASHTO LRFD (2003) and Canadian Highway Design Bridge Code (CHBDC, 2000) LLDF was conservative for exterior girders and non-conservative for interior girders. It was also concluded that the codes underestimated the nominal capacity of the girders.

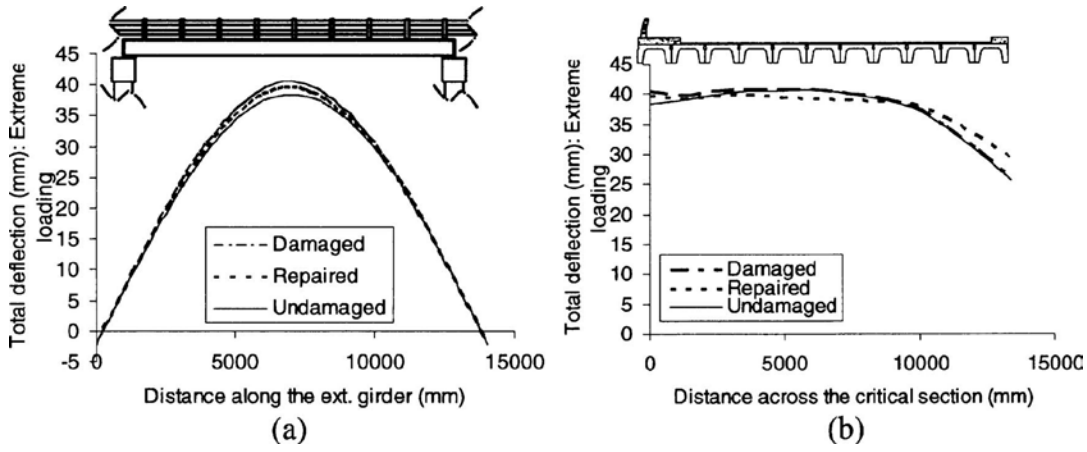

Figure 2-8 Total increase of deflection under the extreme loading: (a) along the exterior girder; (b) transverse deflection profile (Kim et al. 2008)

Cerullo et al. (2013) performed a full-scale testing of an actual bridge girder with a realistic level of damage and cracking. The presented research provides a new shift from laboratory testing to actual-size field testing, where the technology can be demonstrated under realistic conditions. A damaged prestressed girder was transported to the laboratory where it was repaired and strengthened with CFRP laminate. It was shown that the rehabilitated girder could sustain flexural live load demand. The live load capacity of the repaired girder was 33% higher than theoretical capacity. This research was used as a basis for the repair of another impact-damaged bridge with shear deficiency. Montero et al. (2015) performed a live load test on a bridge girder which was impact damaged and subsequently repaired and strengthened with Glass fiber Reinforcement (GFRP). A finite element model of the damaged bridge girder was created and analyzed to compare the strain and deflection results before and after repair. It was found that the strain and deflection response of the repaired bridge girder was less than the damaged bridge girder before repair.

2.3 Bridge Load testing

There are currently 615,002 bridges in the United States and a number of bridges is increasing every year. Along with the increasing number of bridges, the age of the bridge is also increasing and most of the bridges are reaching their 50-year design life period. The average age of bridges in the United States is 43 years old (ASCE 2017) which is one year higher than the reported value in ASCE 2013 Report Card. Most of these bridges are built for a design life of 50 years which shows the aging condition of the nation's infrastructures. Concrete deterioration and steel corrosion are one of the major causes of loss of flexural capacity in concrete bridges. Bridges need to be assessed and evaluated every couple of years to guarantee safety and serviceability of the bridge.

2.3.1 Condition assessment of bridges

Federal Highway Administration (FHWA) uses condition rating to evaluate and code the condition of bridges. Condition ratings are used to describe the existing, in-place bridge as compared to its as-built condition. This can provide a measure of how much deterioration a bridge has undergone through its life period. The rating criteria characterize the overall condition of the bridge including the materials, riding condition, condition of superstructure and substructures. Condition ratings range from 0 to 9 where 0 refers to a failed condition and 9 refers to Excellent Condition (Table 2-6). FHWA Rating and Coding guide provide the general guidelines to quantify the condition of the bridge superstructure and substructure. Condition rating is based on the amount of vibrations, location and density of cracks, riding condition, loss of section or spalling, corrosion in steel and various other factors. It is the responsibility of the inspector to provide an objective condition assessment of the bridge so that necessary safety measures can be taken, if required.

Table 2-6 FHWA General Condition ratings (FHWA, 1988)

Code	Description
N	NOT APPLICABLE
9	EXCELLENT CONDITION
8	VERY GOOD CONDITION — no problems noted.
7	GOOD CONDITION — some minor problems.
6	SATISFACTORY CONDITION — structural elements show some minor deterioration.
5	FAIR CONDITION — all primary structural elements are sound but may have minor section loss, cracking, spalling or scour.
4	POOR CONDITION — advanced section loss, deterioration, spalling or scour.
3	SERIOUS CONDITION — loss of section, deterioration, spalling or scour have seriously affected primary structural components. Local failures are possible. Fatigue cracks in steel or shear cracks in concrete may be present.
2	CRITICAL CONDITION — advanced deterioration of primary structural elements. Fatigue cracks in steel or shear cracks in concrete may be present or scour may have removed substructure support. Unless closely monitored it may be necessary to close the bridge until corrective action is taken.
1	“IMMINENT” FAILURE CONDITION — major deterioration or section loss present in critical structural components or obvious vertical or horizontal movement affecting structure stability. Bridge is closed to traffic but corrective action may put back in light service.
0	FAILED CONDITION — out-of-service beyond corrective action.

FHWA identifies the bridges with condition rating 4 or less as structurally deficient bridges. A structurally deficient bridge is one for which either the substructure or the superstructure has a condition rating below 4. This does not mean that the bridge is in immediate danger or likely to collapse. However, continuous monitoring, inspection, and maintenance need to be carried out to maintain the bridge in service. Some bridges have to be restricted to light vehicles or completely closed to traffic. Although ‘deficient’ bridges do not pose an immediate safety risk, some bridges are not suitable for full American Association of State Highway and Transportation Officials (AASHTO) loads which requires load posting on bridges.

Functionally obsolete bridges are those bridges which were built according to standards which are no longer in use. Inadequate lane widths, not enough vertical clearance or occasionally flooded bridges are some examples which may be classified as functionally obsolete bridges. Although not inherently unsafe, these bridges need rehabilitation and maintenance for full proper usage.

According to FHWA, 9.1% of the nation's bridges were structurally deficient in 2016. 6.3% of the total bridge deck area belonged to structurally deficient bridges and there were around 188 million trips across structurally deficient bridge each day (ASCE 2017). It is also reported that 13.6% of the total bridges are functionally obsolete. Currently, FHWA estimates a cost of $31 billion for the rehabilitation of bridges. This asserts a concerted effort from all sectors for repair, rehabilitation, and strengthening of bridge structures. Deterioration in concrete bridges can occur in different ways including degradation of concrete through aging, corrosion of steel, loss of stiffness of bearing pads and diaphragms. There has been a concerted effort to reduce the number of structurally deficient bridges through repair, retrofit, and replacement over the past decade.

2.3.2 Non-destructive load tests

Proper repair and rehabilitation of bridge structures require a thorough condition assessment of the overall condition of the bridge. Non-destructive evaluation techniques are the best way for condition assessment of bridge structures. Different nondestructive testing techniques have been suggested by various researchers for inspection of concrete bridges. Impact-echo testing (Sack et. al 1995), GPR scanning (Hugenschmidt et al. 2006), Infrared Thermography (Clark et al. 2003) are some of the popular nondestructive techniques for bridge evaluation. They can help locate and identify minor damage, cracks or local flaws in the bridge

superstructure. However, all these methods are limited to local damage and degradation at specific locations and fail to provide a realistic in situ behavior of the overall performance of the bridge structure.

Experimental Load Testing of concrete bridges has been a reliable method used for load rating and evaluation of bridges. One method for more accurately determining a bridge's load-carrying capacity is to conduct an experimental load test (Schulz 1993). Lichtenstein (1995) as part of NCHRP Project 12-28(13) '*Bridge Rating through Nondestructive Load Testing'* developed and documented processes for performing load tests and using the test results to calculate bridge ratings. The findings were reported in the NCHRP Results Digest 234 which presents a detailed information about how nondestructive load testing is superior to the established visual or other NDE inspection techniques.

Nondestructive load testing of bridges has been used primarily as a research tool to provide a better understanding of the way in which loads are carried by and distributed through, the bridge structure (Lichtenstein 1995). Load Tests can be classified into two types: diagnostic tests and proof tests. Diagnostic tests are performed to determine certain response characteristics of the bridge, it's response to loads, distribution of loads; or to validate analytical procedures or mathematical models (AASHTO 2016a). It is often employed to properly understand the behavior of the bridge and remove uncertainties related to material properties, boundary conditions, cross-section contributions and deterioration among other things. It is necessary for the load to be sufficiently high to properly model the physical behavior of the bridge. Proof Tests are used to establish the maximum safe load capacity of a bridge, where the bridge behavior is within the linear-elastic range. (AASHTO 2016a). The load is applied incrementally and the response is regularly monitored so that

early signs of distress or nonlinear behavior can be noted. At that point, the test is stopped so that no damage is caused to the structure and safety is assured.

Diagnostic Tests are preferred when there is an uncertainty in the bridge performance. Bridge structural analysis requires assumptions about material properties, boundary conditions, effectiveness of repairs, unintended composite actions, and the influence of damage or deterioration (Lichtenstein 1995). Bridge characteristics like unintended composite action, the participation of parapets and railings, presence of diaphragms, etc. can significantly affect the bridge response. (Table 2-7).

Table 2-7 Factors Influencing Bridge Load Capacity (Lichtenstein 1995)

Variable \ Bridge Type	Beam and Slab	Concrete Slab	Truss	Box Girder
Unintended composite action	P, I/T	N/A	S[1], I/T	P, I/T
Participation of parapets and railings	P, A	P, A	N/A	P,A
Differences between actual & assumed material properties	S, I/T	S, I/T	S, I/T	S, I/T
Participation of bracing and secondary members	S	N/A	S	S
Differing support characteristics and unintended continuity	S, I/T	S, I/T	S, I/T	S, I/T
Analysis/load distribution effects	P, A	P, A	P, A	P, A
Effects of skew	S, A	P[2]	N/A	S, A

P = Primary factor
S = Secondary factor
A = Include in conventional analysis
I/T = Inspection and or testing needed to verify
N/A = Not applicable

Load tests can also be classified as Static load tests and dynamic load tests. A static load test is conducted using stationary loads to avoid bridge vibrations. The intensity and position of the load may be changed during the test. Dynamic load test is conducted with time-varying load or moving loads that excite vibrations in the bridge

(AASHTO 2016a). Vibration tests are used to determine bridge dynamic characteristics such as frequencies of vibration, mode shapes, and damping.

Nondestructive load testing is an effective method of estimating the load carrying capacity of a bridge (El Shahawy and Garcia 1989, Fu et al. 1992, Bakht and Jaeger 1990, Markey 1991; Moses et al 1994). The load carrying capacity of a bridge is found to be higher than predicted by the conventional analytical procedures (Bakht and Jaeger, 1990; Shekar et al. 1993; Chajes et al. 1997; Saraf 1998; Chajes, et al. 2001; Huang 2004). Many researchers found through load testing that in most cases the load-carrying capacities of bridges are higher than those obtained by analytical methods.

Chajes et al. (1997) performed a load test on a three-span, steel girder, and slab bridge and concluded that there was unintended composite action between the girder and deck. In order to estimate the degree of composite action that can be relied upon beyond the loads applied during a diagnostic load test, the load-deflection curve for an actual load test must be analyzed. During the initial stages of loading, the load-deflection curve is linear and follows that of the predicted fully composite section. The linear region labeled in Figure 2-9 shows two lines; the line with the larger slope corresponds to a load-deflection curve for a composite girder. The observed load deflection line follows that of a composite section then, once the bond becomes compromised, the behavior is nonlinear (Koskie 2008). Unintended composite action, or lack thereof, can be predicted by evaluating the response of a bridge during load tests.

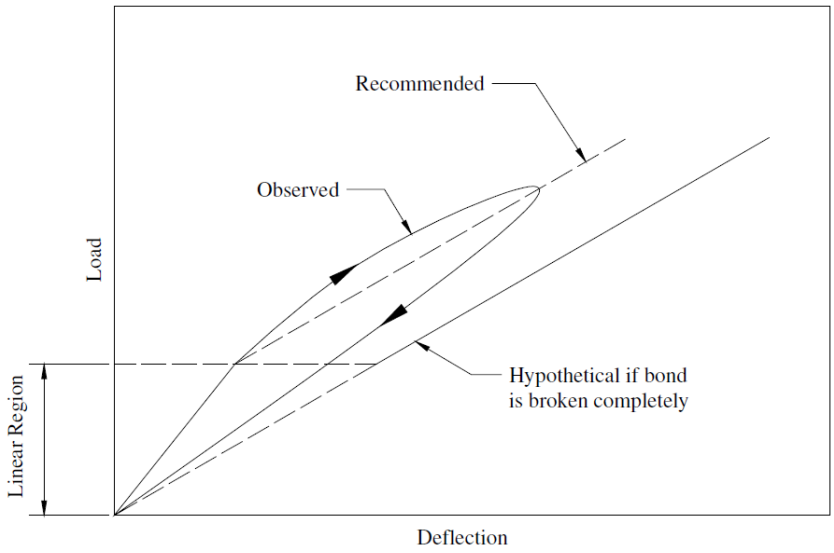

Figure 2-9 Load-Deflection Curve for a Girder with Composite Action.

Barr et al. (2001) performed a live load test on prestressed concrete girder bridge and evaluated the AASHTO LRFD live load distribution factors for three-span, prestressed concrete girder bridges. Changes in LLDFs due to lifts, intermediate diaphragms, end diaphragms, continuity, skew angle, and load types were determined based on an adjusted finite-element model of the bridge. The AASHTO LRFD live load distribution factors were found to be 28% larger than the LLDFs obtained from the model which shows that AASHTO LRFD specifications are conservative compared to actual experimental test. Similar conservatism was noted by Hodson et al. (2012); Dicleli and Erhan (2009); Yost et al. (2005) and Yousif and Hindi (2007); Kalayci et al. (2011). Live load distribution factors (LLDFs) can provide a good assessment of the overall performance of the bridge structure.

Nondestructive load testing is most commonly used to determine the load rating of a bridge (Klaiber et al. 2001; Schulz et al. 1995; Chajes et al. 1997; Cai and Shahawy 2003; Bhattacharya et al. 2005; Lai et al. 2003). The condition and extent of deterioration of structural components of the bridge are considered during rating

procedures. The load rating of an older bridge for its load carrying capacity should be based on recent thorough field investigation (AASHTO, 2011). Load rating of a bridge is a measure of the bridge live load capacity expressed in terms of inventory rating and operating rating. Inventory Rating is that load, including loads in multiple lanes that can safely utilize the bridge for an indefinite period of time. Operating Rating is the maximum permissible live load that can be placed on the bridge. Load rating through load testing has been used to remove load rating on load posted bridges. Load rating through nondestructive load testing takes into account the participation of secondary elements and redundancy of structure which often leads to a higher load carrying capacity of bridges.

2.3.3 Load tests on CFRP strengthened bridges

Some of the common methods of strengthening of concrete bridges are externally bonded steel plates, steel or concrete jacketing, external post-tensioning and externally bonded fiber reinforced polymer (FRP). One of these strengthening techniques, widely accepted and used, is the external wrapping of damaged concrete bridge components with Fiber Reinforced Polymer (FRP) laminates. CFRP strengthening has been widely accepted as an effective method for strengthening and confinement of bridge superstructures. Load testing on strengthened bridges is often carried out to determine the effectiveness of repair procedure. Load tests before and after repair can give an idea about whether the CFRP strengthening is good. Hag-Elsafi et al. (2000) performed load tests on T-beam Bridge before and after repair. Load tests results revealed that, after installation of the laminates, main rebar stresses were moderately reduced, concrete stresses (flexural and shear) moderately increased, and transverse live-load distribution to the beams slightly improved under service loads (Hag-Elsafi et al. 2000). The research also demonstrated a clear

difference in the cost-effectiveness of CFRP rehabilitation ($300,000) compared with the cost of replacement ($1.2 million) of the structure. A repeat load test on the bridge was also carried out after two years in service. Changes in the quality of the bond between the FRP laminates and concrete, at instrumented locations, were investigated, and those in the retrofit system were studied by observing changes in transverse load distribution, effective flange width, and neutral axis location. The results also indicated that the quality of the bond between the FRP laminates and concrete, and effectiveness of the retrofit system have not changed after two years in service (Hag-Elsafi et al. 2003). Mayo et al. (1999) also performed load tests on a bridge strengthened with CFRP and reported a 94% decrease in load- deflection before and after repair of the structure.

Stallings et al. (2000) performed load testing of a bridge before and after strengthening with FRP plates. Application of the FRP plates was found to reduce the reinforcing bar stresses and vertical midspan deflections of the girders. Reductions of reinforcing bar stresses ranged from 4% to 12% for the static tests and from 4% to 9% for the dynamic tests. Girder deflection reductions ranged from 2% to 12% for the static tests, and from 7% to 12% for the dynamic tests (Stallings et al. 2000). Schiebel et al. (2002) performed a load test on three different load posted bridges before and after CFRP strengthening to verify the effectiveness of the repair procedure and a recommendation to remove the load posting was made. The deflections for both bridges slightly decreased after the strengthening was installed. This reflects the added flexural stiffness due to the CFRP laminates (Schiebel et al. 2002). A study to analyze the flexural strengthening potential of CFRP plates on full-scale pre-cracked prestressed concrete beams was performed by Reed and Peterman (2004). Aidoo et al. (2006) transported eight reinforced concrete bridges

from a decommissioned Interstate bridge and tested in the laboratory after retrofitting with different CFRP techniques. Sasher et al. (2008) performed load rating of the bridge after strengthening with CFRP. The as-built and deteriorated structural capacities of the bridge were calculated using WVU's analysis program.

2.3.4 Finite element modeling of load tested bridges

Bridge load rating through diagnostic load testing and finite element modeling is an established method of condition evaluation of bridge structures. Under the diagnostic type test, the selected load is placed at designated locations on the bridge and the effects of this load on individual members of the bridge are measured by the instrumentation attached to these members (Lichtenstein 1995). Traditional analytical models are not very efficient in predicting the overall structural behavior of the bridge. It is hence necessary to create a model which accurately simulates the geometrical properties, material properties, boundary conditions and load distribution in the overall structure. Finite element modeling used in conjunction with load testing has been proven to be efficient in load rating and structural evaluation of bridge structure. Chajes et al. (1997) created a FEM of the structure's main span with thin plate elements superimposed on a two-dimensional grid made up of line elements. Zhang and Aktan (1997) compared a 2D and a 3D method of modeling and concluded that the 2D model can be also be used for modeling because of less computer processing time than a 3D model. However, with advancement in computing and processing capabilities, it is now possible to create detailed 3D models representative of the bridge behavior in a significantly less time.

FE modeling in conjunction with load testing has been used by various researchers for load rating and structural evaluation (Mabsout et al. 1997, Barr et al. 2006). Mabsout et al. (1997) performed Finite Element Analysis (FEA) of a bridge

using two different FEA software and compared the AASHTO LRFD LLDFs with experimental results and performed parametric studies varying the span length and girder spacing. Chung and Sotelino (2010) evaluated four different modeling techniques for bridge superstructure and compared the deflection, strain and distribution factor with experimental results. The FE model was found to be in good agreement with field tests. A calibrated finite element model can be a powerful tool to understand and analyze the overall bridge behavior. Yost et al. (2005) concluded, through load rating of 200 highway bridges that a calibrated FE model provided higher load rating than the ones with traditional FE models. Based on the load tests and load rating of more than 200 highway bridges, approximately 95% of these bridges obtained higher load ratings when the calibrated FEM approach was implemented. Approximately 80% of the bridges experienced significant improvement in the ratings such that current load limits could be relaxed. Posted limits could be eliminated on approximately 45% of the bridges tested. Sanayei et al. (2012) employed the model calibration techniques in a steel multi-girder bridge and compared three different methods of load rating. Sipple et al. (2014) presented a method of finite element model calibration using Frequency-Response Functions.

Chapter 3

Bridge Description

3.1 MacArthur Bridge

3.1.1 Bridge Plans and details

The MacArthur Blvd. Bridge carrying State Highway 183 (S.H. 183) over MacArthur Boulevard in Irving, Texas has two bridges, one carrying East Bound (EB) traffic and the other carrying the West Bound (WB) traffic. The East bound (EB) bridge was selected for this study (Figure 3-1). The average daily traffic (ADT) on the bridge was around 91,000 vehicles. It is located 20 km (12 miles) west of Dallas, TX. The bridge carries four lanes of East-bound traffic, as part of the State Highway 183 traveling from Irving to Dallas. The exact location of the bridge is 32°50'14.1"N latitude 96°57'32.5"W longitude. There is no skew associated with this bridge. A super elevation of 2% was provided on the top of the bridge.

The bridge is a continuous reinforced concrete bridge which was constructed in 1958. The bridge is a four-span, cast-in-place, reinforced, continuous parabolic-beam bridge (Figure 3-2). It has parabolic continuous beams spanning a total of 54.85 m (180 ft.). Spans one and four are 12.4 m (40.6 ft.) and spans two and three are 14.86 m (48.75 ft.) long. The deck thickness is 165 mm (6.5 in.). The section of the bridge is shown in Figure 3-3. It was initially constructed with four parabolic cast-in place continuous beams. The bridge superstructure was designed for a live load of H20-S16 according to the American Association of State Highway Officials (AASHO) Specifications (1951) and Texas Highway Department Specifications Supplement No. 1. All concrete was designed to be Class A, which corresponds to a minimum compressive strength of 20.68 MPa (3,000 psi) (TxDOT 2014). The bridge was

reconstructed in 1970 and five beams were added as part of the reconstruction. Three new beams on the south side and two new beams on the north were added. The design of the bridge during reconstruction was governed by AASHO Standard Specifications (1967). All concrete was designed to be Class C, which corresponds to a minimum compressive stress of 24.82 MPa (3,600 psi) (TxDOT 2014).

The total width of the deck was 18 m (58.5 ft.) measured from outside of the traffic barriers. The clear roadway width inside the barriers was 17 m (56 ft.). The bridge has a total of nine girders spaced at different spacing ranging from 1.7 m (5.5 ft.) to 2.4 m (8 ft.). The reinforcement used in the construction was according to ASTM A305-49 (ASTM A305, 1949) which corresponds to a yield stress of 275.8 MPa (40,000 psi).

Figure 3-1 MacArthur Bridge Side view

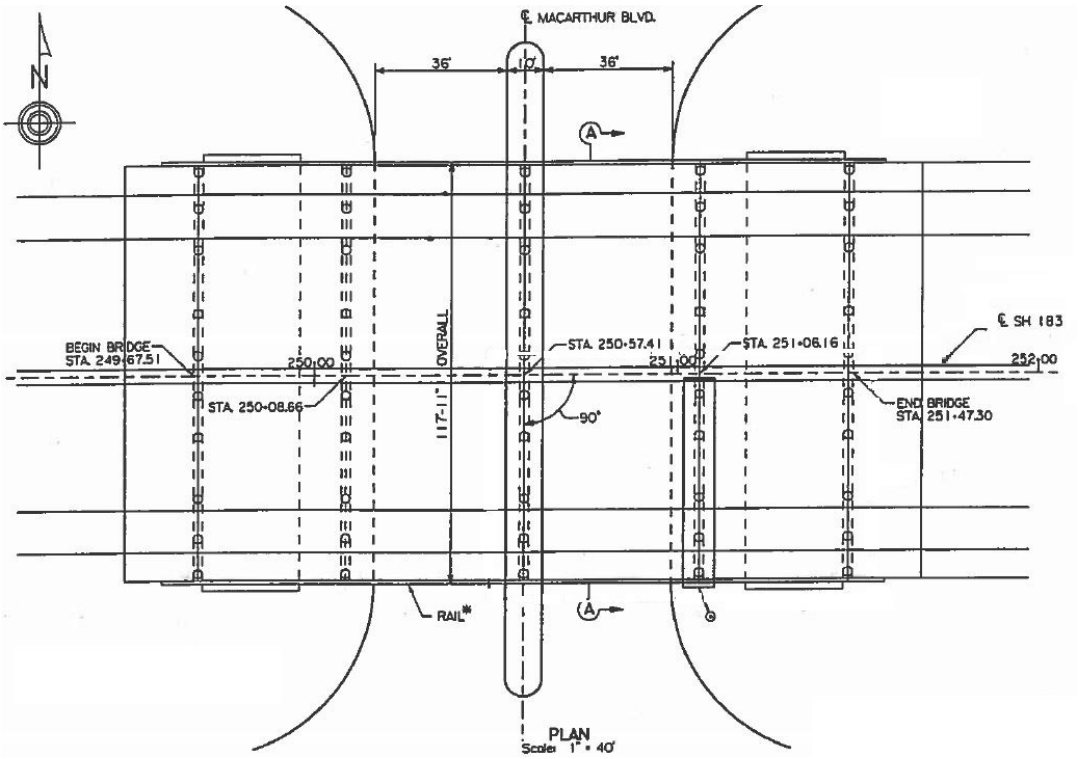

Figure 3-2 MacArthur Bridge Plan

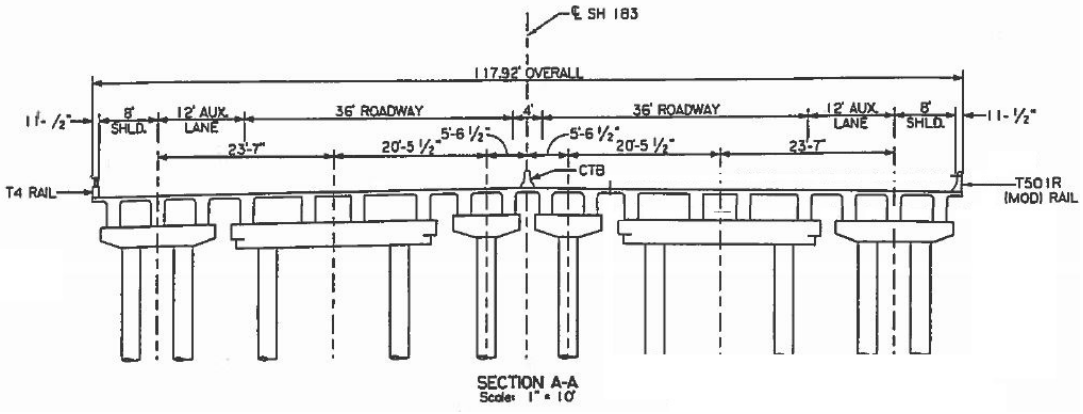

Figure 3-3 MacArthur Bridge cross section

3.1.2 Bridge Damage and Repair

On the morning of Saturday, May 28, 2005, an 11500 l. (3000-gal.) fuel tanker heading east on State Highway 183 barreled through a guardrail and spiraled off a

bridge at about 6:30 a.m. before landing upside down and catching fire on MacArthur Boulevard. It took firefighters 30 minutes to extinguish the blaze. Officials initially closed all lanes in both directions of both roads before reopening State Highway 183 westbound lanes at 11:15 a.m. It took 11 hours to clean up the wreckage. There was extensive heat, and the concrete on the bridge columns and beams spalled and "popped" as a result (Figure 3-4). Gazing at the charred structure, Texas Department of Transportation (TxDOT) engineers said they had never seen anything like the combination of bridge damage and potential traffic headaches confronting them on State Highway 183 due to this accident (Sika, 2006). The east bound traffic was shut down for more than 12 hours and only one lane was open until the bridge could be repaired.

Figure 3-4 Fire damage of MacArthur Bridge (Okafor, Fisher 2005)

A thorough visual inspection of the bridge was carried out by TxDOT engineers. Further sound tapping and hammer tests were also conducted. Four concrete cores were collected from the affected column and the bent cap to determine the condition of structural concrete. Inspection of the cores revealed that the fire had not damaged the reinforcing steel and bond between concrete and steel significantly.

Based on this inspection, it was determined that, although the damage was extensive, the bridge could be repaired.

(a) (b) (c)

Figure 3-5 (a) Removing loose concrete (b) Applying repair mortar (c) Setting forms

The repair involved chipping out of loose concrete and spalled areas. Hollow and unsound area of the concrete was removed using pneumatic and electric hammers. The repair was carried out with factory packaged mortar with silica fume and fibers (Figure 3-5). Galvanized mesh was provided for depths greater than 50 mm. (2 in.). A surface profile of CSP-7 or greater was maintained according to ICRI Technical Guideline No. 310.2R (ICRI, 2013). Steel was cleaned with sandblasting to provide a dust free surface.

Four columns, 6 through 10 along Bent 4 were to be repaired with fiber- reinforced mortar with compressive strength of 21 MPa (3000 psi). Columns 8, 9 and 10 were strengthened with carbon fiber-reinforced polymer (CFRP) wrapping and elastomeric breathable coating was provided. Seven beams were also damaged and needed repair. Seven beams on the south side of the bridge in Span 3 and Span 4 needed extensive repair which was done by a 21 MPa (3,000 psi) fiber- reinforced mortar and six beams were strengthened with CFRP. One layer of CFRP was provided throughout the bottom surface of the parabolic beams and 300 mm (12 in.) U-wraps

were provided every 600 mm (24 in.) spacing. An elastomeric, breathable coating over the CFRP for UV stability and aesthetics was also provided. The damaged area of the deck was repaired with a wet-spray-fiber-reinforced mortar with compressive strength 21 MPa (3,000 psi). The damage location plan can be seen in Figure 3-6.

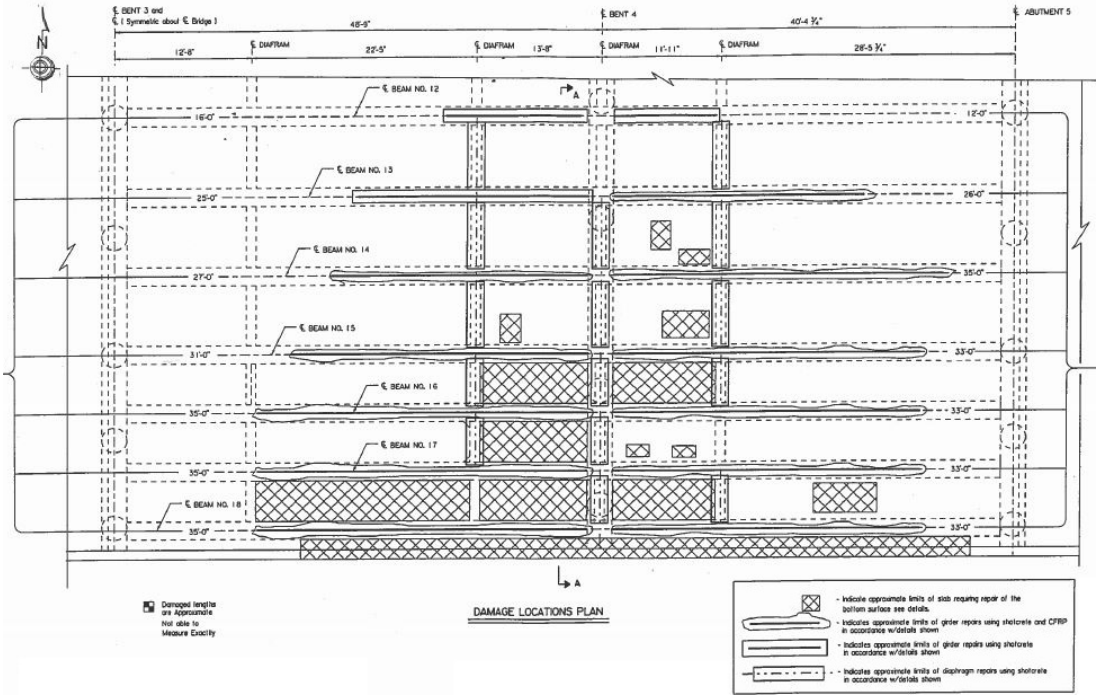

Figure 3-6 MacArthur Bridge beam and deck damage detail

A total of 28.3 m^3 (1000 ft^3) of loose and unsound concrete was removed during the repair process; significantly higher than initially anticipated. The challenges were in maintaining a parabolic shape of the girder and achieving a smooth finish. 28.3 m^3 (1000 ft^3) of mortar was sprayed during the repair process and 9.2 m^3 (12 cubic yard) concrete was poured. Bearing seats were epoxy injected as jacking up and replacing the bearing pad was not feasible for such long span continuous bridge. The CFRP was saturated using automated saturation to control the amount of epoxy. Pull off tests were performed on the FRP-epoxy-concrete after curing to verify the interfacial bond between the concrete and CFRP. The bond between the concrete

and CFRP was found to be satisfactory as reported in Pallempati et al. 2016. The crew was able to successfully complete the repair process within the stipulated time and the bridge was open to traffic within 47 days after the accident (Figure 3-7).

Figure 3-7 Post- repair MacArthur Bridge

3.1.3 Current Condition of the bridge

The latest routine inspection of the bridge was done by the state officials in July 2016. According to the report, the bridge was in '*fair'* condition. The bridge, although functionally obsolete, had a '*satisfactory'* substructure and superstructure condition. The condition rating for the deck, substructure and superstructure was six (UDOT, 1995). The report also mentions the operating rating of 48.5 tons and inventory rating of 35.6 tons. The sufficiency rating of the bridge was calculated to be 94.

A visual inspection was carried out in August 2016 as a part of this study. It was noted that there was minor amount of spalling and cracking on the beams in all spans of the bridge. The cracks ran through out of the section of the beams up to the bottom of the deck. The residual effect of the fire was visible even after the repair on the bottom of the deck [Figure 3-8(a)]. The rebar chairs used during construction had

been corroded which was also the location of the cracks along the girders [Figure 3-8(d)]. Other cracks along the section of the bridge were also noted in the diaphragm and girder interface [Figure 3-8(b)]. Black residue along the crack was observed which was correlated to the result of progression of corrosion in the rebar [Figure 3-8(c)]. Minor spalling and section loss was also seen in different parts the bridge [Figure 3-8(b)]. The effect of temperature exposure was clearly visible in Span 3 and Span 4 of the bridge. The bearing seats of the bridge were epoxy injected as part of the repair process. The mechanical bearing seats were old and it can be safely assumed that they had lost their bearing restraint. The CFRP did not show any visible signs of debonding or delamination. The FRP seemed well bonded to the substrate concrete and the U-wraps were still intact.

Figure 3-8 Current condition of the bridge

3.2 Loop 12 Bridge

3.2.1 Bridge Plans and details

The east bound Loop 12 Bridge carrying State Highway 183 (S.H. 183) over Loop 12 in Irving, Texas was the other bridge selected for this study (Figure 3-9). The East bound (EB) bridge was selected because of the presence of CFRP repair on two girders on the EB side. The bridge was hit by an over-height vehicle which required immediate repair on a few girders. The average daily traffic (ADT) on the bridge was around 55,000 vehicles where 7% of the total traffic was truck traffic. It is located 15 km (9.5 miles) west of Dallas, TX. The bridge carries three lanes of East-bound traffic, as part of the State Highway 183 traveling from Irving to Dallas. The exact location of the bridge is 32°50'12.5"N latitude and 96°54'53.4"W longitude. There is no skew associated with this bridge.

Figure 3-9 Loop 12 Bridge Side view

The bridge is a simply supported prestressed concrete I-girder bridge which was constructed in 1959. The bridge has four-spans with prestressed I-girders and cast-in-place deck on top. (Figure 3-10). The total length of the bridge is 70 m (230 ft.) where the end spans have a span length of 14.85 m (48.75 ft.) and the middle two

spans have a span length of 20 m (65 ft.). The deck thickness is 215 mm (8.5 in.). The section of the bridge is shown in Figure 3-11. It was initially constructed with eight prestressed I-girders. The bridge superstructure was designed for a live load of H20-44 according to the American Association of State Highway Officials (AASHO) Specifications (1953) and Texas Highway Department Specifications Supplement No. 1. All concrete was designed to be Class A, which corresponds to a minimum compressive strength of 20.68 MPa (3,000 psi) (TxDOT 2014). The bridge was reconstructed in 1969 and one girder were added on the south side as part of the reconstruction.

The total width of the deck was 15 m (49 ft.). The bridge had nine prestressed Type C girders which are spaced at 1.68 m (5.5 ft.). The reinforcement used in the construction had a yield stress of 275.8 MPa (40,000 psi). Type C girders have a total depth of 1016 mm (40 in.) and a top and bottom flange width of 355 mm (14 in.) and 559 mm (22 in.) respectively (Figure 3-12). The web width was 178 mm (7 in.). The bridge had a vertical clearance of 4.4 m (14.4 ft.). The deck was a concrete cast-in-place deck which was constructed composite with the girders.

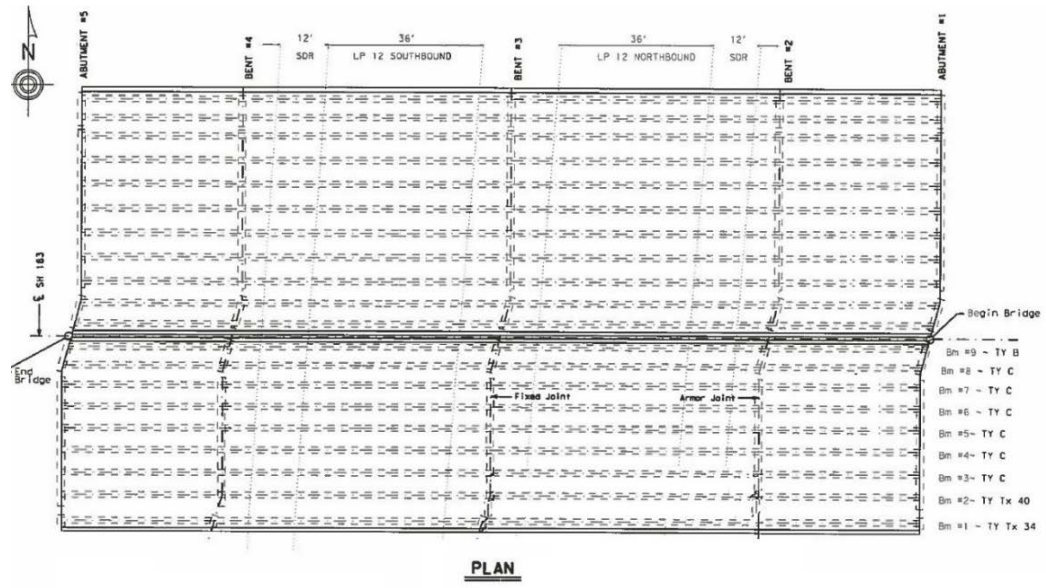

Figure 3-10 Plan view of the bridge

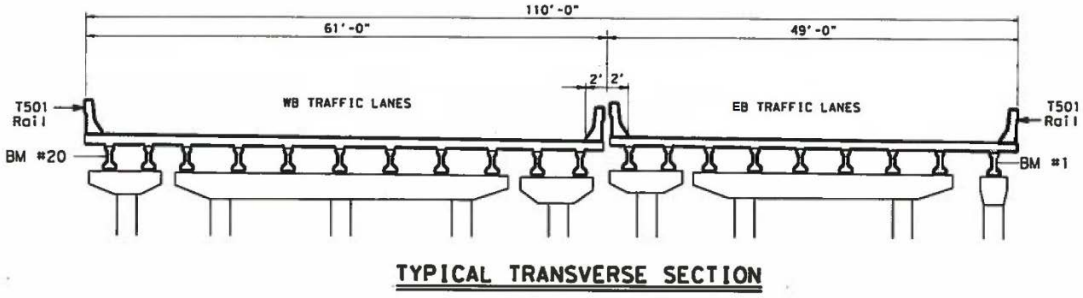

Figure 3-11 Typical section of the bridge

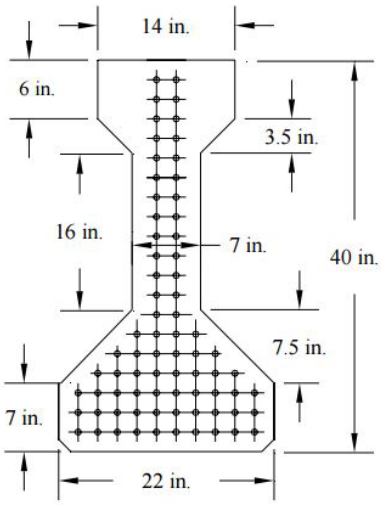

Figure 3-12 Section Geometry of Type C girder (TxDOT 2001)

3.2.2 Bridge Damage and Repair

The bridge has a vertical clearance of 4.4 m (14.4 ft.) which is relatively low compared to other bridges. In 2006, the underside of seven girders along both East-bound and West-bound bridge suffered minor damage from over-height vehicle. Two girders, Beam B3 and Beam B4, on the EB Bridge were damaged and had some scratches and minor section loss at the bottom of the girders. The girders were repaired with mortar and strengthened with CFRP as the level was damage was not severe. Five girders in the West-bound side were also repaired and strengthened with CFRP.

The bridge suffered another significant damage in December 2014 when an over-height garbage hauling truck struck the underside of the bridge and caused significant damage. The garbage hauling truck traveling on North-bound Loop 12 suffered a hydraulic mechanism failure which caused the vehicle to hit three girders and cause significant damage in Beams B1, B2 and B3 of the Eastbound Bridge. TxDOT engineers performed a thorough visual inspection of the damage and the level of severe damage was evident (Figure 3-13).

Figure 3-13 Damage of Loop 12 Bridge by over-height vehicle

It was decided that the two girders, B1 and B2 had to be completely replaced. Beam B1 was replaced with a Texas Type Tx34 prestressed I-girder and the damaged Beam B2 was replaced with a Texas Type Tx40 prestressed I-girder as shown in Figure 3-10. Beam B3, although suffering from significant section loss and severed strands, was adjudged to be repairable and a repair plan was formulated. Beam B3, which was initially repaired in 2006, had a few strands which were exposed as the result of the collision. Several strands were damaged and needed splicing which was done by using a pre-approved '*Grabb-it Cable splice'* (Figure 3-14). The spicing and tightening was done such that a tension of at least 107 KN (20,000 lb.) in each 12.5 mm (0.5 in.) strand was guaranteed. The cracks greater than 0.1 mm (0.004 in.) were all injected with high strength epoxy to seal the cracks.

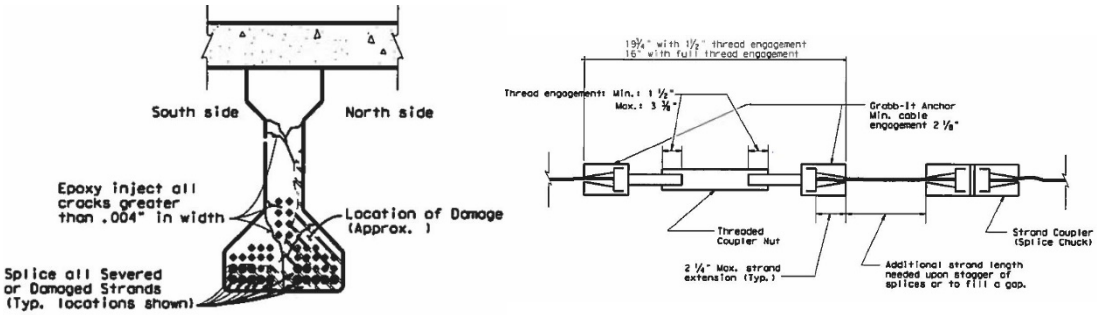

Figure 3-14 (a) Beam B3 concrete and strand damage (b) Schematic of Splice repair installation

The damaged area was repaired with high strength mortar after splicing. Two layers of CFRP were applied on the bottom surface of the girder as shown in Figure 3-14. The length of CFRP along the bottom surface of the girder was 8 m (26 ft.) which extended 1.2 m (4 ft.) outside the repair area. 300 mm (12 in.) wide U-wraps spaced at 600 mm (24 in.) maximum were applied along the 8 m length of the CFRP

for confinement and to prevent delamination of the CFRP. Unidirectional cured laminate CFRP was used for strengthening and also for the U-wraps.

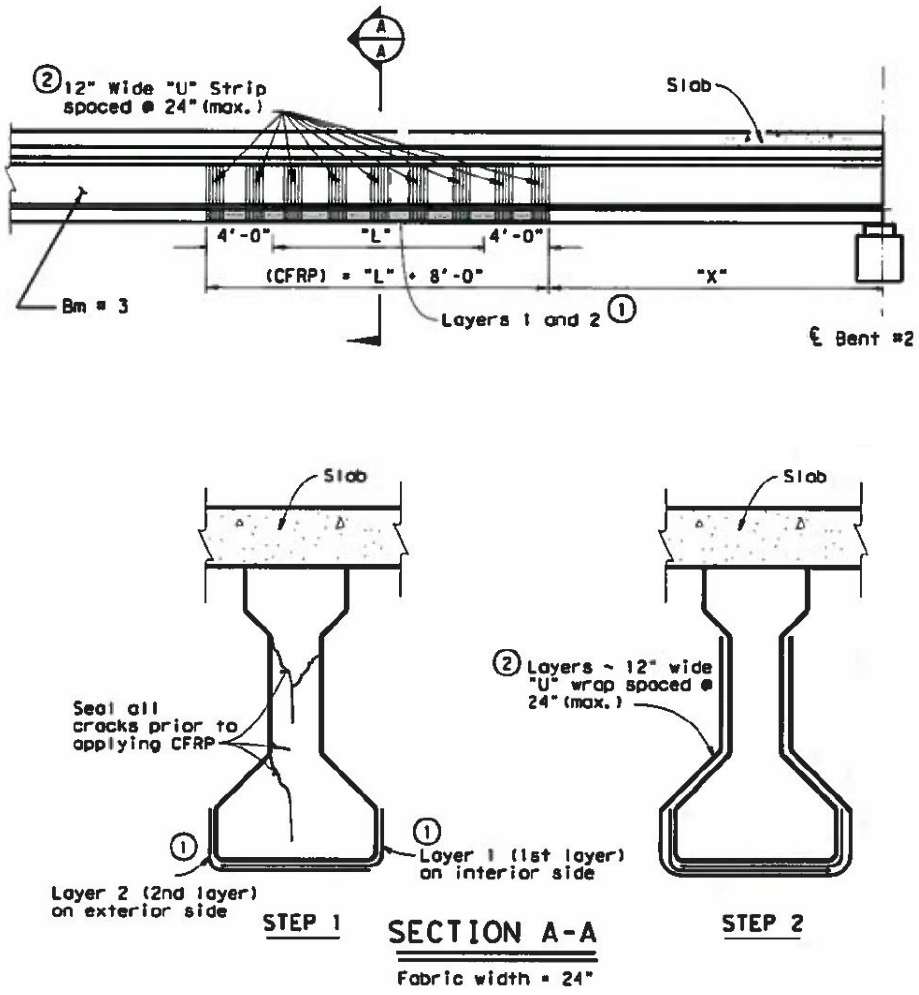

Figure 3-15 CFRP Installation area – North (Exterior) view

3.2.3 Current Condition of the bridge

The latest routine inspection of the bridge was done by the state officials in May 2016. According to the report, the bridge was in '*fair'* condition and there was no load restrictions on the bridge. The bridge had a '*satisfactory'* substructure and deck condition rating (6 out of 9) and a '*fair*' superstructure condition (5 out of 9) (UDOT,

1995). The report also mentions the operating rating of 48.5 tons and inventory rating of 35.6 tons. The sufficiency rating of the bridge was calculated as 79.8.

A visual inspection was carried out in June 2017 as part of this study. The bridge was struck by traffic even after the repair and strengthening process as could be seen from the damage in the south exterior girder. The replaced Tx34 girder had severe section loss due to the over height vehicle impact in Span 2 of the EB bridge. The damage could be categorized as severe damage. Several strands of the girder were exposed and three strand was severed [Figure 3-16(a)]. There was some section loss in Beam B2, a replaced Tx40 girder which was also a result of the vehicle hitting the girder [Figure 3-16 (b)]. Beam B3 was also struck and had some loss of the CFRP jacketing [Figure 3-16(c)]. The severed and spliced strand was visible because of loss of concrete section. Scraping of the surface was seen throughout all the girders in Span 2 [Figure 3-16(d)]. There was visible signs of deterioration of the concrete bents in Bent 3 [Figure 3-16(e)]. The deterioration had caused spalling of concrete and corrosion of the rebar. There were some minor hairline cracks on some of the girders. The CFRP did not show any visible signs of debonding or delamination. The FRP seemed well bonded to the substrate concrete and the U-wraps were still intact. The bridge superstructure did not show significant amount of deterioration other than the section loss and damage due to over height vehicle.

(a)

(b)

(c)

(d)

(e)

Figure 3-16 (a) Loss of concrete exposing strands (b) Bridge bottom showing damage (c) Spliced strands exposed (d) Beam scratched by over height vehicle (e) Bent cap damage

Chapter 4

Testing Procedure

This chapter outlines the details of the instrumentation and the testing procedure incorporated to perform the load test on the bridge. A detail about the desired data, instrumentation plan, instruments used and the procedure followed for load testing is discussed in detail.

Testing for the MacArthur and Loop 12 bridges followed similar procedures, utilizing the same sensors and equipment. Resistance based foil strain gauges were used to obtain the strain data during the test and Linear Varying Deflection Transducers (LVDTs) were used to measure the deflection response of selected girders. Each test required installation of strain gauge to get the strain response of the bridge at critical locations and displacement response at the mid span of the selected girders. Instrumentation and testing procedure is discussed in detail in the following chapter.

4.1 Desired Data

Before a nondestructive load test could be performed, a plan to get the desired data is essential. The main goals of the test was to see the overall performance of the bridge structure and to obtain the distribution factor and the level of damage and strength gain from the CFRP strengthening. Hence, it was decided to use strain gauges to see the response of the structure and the level of local and global damage in the bridge. Strain data can be used as the basis to calibrate the finite element model and to obtain the live load capacity of the bridge girders. Displacement response of the bridge was also desired to evaluate the stiffness of the structural elements.

4.2 Testing Equipment

4.2.1 Strain gauges

Resistance based foil strain gauges with a full Wheatstone bridge were used for the test. Two different types of strain gauges were installed for capturing the strain response for concrete and CFRP. A longer strain gauge is preferred for concrete to cover a larger area and average the strain across the concrete area because of its non-homogenous nature. The Tokyo-Sokki PL-60-11 strain gauge with a gauge length of 60 mm and a resistance of 120 Ω was used for concrete strain. The carbon fiber, however, has fine fibers, which is why a smaller gauge is suitable for composite materials. The Tokyo-Sokki FLA-05-11, with resistance 120 Ω, and gauge length 0.5 mm was used for the CFRP.

Surface preparation of the concrete and FRP surface is an important part of installing strain gauges. Proper surface preparation is required so that they provide accurate and correct measurements. As we were using long strain gauge wires ranging from a length of 6 m (20 ft.) to 30 m (100 ft.), it was necessary to verify that the loss of strain was not observed because of long wires. This was ascertained by comparing the strain response of two regular gauges, placed at the same location, with extension wires, 1.5 m (5 ft.) and 30 m (10 ft.). The strain response was found to be within an error of 3% which was deemed to be accurate enough for our objective.

Installation of strain gauges in the field involved proper surface preparation and attaching them to the surface with the help of a cyanoacrylate-based adhesive. A man lift was used to access and attach the gauges to the bridge structure. The location of the strain gauges were first measured and marked along the beams [Figure 4-1(a)]. The concrete surface was made smooth by grinding and smoothing using a sander to make the surface uniform. It was then cleaned using acetone to

remove the dust and other particles. Water was used to clean off the acetone from the surface [Figure 4-1(b)]. A fast setting epoxy was used as backing for the strain gauges to fill the voids in the concrete and provide a smooth surface [Figure 4-1(c)]. However, epoxy was not used when applying gauges on the CFRP. The strain gauges were then attached to the surface using a cyanoacrylate-based epoxy, a Tokyo-Sokki CN-E for concrete and CN adhesive for CFRP [Figure 4-1(d)]. The wires that were pre-soldered to the strain gauges were then ran along the bottom surface of the beams and taken to the bent caps [Figure 4-1(e)]. A weather proof coating, Epoweld, was used on top of all the strain gauges to protect from rain, dust and moisture infiltration.

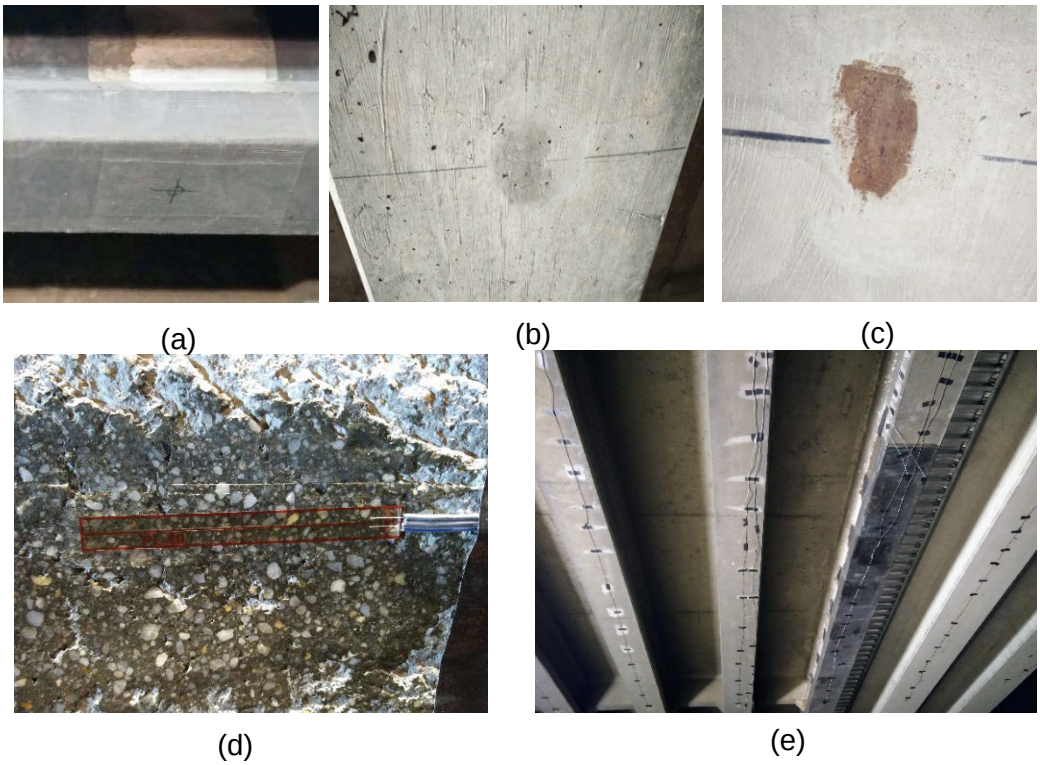

Figure 4-1 Steps of installation of strain gauges on concrete surface (a) marking (b) sanding, cleaning and smoothing (c) epoxy backing (d) attached strain gauge (e) wires pulled to the end of bent caps

4.2.2 Displacement transducers

Deflection measurements are often desired to evaluate the condition of a structural member. It is desirable to ascertain the stiffness parameters of the bridge. It was hence decided to use Linear Varying Displacement Transducers (LVDTs) for deflection measurement. The Tokyo Sokki SDP-200D axial type displacement transducers were used for deflection measurement. The strain gauge type design of the transducer makes it free of noise caused by sliding electrical contact. The LVDTs have a sensitivity of 50 x 10^{-6} strain/mm. The displacement transducers were mounted on top of a 14 ft. step-ladder and clamped firmly as shown in Figure 4-2. Two C clamps were used to secure a CMU block on top of the ladder which was used to clamp the LVDTs and measure the response. The use of step ladders for mounting the LVDTs was only possible because of the level and firm surface. Wires from the transducers were taken to the DAQ and recorded through a laptop.

Figure 4-2 LVDTs mounted on top of ladders

4.2.3 Data Acquisition (DAQ) equipment

The Tokyo Sokki DS 50A data logger with 40 channels was used for recording both the strain and displacement measurements during the test. A

Micromeasurements 8000 model DAQ with 32 channels was also used to connect some strain gauges. The data was recorded simultaneously on both devices at a rate of 100 Hz. All the strain gauges and LVDTs were connected to the data logger and adequate calibration factors were used for each sensors (Figure 4-3). The equipment were grounded against any electrical interference.

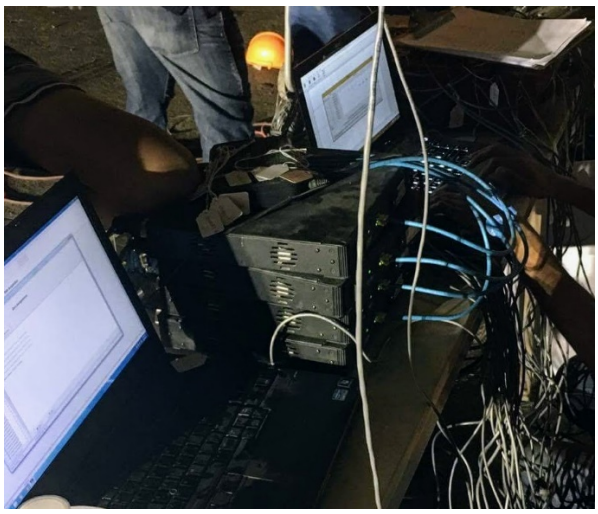

Figure 4-3 Data acquisition systems

4.3 MacArthur Bridge Testing Procedure

The objective of the load test of the bridges is to determine the load carrying characteristics of the bridge structure, given the deterioration of structural components and uncertainties of material properties. The placement of the strain gauges along the structure was governed by the desired objectives. The moment distribution along the beam span, load transfer characteristics between deck and girder and the load distribution across different beams was the governing factor for determining the location of the strain gauges. Damage and CFRP repair also played a major role in selecting the location of strain gauges. This test was also focused on the behavior of the damaged beams compared to the undamaged beams which is

another factor that governed the instrumentation of the bridge. Strain gauges were placed on the most critical locations along the span on all the beams to get the overall response of the bridge.

4.3.1 Instrumentation Plan

MacArthur Bridge is a continuous-reinforced-composite parabolic-beam bridge which had Span 3 and Span 4 exposed to high temperature due to fire. It was the intention of this study to evaluate the performance of that bridge and compare the fire-damaged span with the unexposed span as well as a fire-damaged CFRP-strengthened beam with an undamaged beam. It was hence decided to select a representative damaged beam and another similar representative undamaged beam for the purpose of comparison. Similarly, Span 3, which was exposed to fire damage, was selected to be compared with Span 2, which was not affected by the fire and only exposed to ambient temperature during the fire. Beam 2 was selected as the representative damaged beam and Beam 5 was selected as the representative undamaged beam to see the difference in the displacement and strain values. (Figure 4-4).

Instrumentation of the MacArthur EB Bridge was carried out in May 2017. A total of 66 strain gauges were installed in different critical locations along the beam to evaluate the overall behavior of the bridge. Most of the gauges were installed in a pair so that the compression and tension response can be obtained and the neutral axis of the beam can be estimated. There were a total of 59 strain gauges on concrete and 9 strain gauges on CFRP surface. All four spans of the bridge were instrumented with strain gauges. Gauges were attached on the mid span at the maximum moment region as well as the end of the bridge near supports at the negative moment region of the continuous beam.

The bottom strain gauge was installed in the middle of the bottom surface of the beam. The gauges near the end supports were provided 0.9 m away from the center of the bent cap at the middle of the beam. The top gauges were placed 150 mm below the bottom of the deck surface. It was due to a 100 mm fillet present at the beam-deck interface. Ten sections were selected along the length of the bridge for instrumentation. The layout of strain gauge locations in different sections in the bridge can be seen in Figure 4-4. Data acquisition system was placed in the middle of the bridge under Bent 2. All strain gauge wires were run along the length of the beam to the middle of Bent 2 where they were collected and connected to two data acquisition (DAQ) boxes. A Tokyo Sokki DS 50A and Micro measurements 8000 model DAQ boxes were used to collect the data at 100 Hz.

4.3.2 Load Test Procedure

Load testing on the MacArthur EB Bridge was carried out in June 2017. A preliminary visit to the bridge site was made a few days prior to the test. The bridge was to be demolished as part of the Highway 183 reconstruction which is why the traffic barriers and the asphalt layer was removed prior to the load testing. The traffic was switched to a new bridge constructed adjacent to the existing bridge. This allowed us to work freely on top of the bridge. It was decided to only carry out only a static load test on the bridge. Dynamic effects on the bridge was not within the scope of this research which is why a dynamic load test was not performed.

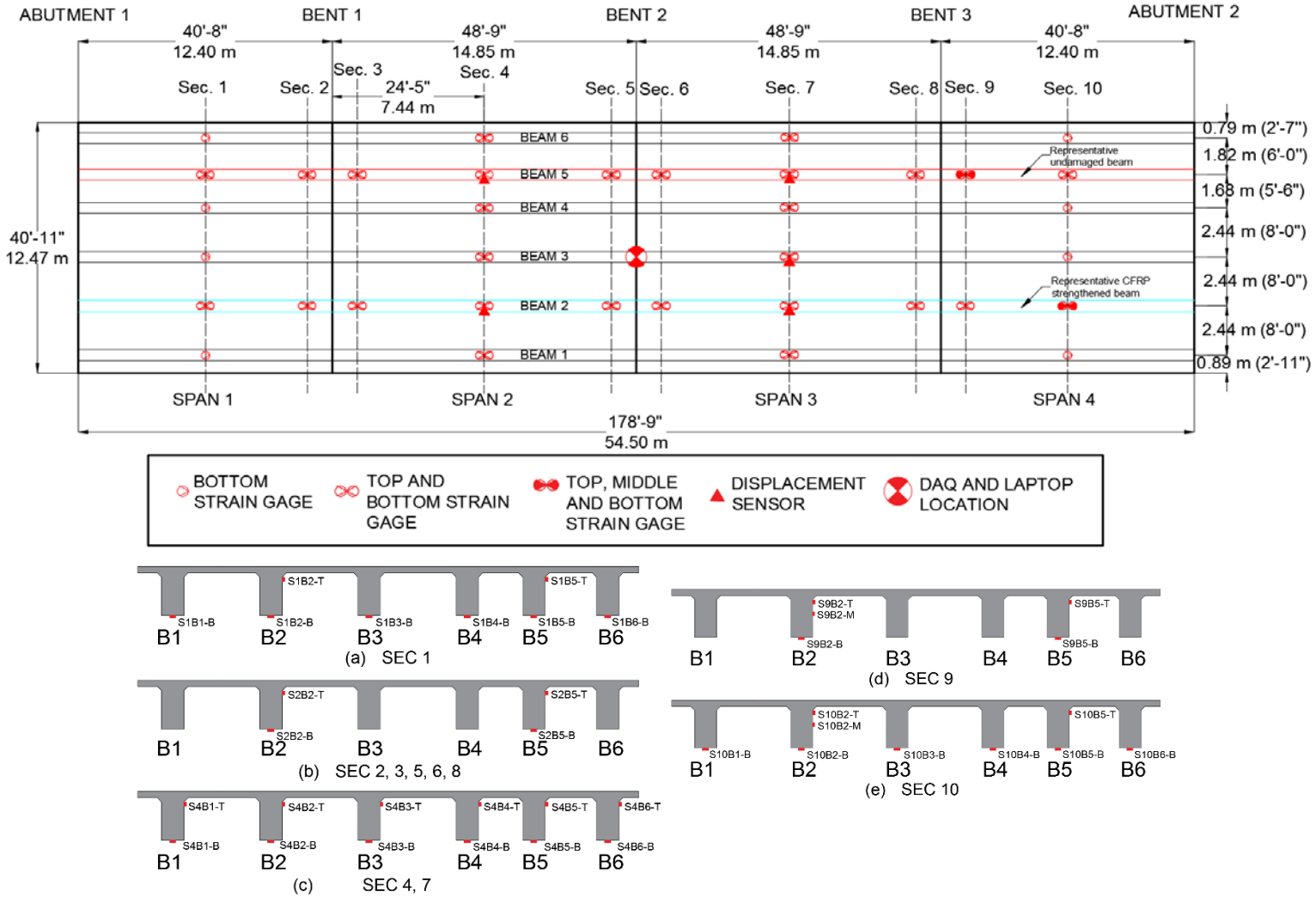

Figure 4-4 Instrumentation plan for MacArthur Bridge

4.3.2.1 Load Vehicle

Two identical trucks, Truck A and Truck B were used for the static load tests. CAT CT660 three axle dump trucks were used for the load test. The trucks were filled with asphalt milled from the roads. The load vehicle was weighed at a CAT weighing station which was able to weigh the axle weights of the truck. Weighing was done prior to the load test and the travel time was less than 5 mins at a moderate speed to assure that there was no difference in axle weight because of shifting of asphalt in the truck. The truck was not weighed after the load test because any change in the truck weight was not expected. The dimensions of the load testing truck is as shown in Figure 4-5.

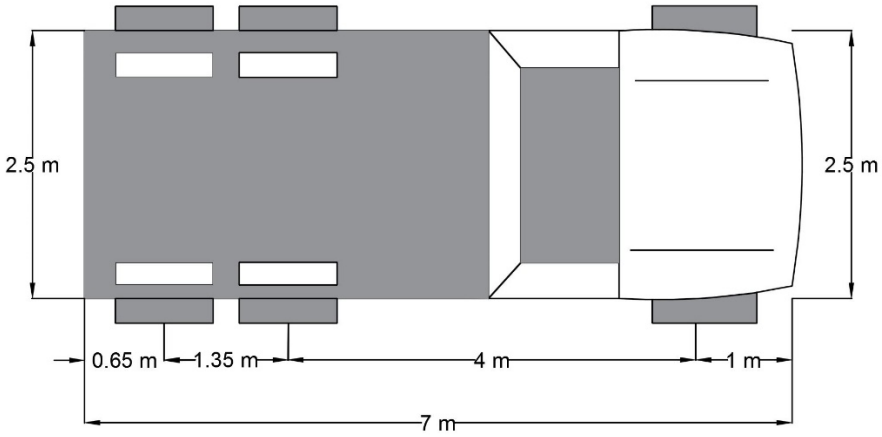

Figure 4-5 Truck dimensions

The weights of each axle of the two trucks is as shown in Table 4-1.

Table 4-1 Test vehicle weights

Weights	Truck A		Truck B	
	(lb.)	(kg.)	(lb.)	(kg.)
Axle 1	19600	8890	18400	8346
Axle 2	23850	10818	19680	8927
Axle 3	23890	10836	19700	8936
Gross Vehicle Weight	67340	30545	57780	26209

It was necessary to co-relate the truck position with the time so that the strain gauge and LVDT response could be evaluated. It was done by using a marker on the truck wheel and taking stop watch readings every revolution of the truck wheel. The wheel revolution distance, defined as the distance covered by the truck wheel in one rotation, was initially calculated by moving the truck for a certain distance. The wheel roll out distance for the trucks was measured to be 3.5 m (136.5 in.).

4.3.2.2 Load test Procedure

The paths for trucks on the top of the bridge were marked on the day of the test. The start of the bridge, end of the bridge and intermediate span locations of the bridge was clearly marked. Two paths Path P1 and Path P2 were selected based on the desired maximum effect on two selected beams (Figure 4-5). Path P1 was marked 3.38 m (10.92 ft.) from the south end of the bridge so as to produce the maximum effect on Beam B2, which was the representative repaired CFRP-strengthened girder for this research. Path P2 was selected at a distance 9.88 m (32.42 ft.) from the south end of the bridge corresponding to the representative undamaged beam, Beam B5.

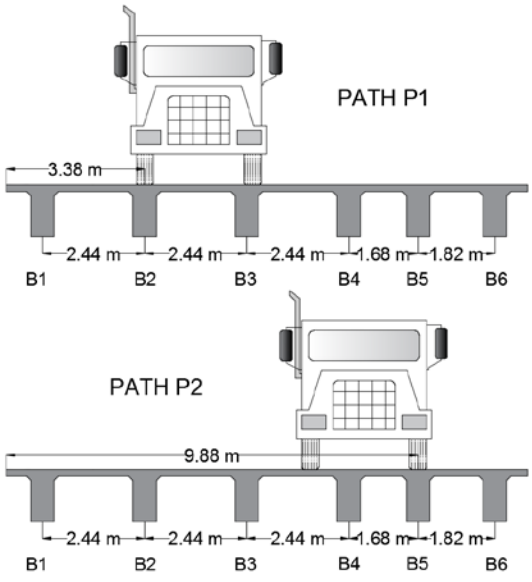

Figure 4-6 Truck paths for load test

Spray paint was used to mark the paths so that it would be visible to the truck during the test (Figure 4-7). Stop locations were also marked along the paths for trucks to stop at certain critical locations.

Figure 4-7 Marking on the top of the bridge

Two types of static load tests were performed for this research. The first type of test is the crawl speed test, where the truck is moved at a slow speed of less than 5 mph. The trucks were moved at a speed of around 1.75 mph on the two predetermined paths. The speed of the truck was kept low so that no vibrations was induced. This helps to avoid dynamic effects on the bridge. Two runs on each path were made for the crawl speed test so that the repeatable data can be collected and the results could be verified. The truck started from the approach slab outside the bridge and went up to the end of the bridge (Figure 4-8). The truck was not able to exit Span 4 of the bridge because construction at the end of the bridge. Right wheel of the truck was kept on the path for Path P1 and the left wheel of the truck was kept on the path for Path P2 to produce maximum effect on the desired representative beams as shown in Figure 4-6.

Figure 4-8 Truck in position for load test

A stop location test was also performed in addition to the crawl speed test. Stop location test is a test where the truck was moved to a predetermined stop location on the bridge so that the effect on the bridge can be recorded. The stop locations were chosen in such a way as to produce maximum positive moment and maximum negative moment on the bridge beams. The stop locations for maximum positive moment was chosen at the mid-span of each span of the beam (Figure 4-9). The trucks were moved along the paths and made stops at the specified stop location for a few seconds so that the reading could be taken and no dynamic effects were induced [Figure 4-11 (a)]. The second axle of the truck, Axle 2 was placed on the stop location to produce the maximum effect on the beam.

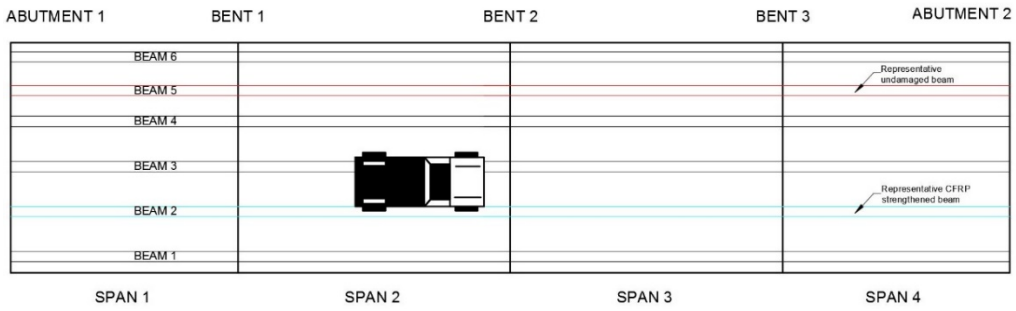

Figure 4-9 Stop locations for positive moment -Typical

The load test was also carried out with two trucks side by side on the mid span of the bridge. Two trucks were placed in such a way that the right wheel of the right truck was on the Beam B2 and left wheel of the left truck was on Beam B5. (Figure 4-10) This allowed us to see the effect on the girder when loaded with 2 trucks. Truck A was on the south side of the bridge and Truck B was on the north side of the bridge [Figure 4-11 (c)].

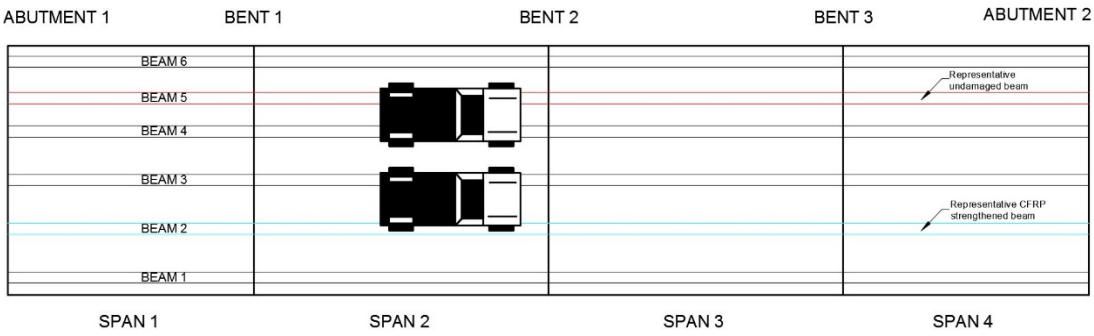

Figure 4-10 Truck positions with multiple trucks

(a)

(b)

Figure 4-11 Trucks in position for producing (a) maximum positive moment (b) Multiple truck presence

4.4 Loop 12 Testing Procedure

This bridge had girders in Span 2 of the East bound (EB) bridge which were damaged by an over height vehicle and repaired and strengthened with CFRP. The EB Bridge was hence selected for the load test. The main purpose of this load test was to ascertain the overall behavior of the bridge and compare the performance of a strengthened girder with an undamaged girder. The effect of severed strands and mortar repair would also be of importance. Since the repair was performed few years before and it was not possible to apply strain gauges on the strands and damaged mortar. However, as mentioned earlier, an exterior girder in Span 2 had suffered another impact damage which was not repaired. It was not possible to load that girder because it was an exterior girder and the truck was unable to get to the end of the width to load it.

4.4.1 Instrumentation plan

The objective of the research was to compare the performance of a relatively undamaged girder with a damaged, repaired and CFRP strengthened bridge girder. It was also the intention to compare the load carrying characteristics and stiffness characteristics of the span with damaged girders and another spans with no damaged girders to see how the distribution factors differ. It was hence, decided to instrument Span 2 and Span 3 of the bridge to achieve the aforementioned objectives. Strain gauges and LVDTs were selected for this test like the other bridge. Beam 3, which was hit by an over height vehicle was selected as the representative CFRP strengthened girder and Beam 7 which was in a relatively sound condition was selected as the representative undamaged girder (Figure 4-12).

Instrumentation of the Loop 12 EB Bridge was done in September 2017. All nine girders in Span 3 and Span 2 were instrumented. There were a total of 34 strain gauges installed and four LVDTs were also installed in addition to the strain gauges. There were 29 strain gauges which were on the concrete surface and the remaining 5 strain gauges were on the CFRP surface. Most of the gauges were installed in a pair so that the compression and tension response can be obtained and the neutral axis of the girder can be estimated. It was not possible to reach the mid span of the girder because of traffic closure issues which is why the gauges were installed at 8.69 m (28’-6’’) from Bent 4 for Span 3 and from Bent 3 for Span 2. Quarter span gauges at 4.95 m from the end and gauges on CFRP were also installed in selected girders.

The bottom strain gauge was installed in the middle of the bottom surface of the beam. The top gauges were placed 50 mm below the bottom of the deck surface. The bridge instrumentation plan can be seen in Figure 4-12. Two data acquisition devices were used for two different spans and were placed in the middle of the span.

All strain gauge wires were run along the length of the beam to the middle of Bent cap where they were collected and connected to two data acquisition (DAQ) boxes. A Tokyo Sokki DS 50A was used for Span 2 and Micro measurements 8000 model DAQ box was used for Span 3. The data was collected at a rate of 100 Hz.

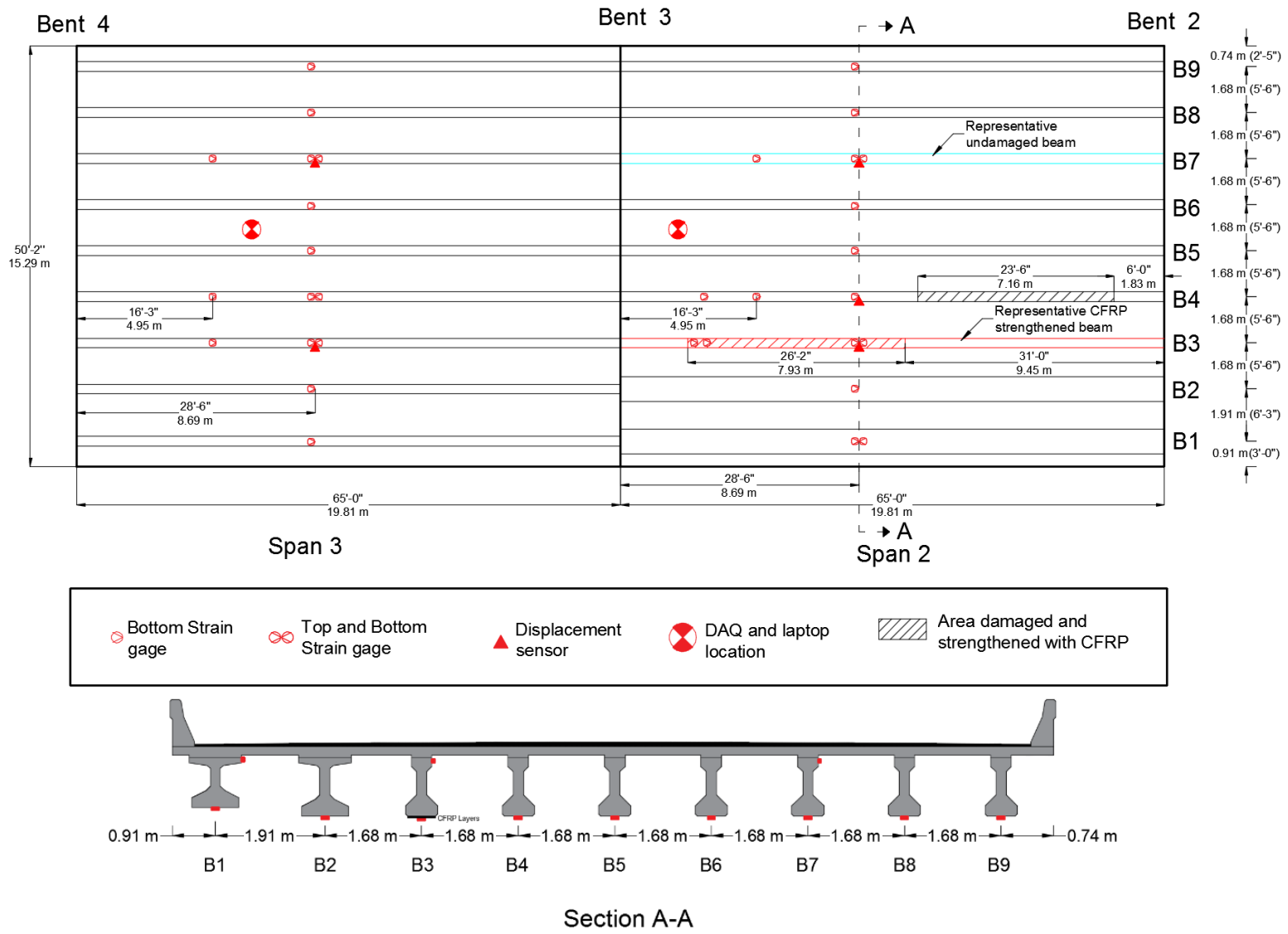

Figure 4-12 Instrumentation plan for Loop 12 Bridge

4.4.2 Load Test Procedure

Load testing on the Loop 12 EB Bridge was carried out in January 2018. A preliminary visit to the bridge site was made a few days prior to the test to check if the gauges were in working condition. It was noticed from visual inspection that there was no debonding of the strain gauges and the wires were properly connected. The load test was then scheduled for the night of January 22. The bridge was to be demolished as part of the Highway 183 reconstruction which is why the traffic was switched to a new bridge constructed adjacent to the existing bridge. This allowed us to work freely on top of the bridge.

4.4.2.1 Load Vehicle

Two identical trucks, similar to the MacArthur bridge test (Figure 4-5) were used for the Loop 12 test as well. The trucks were loaded with asphalt and weighed in the weighing station to get the axle weights. Proper precautions were taken to avoid shifting of load in the dump truck. The weights of the trucks, Truck AL and Truck BL were used for the static load tests. The weights of each axle of the two trucks is as shown in Table 4-2.

Table 4-2 Truck weights for Loop 12

Weights	Truck A		Truck B	
	(lb.)	(kg.)	(lb.)	(kg.)
Axle 1	12440	5640	13300	6030
Axle 2	18600	8440	19120	8670
Axle 3	19200	8700	19600	8890
Gross Vehicle Weight	50240	22790	52020	23595

The wheel roll out distance was 3.5 m (136.5 in.) similar to the MacArthur test.

4.4.2.2 Load test Procedure

The paths for trucks on the top of the bridge were marked on the day of the test. The start of the bridge, end of the bridge and intermediate span locations of the bridge was clearly marked. Two paths Path P1 and Path P2 were selected based on the desired maximum effect on two selected beams (Figure 4-13). Path P1 was marked 4.75 m (14.75 ft.) from the south end of the bridge so as to produce the maximum effect on Beam B3, which was the representative repaired CFRP-strengthened girder for this research. Path P2 was selected at a distance 12.88 m (42.25 ft.) from the south end of the bridge corresponding to the representative undamaged beam, Beam B7.

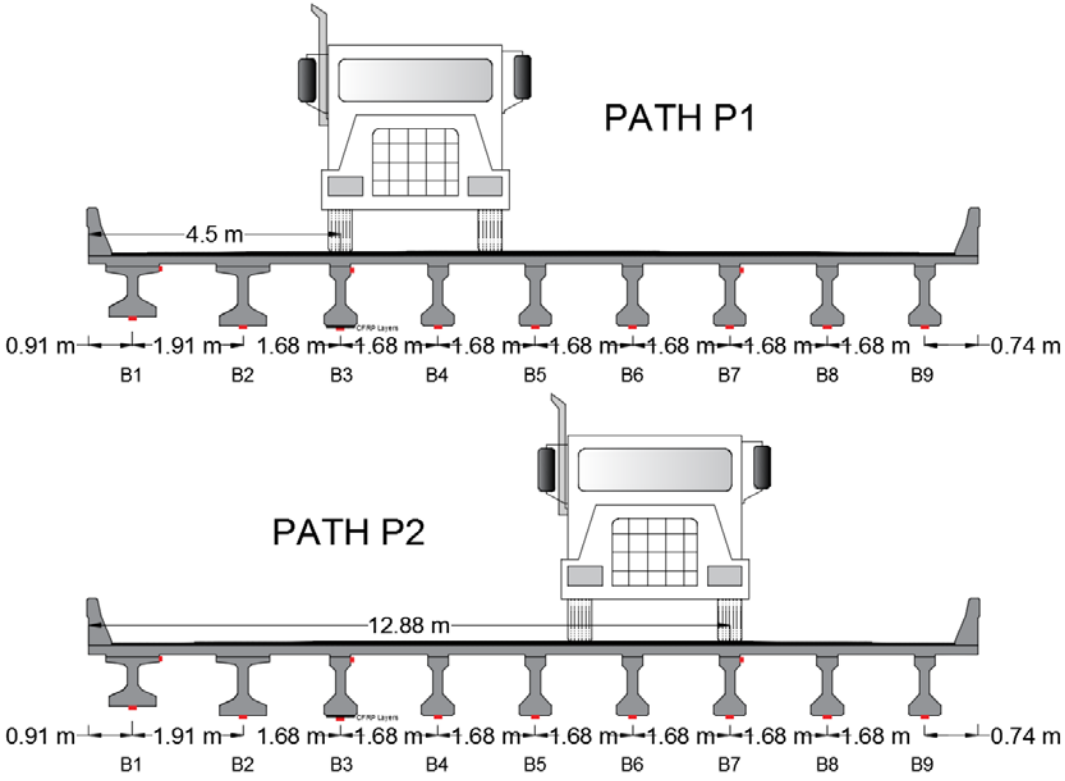

Figure 4-13 Truck paths for Load test

Truck paths were marked on top of the bridge deck using spray paint on the day of the test (Figure 4-14). Start of Bridge and span intersections were also marked. Stop locations at the mid span of the bridge was also marked.

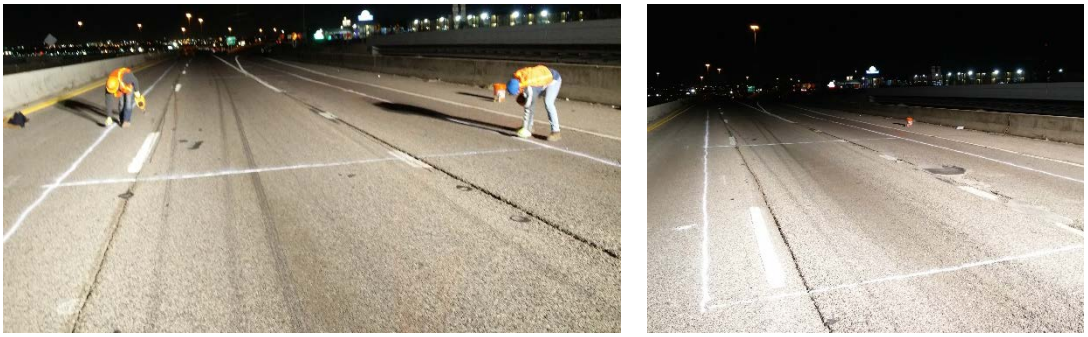

Figure 4-14 Marking on the Roadway

Only static load tests were performed in the bridge. The load test procedure was similar to the one followed in MacArthur bridge. Two Crawl speed tests on each paths were done by moving the truck from the start of the bridge to the end of the bridge along the marked pathways. The speed was kept low to avoid any dynamic effects. Right wheel of the truck was kept on the path locations to produce maximum effect on the representative bridge girders (Figure 4-15).

Figure 4-15 Truck in position for load test

A stop location test similar to the MacArthur Bridge was also performed in addition to the crawl speed test. The trucks were moved and stopped at mid span of Span 2 and Span 3 along the paths so that maximum positive moment can be induced on the bridge girder. The second axle of the truck was aligned with the stop location so that maximum effect can be achieved.

A test with two trucks simultaneously placed side by side on the top of the bridge was also performed. One truck was aligned along Path P1 and the other was aligned along Path P2. The trucks were placed at the mid span of respective girders and moved to another span where they were stopped at the mid span again. The trucks were placed in such a way that the right wheel of Truck A was on the Beam B3 and right wheel of Truck B was on Beam B7 (Figure 4-16). This allowed us to see the effect on the girder when loaded with two trucks. Truck A was on the south side of the bridge and Truck B was on the north side of the bridge.

(a) (b)

Figure 4-16 (a) Trucks in position at the mid span (b) Multiple trucks loaded on top

Chapter 5

Finite Element Modeling

A finite Element model (FEM) of the whole bridge was created in ABAQUS CAE (ABAQUS 2016) to simulate the geometric and material properties of the bridge as closely as possible. Few assumptions were made to simplify the model and reduce the computational time. The geometry of the beam was changed in such a way that the fillet between the deck and the girder was not included in the model. The chamfer provided on the bottom of the beam for aesthetic reasons was also not included to simplify the beam cross section to be rectangular for ease of modeling. In addition, a uniform material property was defined for all the girders and diaphragms, for the preliminary model before a calibrated model was developed. This chapter describes the modeling techniques employed to come up with a final calibrated model for both the bridges.

Finite Element modeling of the bridge included creating a geometric model to simulate the overall geometry of the bridge, defining the initial material properties, defining interactions and boundary conditions and defining the truck load. All these steps will be discussed in detail in this chapter. The initial material property definition, for both the bridges, was similar, which will be discussed first.

5.1 Material Properties

5.1.1 Concrete

Concrete used in the construction was mentioned as a Class C concrete which corresponds to 24.82 MPa (3600 psi) compressive strength. There are different constitutive models available to model the behavior of concrete. However, the smeared crack model and the plastic damage model are the two most commonly

used methods. In this research, concrete compressive and tensile properties were modeled as concrete damaged plasticity as defined in ABAQUS. Concrete damaged plasticity has higher probability of convergence than the smeared crack model. Crack development, pattern and propagation through the structural member was not the purpose of this study. The nonlinear behavior of concrete is attributed to the process of damage and plasticity which can be attributed to microcracking, strain softening and volumetric expansion. This leads to loss of strength and stiffness of concrete (Cicekli et al. 2007; Grassl and Jirásek 2006; Lubliner et al. 1989). ABAQUS uses the plasticity model proposed by Lubliner et al. (1989).

The compressive and tensile behavior of concrete is as shown in Figure 5-1. Under uniaxial tension the stress-strain response follows a linear elastic relationship until the value of the failure stress, σ_{to}, is reached. The failure stress corresponds to the onset of micro-cracking in the concrete material. Beyond the failure stress the formation of micro-cracks is represented macroscopically with a softening stress-strain response, which induces strain localization in the concrete structure. Under uniaxial compression the response is linear until the value of initial yield, σ_{co}. In the plastic regime the response is typically characterized by stress hardening followed by strain softening beyond the ultimate stress, σ_{cu} (ABAQUS, 2014). The stiffness degradation of concrete after the onset of microcracking is defined by a damage factor, *d* which has a value of zero for undamaged section and one for the damaged section. Lubliner et al. (1989) proposed a simple damage model that plastic degradation occurs only in the softening range and is proportional to the compressive strength of the concrete. Damage factor, *d* is defined by the Equation 5-1

$$d = 1 - \frac{\sigma}{f} \qquad \text{Equation 5-1}$$

in which *f* is either the compressive strength or the tensile strength of concrete.

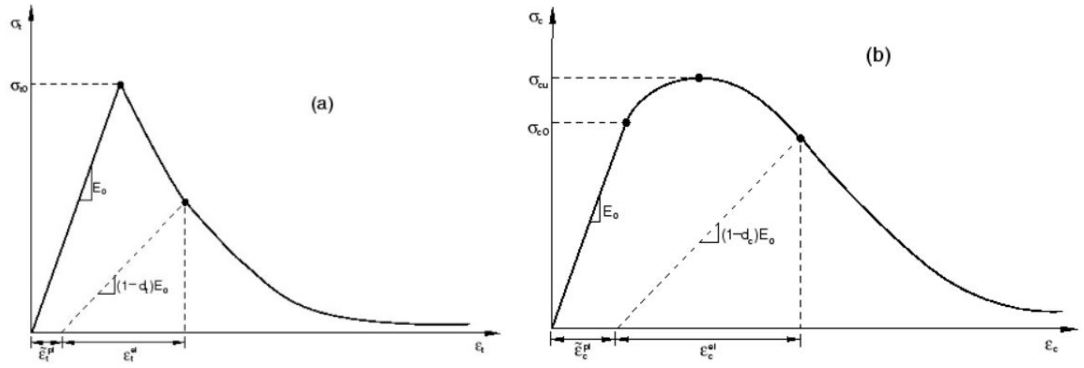

Figure 5-1 Response of concrete to uniaxial loading in (a) tension and (b) compression. (ABAQUS, 2014)

The behavior of the bridge during the load test was within linear elastic range as observed by the strain and deflection response. Although this damage model was used to model the concrete compressive and tensile behavior, only the elastic range of concrete model would be useful for this research. However, a complete non-linear concrete behavior was incorporated into the initial model so that damage and failure analysis could be modeled in the future if required. The material properties of the concrete were further changed based on the core test results, a fire model and a heat transfer model during the calibration process which will be discussed later in this chapter.

5.1.2 Steel Reinforcement

Steel reinforcement which corresponds to the ASTM A306-49 was used in the bridge. The minimum yield strength of the reinforcement was 275.8 MPa (40,000 psi). The nonlinear stress-strain relationship of steel was approximated as a bilinear strain hardening model having different slopes (Figure 5-2). The ultimate stress of the steel was taken as 430 MPa (62,000 psi) based on the ultimate strain of 0.021 calculated

according to Eurocode 1993-1-1:2005 (CEN 2005). The ultimate strain in steel was defined as 15 times the yield strain.

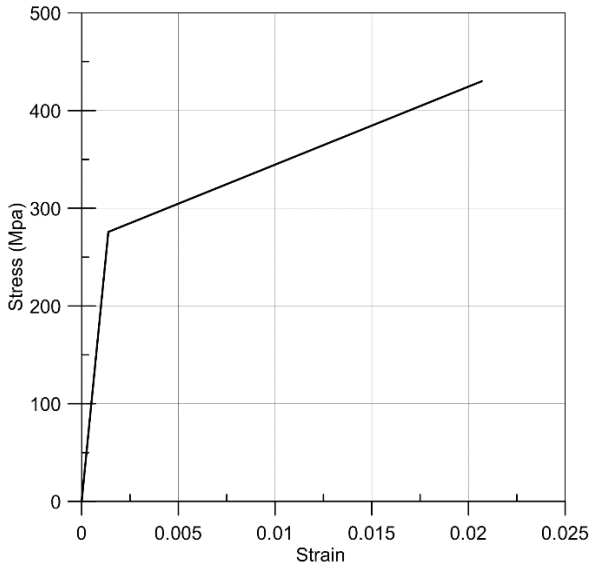

Figure 5-2 Bilinear Stress strain model for Steel

5.1.3 Carbon Fiber Reinforced Polymer (CFRP)

The CFRP used in the bridges was a high strength unidirectional carbon fiber sheet called SikaWrap 117C which was impregnated with a SIkadur 300 Epoxy to create the CFRP laminate. The wet lay-up laminate properties were used as material properties of the CFRP laminate. The behavior was assumed to be linear elastic up to failure. Elastic modulus, Poisson's ratio and tensile strength of the CFRP as reported by the manufacturer were used for the preliminary model as shown in Table 5-1.

Table 5-1 Material Properties of CFRP laminate

Material Properties	US units	SI units
Tensile Strength	105000 psi	724 MPa
Tensile Modulus-Fiber Direction(E_1)	8200000 psi	56500 MPa
Tensile Modulus-Transverse Dir.(E_2)	870000psi	6000 MPa
Thickness (t)	0.02 in.	0.51 mm
Elongation at Break (ε_u)	0.01	0.01
Poisson's Ratio	0.22	0.22
Shear Modulus	610000 psi	4200 MPa

The interface between the FRP surface and the concrete substrate is another important parameter that can affect the behavior of the CFRP laminate strengthened beam. A cohesive surface model which has been found to provide good results in the past, was used for the preliminary model. The cohesive model was later compared with a tie model where the concrete substrate was tied with the CFRP surface. The changes in the structural response between the two models was not significant. This could be because the CFRP laminate does not provide flexural strength as long as the response of the beam is within the elastic limit. It has hence decided to use the tie model for further model calibrations for ease of use and to optimize the run time of the model.

5.1.4 Prestressing Strands

Seven wire 0.5 in. low-relaxation prestressing strands with an ultimate strength of 1860 MPa (270 ksi) was used for the prestressed girders. The PCI (PCI 2004) approximation of the material properties of prestressing strands was used to obtain the stress-strain relationship as shown in Figure 5-3. Although it was decided not to model the prestressing force in the reinforcing strand, the prestressing force was not ignored. Various options of applying the prestressing forces were explored including prestress through temperature difference (Ren et al. 2014) and also through

cohesive bond between concrete and strand surface (Abdelatif et al 2014). However, it was deemed suitable to apply the prestressing force as a predefined field with an initial mechanical stress for the purpose of this study. The prestressing strands were then embedded into the concrete surface so that the prestressing force would be transferred to the concrete.

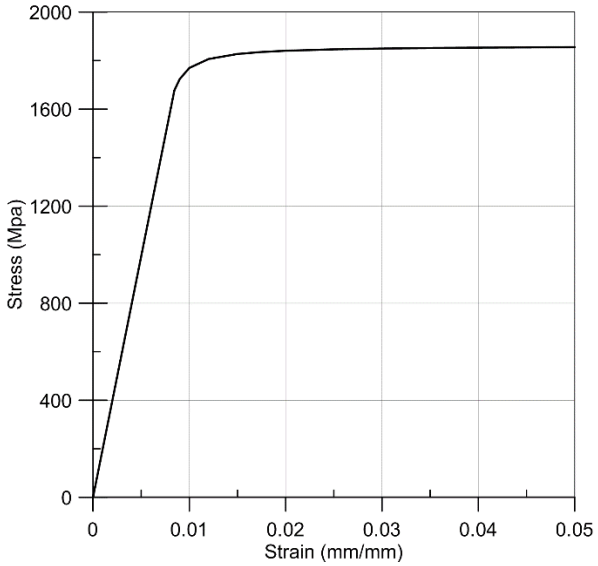

Figure 5-3 Stress Strain Relationship of a Low-lax prestressing strand

5.2 Element and Mesh Selection

Another major issue that needs to be addressed for any finite element model is the mesh size and the element selection to ensure a balance between convergence, accuracy of model and run time. Several analyses of the basic model were run to ascertain the optimum mesh size for the model. Mesh sizes of 6 in., 5 in., 4 in., and 3 in. were used to determine the optimum size of mesh. The AASHTO provisions for the aspect ratio as mentioned in the AASHTO LRFD bridge specifications; “the aspect ratio of finite elements and grid panels should not exceed 5.0” was considered (AASHTO 2016b). The computational burden was another main

aspect for determining the mesh size as shown in Figure 5-4. The computational time for the MacArthur model, for a 3 in. mesh was almost 4 times the time required for a 4 in. mesh; with no significant change in the accuracy and stress values. It was hence decided to use a mesh size of 4 in. for the MacArthur model. Similar mesh sensitivity analysis was done for Loop 12 bridge and a 3 in. mesh was selected for the bridge.

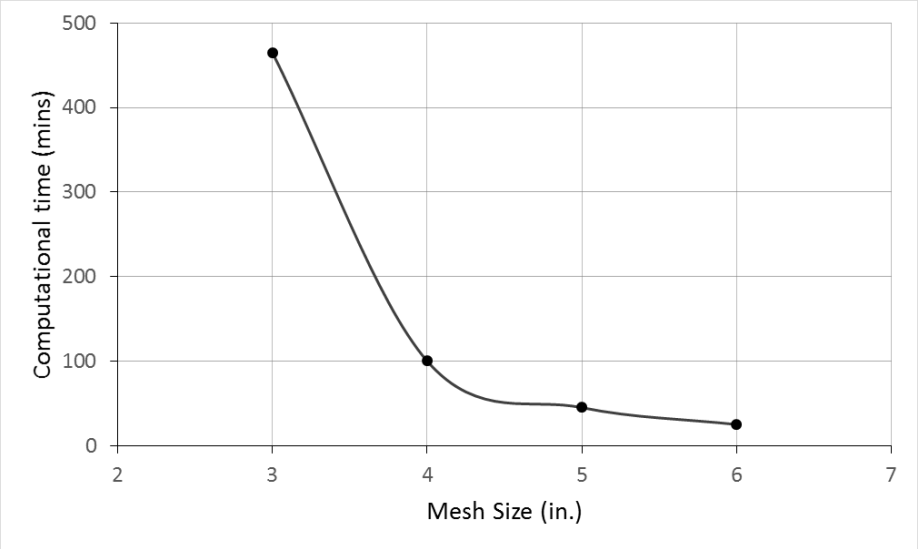

Figure 5-4 Mesh Size vs. Computational Time

The element selected for most of the solid components of the model was 8-node brick elements. ABAQUS uses brick elements called C3D8R, which incorporates reduced integration and hourglass control along with translational degrees of freedom in three global directions of each node. A 2 node linear beam element was used for rebar and prestressing strands. FRP was modeled as shell elements as the dimension of one direction, the thickness, is significantly larger than the other dimensions. The element used for the shell elements was S4R, a 4-node doubly curved thin or thick shell, with reduced integration and hourglass control. The selected elements provided accurate results for the purpose of this study.

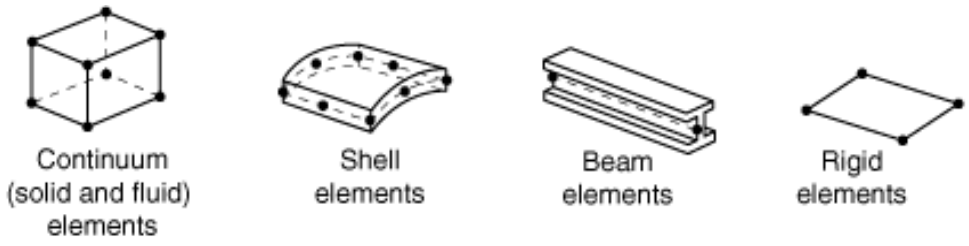

Figure 5-5 Element families in ABAQUS

5.3 MacArthur Bridge Model

The numerical analysis of the MacArthur Bridge was carried out with an aim to obtain a calibrated bridge model that represents the original bridge geometry, condition and in-service condition such that the performance and load distribution characteristics of the bridge could be evaluated. The numerical analysis of the MacArthur Bridge consisted of four steps: basic ABAQUS model, fire analysis, heat transfer analysis, and live load analysis and calibration. The basic model was created in ABAQUS with original geometric and boundary conditions. Fire analysis was performed in Pyrosim software to simulate the fire damage that the bridge suffered. Pyrosim (2018) is a graphical user interface of the Computational fluid dynamics (CFD) based Fire Dynamics Simulator (FDS) software developed by National Institute of Science and Technology (NIST) [NIST 2014]. The third step was to perform a heat transfer analysis to obtain the transient nodal temperature throughout the bridge superstructure. The temperature values were then used to calibrate the basic FE model based on the live load test.

5.3.1 Finite Element Model

5.3.1.1 Geometric Properties

MacArthur Bridge is a continuous reinforced concrete bridge with parabolic girders. The beams, reinforced deck and the diaphragms were built as solid elements. The beam cross section varied along the length of the bridge which was considered during the modeling phase. The beam was modeled continuous throughout all four spans of the bridge. Geometric shape of the beams were simplified in an acceptable manner to aid in proper meshing and to reduce the computational burden. The beam cross section before and after the refinement can be seen in Figure 5-6.

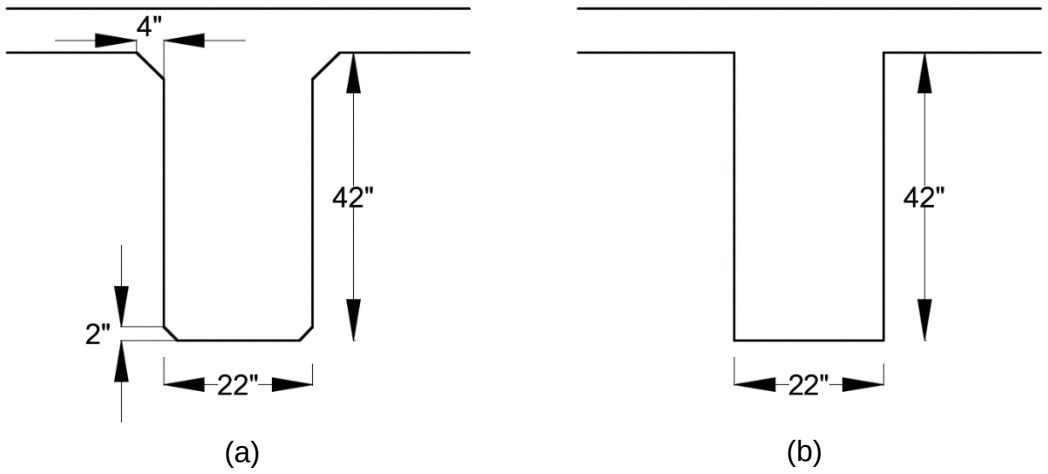

Figure 5-6 Typical Beam Cross Section (a) Actual (b) Simplified

The reinforced concrete deck cross section was assumed to be uniform and continuous across all four spans. A rectangular cross section of the deck was assumed reasonable and accurate for this research purpose.

Diaphragms were also simplified like the beam cross section and chamfers and fillets were simplified as regular rectangular section. The diaphragm cross section was extruded from the beam cross section up to the other beam. Tie constraint was

used between the diaphragm and the beam and also between the deck and the beam to create composite action between the solid surfaces. Tie constraint joins the adjoining nodes together and allows equal amount of displacement and rotation for both nodes which is assumed for composite action between the deck and beam. The assembly of deck diaphragm and beams can be seen in Figure 5-7.

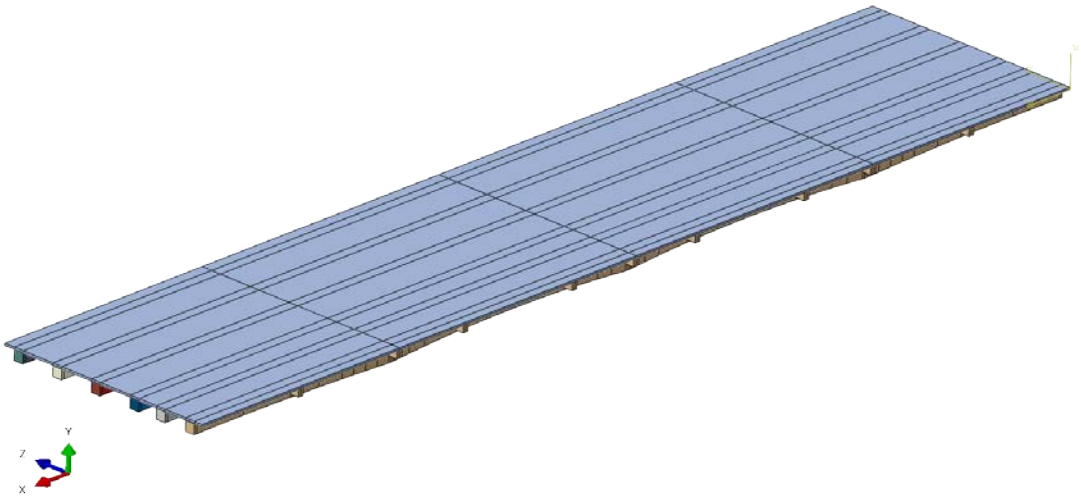

Figure 5-7 Bridge Assembly showing beam, deck and diaphragm

Railings and asphalt layer was removed before the load test which is why they were not included in the model. All the reinforcement were also modeled explicitly for both the beam and the deck as beam elements and embedded into the beam cross section as shown in Figure 5-8. “The embedded element technique… is used to specify an element or a group of elements that lie embedded in a group of host elements whose response will be used to constrain the translational degrees of freedom of the embedded nodes (i.e., nodes of embedded elements)” (ABAQUS 2014). This assumption assumed a perfect bond between the rebar and concrete. CFRP was modeled as 3D deformable shell element with a finite thickness of 0.5 mm.

It was constrained to the concrete surface as tie constraint as discussed in section 5.1.3.

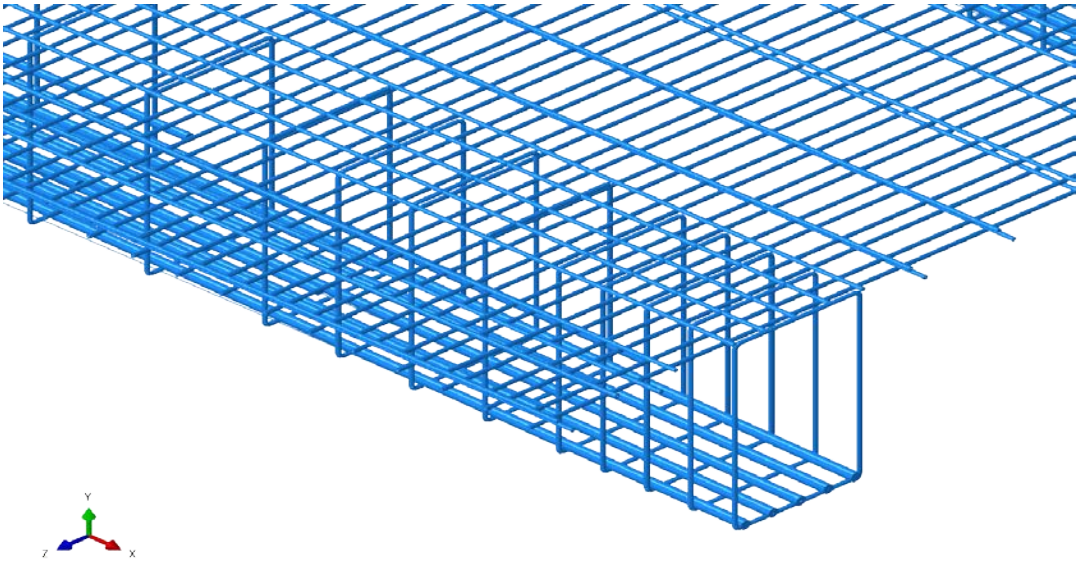

Figure 5-8 Typical reinforcement in Beam and Deck

5.3.1.2 Loads and Boundary Conditions

Only the bridge superstructure was modeled for the purpose of this study. The boundary conditions were defined at the end of each beam span as pinned support and roller support to approximate the behavior of the beams sitting on mechanical rocker bearings. The bearings were old and seemed to have lost any bearing support. Hence, the vertical deformations of the bearings were not considered for this study.

The load from the truck wheels were applied as patch loads. AASHTO LRFD (2016b) suggests that the wheel load can be approximated to be distributed over the area of the wheel contact surface. The wheel contact surface was calculated to be 150 mm (6 in.) based on the pressure of the tires, radius of tires and total load of the truck. The width of the tires was taken as 250 mm (10 in.). Tandem wheels of the rear

axle were modeled as four different wheels on each side. The front wheels were modeled as one wheel on each side. The wheel layout on the deck can be seen in Figure 5-9. The load was applied to the planar surface through which it would be distributed to the deck and eventually to the girders. The planar surface was made 2.5 mm (1 in.) thick and had the same material properties as the deck.

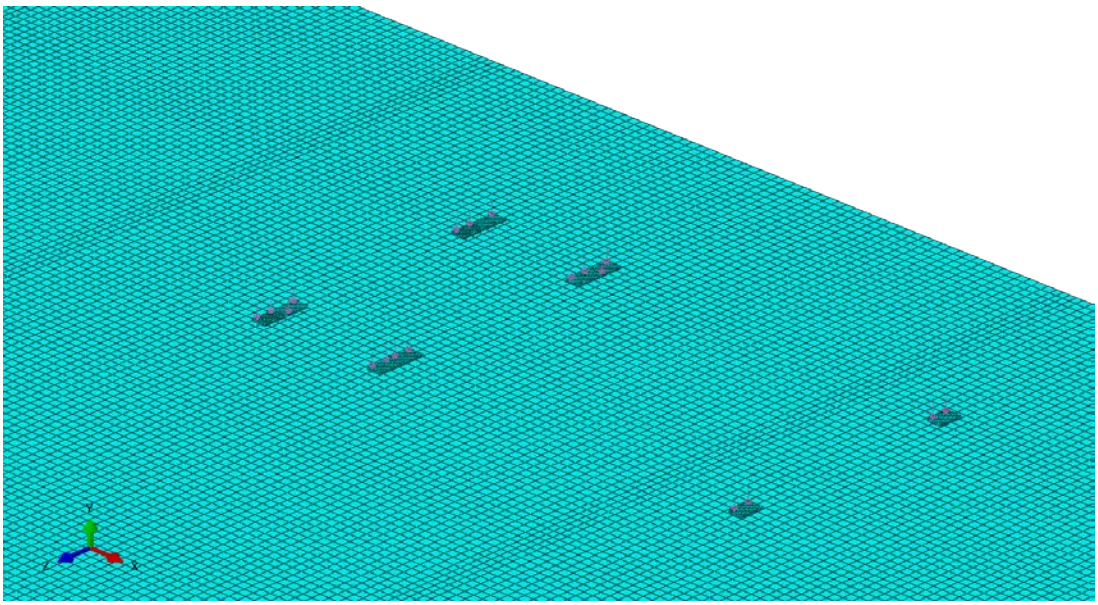

Figure 5-9 Wheel loads applied as patch load

The final step in the modeling process was to mesh all the elements of the bridge superstructure. The mesh size was obtained from the mesh sensitivity analysis as discussed in Section 5.2 and shown in Figure 5-4. Proper care was taken in the meshing such that the meshes of the beam and the deck aligned. This was important for convergence and to reduce the computational time. Meshed finite element model can be seen in Figure 5-10.

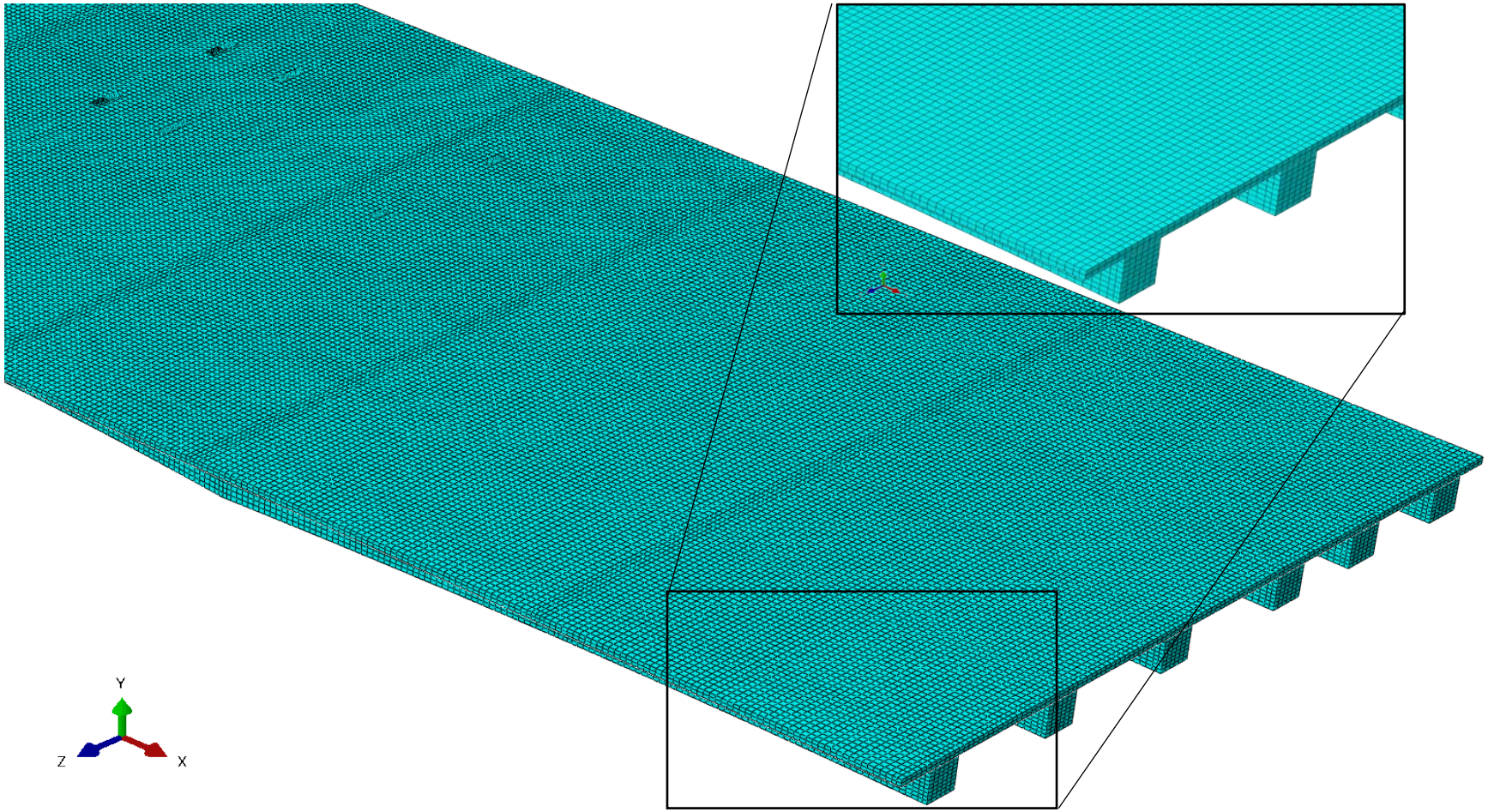

Figure 5-10 MacArthur Bridge Model showing 4 in. mesh

5.3.2 Fire Model

A CFD based fire model for the MacArthur bridge was created using Pyrosim software to simulate the fire damage. Modeling in Pyrosim involves defining the geometry of the bridge structure, creating obstructions and inert surfaces, defining computational domain, material properties, fire combustion properties and source. Thermocouple devices were defined on different locations along the beam span and deck so that the temperature response of the bridge can be obtained. The first step of the modeling process was to create the bridge geometry in Pyrosim. The concrete surfaces were all modeled as inert surfaces. “Inert surfaces are surfaces that remain fixed at the ambient temperature. Heat transfer does occur from gases to inert surfaces.” (Pyrosim 2018). Both EB and WB Bridge were modeled together so that realistic fire results could be obtained. All nine girders that were part of the EB Bridge during the fire in May 2005 were modeled in Pyrosim. Obstructions were modeled on the floor and sides of the bridge to simulate the ground surfaces. Columns, bent caps, deck and railings were also included in the model as shown in Figure 5-11.

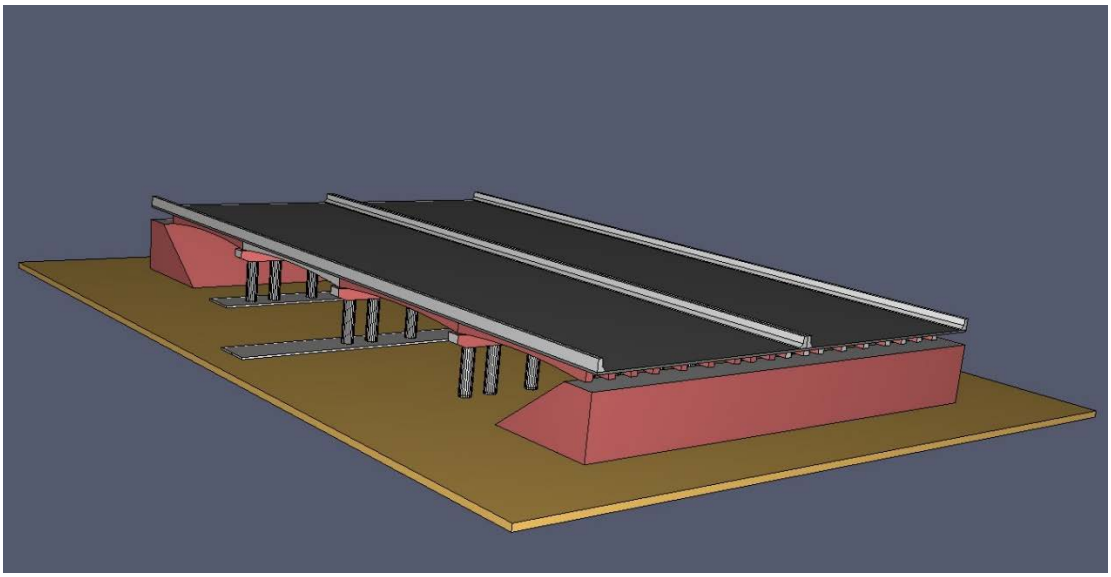

Figure 5-11 Bridge Geometry in Pyrosim

5.3.2.1 Fire Characteristics

The next step in fire modeling was to determine the computational domain. Given the large size of the bridge model, the computational domain of the bridge was selected such that a balance between required accuracy and computational time was obtained. The height of the computational domain was determined based on the pool fire flame height proposed by Heskestad (2016). The flame height was calculated based on Equation 5-2.

$$H_f = 42\, D\, (m''/ r_a \sqrt{(g\, D)})^{0.61} \qquad 5\text{-}2$$

Where

H_f = pool fire flame height (m)

m'' = mass burning rate of fuel per unit surface area $(\mathrm{kg/m^2\text{-}sec})$

r_a = ambient air density $(\mathrm{kg/m^3})$

D = pool fire diameter (m)

g = gravitational acceleration $(\mathrm{m/sec^2})$

The pool fire diameter was estimated based on the size of the fuel tanker and the area of fuel spill. The mass burning rate of gasoline fuel per unit square area was taken as 0.055 as suggested in Table 26.21 of SFPE Handbook (2016). The ambient air density was 1.20 kg/m^3. The flame height based on Equation 5-2 was calculated to be 24.52 m (80.46 ft). Based on these assumptions a computational domain of 70 m x 55 m x 30 m was selected for the fire study as shown in Figure 5-12.

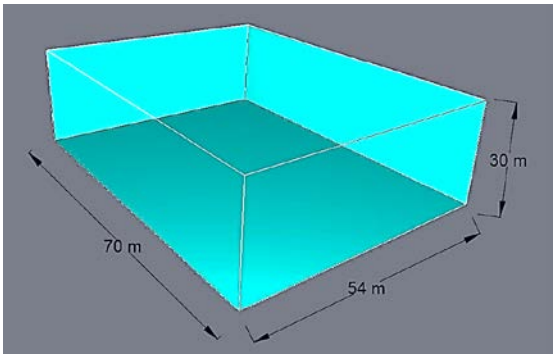

Figure 5-12 Computational domain for fire analysis

The most important aspect of the fire model was to calculate the heat release rate per unit area (HRRPUA) of the fire. The heat release rate of gasoline fire was calculated based on Equation 5-3 as mentioned in SFPE Handbook of fire Engineering (2016).

$$\dot{q} = \triangle h_c \dot{m}''(1 - e^{-k\beta d}) A \qquad 5\text{-}3$$

Where,

$\dot{q}$ = pool fire heat release rate $\left(\text{kW}\right)$

$\dot{m}''$ = mass burning rate of fuel per unit surface area $\left(\text{kg/m}^2\text{-sec}\right)$

Vh_c = effective heat of combustion of fuel $\left(\text{kJ/kg}\right)$

A= surface area of pool fire $\left(\text{m}^2\right)$

kβ= empirical constant $\left(\text{m}^{-1}\right)$

D = diameter of pool fire $\left(\text{m}\right)$

Mass Burning rate of fuel was taken as 0.055 from Table 26.21 of the SFPE Handbook of Fire Protection. The surface area of pool fire was determined based on the dimensions of the truck and fuel spill area as seen in Figure 5-13. The pool fire area was estimated as a rectangular surface on the floor with dimensions 15.25 m (50ft.) x 9.14 m (30 ft.) covering some area across Spans 3 and 4. The surface area of pool fire was 140 m^2 (1500 ft^2).

Figure 5-13 Aftermath of fire on MacArthur Bridge

The heat of combustion of Gasoline fuel was calculated based on the components of Gasoline fuel. The fuel in the presence of Oxygen yields Carbon monoxide (CO), and Soot (NIST 2010). The values of CO yield, ν_{CO} and Soot yield were taken as 0.011 and 0.038 respectively from the SFPE Design handbook (2016). The typical composition of gasoline hydrocarbons (% volume) is 4-8% alkanes; 2-5% alkenes; 25-40% isoalkanes; 3-7% cycloalkanes; 1-4% cycloalkenes; and 20-50% total aromatics (0.5-2.5% benzene) (IARC 1989). Due to the complex composition of Gasoline fuel, it is often approximated as Octane (SFPE 2016). These values of the fuel composition were used to determine the Heat of Combustion which was calculated as 44438.45 KJ/kg. The value obtained was similar to the value reported in the SFPE handbook of 43,700 KJ/kg. '*kβ'* was taken as 2.1. Diameter of the pool fire calculated from the Area of fuel was 13.32 m. The heat release rate of 334,938.68 KW (317,461.58 Btu/sec) was obtained from the calculation. The HRRPUA value was input into the Pyrosim model in such a way that the maximum value was reached within 30 secs and remained constant throughout the fire for 1770 secs (29 mins 30 secs).

A burner surface was created on the bottom of the bridge to simulate the area of fuel spill as shown in Figure 5-14. The fire properties and HRRPUA values were provided in the burner surface.

Thermocouple devices were defined in different surfaces and different sections of the EB bridge so that the temperature values can be obtained. Thermocouples were defined on the midspan of each span of each beam. Other thermocouples were also defined at the end of the span. Few thermocouples were defined on the concrete deck. Figure 5-15 shows the locations of the thermocouples on the bridge.

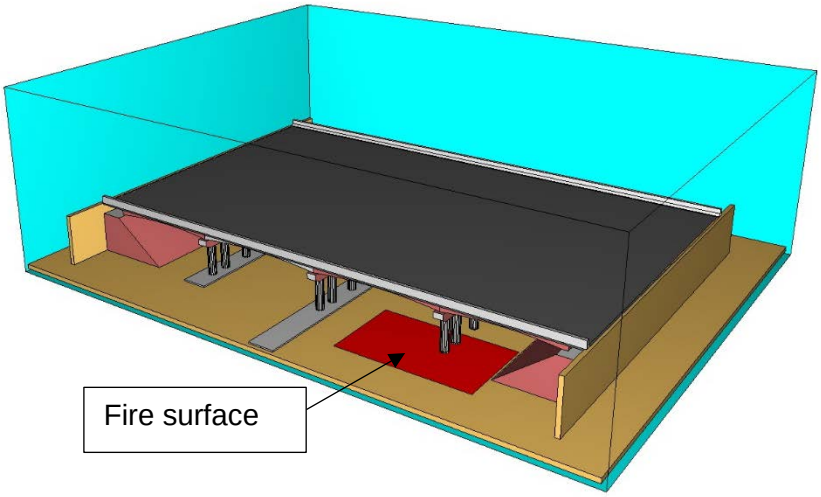

Figure 5-14 Pyrosim model showing Burner surface

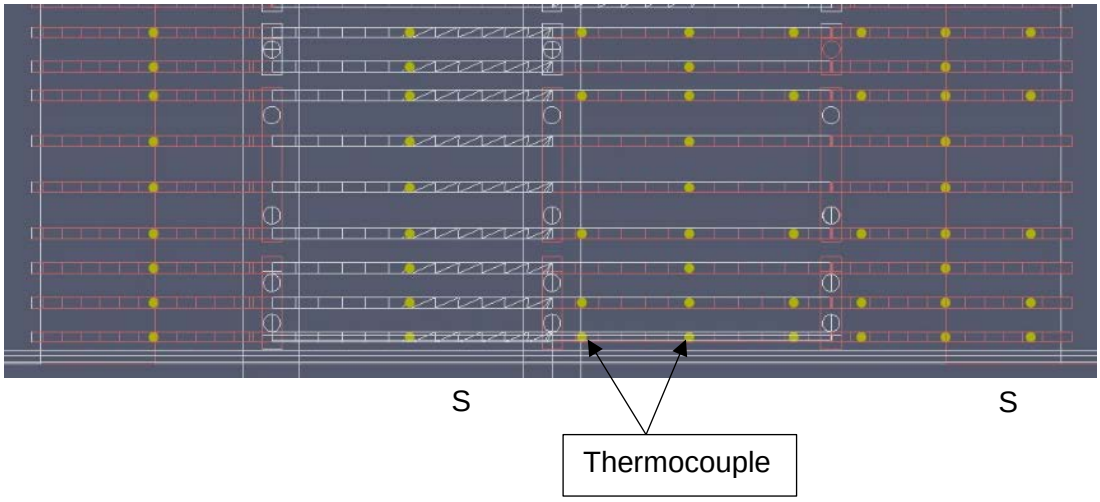

Figure 5-15 MacArthur EB Bridge thermocouple locations

The wind speed and ambient temperature of the morning of May 25, 2005 for Irving, Texas was checked in www.wunderground.com. It was found that the wind speed was 5 mph blowing in the North-west direction. The ambient temperature was 20°C. The wind parameter and the ambient temperature were input in the Pyrosim model as simulation parameters.

5.3.2.2 FDS Results

The results from the FDS is used to predict the boundary fire temperature at the exterior surfaces. One important aspect for the validity of the fire model was to verify the temperature obtained from the model. However, temperature readings and other structural identification tools were not used during or immediately after the extreme event. Few pictures that were available immediately after the fire event during the fire inspection were taken as the basis for the model results verification. Figure 5-16 shows the heat release from the fuel source and the extent of flames during the fire test.

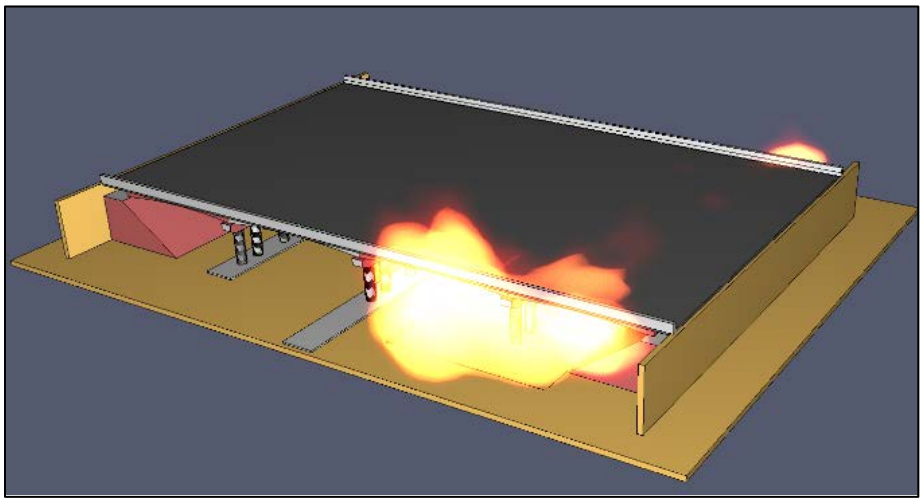

Figure 5-16 Fire from Gasoline during fire

To obtain the temperature profile of the fire at different levels, temperature slices were defined at three different heights: (a) Bottom of the bent cap (b) bottom of the girders (c) Top of the railings. The top of the railings observed a sustained temperature of around 600^{o}C to 700^{o}C throughout the fire as seen from the temperature display shown in Figure 5-18. It can be seen that the temperature remained around 700^{o}C from Bent 2 to Abutment 2 covering Span 3 and Span 4. It

has been reported in literature that steel starts to lose its elastic behavior around 700°C and starts to show plastic deformation with no significant increase in strain. Outinen and Makelainen 2004) performed tensile tests on steel exposed to elevated temperature and observed significant plastic deformation at 700°C (Figure 5-17). This was verified by the deformation seen on the railing steel as seen in Figure 5-19.

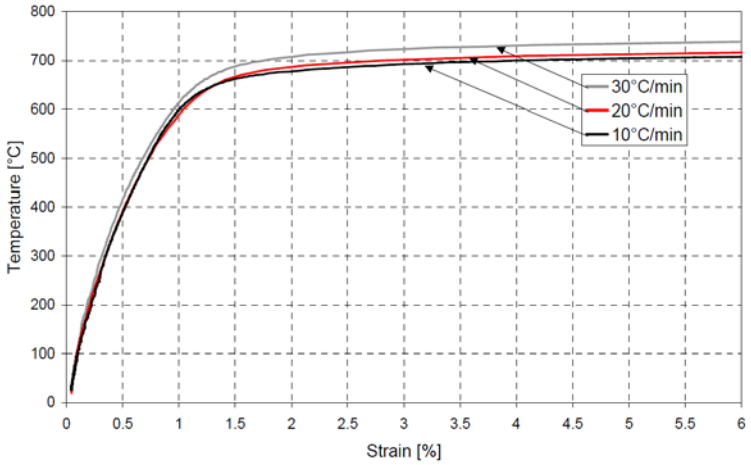

Figure 5-17 Elongation of steel at elevated temperature (Outinen and Makelainen, 2004)

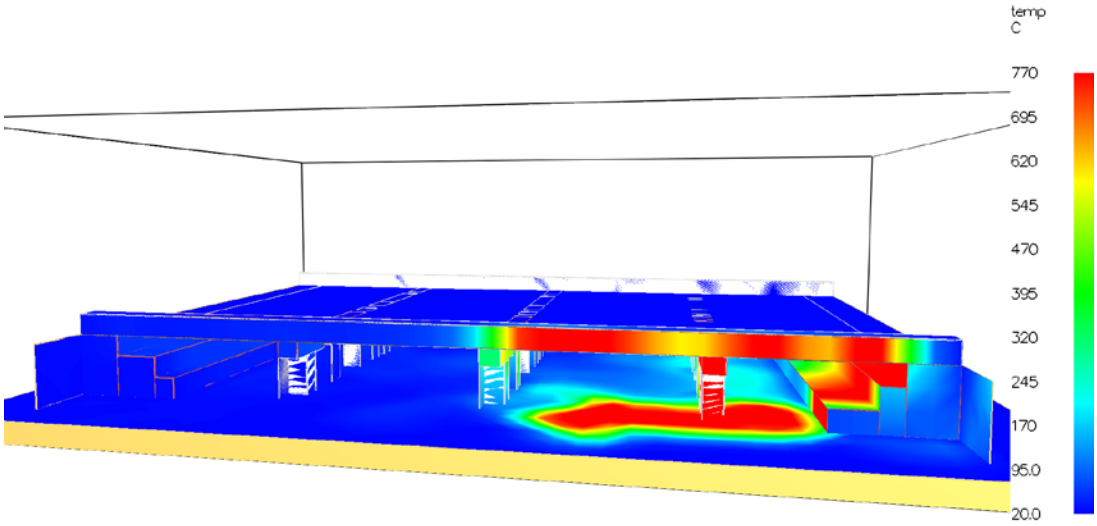

Figure 5-18 Surface temperature of bridge during fire

Figure 5-19 Deformation of Steel

There was significant spalling and loss of concrete section on the location of the fire. Severe thermal shock and sudden change in temperature gradient caused the concrete to pop and spall. The Eastbound side of the bridge was severely damaged as seen from Figure 5-20. Seven girders in Span 3 and Span 4 of the bridge suffered significant fire damage and had section loss ranging from 1 in up to 3 in. depth as a result. The FDS fire model was able to replicate the range of severe damage as seen from the temperature slice output shown in Figure 5-21. This can also be used as a verification for the fire model. Soot deposition was also seen throughout the bridge. Soot deposition could be seen on both the EB and the WB bridge and extended as far as Span 1. However, the most heavy soot deposition was seen in the girders and bent cap on Span 3 and Span 4. The level of spalling seen on the concrete substrate also shows that the concrete was exposed to high temperatures.

Figure 5-20 Damage on the girders, bent cap and columns

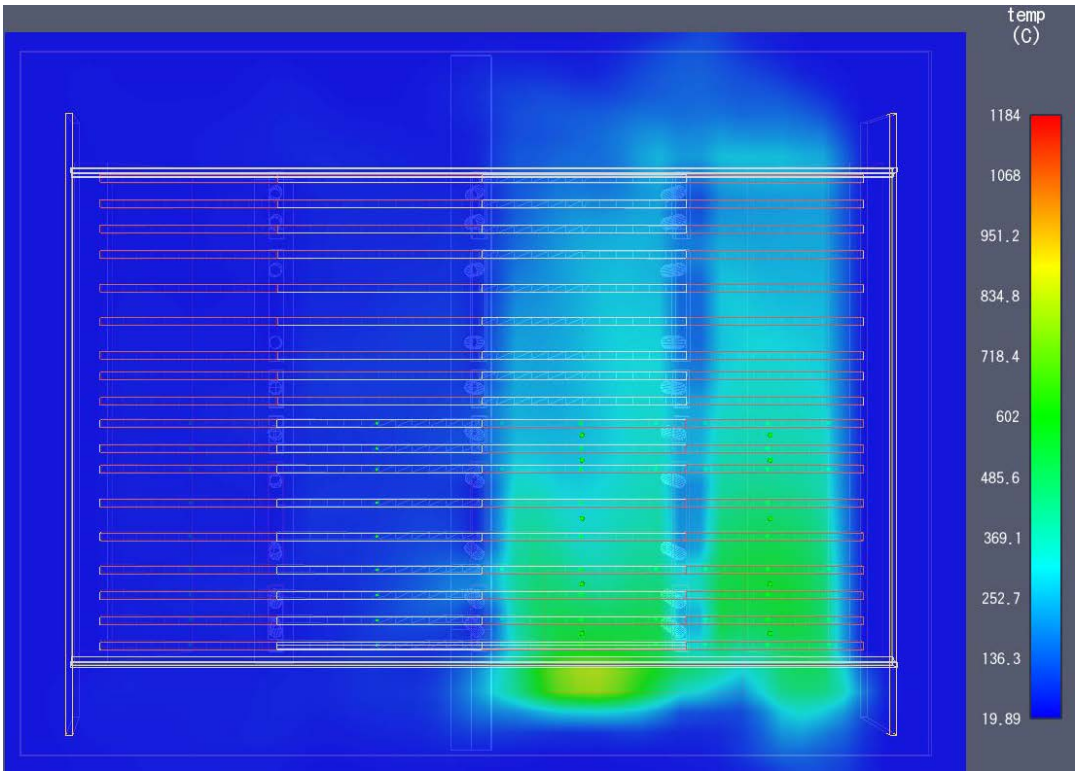

Figure 5-21 Temperature profile at the bottom of the girder

The temperature time history output from the fire test was evaluated to see the temperature of all the beams at different sections along the length of the beam. The

temperature output from the thermocouple had a lot of noise, as expected, for any fire-exposed concrete surface. The temperature, however, followed a clear channel which could be generalized as shown in Figure 5-22 (a). This simplification was required for reduction in the computational time during the heat transfer model. Based on the generalized temperature, the bridge superstructure was divided into 11 different sections with similar temperature range as shown in Figure 5-23 (b). This division provided an optimum balance between accuracy of the model and computational time. Although higher division of sections would increase the accuracy of the heat transfer model, the computational burden required would be immense.

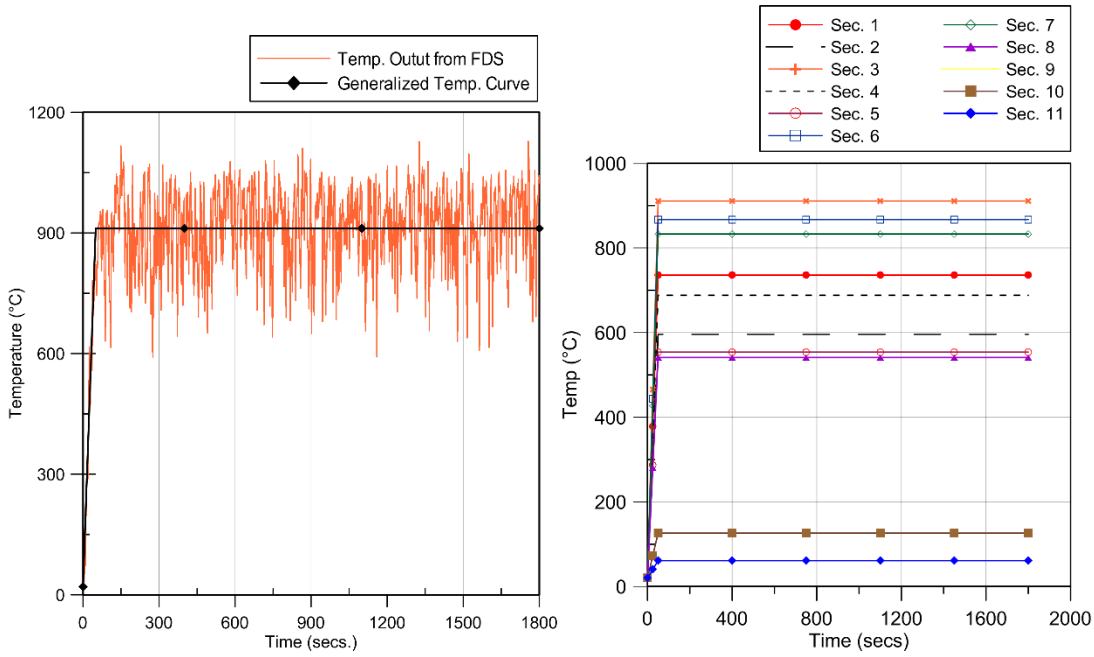

Figure 5-22 Temperature output from Pyrosim (a) Generalized Temp. curve (b) Temp. curve at different sections

5.3.3 Heat Transfer Analysis

Heat Transfer analysis is a mode of analysis which is used to determine the temperature field of a given structure where temperature is taken as the load on the structural member. Conduction, convection and radiation are the three different modes of heat transfer on any solid. The heat transfer analysis is hence used to determine the transient nodal temperature based on these three modes of heat transfer. FDS was used to determine the heat flux of the bridge structure through convection and radiation. However, the heat flux inside the concrete surface is a direct result of conduction and some radiation from other solids. The heat conduction phenomenon occurs within a solid or solids on perfect contact. The heat transfer occurs until the solid is in equilibrium and a steady state is achieved. The heat conduction phenomenon is governed by Equation 5-4.

$$\rho c \frac{\partial T}{\partial t} = \frac{\partial}{\partial x}\left(k \frac{\partial T}{\partial x} \right) + \frac{\partial}{\partial y}\left(k \frac{\partial T}{\partial y} \right) + \frac{\partial}{\partial z}\left(k \frac{\partial T}{\partial z} \right) + \dot{Q}_v''' \qquad 5\text{-}4$$

where k, ρ and c denote the temperature-dependent thermal conductivity, density and specific heat capacity, respectively. Q_v''' is the inherently generated heat; and t is the time variable.

Equation 5-4 can be solved by using the initial condition in Equation 5-5.

$$T(x, y, z, t)\big|_t = T_o(x, y, z) \qquad 5\text{-}5$$

Where $T_o(x, y, z)$ is the ambient temperature of the test specimen.

The radiation and convection from the fire to the exterior surfaces of the bridge superstructure was evaluated based on the Robin boundary condition (Purkiss 2007):

$$\dot{h}_{net} = \alpha_c(\theta_g - \theta_m) + \varepsilon_m \varepsilon_f [(\theta_g + 273)^4 - (\theta_m + 273)^4] \quad 5\text{-}6$$

Where $\dot{h}_{net}$ is the net heat flux; αc is the convective heat transfer coefficient. Its value is 50 W/(m^2. K) for hydrocarbon fire and 9 W/(m^2. K) for unexposed surface (EN 1992-1-2 2002); θ_g is the fire temperature; θ_m is the surface temperature of the structural member; σ is the Stefan–Boltzmann constant and is equal to 5.67x10^{-8} W/(m^2. K^4); ε_m and ε_f are the emissivity of the exposed surfaces and the fire, respectively. As per the provision of EN 1992-1-2 2002, ε_m=0.8 and ε_f=1.0.

Heat transfer analysis was carried out on the basic model created in ABAQUS. The modeling process involved defining the temperature load, boundary conditions, ambient temperature and temperature dependent material properties. The bridge superstructure was divided into 11 different sections based on the FDS model. The bridge girders and deck lying within the section were assumed to have the same surface temperature. The temperature was assumed to be rising from ambient temperature to maximum temperature within 50 secs and then stayed constant throughout the duration of the fire (1800 secs) as shown in Figure 5-22. The maximum temperature and different section divisions can be seen in Figure 5-23.

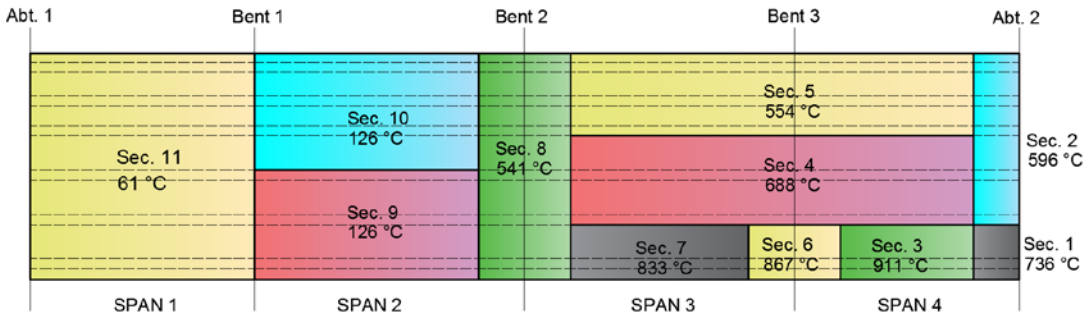

Figure 5-23 Bridge sections showing different temperature

5.3.3.1 Material Properties at elevated temperature

Heat transfer analysis depends on the density and thermal properties of the material. Thermal properties that need to be defined for the model include thermal conductivity and specific heat capacity. The thermal conductivity and specific heat capacity of concrete were defined based on the Eurocode 2 (2004) as shown in Figure 5-24. The figure shows a spike in the specific heat capacity of concrete from 100°C to 115°C which is a result of the loss of moisture from concrete at the evaporation temperature of water. A specific heat capacity of 2020 KJ/(kg.K) was used for the purpose of this study assuming a 3% moisture in concrete which gets evaporated during the fire event. The density of concrete was taken as 2320 kg/m^3 (145 pcf). The thermal conductivity of concrete decreases gradually with increase in temperature.

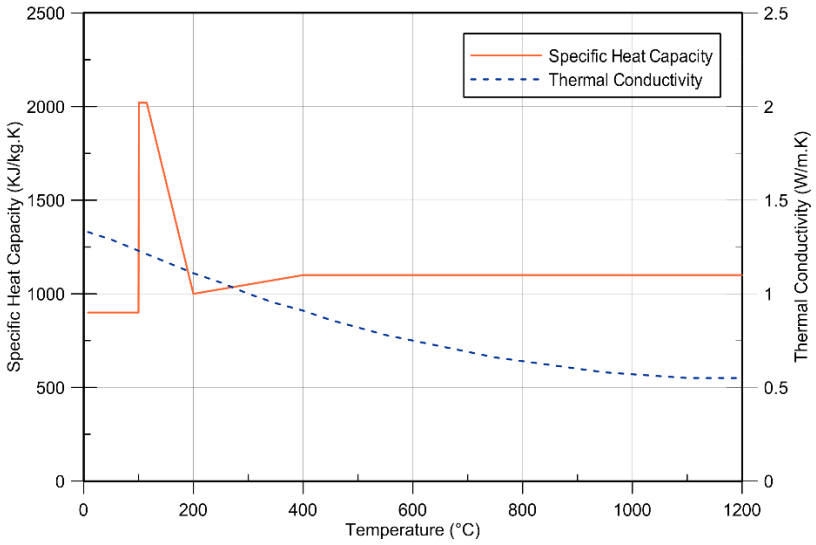

Figure 5-24 Specific Heat Capacity and Thermal Conductivity of Concrete

The coefficient of thermal expansion of concrete was taken according to the provisions of Eurocode 1993-1-2 (2004). The linear coefficient of thermal expansion was used for simplicity to reduce the computational time. The change in material properties of the reinforcement as suggested by Eurocode was not taken into account

in this model as the author was only interested in the core temperature of the concrete girders to see the changes in the material properties of concrete. The temperature values obtained at the end of the heat transfer analysis was used to change the modulus of elasticity of concrete based on Eurocode 1993-1-2 and calibrate the basic finite element model. The typical temperature output (in °F) at the mid span of girders on Span 3 is shown in Figure 5-25.

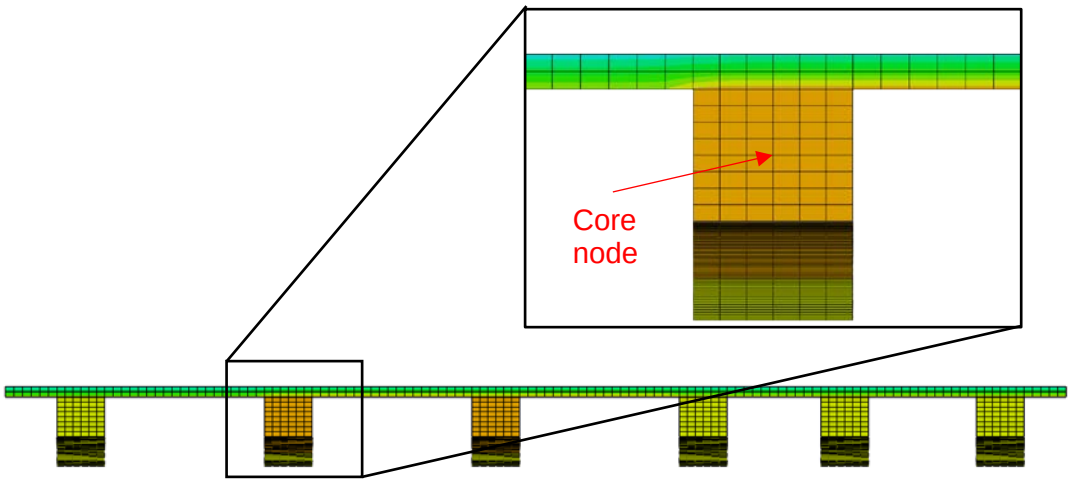

Figure 5-25 Temperature Distribution over the mid span of Span 3 at t = 30 mins.

It is clearly visible from Figure 5-25 that the whole section of the beam was exposed to the same temperature as the surface fire temperature. The beam was exposed to thermal effect from three faces which could be the reason for complete beam section to have the same temperature as the surface. The deck was exposed to ambient temperature of 20 °C on the top surface and only exposed to fire on the bottom surface which is why a temperature gradient along the deck cross section after heat transfer analysis can be seen. A time history temperature response of the core node of the concrete beam section can be plotted as in Figure 5-26. The heat transfer to the core of the beam was completed at around 600 secs and the

temperature remained constant throughout the fire. The heat transfer model does not take into account the effect of spalling and loss of concrete.

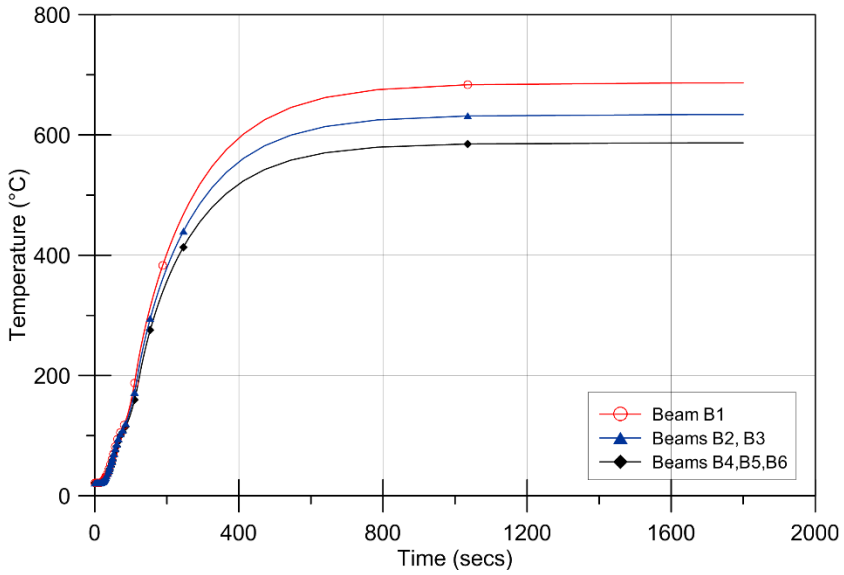

Figure 5-26 Core temperature after heat analysis at mid span, Span 3

The results of the heat transfer model was used to calculate the modulus of elasticity of concrete at elevated temperatures. The stress-strain behavior of concrete at elevated temperature based on Eurocode (2004) and ASCE (1992) was used to calibrate the finite element model in ABAQUS. The calibration and model validation are discussed in more detail in Section 6.2.

5.4 Loop 12 Bridge Model

5.4.1 Finite Element Model

5.4.1.1 Geometric Properties

Loop 12 bridge is a prestressed concrete bridge with four spans. Only Span 2 and Span 3 of the bridge were within the scope of this study. Each span of the bridge is simply supported and each girders are resting on bearing pads. The deck

superstructure is also separated by armor joints and expansion joints on top of each bent. It is hence accurate to model the two different spans separately as two different FE models. Different FE models for Span 2 and Span 3 were created and analyzed separately. The girders, reinforced deck and railings were modeled as solid elements. Two girders in Span 2 were replaced after the impact damage. The girders were included in the full model. The deck cross section was not uniform throughout the span. The deck cross section was thickened around the exterior girders which was taken into account during the modeling phase. Railings were modeled together with the deck cross section. Deck and girders were connected together using tie constraint to simulate composite action. The assembly of deck, railings and girders can be seen in Figure 5-11.

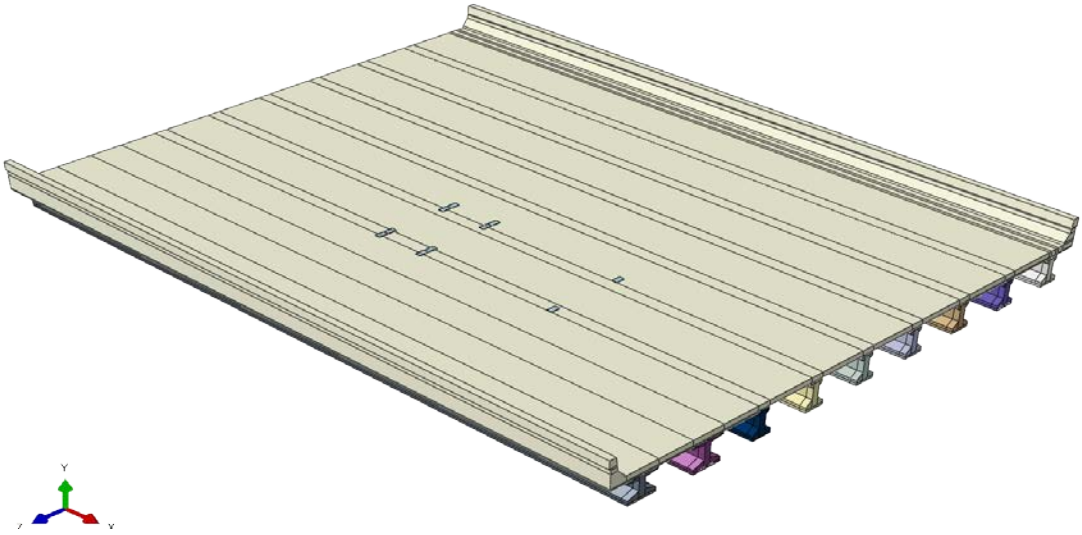

Figure 5-27 Bridge Assembly showing girders, deck and railings

Mild reinforcement were also modeled explicitly for both the girder and the deck as beam elements and embedded into the beam cross section. This assumption assumed a perfect bond between the rebar and concrete. Prestressing strands were also modeled in the FE model with circular cross section. The prestressing force in the strands was applied as predefined field on the strands as discussed in Section

5.1.4. As mentioned earlier, one of the strands in Beam 3 of Span 2 was severed. Hence, girder 3 was modeled with one less strand than other similar Texas Type C girders. Reinforcement model can be seen in Figure 5-12. Section loss and crack pattern due to impact on the girder and mortar repair was not modeled explicitly. CFRP was modeled as 3D deformable shell element with a finite thickness of 0.5 mm. It was constrained to the concrete surface as tie constraint as discussed in section 5.1.3. U wraps along the section of the girders were also modeled and tied to the flexural FRP surface on the bottom as seen in Figure 5-13. 300 mm U-wraps were provided with a spacing of 600 mm. The length of the FRP was 8 m. The damaged area of the girder was strengthened with two layers of FRP laminates.

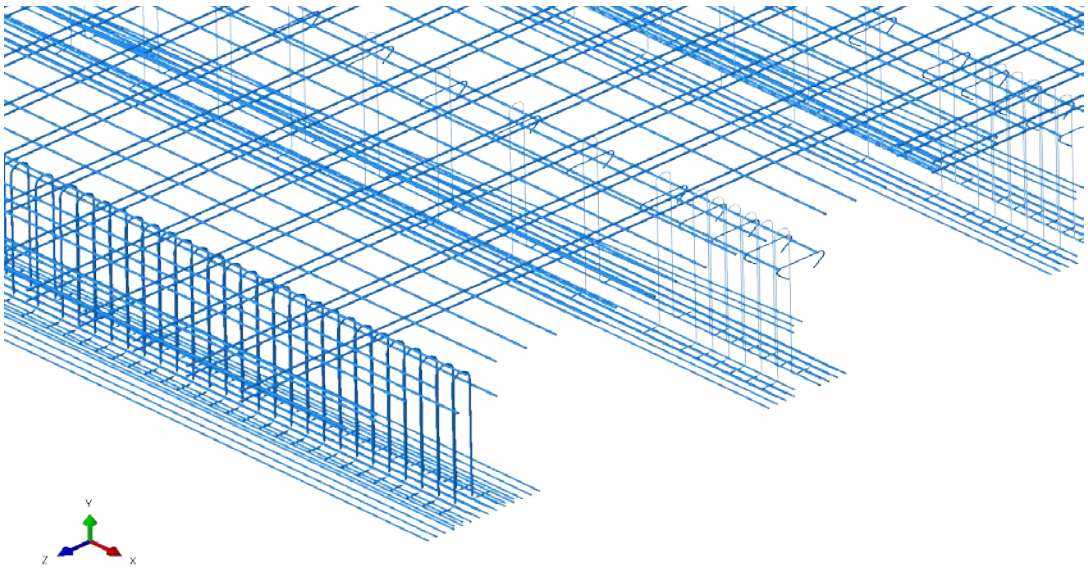

Figure 5-28 Typical reinforcement in Beam and Deck

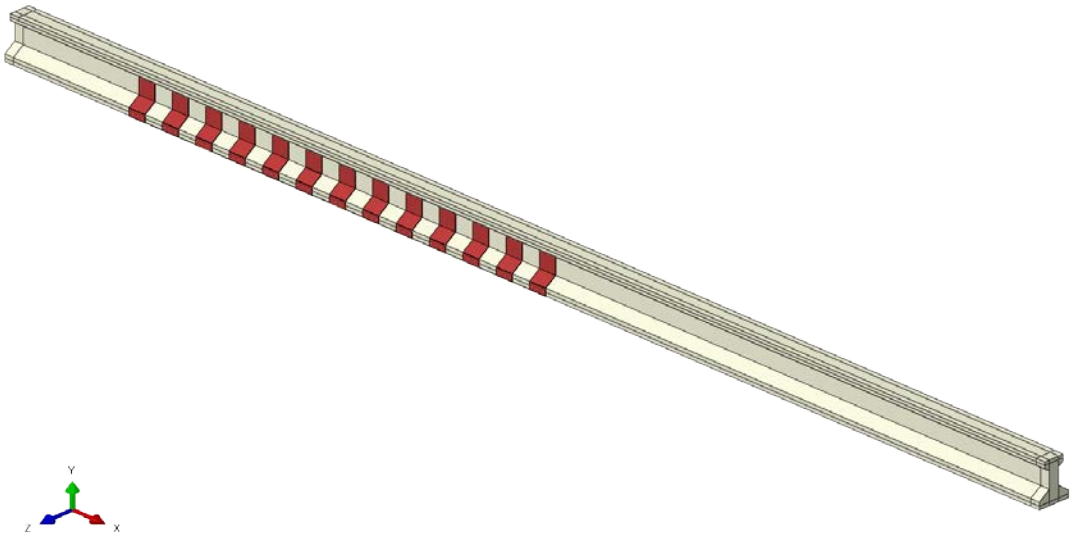

Figure 5-29 Repaired girder with CFRP laminate and U wraps

5.4.1.2 Loads and Boundary Conditions

The boundary conditions were defined at the end of each girder span as pinned support and roller support to approximate the behavior of the girders sitting on bearing pads. Vertical deformations of the bearings were not considered during the modeling.

The load from the truck wheels were applied as patch loads similar to the MacArthur model with a tire contact area of 150 mm x 250 mm (6 in. x 10 in.). The wheel layout on the deck was similar as shown in Figure 5-9. The planar surface had the same material properties as the deck superstructure.

The final step in the modeling process was to mesh all the elements of the bridge superstructure. The mesh size of 3 in. was chosen based on mesh sensitivity analysis as discussed in Section 5.2. Alignment of deck mesh with girder mesh was important for convergence and tie constraint. Meshed FE model for Loop 12 bridge is shown in Figure 5-14.

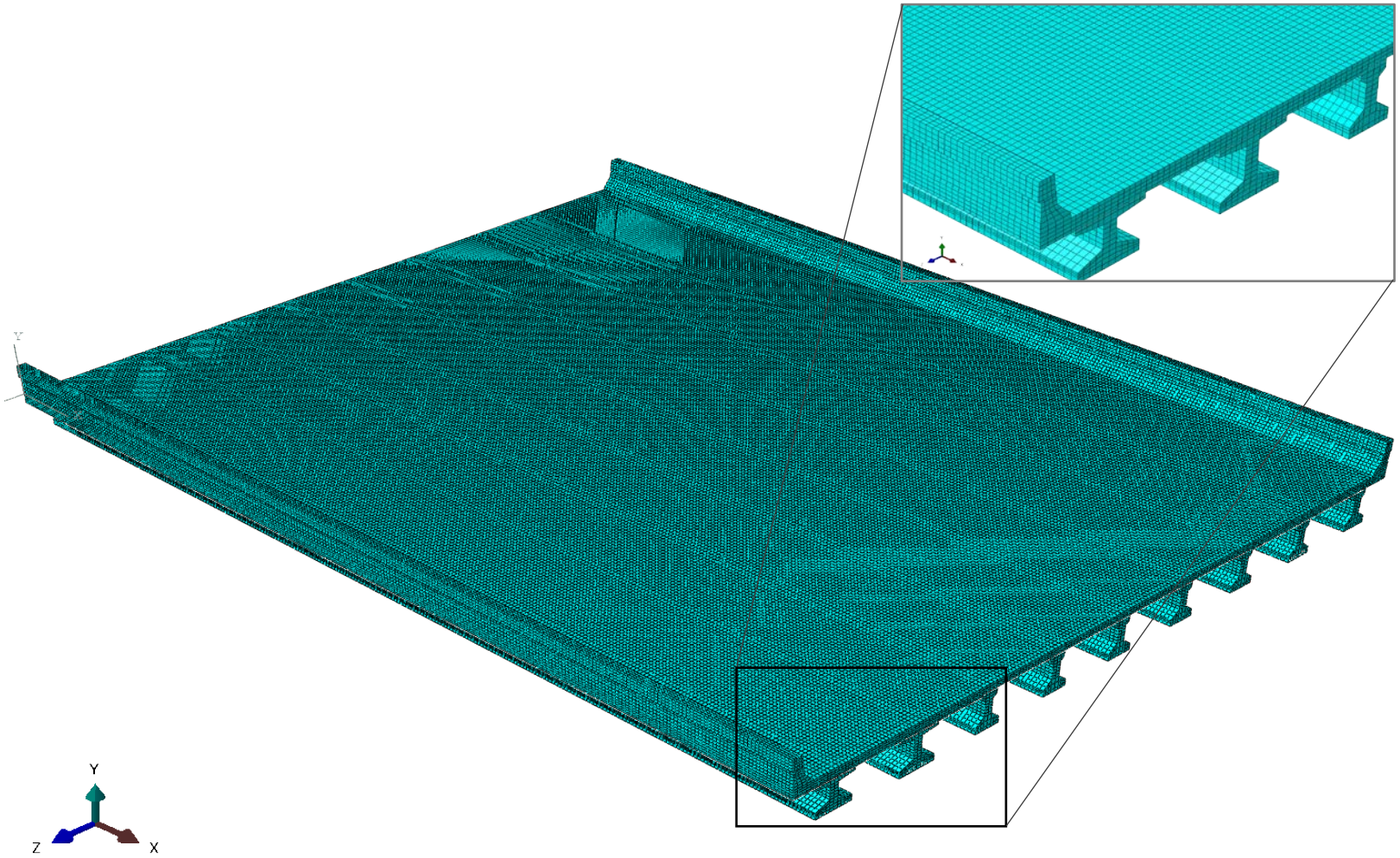

Figure 5-30 Loop 12 Bridge Model showing 3 in. mesh

Chapter 6

Non Destructive and Modeling Results

6.1 MacArthur Bridge

6.1.1 Experimental Results

Non-destructive test on the MacArthur bridge was done in June 2017. The data was recorded at 100 Hz using a laptop connected to the DS 50A DAQ and a Micro measurement 8000 DAQ. The data obtained from the DAQ was taken to the computer and analyzed using Microsoft Excel. The large volume of data created during the load test was a challenge to analyze and present. The first step during the data reduction process was to verify the quality of data and to identify the gauges which did not provide usable data. The data obtained from the DAQ was a function of time. Stop watch readings were taken at different intervals and time in the DAQ was noted when the truck crossed each bent and midspan. The noted stop watch time along with the wheel rotation distance was used to correlate the time history with position of truck. It should be noted that the position shown in all the subsequent graphs is the position of the second axle of the truck. The second axle was taken as the reference of the truck position as it directly correlates with the strain and displacement response of the bridge, being the heaviest axle. Data recording started before the vehicle entered the bridge in Span 1 of the bridge and stopped when the vehicle exited the bridge in Span 4.

Although the readings were balanced to zero before the test, some strain gauges and displacement transducers gave some initial reading. These initial readings were adjusted to zero by applying an initial offset to all the readings by subtracting the initial readings from all data points. Initial plot of the data showed that

the strain and displacement readings started at zero and returned approximately to zero at the end of the test. This shows that the response of the bridge was within linear elastic range and no non-linearity was observed.

Negative strain readings are indicative of compression and positive strain readings indicate tension response on the beams. All strain gauges and displacement transducers showed similar trend and peak magnitude with the maximum strain occurring when the middle wheel of the truck passed directly above the strain gage location. The truck load was distributed from the deck onto the beams causing tension on the bottom fiber and compression at the top of the deck.

6.1.1.1 Strain Response of MacArthur Bridge

As mentioned in Section 4.3.2, two paths were selected on the bridge so that a maximum effect on selected girders can be induced. This allows us to investigate the load distribution characteristics and the moment on the girders. It has been well established that the girder that is directly under the truck load resists majority of the load and the load goes on decreasing on the girders further away (Barr et al. 2001; Gheitasi and Harris 2014). This behavior of the bridge is used to calculate distribution factors for interior girders. The strain response of all the girders at the mid-span of the span were analyzed for two spans, Span 2 and Span 3. Only the results of Span 2 and Span 3 of the bridge is presented as they were the subject of comparison for this study. It was evident from the response that Beam B2 had the maximum response when the truck moved in Path P1 and Beam B4 had the maximum response when the truck was on Path P2 as the gauges were directly under the truck wheel path. The strain reading decreased subsequently on further girders. Strain response of all six girders in Span 2 and Span 3 when the truck passed on Path P1 is presented in Figure 6-1 (a) and Figure 6-1 (b) respectively.

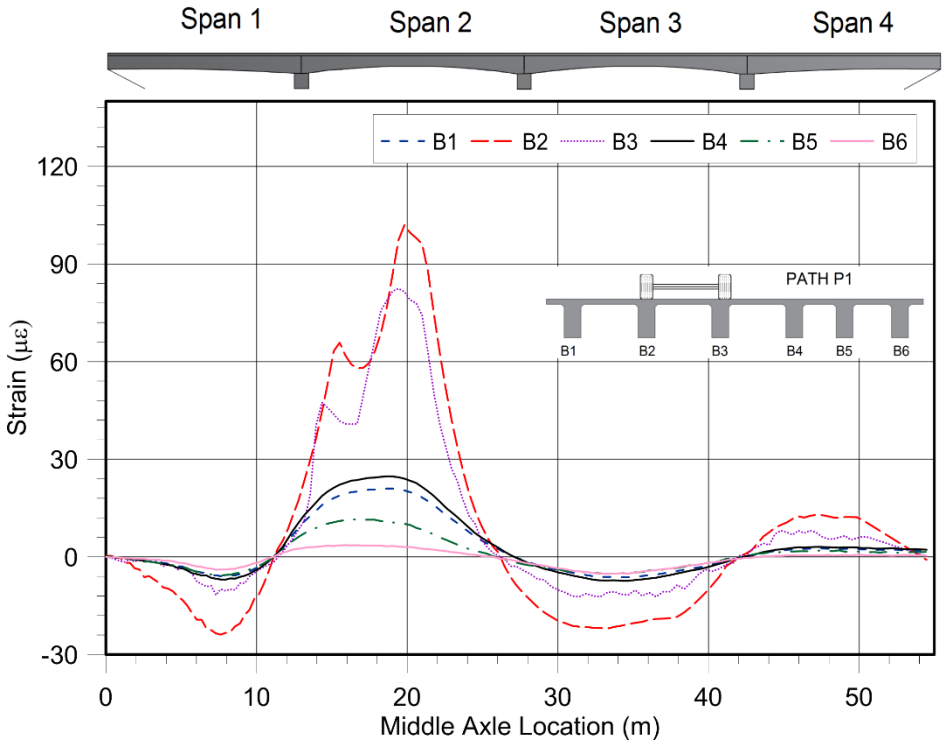

(a) Span 2

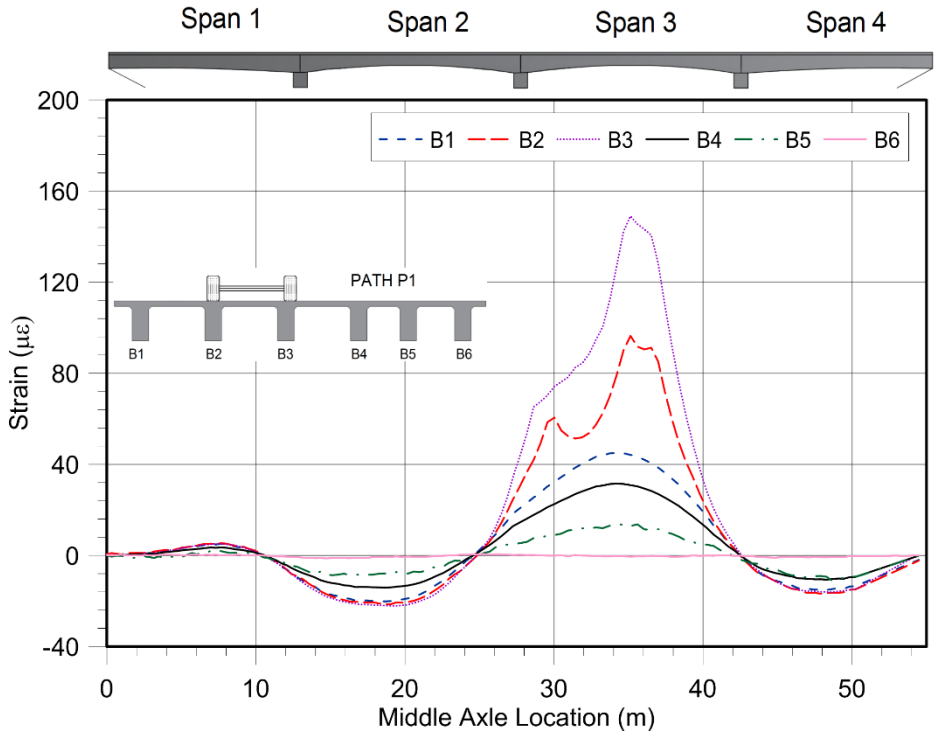

(b) Span 3

Figure 6-1 Strain time series at mid span for Truck Path P1

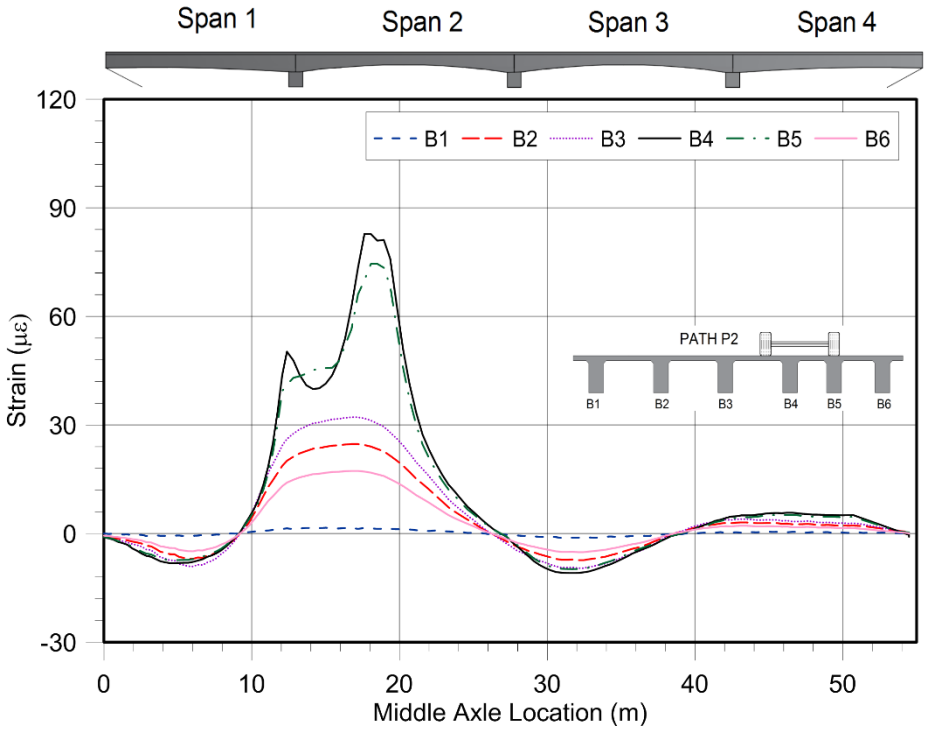

(a) Span 2

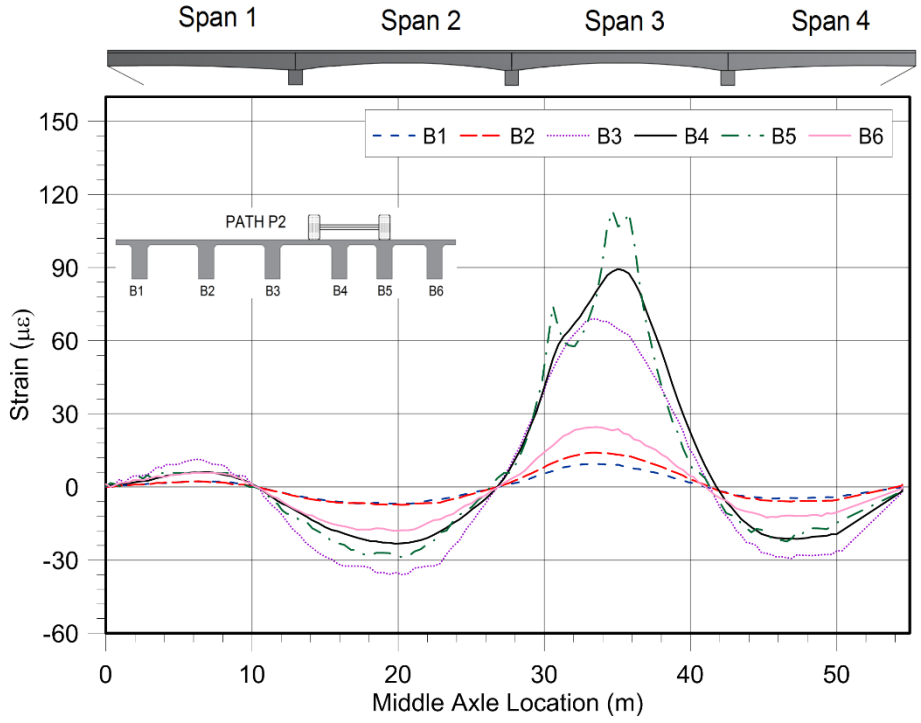

(b) Span 3

Figure 6-2 Strain time series at mid span for Truck Path P2

Similarly, the strain response of the strain gauges at the mid span of Span 2 and Span 3 when the truck is in Path P2 is shown in Figure 6-2(a) and Figure 6-2 (b). It can be seen that, for Path P1, the strain response of the beams B2 and B3 were the maximum as they were directly under the truck load and it decreased for other beams in the span. Similarly, for Path P2, the strain response was maximum for beams B4 and B5 that were under the highest influence of the truck load and decreased subsequently. It should be noted that the beam that was farthest from the effect of the truck load, beam B6 for Path P1 and beam B1 for Path P2 exhibited a very low strain which shows that the beams were not active in live load distribution. Traffic barrier and asphalt overlay on top of the bridge deck were removed before the load test. Strain gauges were applied near the bent cap locations on Beam B3 and B5. However, the strain gauges didn't provide significant readings. This could be because the location of the gauges were around the point of contra flexure for moment.

Another important observation that was visible from the strain response is that the strain values showed some response even when the truck load was on the adjacent span. It can be seen that negative values of strain corresponding to compression on the bottom fiber of the beam was seen. This phenomenon was consistent across all the girders. This is because of the continuous nature of the beams. This proves that there is continuity between the beams and also between decks in adjacent span. That was the reason why all the spans of the bridge were modeled together during the modeling phase. The strain values also showed a consistent pattern of increasing from the start of the bridge and returning back to 0. This shows that the strain response was within the elastic range and no residual strain

was observed. The test was stopped before the truck could exit Span 4 of the bridge which is why small amount of residual strain was observed.

Diaphragms were provided at each bent and also at certain locations along the span of the beam. This provided a cross bracing between the beams and allowed the beam to act as a whole. This was demonstrated by the presence of end restraint in the beams. The presence of compression when the truck was in subsequent span shows that adequate end restraint was present to consider the beam as continuous beam. The consistency in the strain readings was also demonstrated as the beams showed maximum readings when the middle wheel of the truck on the strain gauge location. The slight dip in strain seen in the ascending arm of the strain reading could be because of the result of front wheel passing the gauge location and before the second wheel of the truck approached the gauge location.

6.1.1.2 Displacement Response of MacArthur Bridge

Strain response in structural elements can be affected by the presence of cracks or other minor structural abnormalities. Presence of microcracks in concrete or reinforcement can affect the reliability of the strain gauge readings. The displacement response, however, can be representative of the overall beam stiffness and provide accurate representation of the bridge behavior. LVDTs were installed on three beams in Span 3 and two beams in Span 2 of the bridge to obtain the deflection response of the bridge. Beam B2, B3 and B5 were instrumented in Span 3 and Beam B2 and B5 were instrumented in Span 2. Displacement response of the beams when the truck is moving in Path P1 and Path P2 is shown in Figure 6-2 and Figure 6-4.

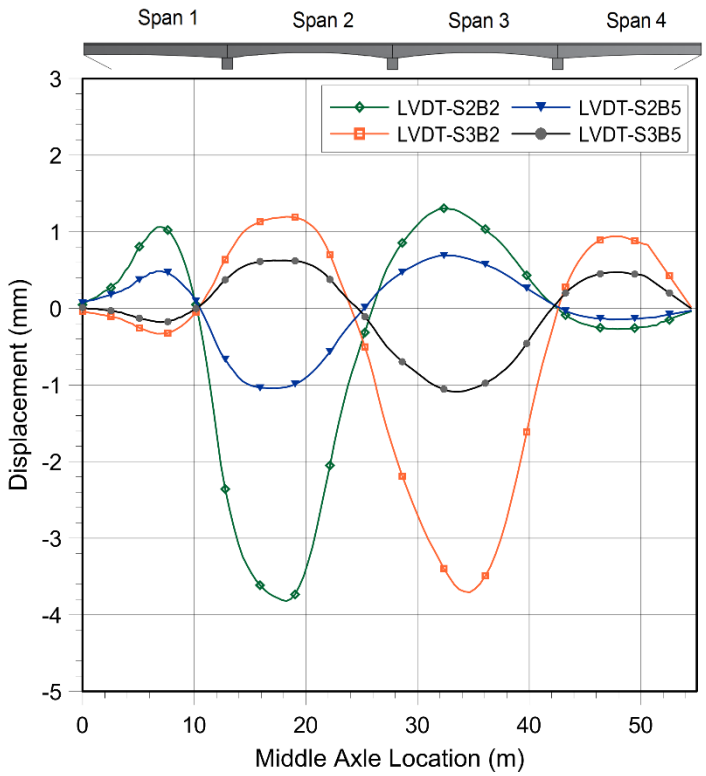

Figure 6-3 Displacement response for Path P1

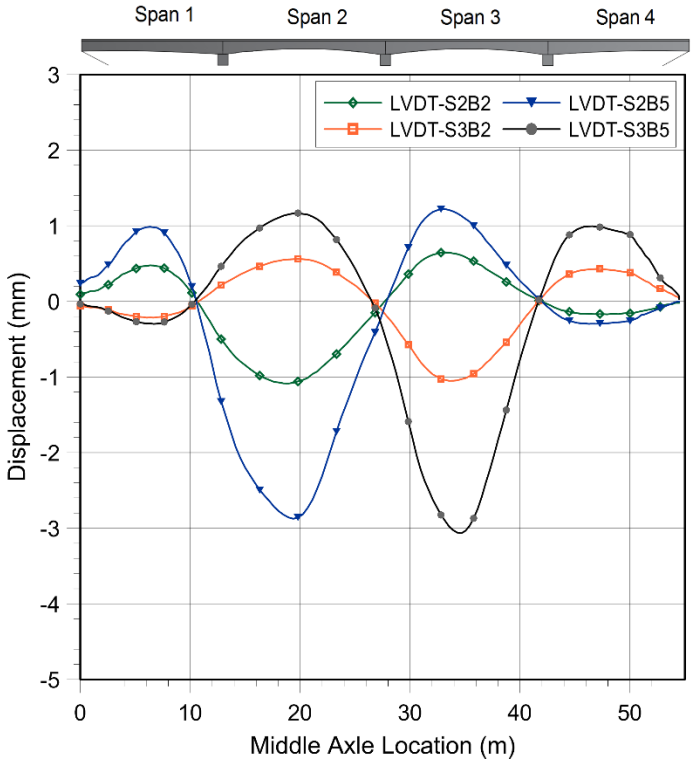

Figure 6-4 Displacement response for Path P2

It can be seen from the graphs that the displacement response of the beam B5 was lower than the displacement of Beam B2. This could be because of the fact that the beams were constructed in two different times. Beam B2 was part of the original construction which had a concrete design compressive strength of 3600 psi. However, Beams B5 and B6 were part of the reconstruction in which the design compressive strength of concrete was 5000 psi. This could be the reason why all the displacements for Beam B5 is lower than the displacement for Beam B2 for all runs.

The deflection response also start from zero at the start of the bridge and return back to zero when the trucks exits the bridge. This reiterates the fact that the bridge is within a linear elastic range. The peak in displacement also occurs when the middle axle of the truck is on top of the strain gauge location. Deflection comparison between different beams are presented in Section 6.1.1.6.

6.1.1.3 Live Load Distribution Factor

The study by Nutt, Schamber, & Zokaie (1988) has been the basis of live load distribution factor for slab on beam bridges and incorporated into the AASHTO LRFD Bridge Specifications (2016b). It has been studied and verified by various researchers that the Live load distribution factor obtained from AASHTO provisions are conservative and underestimate the load carrying capacity of a girder. This section summarizes the findings of this research about the lateral live load distribution factor on a fire damaged parabolic reinforced concrete bridge with beams repaired and strengthened with CFRP wrapping. The live load distribution factors from the non-destructive load test is calculated based on the maximum strain response and compared with the AASHTO LRFD distribution factors for moment (DFM). The calculation for the live load distribution factors for moment for the MacArthur bridge is presented in Appendix C. Lateral live load distribution factor is the function of span

length, spacing between girders and the stiffness parameters representative of the geometry and material properties of the girder. This is the reason the live load distribution on a bridge can vary as the bridge undergoes deterioration or damage. The loss of elastic stiffness can be a contributing factor which can increase the moment on the bridge significantly. The AASHTO Live load DFMs calculated for the MacArthur bridge is summarized in Table 6-1.

Table 6-1 AASHTO live load Distribution Factors

	Distribution Factor for moment	
Girders	One lane loaded	Two lane loaded
Interior	0.420	0.561
Exterior	0.600	0.617

The structural response of the bridge was analyzed based on the strain readings obtained at mid span of Span 2 and Span 3 of the bridge. Strain gauge readings of each beam at the bottom surface was plotted and the peak strain was compared to evaluate the transverse strain distribution across the bridge. This provides an idea about how much strain is distributed to the girder directly below the truck load and how much of it is taken by the girders further away. Peak strain readings were taken from the crawl speed tests and verified using the values from the stop location test. The strain readings were almost the same with only a slight variation. The load distribution for the negative moment region is not plotted as only two beams were instrumented in the negative moment region. The strain distribution was plotted for the two spans, Span 3 and Span 2 of the bridge for two different paths Path P1 and Path P2. This provided four strain distribution plots for the bridge which is presented in Figure 6-5 and Figure 6-6.

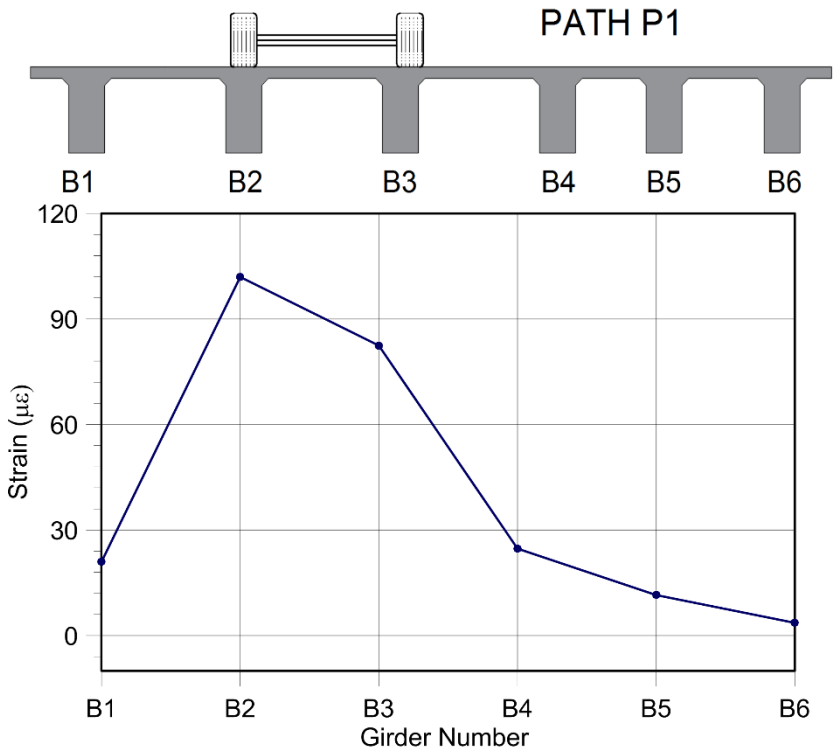

(a) Span 2

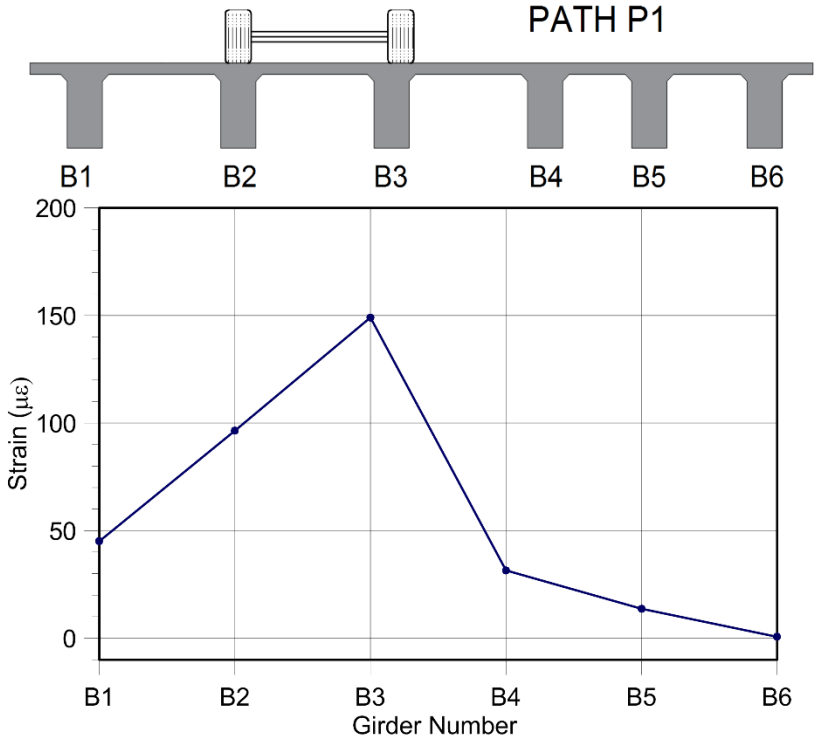

(b) Span 3

Figure 6-5 Transverse strain distribution at Mid-span of the girders for Path P1

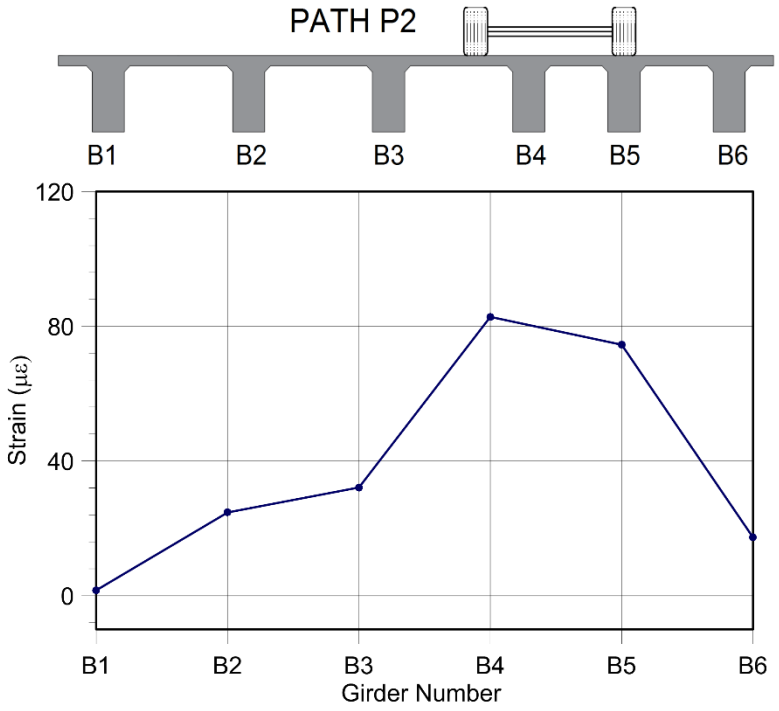

(a) Span 2

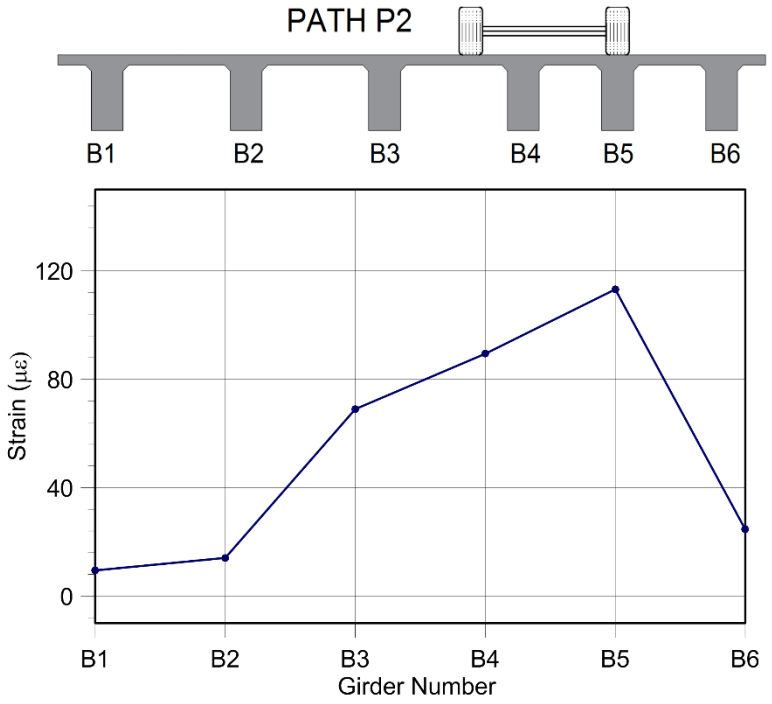

(b) Span 3

Figure 6-6 Transverse strain distribution at Mid-span of the girders for Path P2

Straight lines are used to connect the peak readings of the plots for visualization; although the strain response between the girders is not linear. It can be seen from the figures that the strain is highest on the girder under the truck load and decreases further away. The strain in the furthermost girder is either very low or negative as the truck load has minimal effect on far girders. These beams can be assumed to be non-participating girders during load distribution calculations. The peak strain values can be then be used to calculate the DFM for the corresponding span of the bridge.

The overall performance of the bridge superstructure can be evaluated based on the transverse load distribution characteristics of a bridge. The load distribution is often used to determine the fraction of the total load that is carried by one beam. The peak strain response of the bridge girders at specific location, when the truck is moving longitudinally along the length of the bridge, is taken to calculate the distribution factor. Transverse distribution factor from experiment can be calculated by dividing the maximum response by the sum of all girder responses recorded at the same time. Strain response is used to calculate the distribution factor in this case. Equation 6-2 can be used to calculate the distribution factor from Experiment.

$$g_i = \frac{\varepsilon_i}{\sum_{j=1}^{n} \varepsilon_j} \qquad \text{Equation 6-2}$$

Where g_i is the distribution factor of the i^{th} girder, ε_i is the maximum strain response recorded in the i^{th} girder, n is the total number of girders, and ε_j is the strain response of each of the other girders at the same point in time when the maximum strain was recorded in the i^{th} girder (Fu, et al 1996). This equation is used for the calculation of DFM for one lane loaded case. The equation needs to be

multiplied by m, as shown in Equation 6-3 when the bridge is loaded with vehicles in more than one lanes.

$$g_i = \frac{\varepsilon_i m}{\sum_{j=1}^{n} \varepsilon_j} \qquad \text{Equation 6-3}$$

Where m is the number of lanes loaded. ε_i is taken as the peak strain for that girder and ε_j is the strain in the other girders at the same point in time. The response of the furthermost girder was not included during the calculations if a negative value was observed. The distribution factors for beams with the maximum strain for all four cases when the bridge was loaded with one truck was calculated using this method and summarized in Table 6-2.

Table 6-2 Distribution Factors from Experiment

Distribution Factor for moment		
Girders	Span 2	Span 3
B2	0.416	0.443
B4	0.355	0.354

6.1.1.4 Comparison between CFRP strengthened vs. undamaged beam

MacArthur bridge was exposed to fire hazard and sustained fire damage which causes spalling and loss of concrete section in the beams and girders. As a result, the damaged beams were chipped off, repaired with mortar and strengthened using CFRP laminate. Two beams in Span 3, Beam B1 and Beam B2, were strengthened and other beams were not strengthened as large amount of spalling was not observed in the concrete. Span 2 of the bridge sustained less amount of fire and damage which is why the beams did not require any repair. This provided us an opportunity to compare the behavior of two beams of equal spans, undamaged with

a CFRP strengthened beam. Beam B2 was taken as a representative beam for comparison as Beam B1 was too close to the exterior edge of the deck. Strain response of the beams when the truck was moving across the bridge on top of beam B2 was used to compare the response as seen in Figure 6-7.

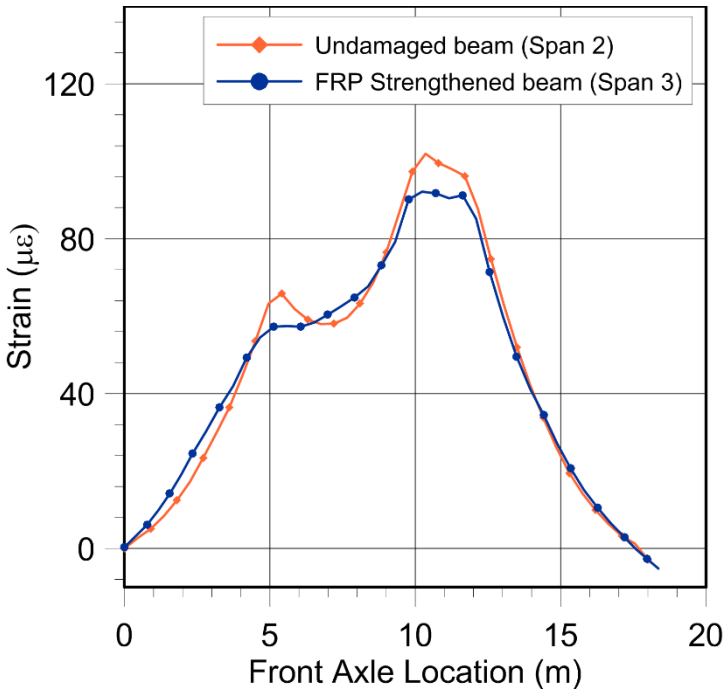

Figure 6-7 Strain comparison between undamaged and FRP strengthened girder

The strain response of the strain gauge was isolated so that the response of the gauge only when the truck entered that span can be considered. The distribution of the strain can be assumed to follow a normal distribution as shown in Figure 6-7. A one tailed hypothesis test was performed to verify the difference in the strain values. The z-test showed that the strain obtained for the undamaged beam was higher than the strain obtained for the CFRP strengthened beam as demonstrated by a Z value of 2.22 when compared to the significance level of 0.05. We can hence conclude with a 95% confidence that the strengthened beam, in Span 3 of the bridge, exhibited a lower strain when compared to the undamaged beam in Span 3 of the bridge. The

damaged beam was exposed to higher thermal effects as a result of fire and subsequently repaired and strengthened with CFRP. The aim of this comparison was to find the effectiveness of the repair procedure, a decade after the strengthening to see the adequacy of the strengthening procedure. The strain in the strengthened beam was lower than the similar undamaged beam, even though the beam had a higher loss in stiffness due to fire. The strain in the strengthened beam was 9% lower than the undamaged beam. This could be because FRP, in addition to the confinement of concrete, prevents the transverse cracks in the bridge from expanding. The bond between the FRP and concrete was still intact during the load test. FRP doesn't only prevent the cracks in the beam from growing, but also prevents new cracks from forming which could be the reason for the decrease. Apart from that, steel reinforcement also loses its load carrying capacity when exposed to thermal effects. The yield strain in steel reinforcement can increase as a result of thermal effect which decreases the moment capacity of the beam. However, a properly designed FRP laminate strengthening system can help alleviate this problem and restore the flexural capacity of the beam.

The strength and stiffness recovery of the fire damaged beam is also evident from deflection response of the two beams as shown in Figure 6-8.

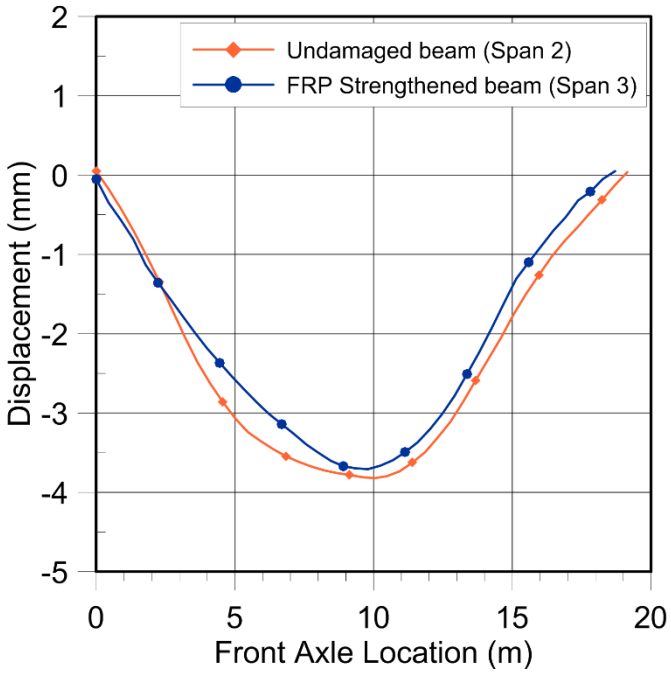

Figure 6-8 Displacement comparison between undamaged and FRP strengthened girder

The deflection observed for the damaged and strengthened girder was 3 % lower than the undamaged girder. There was no significant difference in the deflection response between the two girders which shows the effectiveness of FRP. FRP bond with concrete can increase the stiffness of the concrete in two ways; by providing confinement to the mortar and concrete substrate and increasing the overall elastic stiffness of the beam because of the laminate's large modulus of Elasticity.

The transverse strain distribution across all the girders for Span 2 and Span 3 was compared to see the overall performance of all the beams in Span 2 compared with the beams in Span 3. It should be noted that Span 3 of the bridge suffered a higher amount of temperature exposure, however, Span 2 was only exposed to some thermal effects. The strain response for all six girders when the truck is moving in Path P1 is shown in Figure 6-9.

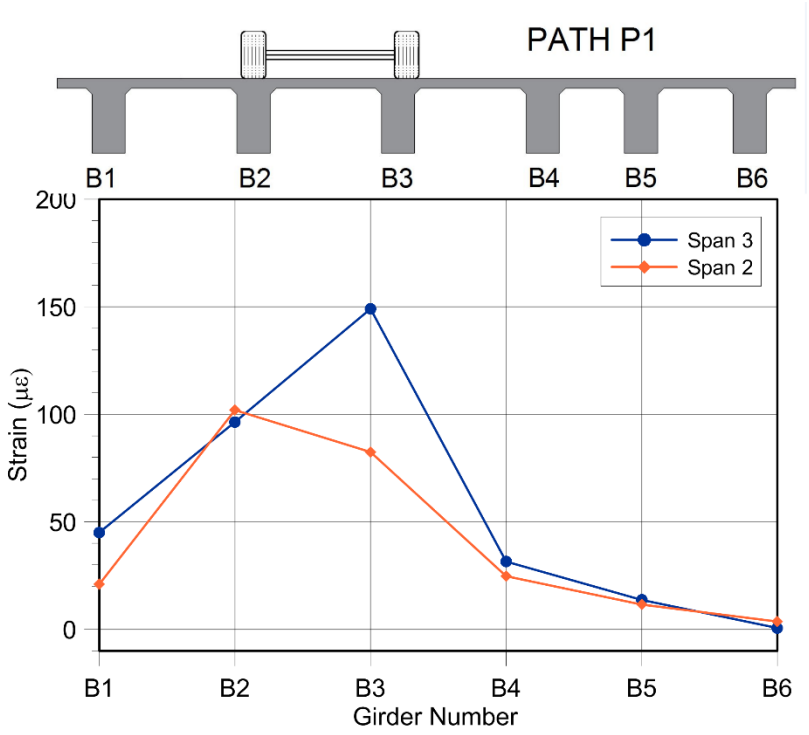

Figure 6-9 Strain comparison between Span 2 and Span 3 (Path P1)

The strain response of the beams in Span 2 was comparable to the strain response of beams in Span 3. It was seen that Span 3 which was most heavily damaged exhibited higher strain than the values for corresponding beams in Span 2, except B2. Beam B2 exhibited lower strain because of the repair and CFRP strengthening. However, Beam B3 was only repaired with mortar and not strengthened with CFRP laminate. There was no visible spalling and section loss in Beam B3 which warranted FRP repair. That could be the reason why no strengthening was done for the beam. However, the beam was exposed to similar thermal effects which could be the reason for the large strain value obtained for beam B3. Another reason for this could be the thermal effects on the reinforcement which can reduce the load carrying capacity of the beam significantly. This large strain response in Beam B4 was verified by other gauges on the same span as well. This

shows that the response was not due to the presence of local crack or deformity, but due to the reduction of overall stiffness of the beam. This can be used to verify that FRP laminate strengthening significantly contributes to the flexural capacity and increases the stiffness of the beam. It could also be concluded that beams which are exposed to thermal effects, however, do not exhibit spalling or section loss, still need to be strengthened with FRP laminate to prevent any microcracks from expanding.

Similar behavior was observed for Beam B3 when the truck was on Path P2. The strain response for Beam B3 was higher for Span 3 when compared with Span 2. Figure 6-10 shows the response of all the girders when the truck in on Path P2. It can be seen that all the beams except Beam B2 exhibited a higher strain for Span 3 when compared with Span 2. This could be because of the thermal effects on the beams and presence of microcracks even after repair. Another reason could be the loss of modulus of elasticity of the steel reinforcement.

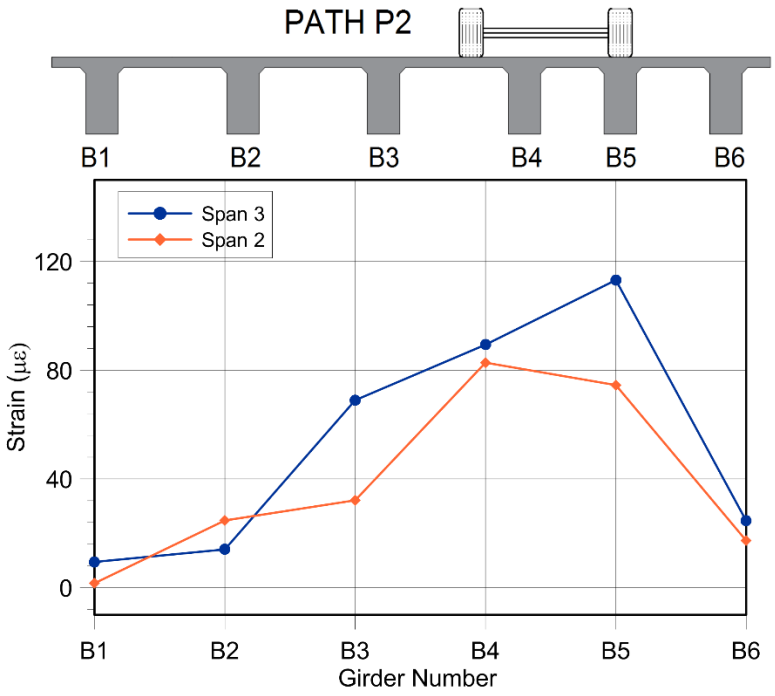

Figure 6-10 Strain comparison between Span 2 and Span 3 (Path P2)

6.1.2 Model Verification and Calibration

An initial finite element model, fire model and a heat transfer model were used to obtain a calibrated model for MacArthur bridge. The process of modeling, material properties and assumptions for modeling in discussed in Chapter 5. Current material properties of structural elements, concrete and FRP can serve as the starting point for model verification and calibration.

6.1.2.1 Concrete Material Properties

Material properties of concrete used in the initial model was based on the design compressive strength. However, it is known that the concrete compressive strength can change with time and factors like chlorine ingress, cracks and deterioration can adversely affect the compressive strength. Concrete cores can be used to get an initial approximation of the current material properties of concrete. Core samples were collected from Span 1 which were not affected by fire and thermal effects. Concrete cores from the fire damaged spans, Span 3 and Span 4 were not collected.

Five core samples were collected from the web of three different girders in Span 1 of the bridge to obtain the compressive strength of concrete. Three cores were taken from Beam B2 and Beam B3 which were part of the original construction. The design values for concrete for these beams was 25 MPa (3600 psi). Two core samples were taken from Beam B5 of the bridge. The design compressive strength for these cores was 34.5 MPa (5000 psi). The concrete cores were all 100 mm (4 in.) in diameter and a length of around 200 mm (8 in.)[Figure 6-11 (a)]. The concrete cores were stored in a cool dry place to prevent any absorption of moisture. The core samples were cut to the same length and capped using Sulphur capping to make the surface level [Figure 6-11 (b)]. The samples thus prepared were tested to obtain the

compressive strength of concrete using a MTS compression testing machine at a constant rate of around 0.25 ± 0.05 MPa/s (35 ± 7 psi) [Figure 6-11(c)]. Strain gauges were attached on two sides of the core sample to get the stress strain response and Elastic modulus of the concrete samples.

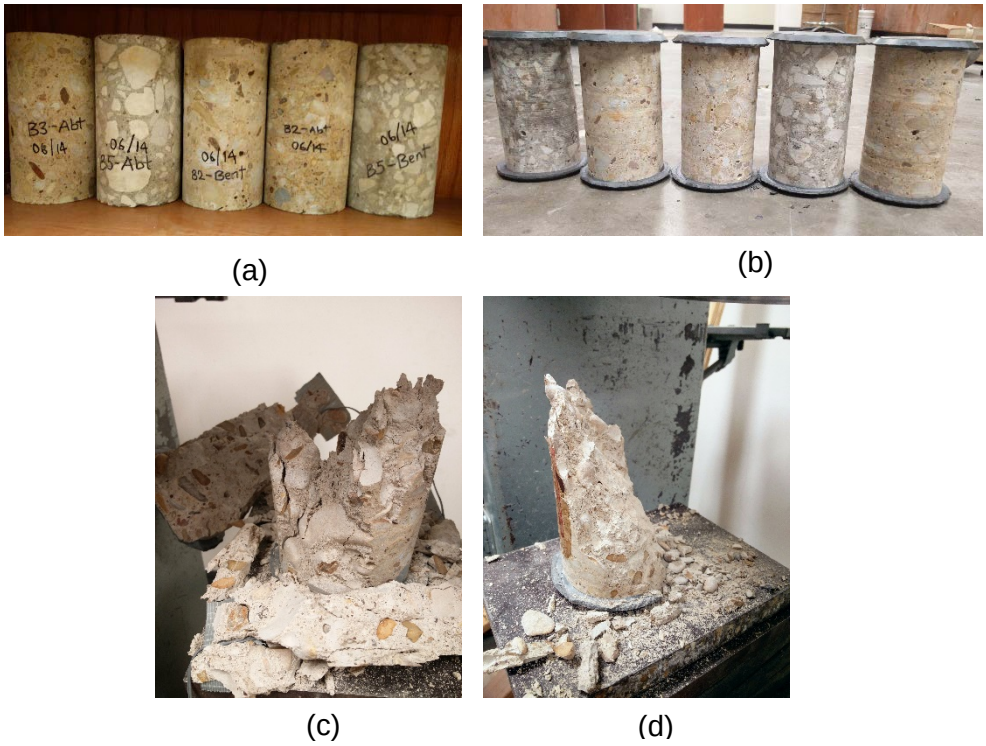

(a) (b)

(c) (d)

Figure 6-11 Concrete core samples (a) Cut into proper dimensions (b) Capped core samples (c) Tested core sample (d) Tested core sample

The core dimensions and compression test results are shown in Table 6-3.

Table 6-3 Concrete compressive stress from core tests

Core	Diameter (mm)	Length (mm)	Area (mm^2)	Density (kg/m^3)	f'_c (MPa)	E (MPa)
B2-A	95	184	7154	2257	22.88	22050
B2-B	95	184	7137	2294	25.95	24071
B3-A	95	184	7145	2246	18.49	19682
B5-A	96	183	7173	2246	33.67	26563
B5-B	95	183	7146	2336	49.40	31424

The compressive strength of the concrete cores was calculated from the failure load obtained from the compression test. The compressive strength for the first three cores were calculated as 22.44 MPa (3255 psi) and the compressive strength for the last two cores was calculated as 41.54 MPa (6025 psi). The modulus of Elasticity was also calculated separately for the two sets. The modulus of Elasticity (E) of concrete was calculated using Equation 6-4 reproduced from ACI (ACI 318 2014). The average E value obtained for the two sets was 21930 MPa and 30350 MPa for the 22.44 MPa concrete and 41.54 MPa concrete respectively.

$$E_c = w_c^{1.5} 0.043 \sqrt{f'_c} \qquad \text{Equation 6-4}$$

Where w_c is the weight of concrete in kg/m^3, and f'$_c$ is the compressive strength of concrete in MPa. These values provided an initial approximation of the E value.

Concrete compressive stress decreases as it is exposed to higher temperatures and the strain increases. As a result, the modulus of Elasticity also reduces significantly with exposure to elevated temperatures. There have been different studies showing the effect of elevated temperature on concrete (Eurocode 1992-1, ASCE 1992, Hertz 2005, Li and Purkiss 2005, BSI 1985). The stress strain relationship and also the modulus of elasticity relationships are presented by different authors for loaded and unloaded concrete. The equation suggested by Li and Purkiss (2005) for the modulus of Elasticity at elevated temperatures was used to calculate the E values at different temperature. The relationship is shown in Equation 6-5.

$$E_{ciT} = \frac{800 - T}{740} E_{ci} \leq E_{ci} \qquad \text{Equation 6-5}$$

Where E_{ciT} is the Initial modulus of elasticity at Elevated temperature, E_{ci} is the initial modulus of Elasticity at ambient temperature, and T is the fire temperature in °C ($\leq 20°C$) of concrete. Figure 6-12 (a) shows the change in Elastic modulus at elevated temperatures for two sets of concrete compressive strength and Figure 6-12 (b) shows the stress strain relationship of concrete at elevated temperature based on the ASCE model (ASCE 1995).

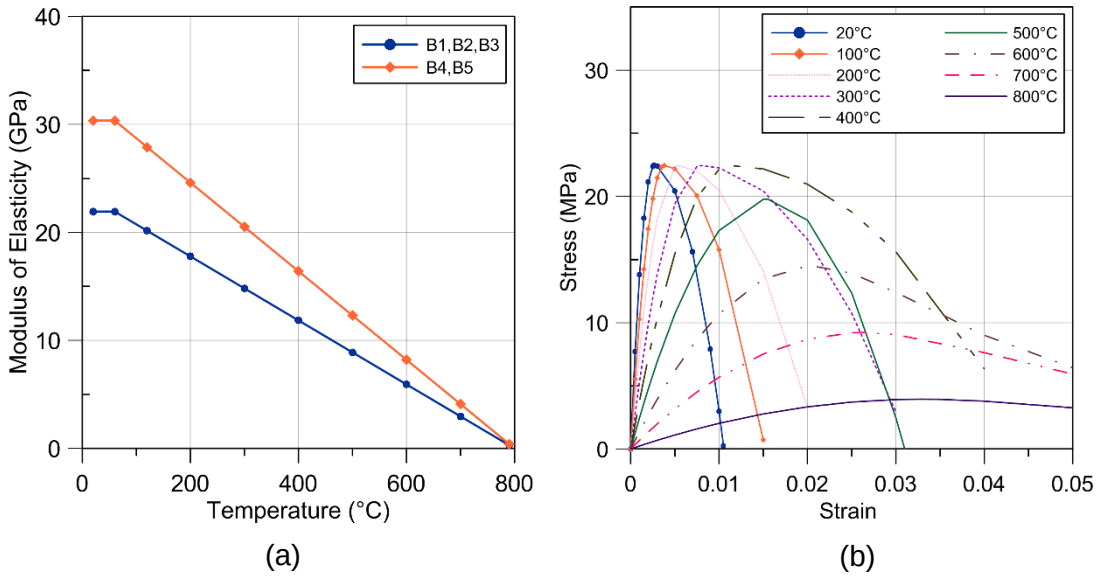

Figure 6-12 (a) Variation of Modulus of concrete at elevated temperatures
(b) Variation of stress-strain diagram for concrete at elevated temperature

6.1.2.2 FRP Material Properties

FRP samples were not collected during the initial repair and strengthening of fire damaged beams in 2005. Hence, the material properties of FRP was modeled based on the manufacturer provided specification sheet. However, the material properties of the FRP laminate depends on the thickness of FRP and the amount of epoxy used during the laminate preparation. Various researchers (Chin et al. 1998; Zheng and Morgan 1993; Benmokrane et al. 2000, Grace et a;. 2005) have studied

the effect of thermal-mechanical cycles, effect of alkaline solutions and wetting and drying cycles to conclude that significant reduction in stiffness and tensile strength can occur due to change in these environmental conditions. The material properties of FRP was hence expected to change from the day of application. Pallempati et al. (2016) carried out pull off test on the bridge beam after application and concluded that the bond between CFRP and concrete was satisfactory.

A representative FRP sample was collected from the U-wrap of the beam after the load test and five coupon samples were prepared for tensile test. Since, FRP coupons were not tested during the initial application, a new sample of FRP laminate using same fiber and epoxy was created in the lab for comparison purposes. Although the thickness of FRP and the amount of epoxy was aimed to make similar, there was a discrepancy in the thickness of the samples. The lab sample was thicker than the samples obtained from the field. It could be because automated saturation was used during the initial application whereas a roller epoxy application was used during sample preparation for the lab samples. One coupon sample had some concrete on the FRP surface which is why it was discarded during the analysis. Four similar coupons were created from the lab FRP sample. The FRP samples were cut to the suggested dimensions and tabbed using the same CFRP unidirectional fiber material [Figure 6-13 (a)]. Strain gauges were installed on the middle of the FRP sample [Figure 6-13(b)] to obtain the stress strain diagram and eventually the modulus of Elasticity (E) of FRP sample. Tensile test was carried out on the coupon samples according to ASTM D3039 (ASTM, 2014b) to obtain the tensile stress. Figure 6-13(c) and Figure 6-13(d) present the failure modes for two coupon samples.

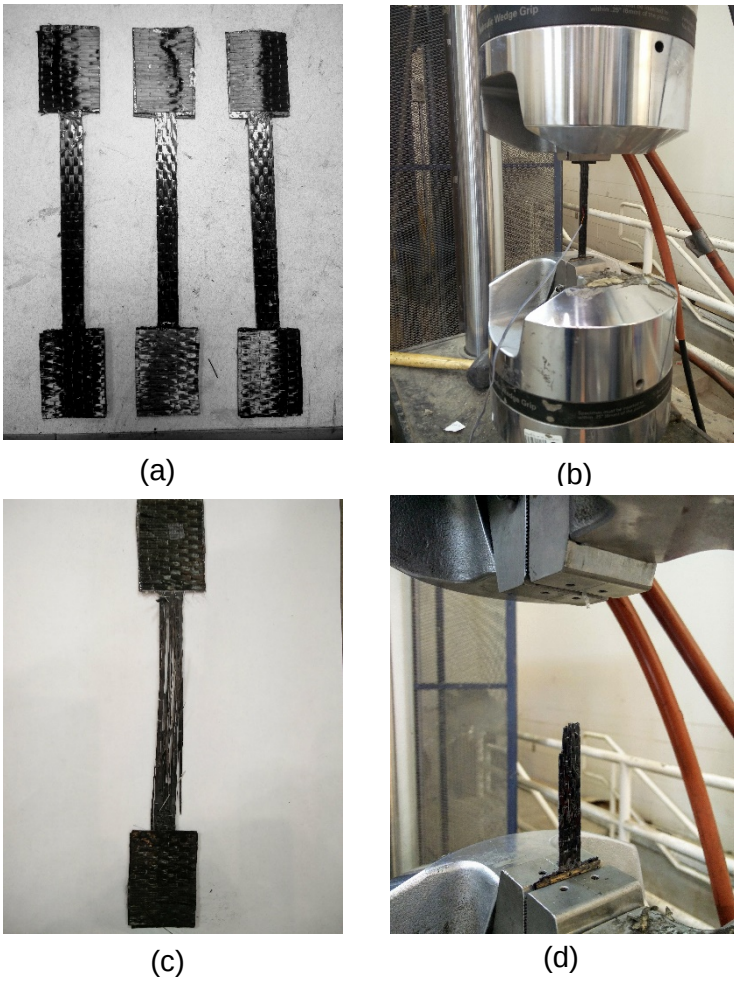

Figure 6-13 Tensile test of FRP laminate (a) Sample preparation (b) Tensile test set up (c) Failure mode (d) Failure mode

The failure load, displacement and strain were analyzed and stress-strain diagram for the coupon samples were plotted. Figure 6-14(a) shows the stress-strain diagram for field samples and Figure 6-14(b) shows the stress strain diagram for lab samples. It can be seen that the modulus of elasticity of field samples was similar with slight variability in the fail stress. The lab samples, however, had some variability in the elastic modulus as well as fail stress. The elastic response of the FRP samples is seen to be almost linear until failure.

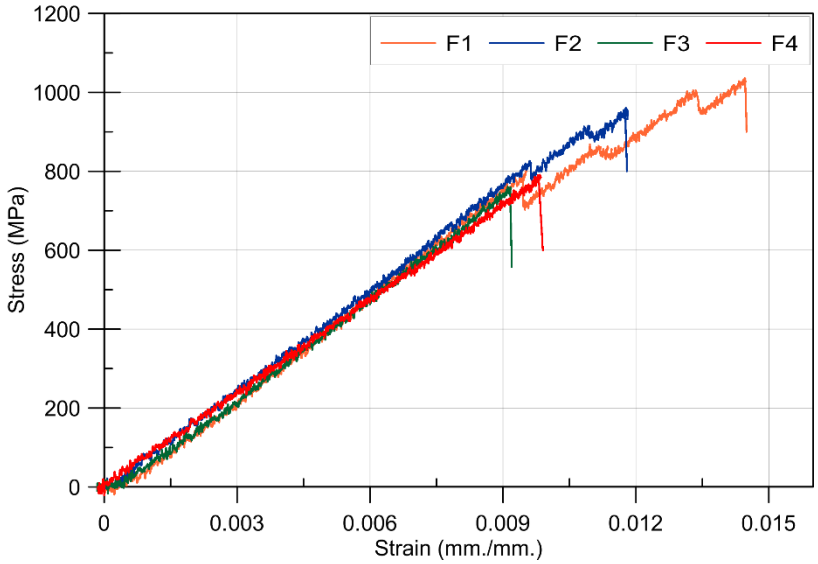

(a)

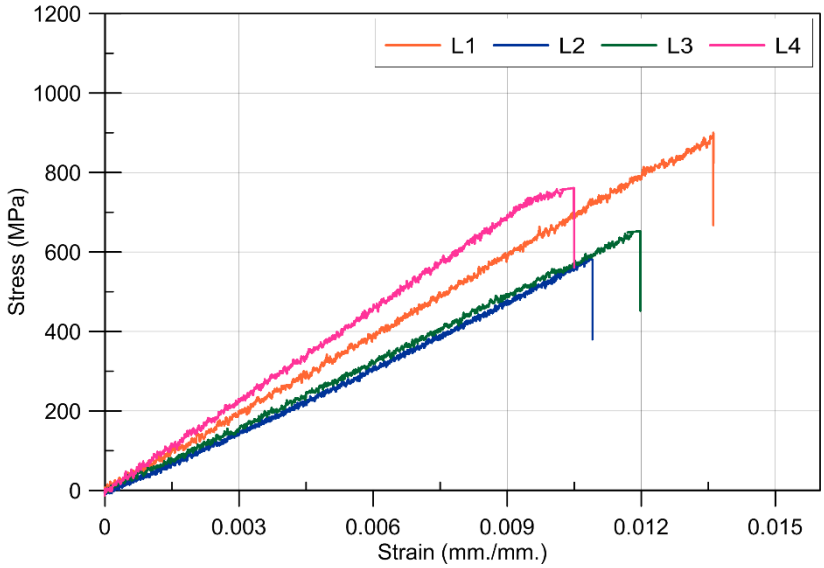

(b)

Figure 6-14 Stress strain diagram for FRP coupon samples (a) Field Samples (b) Lab samples

The dimensions, thickness and material properties obtained from the tensile test for the field samples and lab samples are presented in Table 6-4 and Table 6-5 respectively. The failure modes mentioned in the tables are based on ASTM D3039 (2014) and reproduced here in Figure 6-15.

Table 6-4 Tensile test results for Field Samples

Sample	Width (mm)	Thickness (mm)	Area (mm^2)	Modulus of Elasticity (MPa)	Fail Stress (MPa)	Fail Strain	Failure mode
F1	13.6	0.42	5.7	87236	1035	0.0145	SGR
F2	13.9	0.40	5.5	81205	961	0.0118	SGR
F3	13.8	0.39	5.6	85547	766	0.0092	SGR
F4	14.1	0.44	6.2	80616	904	0.0105	SGV
Average	13.8	0.41	5.8	83651	916	0.0115	

Table 6-5 Tensile test results for Lab samples

Sample	Width (mm)	Thickness (mm)	Area (mm^2)	Modulus of Elasticity (MPa)	Fail Stress (MPa)	Fail Strain	Failure mode
L1	14.2	0.48	6.7	65960	900	0.0136	XGM
L2	14.2	0.72	10.2	53746	589	0.0109	AGM(1)
L3	13.2	0.67	8.9	57482	652	0.0120	LAT
L4	14.9	0.52	7.7	75126	761	0.0105	GAT
Average	14.1	0.60	8.4	63078	725	0.0117	

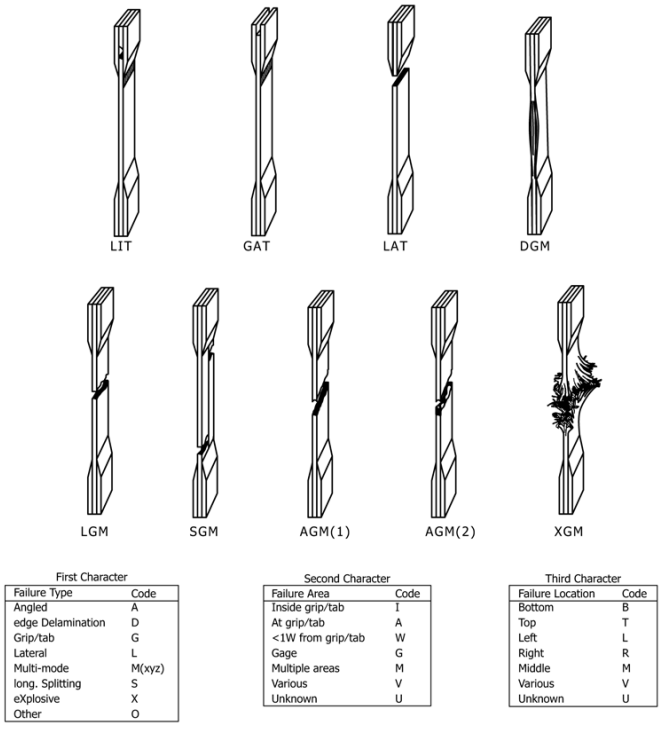

Figure 6-15 Tensile test Failure Codes/Typical modes (ASTM 2014b)

The modulus of Elasticity of the field samples was found to be higher than the Elastic modulus of the lab samples. Similar difference was found in the fail stress of FRP as well. However, it should be noted that the thickness of these samples was not same which can be the reason for the difference. FRP laminate is constitutes Fiber and matrix. The material properties of FRP depends on the material properties of fiber and epoxy. The volume fraction of epoxy and fiber in the laminate directly affects the laminate properties. Unidirectional carbon fiber has a very high tensile strength and modulus of Elasticity. However, the resin used in the laminate has a lower elastic modulus which in turn reduces the elastic modulus and tensile strength of FRP laminate. Equation 6-6 shows the relationship of Elastic modulus of laminate with the E value of fiber and matrix.

$$\frac{\nu_l}{E_l} = \frac{\nu_f}{E_f} + \frac{\nu_m}{E_m} \qquad \text{Equation 6-6}$$

Where ν_l, ν_f, ν_m are the volume of laminate, fiber and matrix respectively. E_l, E_f, E_m are the elastic modulus of laminate, fiber and matrix respectively. The width and the length of the FRP coupons are similar. Hence the volume of fiber and matrix are dependent only on the thickness of fiber and matrix. The thickness of fiber as well as the thickness of laminate is known. The E of fiber is also known in the above equation. This means the E of laminate is only a function of E_m, the elastic modulus of matrix and thickness of matrix. Equation 6-6 can be reduced to Equation 6-7 in the following way.

$$\frac{t_l}{E_l} = \frac{t_f}{E_f} + \frac{t_l - t_f}{E_m} \qquad \text{Equation 6-7}$$

Calculating E_m from Equation 6-7, the field sample can be converted to the same thickness as the lab sample assuming that E_f doesn't change. This process provides a logical comparison between the samples as they are both the same thickness and have the same volume fraction of epoxy.

Similar comparison can be made between the fail stresses of the field sample and lab sample by using the same thickness of laminate. Table 6-6 shows the comparison between the lab sample and converted field sample.

Table 6-6 Comparison between Field CFRP and lab CFRP

	Field Sample	**Lab Sample**
Modulus of Elasticity (MPa)	54624	63078
Fail Stress (MPa)	570	725
Fail Strain	0.0115	0.0117

It can be seen that the field sample had a lower elastic modulus than the lab sample for same thickness. There was a reduction of 13% in the elastic modulus and a reduction of around 21% in the tensile strength of FRP laminate. This reduction can be because of various reasons including wetting and drying, fatigue cycles, change in temperature. This shows that there is reduction in the material properties of FRP laminate when exposed to environmental conditions.

However, the actual material properties of CFRP obtained by the tensile test was used in the calibration of the model. Fail stress, fail strain and modulus of elasticity in both directions were determined from experiment and the shear modulus was calculated using the relationship.

6.1.2.3 Model Calibration

The concrete modulus of Elasticity and stress strain diagram was modified based on the material properties of core samples and the temperature values obtained for different sections after the heat transfer analysis. The heat transfer analysis of the bridge showed that the beams were subjected to a temperature of around 500°C to 700°C in Span 3 and Span 4 of the bridge. Span 1 was exposed to a temperature around 60°C and Span 2 had a temperature of the beam of around 120°C. The deck in Span 3 and Span 4 was subjected to a temperature of 400°C and a temperature of 120°C for Span 2. First analysis of the model was carried out based on the temperature obtained from the heat transfer analysis. It was seen that the model provided a good correlation with experimental results. However, there was still some discrepancy in the model and experimental results, mostly in Span 2 and Span 3 of the bridge. It was observed that the stiffness of Span 2 needed to be reduced more. This could be because of the effect of fire near the supports and continuous span of the beam. Manual model updating was done until a good correlation was obtained between the modeling and experimental results.

Manual model updating is an effective method of obtaining an accurate FE model which can capture all aspects of structural behavior and represent the structural performance of the bridge. The procedure incorporated successfully reduces the modeling errors of an initial FE model. The analytical results from the FE model were compared with the field responses to validate the model's accuracy and obtain a representative structural model capable of reducing uncertainties and estimating uncertain structural parameters. The process of model calibration involved an iterative process of optimizing the material properties to obtain the closest correlation between the model and experimental results. An iterative trial and error

procedure based on engineering judgement was used to obtain a representative FE model. Correlation coefficient as shown in Equation 6-5 was used as the basis of comparison and to determine the accuracy of the model.

$$\frac{\sum(\varepsilon_m - \overline{\varepsilon_m})(\varepsilon_c - \overline{\varepsilon_c})}{\sum\sqrt{(\varepsilon_m - \overline{\varepsilon_m})^2(\varepsilon_c - \overline{\varepsilon_c})^2}} \qquad \text{Equation 6-8}$$

Where ε_m is the measured response, ε_c is the model response and $\overline{\varepsilon_m}$ and $\overline{\varepsilon_c}$ are the means of the measured and model responses respectively. The correlation coefficient determines the linearity between the measured and model responses. The value of correlation coefficient ranges from -1 to 1 where 1 represents a perfect correlation and -1 represents an exact opposite linear relationship. A correlation coefficient greater than 0.9 is considered to be a good correlation.

The truck patch loads were modeled on top of the bridge and analyzed to see the reponse when the truck was on different positions. Truck positions corresponding to the experiment were used for the calibration process until a good correlation was obtained. The truck was then moved to another span and the same process was repeated. After number of iterations and manual model updating, a calibrated finite element model was obtained.

Figure 6-14 shows the correlation between the experimental and model responses. The correlation of 0.841 shows that the correlation was not very good when all the strain values and displacement were compared [Figure 6-14(a)]. However, the calibration process was more focused on the calibration using the displacement values rather than the strain values which can be seen by the correlation coefficient of 0.996 in Figure 6-14(b). This shows that a good correlation was obtained between the experimental and modeling results.

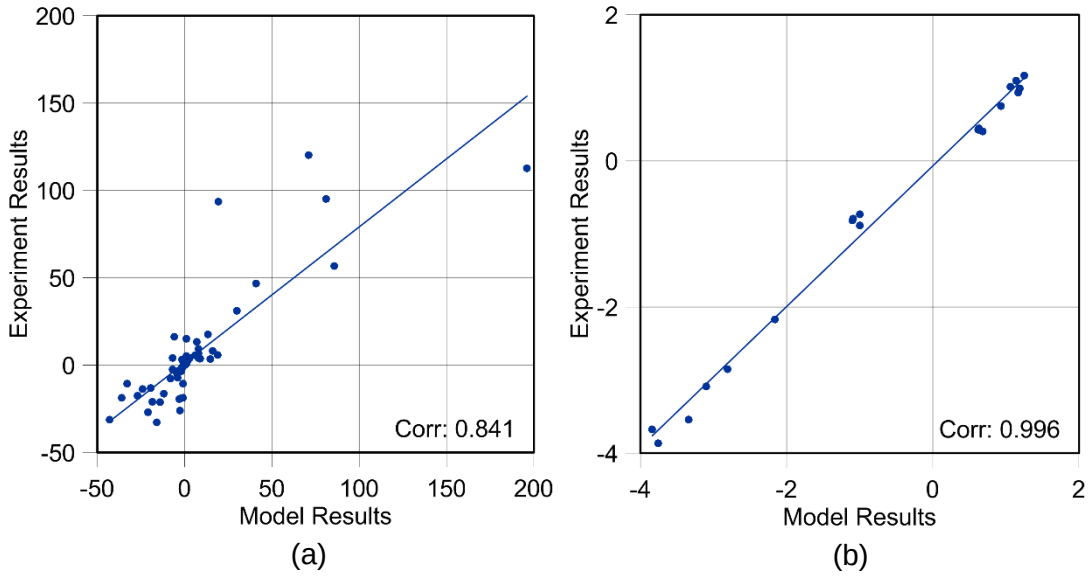

Figure 6-16 Correlation between experimental and modeling results (a) All results (b) Displacement results only

The values of E for concrete obtained after the model calibration was not very different than the values obtained from the Li-Purkiss model for concrete material properties at elevated temperatures. Table 6-7 shows the final values of E for different beams and spans after model calibration. It can be seen that the modulus of Elasticity of concrete was reduced significantly as a result of fire damage. Some of the beams which exhibited large amount of thermal effect had a modulus of Elasticity reduced to almost 30% of the undamaged beam. All the beams in Span 3 and Span 4 had a reduction in E value of more than 50%. This shows that the stiffness of fire damaged beams can decrease significantly because of the effect of temperature. The deck also exhibited a loss of elastic stiffness of more than 50%.

Span	Beam	Modulus of Elasticity (MPa)	Temperature (˚C)
S1	B1	21925	60
	B2	21925	60
	B3	21925	60
	B4	21925	60
	B5	21925	60
	B6	21925	60
	Deck	21925	60
S2	B1	15580	420
	B2	15580	420
	B3	19680	320
	B4	19680	320
	B5	21720	270
	B6	21720	270
	Deck	19680	420
S3	B1	5380	620
	B2	5380	620
	B3	6690	575
	B4	6690	575
	B5	14750	440
	B6	14750	440
	Deck	8000	500
S4	B1	5380	620
	B2	5380	620
	B3	6690	575
	B4	6690	575
	B5	14750	440
	B6	14750	440
	Deck	8000	500

6.2.3 Modeling Results

The final calibrated model obtained after the calibration process was used to compare the experimental results with the modeling results. A moving load analysis was then carried out to simulate the crawl speed test on the bridge. A user subroutine was used to move the truck patch loads across the span of the bridge in ABAQUS. The mid-span displacement for beam B5 at Span 3 of the bridge was compared with

the modeling results to verify the model. The comparison between experimental and modeling results is presented in Figure 6-17. It shows that the final bridge model showed a good match of displacement for the moving load analysis.

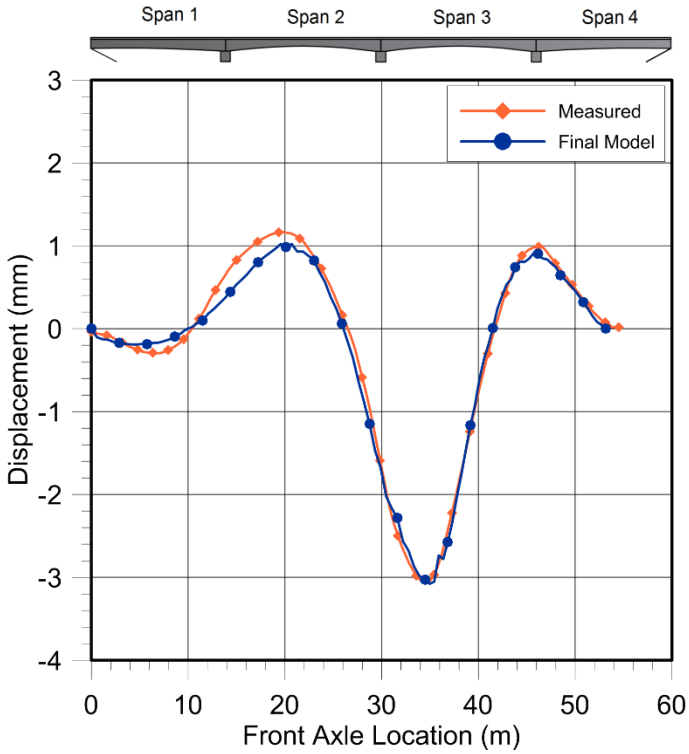

Figure 6-17 Modeled and measured displacement at mid-span of beam B5, Span 3

The strain results did not show as much correlation as the displacement results for the bridge. Few strain results were comparable and few results were a little far off than the experimental results. The profile of the strain results showed good correlation which showed that the boundary conditions applied was a good fit for the model. Figure 6-18 shows the strain response of mid-span of beam B5 in Span 3 of the bridge when the truck moves from one end of the bridge to the other. It can be seen that the model and experimental results show a good correlation.

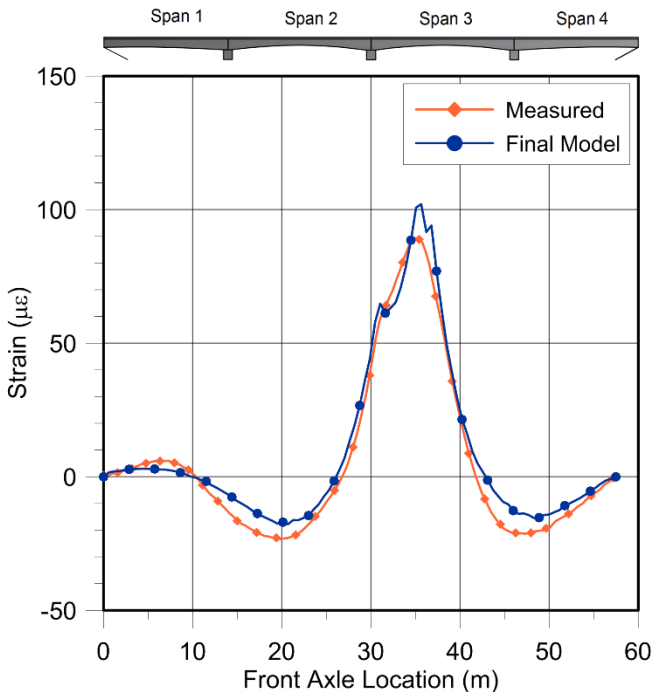

Figure 6-18 Modeled and measured strain at mid-span of beam B4, Span 3

6.2.4 Distribution Factor Comparison

Once the structural response of the bridge girders were verified with the moving load analysis; the peak strain values were used to make a comparison between the model and measured strain distribution across the girders. The peak strain values were taken from the crawl speed tests and compared with those obtained from moving load analysis. This allowed us to make a comparison in the distribution factor of the girders between model and experimental results. Figure 6-19 and Figure 6-20 shows the transverse strain distribution obtained from the model compared with their measured values for both Spans 2 and 3.

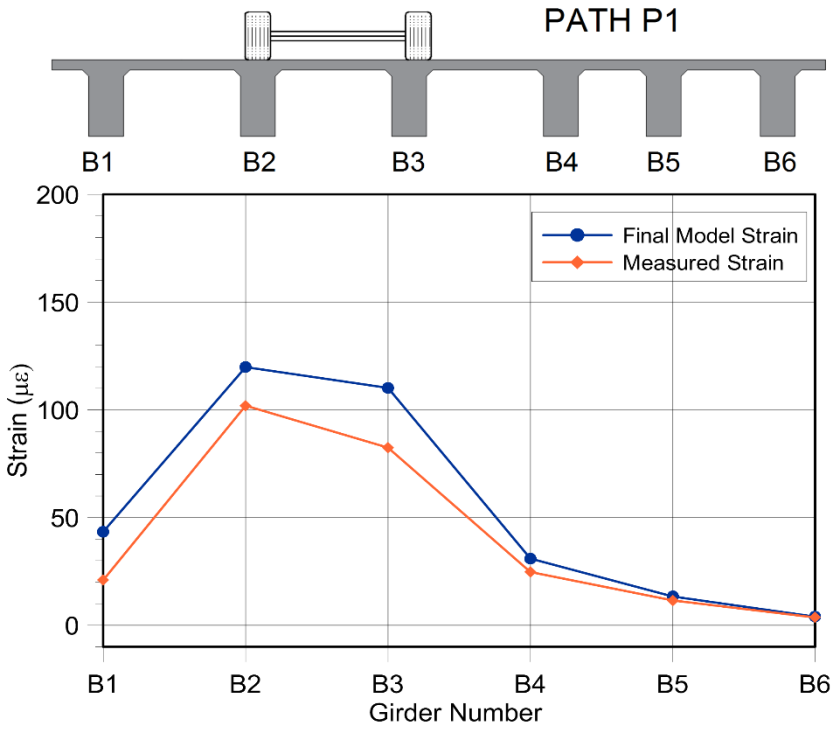

(a) Span 2

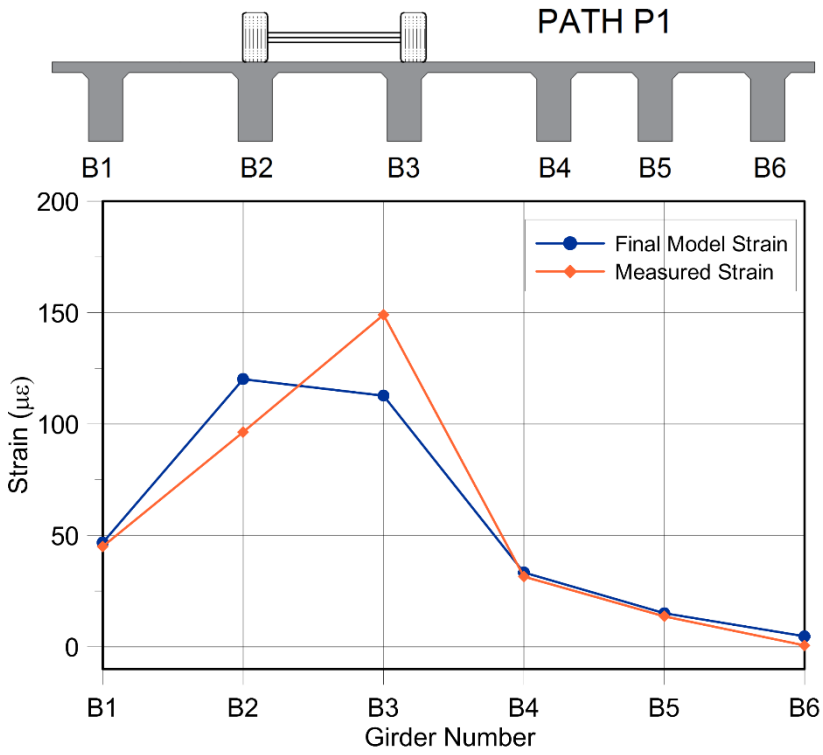

(b) Span 3

Figure 6-19 Measured and modeled strain distribution across all girders for Path P1

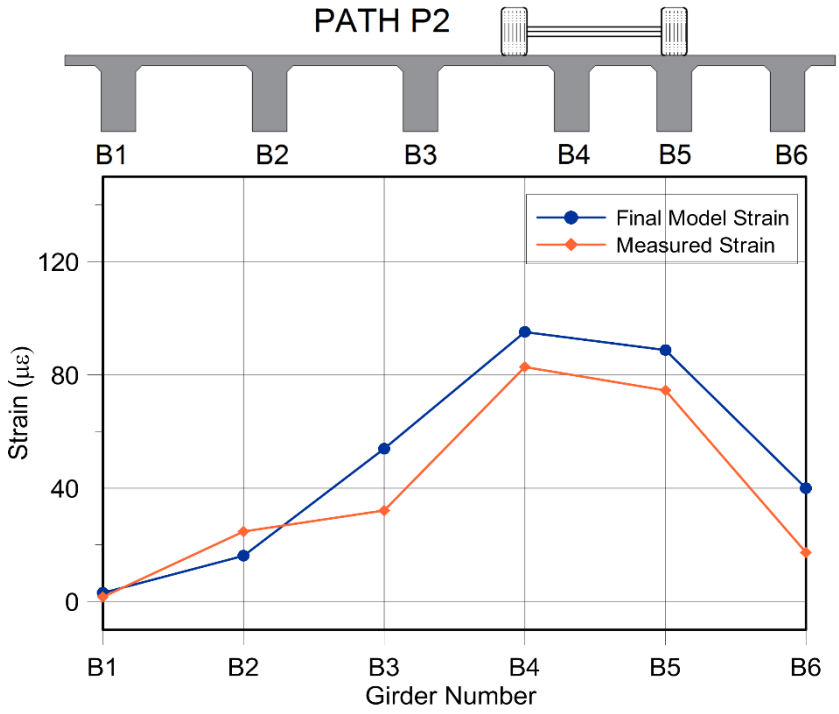

(a) Span 2

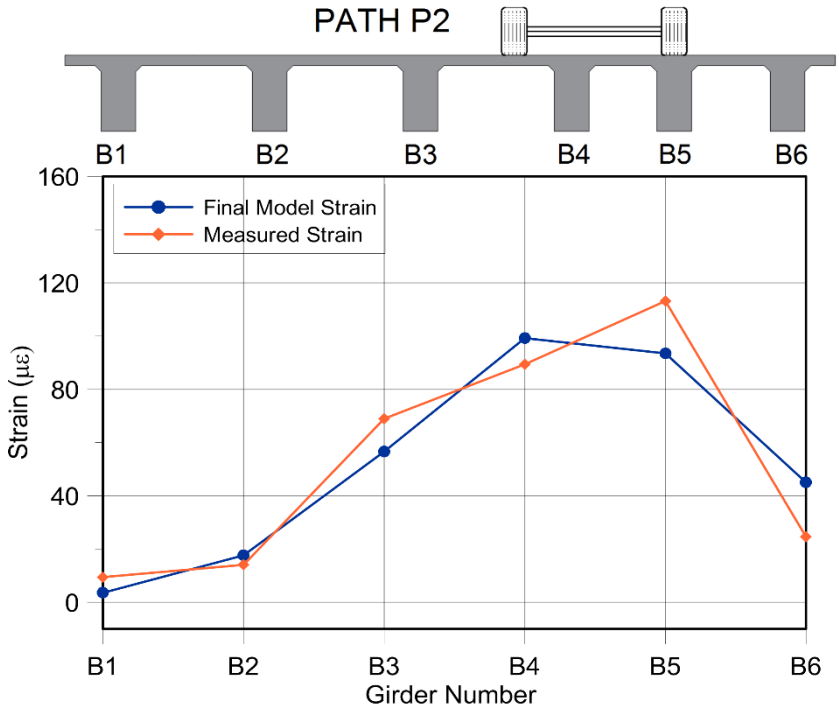

(b) Span 3

Figure 6-20 Measured and modeled strain distribution across all girders for Path P2

The strain response from the calibrated model was used to calculate the distribution factors for Path P1 and Path P2 based on the modeling results. The results of the distribution factors thus obtained is shown in Table 6-7. The distribution factors obtained from the model was similar to the values obtained from experiment and presented in Table 6-2. However, the distribution factor of Span 3, Path P1 was controlled by Beam B3 in the experiment rather than Beam B2 as seen from the model results. This was because of a large strain response of Beam B3 in Span 3 of the bridge.

Table 6-7 Distribution Factors from final model

Distribution Factor for moment		
Girders	Span 2	Span 3
B2	0.372	0.340
B4	0.320	0.314

The transverse strain distribution obtained from non-destructive load test was used to calculate the distribution factor for Span 2 and Span 3 of the bridge. Similar calculations were carried out to calculate the Live load DFM based on the modeling results. Figure 6-22 compares the distribution factors obtained from model and experiment with the AASHTO LRFD distribution factors.

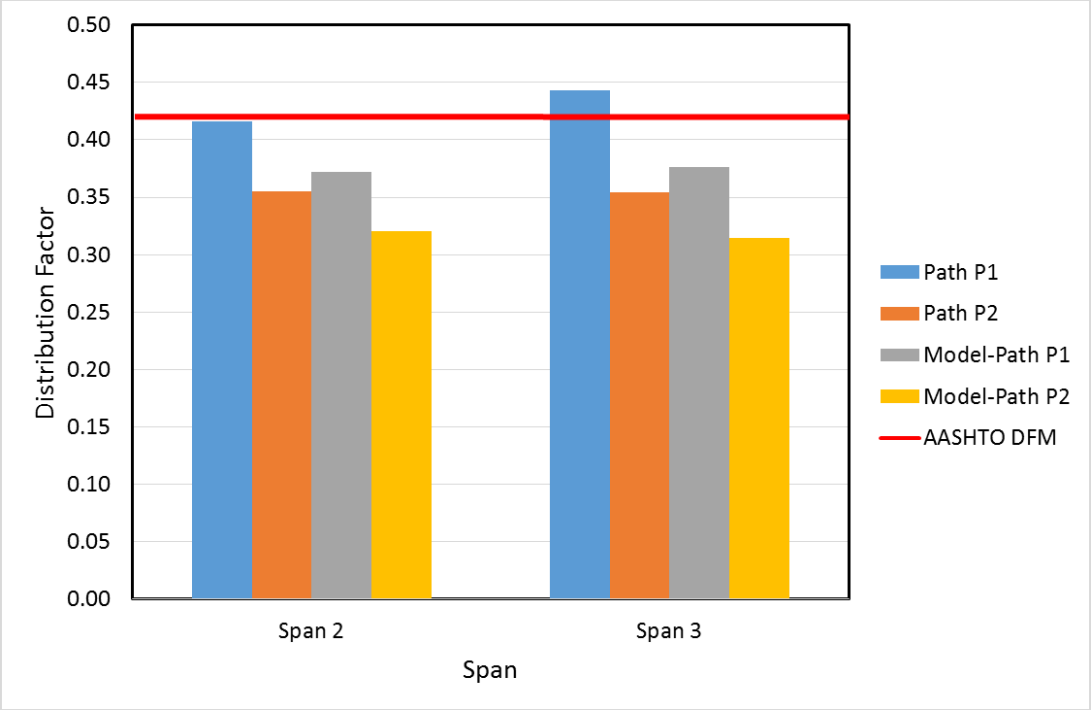

Figure 6-21 Comparison of Distribution Factor with AASHTO Distribution factor

The distribution factor obtained from Path P1 and Path P2 based on the experiment and modeling results were compared with the AASHTO calculations. It was observed that the distribution factor was almost similar to the values obtained from AASHTO. The value obtained for Path P1, corresponding to Beam B3 in Span 3 of the bridge was found to be higher than the AASHTO DFM. The horizontal line shows the value of distribution factor for one lane loaded condition obtained from AASHTO. Various researchers have found that the distribution factors obtained from AASHTO is conservative and over estimates the load carried by the girder. However, based on the results obtained for the fire damaged MacArthur bridge, it was observed that the DFM can be indeed higher than expected. Fire damaged girders can exhibit a highly irregular and unpredictable behavior which is why it is necessary to properly analyze the performance of the bridge structure.

6.2 Loop 12 Bridge

6.2.1 Experimental Results

Non-destructive test on the Loop 12 bridge was done in January 2018. The data was recorded at 100 Hz using a laptop connected to the DS 50A DAQ and a Micro measurement 8000 DAQ. Same procedure for data analysis was done as the MacArthur bridge. Lessons learned and experience gained from the initial test helped in analyzing the data in a smoother manner. The data obtained from the DAQ was taken to the computer and analyzed using Microsoft Excel. The large volume of data created during the load test was a challenge to analyze and present. The same process of processing the data and correlating the data with the position was done. Stop watch readings and time noted during the test were used to correlate the data with position of truck. Data recording started before the vehicle entered the bridge and stopped when the vehicle exited the bridge. The strain and displacement values did not always start from zero although the gauges were balanced before the test. The residual strain was subtracted from the initial reading to get the actual strain values.

Initial plot of the data showed that the strain and displacement readings started at zero and returned approximately to zero at the end of the test. This shows that the response of the bridge was within linear elastic range and no non-linearity was observed. Two different runs were carried out for each test to verify the accuracy of the data obtained. This is important to establish repeatability of data and to ensure that the gauge readings obtained are reliable for further analysis. The response of a strain gage pair S2B4B, a strain gage at the mid span of the Girder 4 is presented in Figure 6-23(a). Similar strain response was seen in the top strain gauges [Figure 6-23(b)] and displacement response [Figure 6-23(c)]. Negative readings are indicative

of compression and positive strain readings indicate tension response of the girders. All strain gauges and displacement transducers showed similar trend and peak magnitude in both test runs; which is why the average of the two is taken for further analyses.

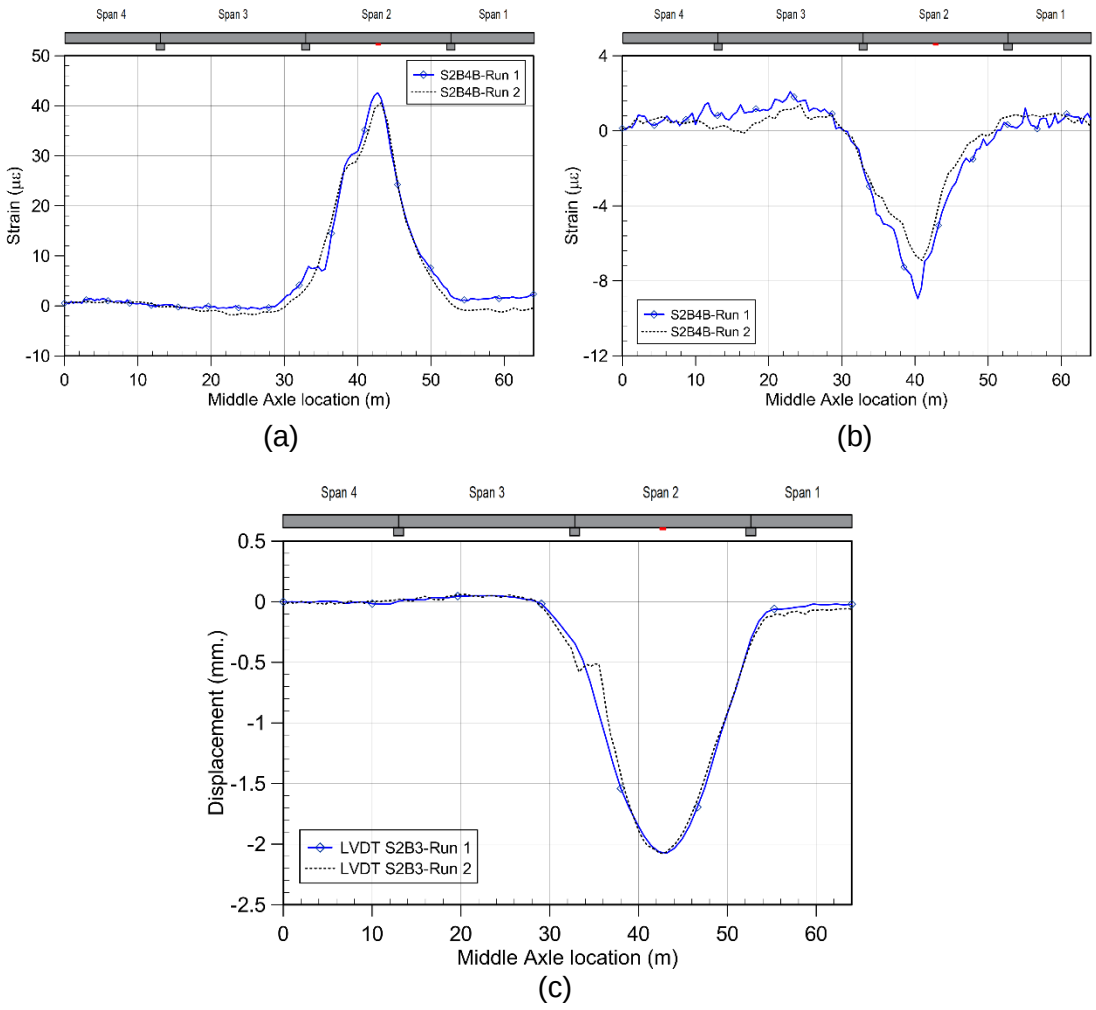

Figure 6-22 Repeatability of results for (a) Bottom Strain gauge (b)Top Strain gauge (c) Displacement Transducer

6.2.1.1 Strain Response of Loop 12

As mentioned in Section 4.4.2, two paths were selected on the bridge so that the load distribution characteristics of the whole bridge can be studied. The strain response of all the girders at 8.69 m from the adjacent bent were analyzed for two spans, Span 3 and Span 2. It was evident from the response that Beam B3 and Beam B4 which were directly under the truck wheels had the maximum strain response and the strain reading decreased subsequently on further girders. Strain response of all girders in Span 2 and Span 3 when the truck was moved in Path P1 and Path P2 is presented in Figure 6-24 and Figure 6-25 respectively.

It can be seen that, for Path P1, the strain response of the girders B3 and B4 were the maximum as they were directly under the truck load and it decreased for other girders in the span. Similarly, for Path P2, the strain response was maximum for girders B7 and B6 that were under the highest influence of the truck load and decreased subsequently. It should be noted that the girder that was farthest from the effect of the truck load, girder B9 for Path P1 and girder B1 for Path P2 exhibited negative strain corresponding to compression on the bottom flange. This could be due to the presence of the traffic barrier over the exterior girders.

Another important observation that was visible from the strain response is that the strain observed in Span 3 of the bridge was higher than the strain observed in Span 2 of the bridge. This could be because the deck and two girders in Span 2 were damaged and subsequently replaced. Beam B3 and B4 of Span 3 also exhibited a lower strain which could be attributed to the fact that these girders were repaired with mortar and strengthened with CFRP laminate. A comparison between strengthened and undamaged girders is presented later in Section 6.2.1.6.

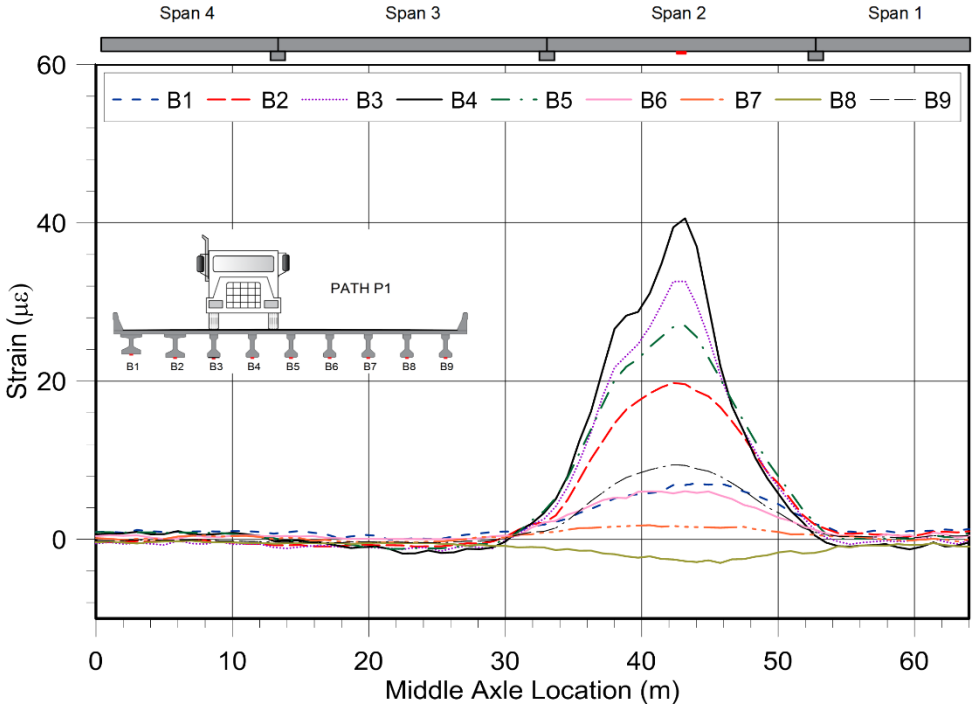

(a) Span 2

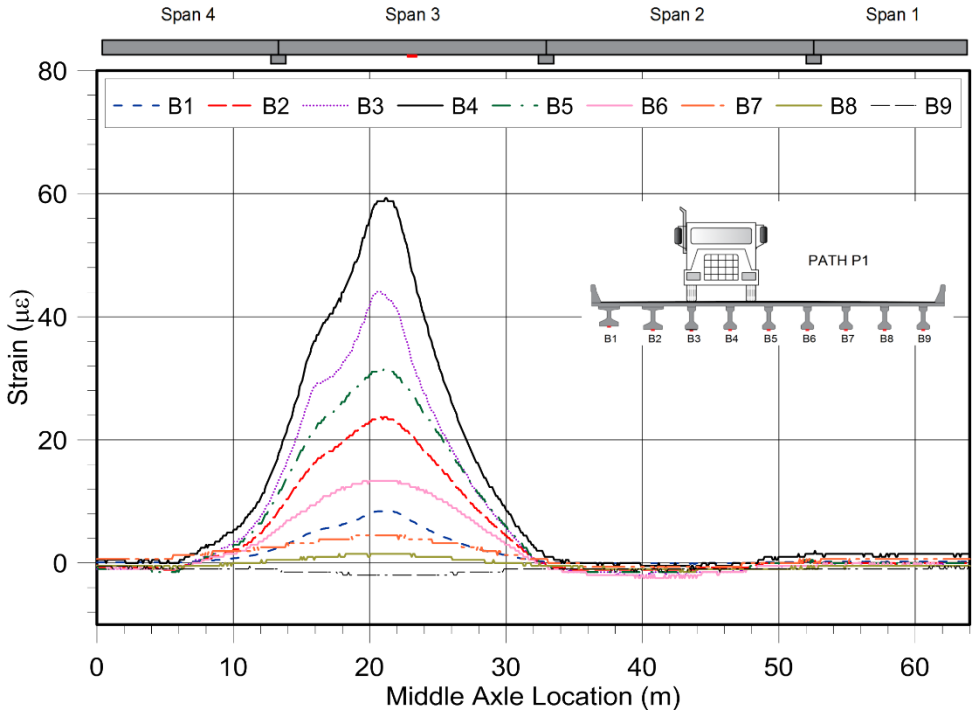

(b) Span 3

Figure 6-23 Strain time series at mid span for Truck Path P1

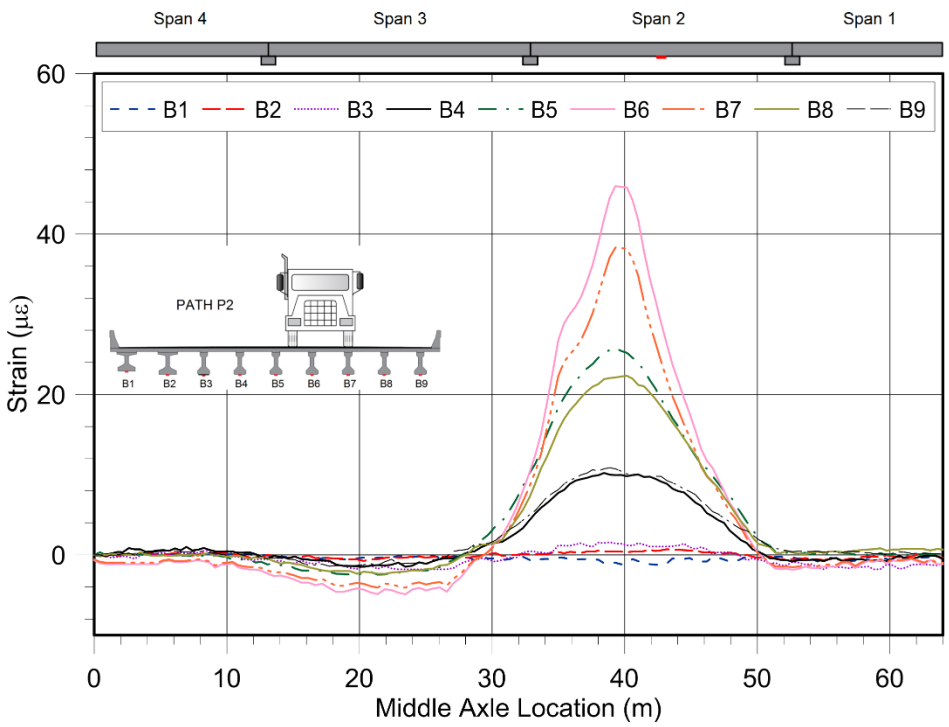

(a) Span 2

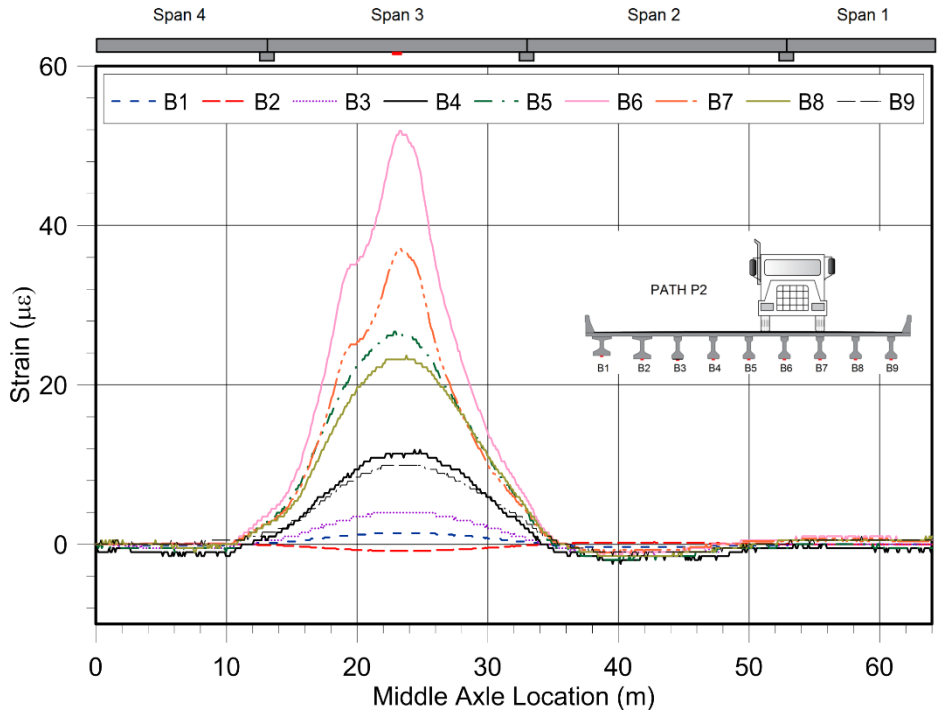

(b) Span 3

Figure 6-24 Strain time series at mid span for Truck Path P2

The time series of strain data shown in Figure 6-24 and Figure 6-25 show that the strain in the girders increased from zero as the truck enters the Span and returns to zero as the truck leaves the span. This shows that there is no residual strain in the adjacent span when the truck is in other span. Hence, it can be assumed that the girders are simply supported and there is no significant continuity between the spans. The prestressed girders were sitting on bearing pads and expansion joints were present on the deck between spans. This deduction is important as Span 2 and Span 3 were modeled and analyzed separately as two different bridges during Finite Element Modeling.

6.2.1.2 Displacement Response of Loop 12

Displacement response of a bridge girder is important to ascertain the stiffness and ductility of a concrete girder. Deflection response is generally preferred to strain response because it is unaffected by local irregularities and cracks. Local abnormalities in concrete girder can significantly affect the strain response of a bridge girder. However, displacement results are often representative of the overall girder. Displacement response of girders B3 and B7 of Span 2 and Span 3 of the bridge is presented in Figure 6-26 and Figure 6-27.

The deflection response of the girders reiterate the fact that the structure is within the linear elastic range as the deflection response returns to zero as the truck leaves the span. It can be noted from the deflection response that the deflection was maximum for Beam B3 when the truck is on Path P1 and decreases for Beam B7. Similar behavior is seen for Path P2 with the maximum displacement on Beam B7.

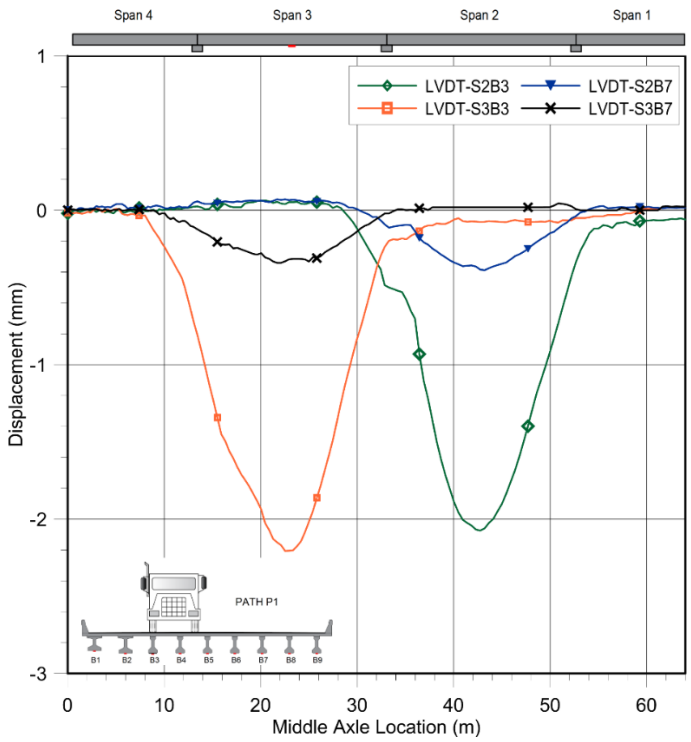

Figure 6-25 Displacement response for Path P1

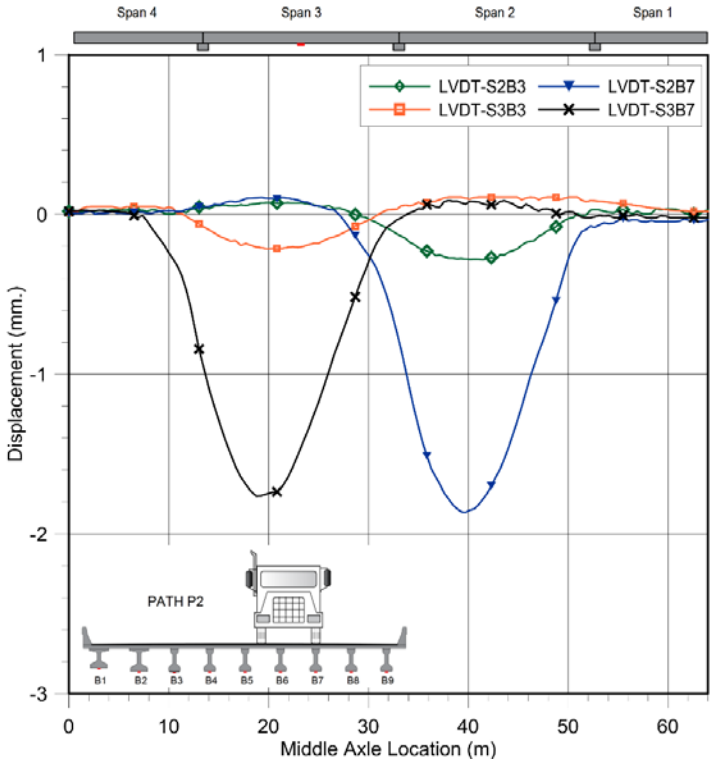

Figure 6-26 Displacement response for Path P2

6.2.1.3 Neutral Axis Calculation

Neutral axis depth of a composite concrete girder can be taken as an indicator of the overall health of the girder. Consistency in neutral axis location when the truck passes over a girder shows the nature of the girder structural health. Comparison of neutral axis depths between different beams can also provide an understanding of the structural performance of bridge girder. Strain gage were installed in pair of top and bottom strain gages, in 6 girders in Loop 12 bridge. Figure 6-28 shows the process of calculation of neutral axis based on the top and bottom strain gage readings.

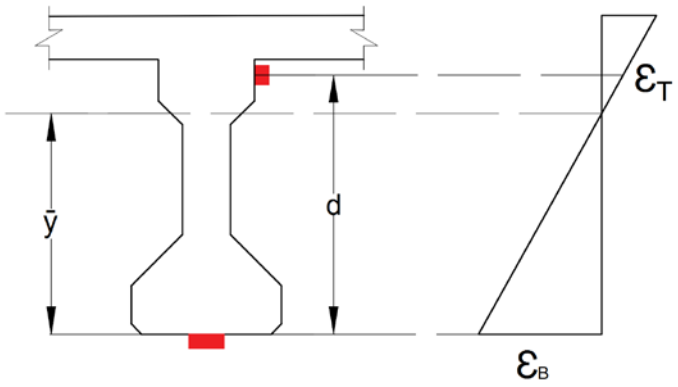

Figure 6-27 Illustration of neutral axis calculation

The strain gage location, $\bar{y}$ from the bottom of the girder can be calculated using Equation 6-1.

$$\bar{y} = \frac{\varepsilon_B d}{\varepsilon_B - \varepsilon_T} \qquad \text{Equation 6-1}$$

Where

$\bar{y}$ = Neutral axis location from bottom (mm.)
d = distance between the top and bottom gauges
ε_B = Strain in bottom gauge ($\mu\varepsilon$)
ε_T = Strain in top gauge ($\mu\varepsilon$)

The neutral axis locations were calculated for Beam B3 when the truck was on Path P1 corresponding to truck on B3 and Beam B7 when the truck was on Path P2 corresponding to truck over B7. The top strain gage was placed 50 mm below the bottom face of the deck and the bottom strain gauge was located on the bottom flange of the girder. This is why distance, '*d*' was fixed for neutral axis calculations. It is not uncommon for top strain gauges to provide a strain reading close to zero during a load test. This can be because the location of the top strain gauge is close to the neutral axis location. Similar behavior was observed during the Loop 12 load test on a few strain gauges. Hence, only the strain gauges that provided significant strain response were used for neutral axis calculations. Neutral axis locations along with the corresponding top and bottom strain gage time history is shown in Figure 6-29 and Figure 6-30.

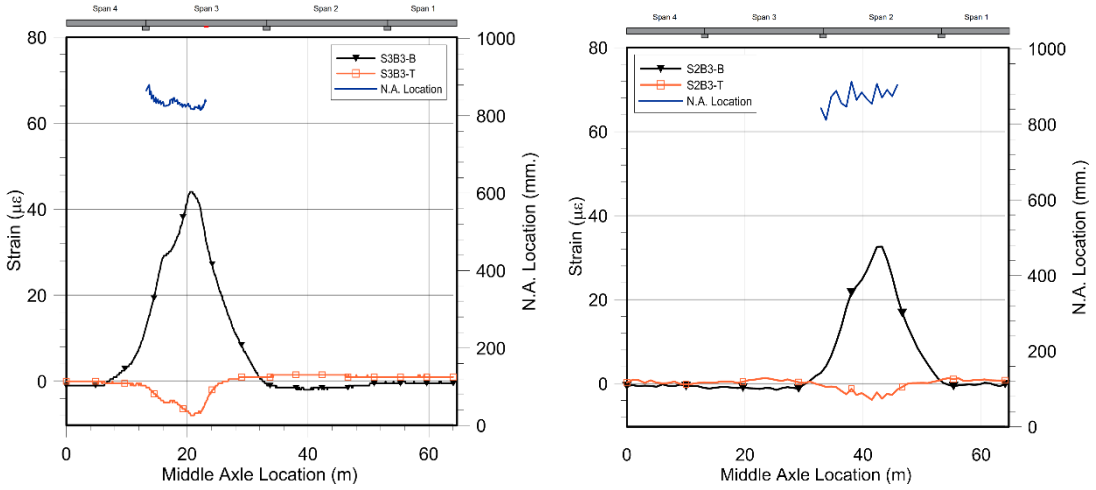

(a) Span 3 (b) Span 2

Figure 6-28 Strain history of top and bottom strain gauges for Beam B3 showing neutral axis location

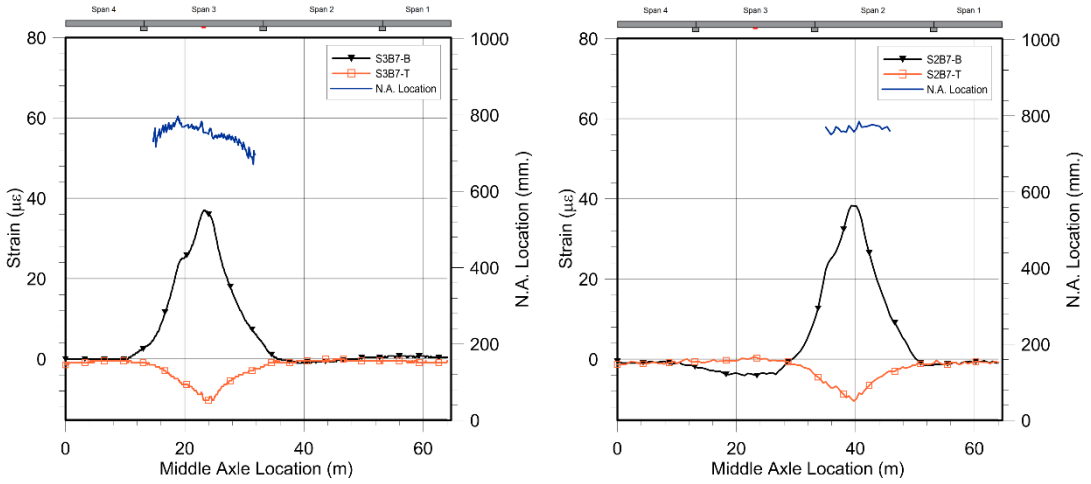

(a) Span 3 (b) Span 2

Figure 6-29 Strain history of top and bottom strain gauges for girder B7 showing neutral axis location

Only the significant strain measurement higher than 3 με were taken for the calculation of neutral axis. Small values of strain produce a large amount of error during the calculations. Vibrations and accuracy of the instruments can also be the reason for the slight change in neutral axis with time history of strain. This can be expected for any experimental results.

6.2.1.4 Live Load Distribution Factor

This section summarizes the findings of this research about the lateral live load distribution factor on a prestressed concrete bridge span with girders repaired and strengthened with CFRP wrapping. The live load distribution factors from the non-destructive load test is calculated based on the maximum strain response and compared with the AASHTO LRFD distribution factors for moment (DFM). The calculation for the live load distribution factors for moment for the Loop 12 bridge is presented in Appendix C. Lateral live load distribution factor is the function of span length, spacing between girders and the stiffness parameters representative of the geometry and material properties of the girder. This is the reason the live load

distribution on a bridge span can change as a result of maintenance and rehabilitation of bridge structure. The AASHTO Live load DFMs calculated for the loop 12 bridge is summarized in Table 6-8.

Table 6-8 AASHTO live load Distribution Factors

	Distribution Factor for moment	
Girders	One lane loaded	Two lane loaded
Interior	0.358	0.479
Exterior	0.432	0.452

The structural response of the bridge was analyzed based on the strain readings obtained at mid span of each span of the bridge. Transverse strain distribution at each girder was plotted and compared based on the strain gauge readings at the bottom of the girder. This presents an idea about how much strain is distributed to the girder directly below the load and how much of it is taken by the girders further away. The peak strain were taken from the crawl speed tests and compared with the readings from the stop location test. The strain readings were almost the same with only a slight variation. The strain distribution was plotted for the two spans, Span 3 and Span 2 of the bridge for two different paths Path P1 and Path P2. This provided four strain distribution plots for the bridge which is presented in Figure 6-31 and Figure 6-32.

Straight line is used to connect the peak readings of the plots; although, the response of the bridge between the girders is not linear. It can be seen from the figures that the strain reading is greatest on the girder under the truck load and decreases further away. The strain in the furthermost girder is negative which could be attributed to the presence of barrier near the exterior girder. These peak strain reading can be used to calculate the DFM for the corresponding span of the bridge.

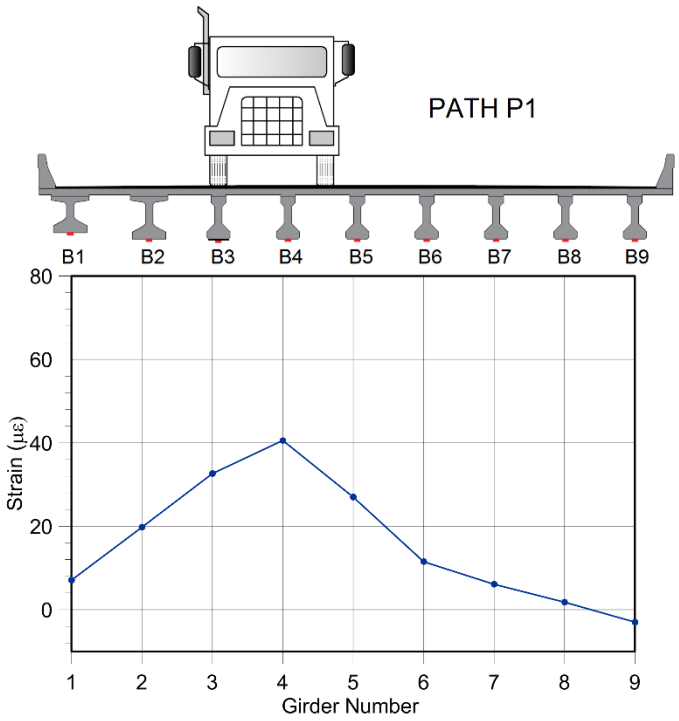

(a) Span 2

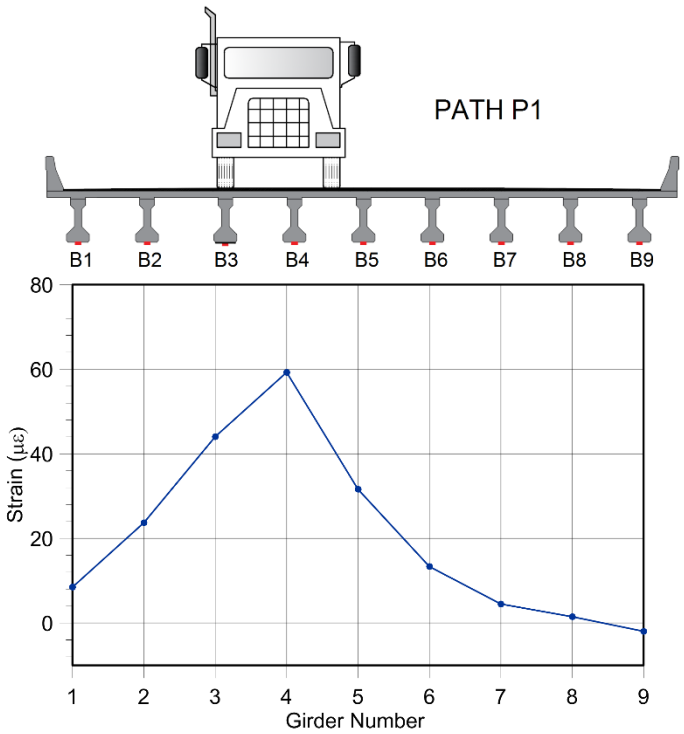

(b) Span 3

Figure 6-30 Measured strain distribution at Mid-span of the girders for Path P1

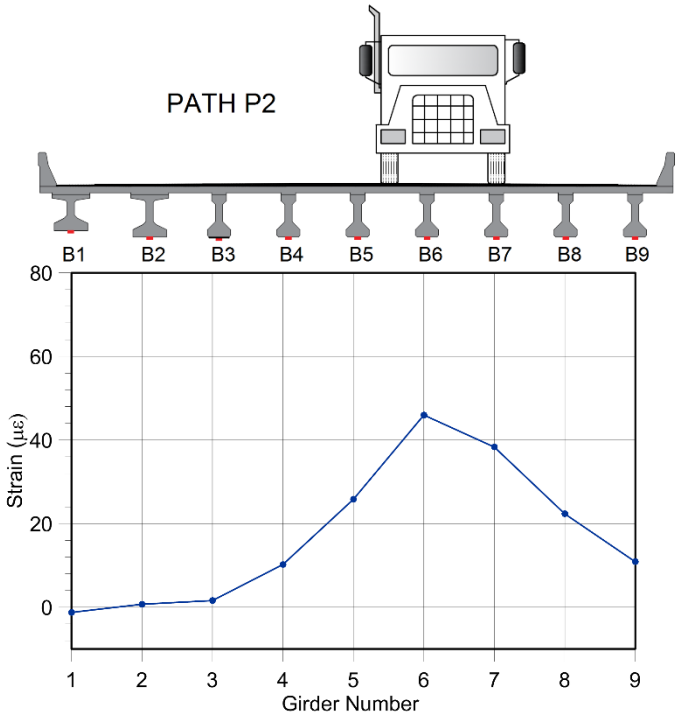

(a) Span 2

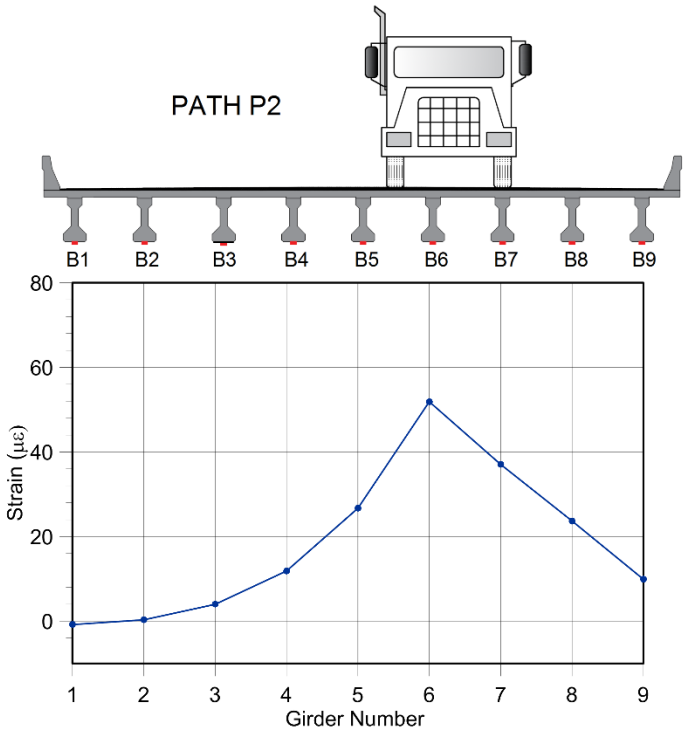

(b) Span 3

Figure 6-31 Measured strain distribution at Mid-span of the girders for Path P2

The bridge distribution factor for Loop 12 bridge was calculated from the experiment using Equation 6-2 discussed in Section 6.1.1.3. The peak strain from the crawl speed tests was verified with the results of stop location tests and used to calculate the DFM. It can be seen that the response in the furthermost girder was negative when the maximum strain occurred on the nearest girder. These strain values were not used while calculating the distribution factor. The distribution factors for Beam B4 and Beam B6 for one lane loaded scenario is summarized in Table 6-9.

Table 6-9 Distribution Factors from Experiment

Distribution Factor for moment		
Girders	Span 2	Span 3
B4	0.277	0.321
B6	0.295	0.278

6.2.1.5 Multiple Truck Results

The distribution of strain among the girders when two trucks are on top of the bridge deck can be considerably different as there can be an uplift effect. This change in load distribution characteristics of the bridge is incorporated into AASHTO (2016b) by the use of multiple presence factor which takes into account the effect of two trucks on the bridge. The strain is distributed more evenly across all the girders when two trucks are present on the deck. Figure 6-11 shows the transverse distribution of strain as a result of two trucks on Span 2 and Span 3. It can be seen that the strain distribution on Girder B4, B5 and B6 of the bridge was highest which was directly under the truck load. The strain in the other adjacent girders, however, decreased significantly. This could be because of the presence of a thickened slab under the outer three girders in both sides of the bridge. It should also be noted that the exterior girders did not exhibit a high amount of strain which could be attributed to the presence of barriers which increases the stiffness of the deck at that region.

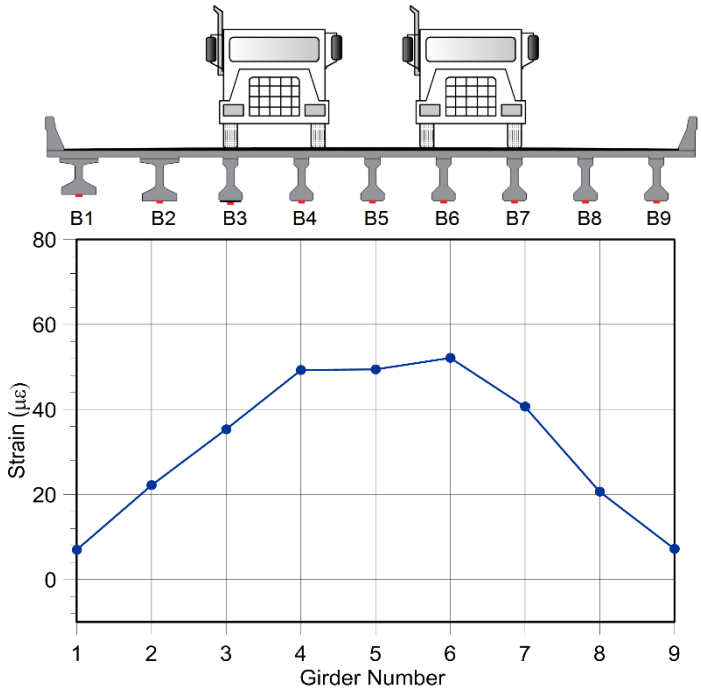

(a) Span 2

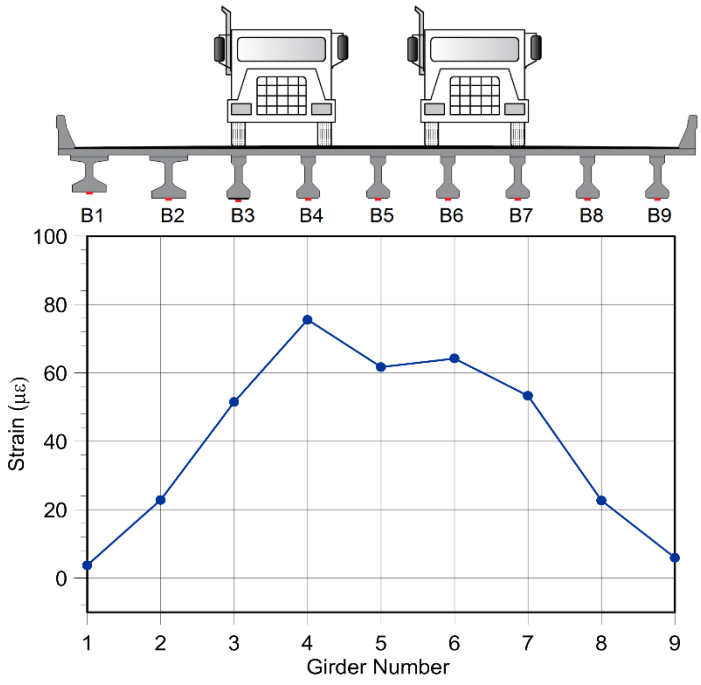

(b) Span 3

Figure 6-32 Measured strain distribution at Mid-span of the girders for multiple trucks

The distribution factor for the girders was calculated based on Equation 6-3. The equation takes into account the number of lanes that were loaded during the experiment. The distribution factors obtained from the experiment for multiple trucks is summarized in Table 6-10.

Table 6-10 Distribution Factor for two lane loaded

Distribution Factor for moment	
Span 2	0.367
Span 3	0.418

6.2.1.6 Comparison between CFRP strengthened vs. undamaged girder

The bridge had a couple of girders which were repaired and strengthened with CFRP as a result of over-height vehicle damage, which provided us an opportunity to compare the response of these girders with an undamaged similar girder. Girders, B3 and B4 in Span 2 of the bridge were damaged and strengthened with CFRP. B3 was selected as the representative CFRP strengthened girder for this study. The strain and deflection response of the girder was compared with the identical girder, B3 in Span 3 of the bridge which was not damaged. The girders had undergone similar age related deterioration and the effect of weather and external parameters was assumed to be similar. The load and fatigue effect on the girders can be assumed to be similar because they observe the same amount of traffic and similar live load effect. Strain response on the girders when the truck was moving on top of girder B3 was used to compare the response as seen in Figure 6-34.

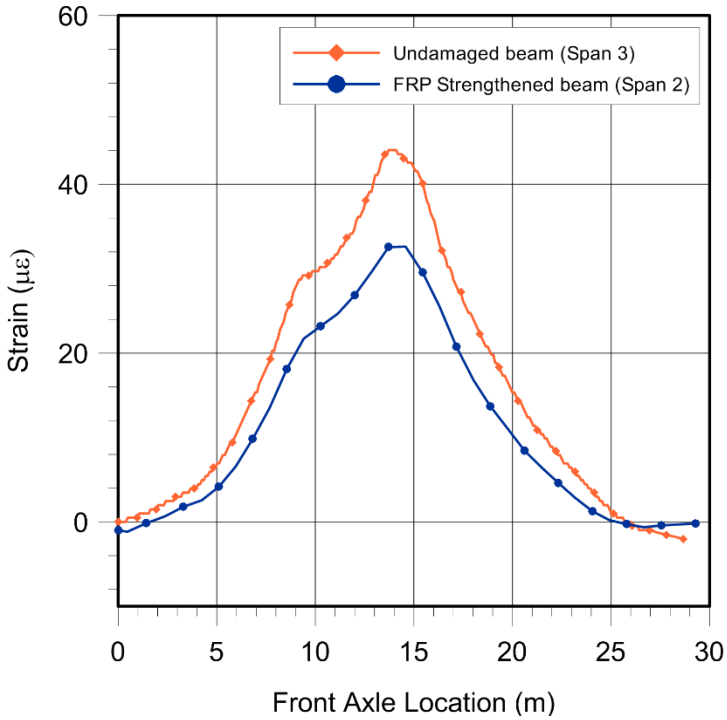

Figure 6-33 Strain comparison between undamaged and FRP strengthened girder

It can be seen that the strengthened girder, in Span 2 of the bridge, exhibited a lower strain when compared to the undamaged girder in Span 3 of the bridge. The damaged girder had cracks and a severed strand which was spliced as part of the repair. The cracks were epoxy injected and the lost section was repaired with mortar. The girder was strengthened for flexure with CFRP laminate and wrapped using transverse U-wraps. A higher strain value would be expected on the damaged girder because of the amount of damage and loss of strands. However, the inverse was seen to be true, which presents the effectiveness of the repair procedure and strengthening technique, in an in-service bridge. The strain in the strengthened girder was 27% lower than the undamaged girder. A z-test was performed on the strain data series for two spans of the bridge. The test showed that the strain was indeed higher as demonstrated by the z value of 2.34 which is higher than 1.96, the critical value for a significance level of 0.05. Hence, it can be said with a 95% accuracy that the strain

obtained from the strengthened girder was lower than the undamaged girder. Although, other factors like deck condition, composite action between the deck and girder and local abnormalities can affect the strain response, it can be safely assumed that the strengthening scheme was able to recover the flexural capacity of the damaged girder.

The strength and stiffness recovery of the damaged girder can also be seen looking at the deflection response of the two girders. The deflection response of the two girders discussed above is presented in Figure 6-35.

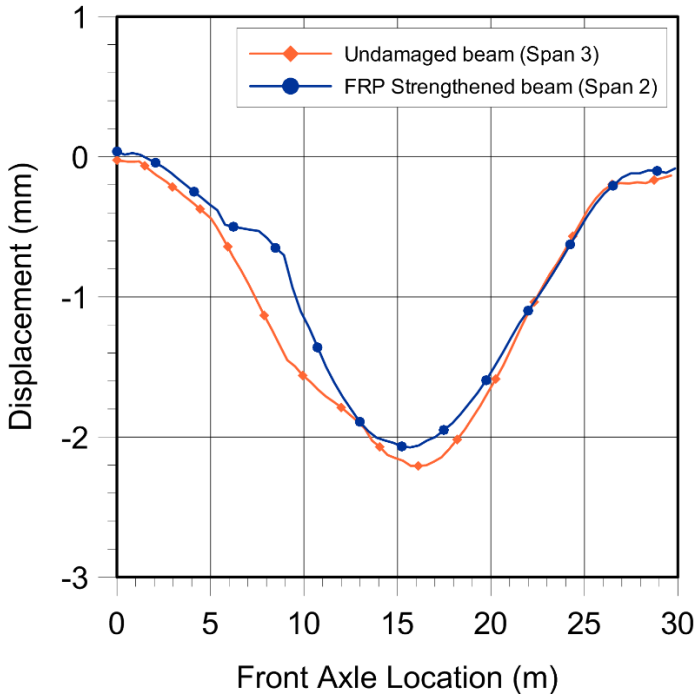

Figure 6-34 Displacement comparison between undamaged and FRP strengthened girder

The deflection observed for the damaged and strengthened girder was 6 % lower than the undamaged girder. This shows that the repair and CFRP application on the damaged girder was successful to recover the elastic stiffness of the bridge

girder. Reduction in displacement also shows that the girder became stiffer due to repair and CFRP application which can be attributed to the brittle nature of CFRP laminate.

The transverse strain distribution across all the girders for Span 2 and Span 3 was compared to see the overall performance of the two bridge spans. The strain response for all nine girders is shown in Figure 6-36.

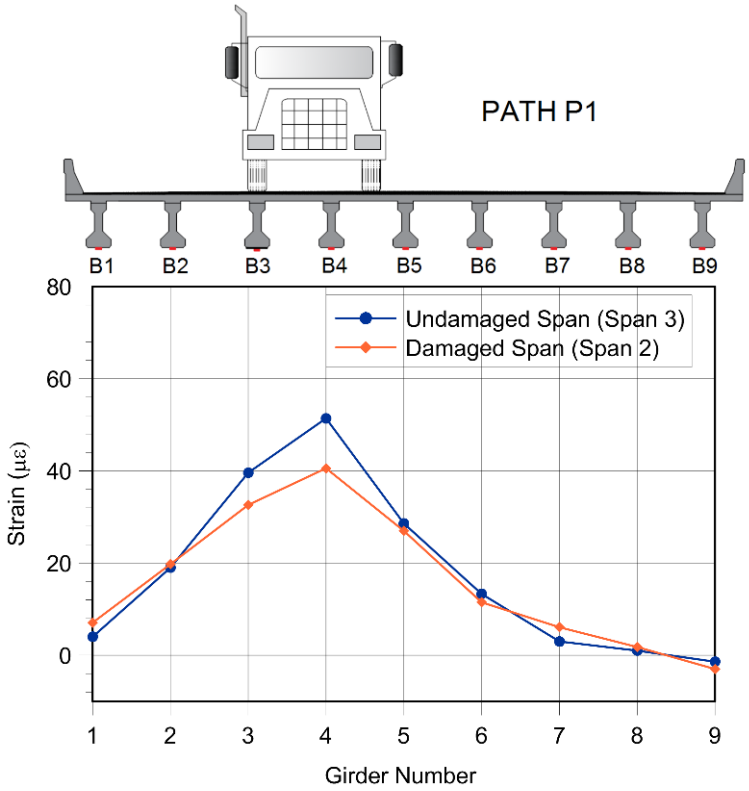

Figure 6-35 Strain comparison for all girders between Span 2 and Span 3

The strain response in two strengthened girders was lower than the undamaged girders. Although the strain response for other bridge girders was almost the same for both the spans, there was a significant difference in the strain values for Beam B3 and B4 which were the girders strengthened with CFRP. This shows that

the strengthened girder induced lower strain which can be attributed to increase in flexural capacity due to CFRP laminate strengthening.

6.2.2 Model Verification and Calibration

An initial model was created using the material properties available in literature based on theoretical models and specifications. Concrete and steel were modeled using the design compressive strength and design yield stress respectively. Material properties available in the factory specifications were used for the properties of FRP laminate. However, material properties can change with age, especially for an old and deteriorated bridge. Hence, it was decided to collect representative samples from the bridge to obtain the current material properties.

Five core samples were collected from the web of four different girders in Span 1 of the bridge to obtain the compressive strength of concrete. The concrete cores were all 75 mm (3 in.) in diameter and a length of around 150 mm (6 in.). The web of the girder was the only location of the bridge where the concrete cores could be taken without damaging the strands and reinforcement. The web width for the girders was 175 mm (7 in.) which prevented cores of 100 mm, so as to maintain the length to diameter ratio of around 2 as recommended in ASTM (ASTM C39 2014). The concrete cores were stored in a cool dry place so it did not absorb any moisture. The core samples were cut to the same length and capped using Sulphur capping to make the surface even (Figure 6-36). The samples thus prepared were tested to obtain the compressive strength of concrete using a MTS compression testing machine at a constant rate of around 0.25 $\pm$ 0.05 MPa/s (35 $\pm$ 7 psi). Strain gauges were attached on two sides of the core sample to get the stress strain response and Elastic modulus of the concrete samples.

(a)

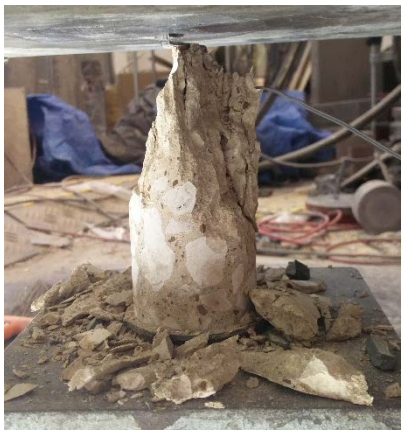

(b)

(c)

Figure 6-36 (a) Core Samples ready for test (b) Tested core sample (c) Tested core sample

Core dimensions and compression test results is presented in Table 6-11.

Table 6-11 Concrete compressive stress from core tests

Core	Diameter (mm)	Length (mm)	Area (mm^2)	f'_c (MPa)	E (MPa)
B3-1	70	153	10666	29.91	25380
B7	70	152	10656	25.93	23630
B3-2	70	154	10722	18.06	19724
B4	70	150	10535	30.66	25695
B6	70	151	10551	23.05	22279
Average	70	152	10626	25.52	23342

The compressive strength of the concrete cores was calculated as 25.52 MPa (3701 psi) and the modulus of elasticity was calculated as 23342 MPa (3400 ksi). The modulus of Elasticity (E) of concrete was calculated using Equation 6-4.

The values thus obtained were lower than the design strength of 34.5 MPa (5000 psi) mentioned in the design drawings. These values were used for the initial model verification and the experimental results were compared with the modeling results. It was evident from the model results that the concrete compressive stress and Elastic Modulus obtained concrete core samples was not representative of the concrete strength.

FRP samples could not be salvaged from the bridge as it was not possible to remove a clean FRP sample without concrete attached to it. The results obtained from the MacArthur bridge FRP coupon test were used for the calculation of Modulus of Elasticity and Fail Stress for the bridge.

Two separate models were created for Span 2 and Span 3 of the bridge and the model responses were compared with the corresponding experimental results. Figure 6-37 shows the correlation between the experimental and model responses. A good correlation was obtained between the experimental and modeling results as demonstrated by the correlation coefficient value of 0.991. The value of E of concrete for the calibration of Span 2 was 37700 MPa (5400 ksi) and for Span 3 of the bridge was around 40000 MPa (5800 ksi) which is higher than the design strength reported. Further analyses were carried out once a satisfactory calibrated model was obtained with good correlation.

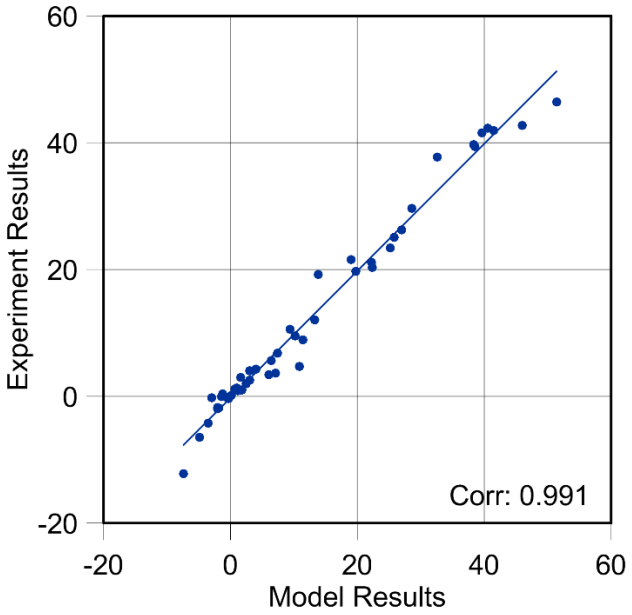

Figure 6-37 Correlation between experimental and modeling results

6.2.3 Modeling Results

The calibration process involved comparing the values of strain and displacement results from the experiment with the model when the truck was stationary on the mid span of the bridge. It was observed that the girder and deck stiffness had a major influence in the structural response. As a result, the model refinement was done by investigation of structural response by varying the concrete and deck modulus of elasticity in the model. The values of E of girder and deck were changed for each position of the truck. Two different locations, mid span of Beam B3 and mid span of Beam B7, on each span were evaluated and the values of E that provided the best correlation were used as the final refined model parameters. A moving load analysis was then carried out to simulate the crawl speed test on the bridge. The displacement response at mid span of girder B3 is presented in Figure 6-38. It shows that the final bridge model showed a good match of displacement response for the moving load analysis.

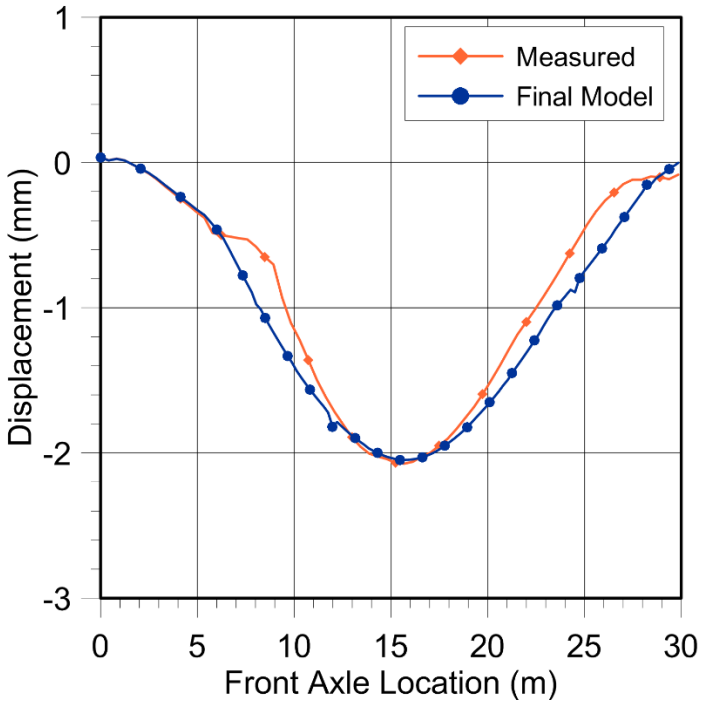

Figure 6-38 Modeled and measured displacement at mid-span of girder B3, Span 2

The measured and model strain of the girder directly below the truck path demonstrated a strong correlation for the crawl speed tests. Similar correlation was observed in girders further away from the truck path. Figure 6-39 shows the strain response of mid-span of girder B3 in Span 3 of the bridge. It can be seen that the model and experimental results are fairly close. The model was also able to provide close results for girders with repair and FRP strengthening. However, it was unable to clearly demonstrate the decrease in strain value due to FRP strengthening as the bond behavior between FRP and concrete was not modeled in a detailed manner. A tie constraint was used to represent the bond between FRP and concrete. Over-height vehicle damage, epoxy injection of cracks, as well as the splicing of strands was also not modeled.

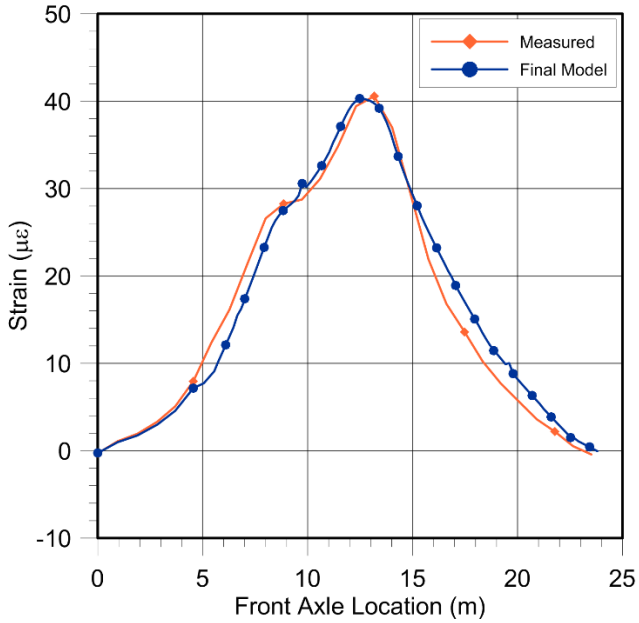

Figure 6-39 Modeled and measured strain at mid-span of girder B3, Span 2

Once the structural response of the bridge girders were verified with the moving load analysis; the peak strain values were used to make a comparison between the model and measured strain distribution across the girders. The peak strain values were taken from the crawl speed tests and compared with those obtained from moving load analysis. This allowed us to make a comparison in the distribution factor of the girders between model and experimental results. Figure 6-40 and Figure 6-41 shows the transverse strain distribution obtained from the model compared with their measured values for both Spans 2 and 3.

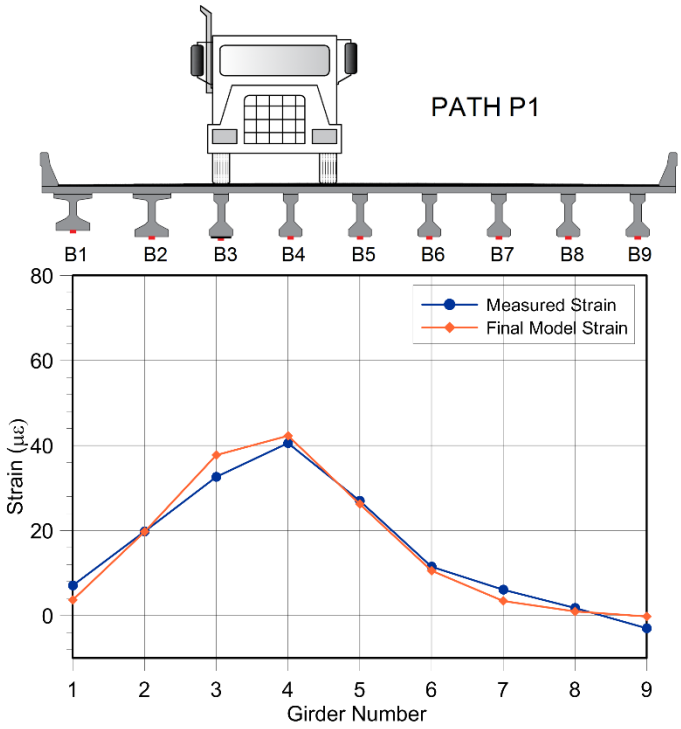

(a) Span 2

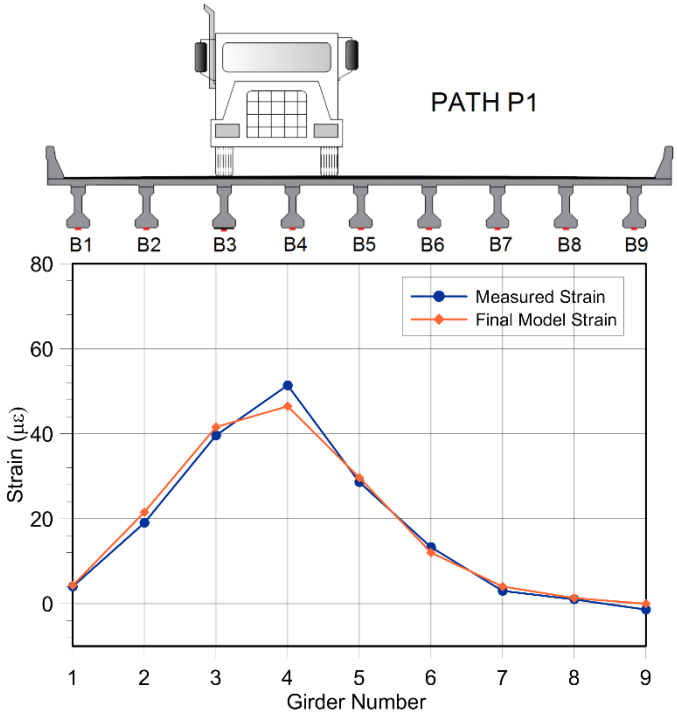

(b) Span 3

Figure 6-40 Measured and modeled strain distribution across all girders for Path P1

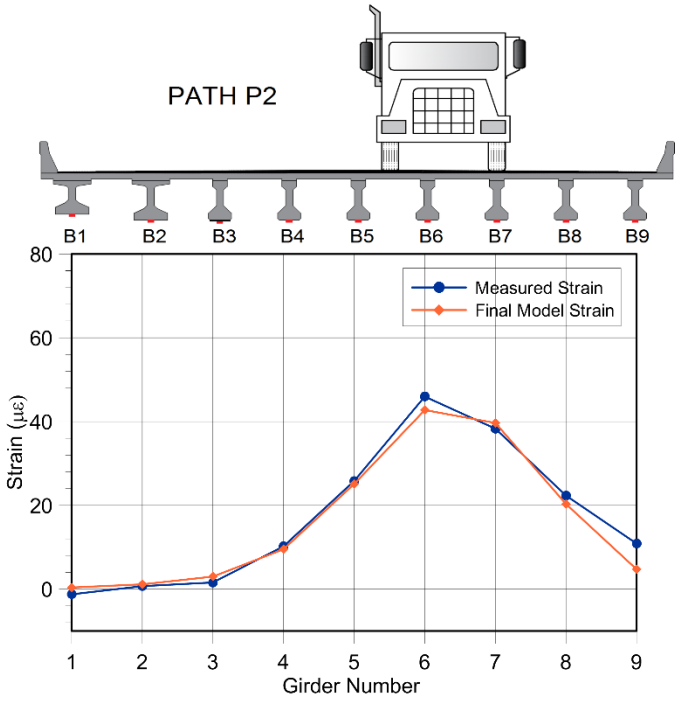

(a) Span 2

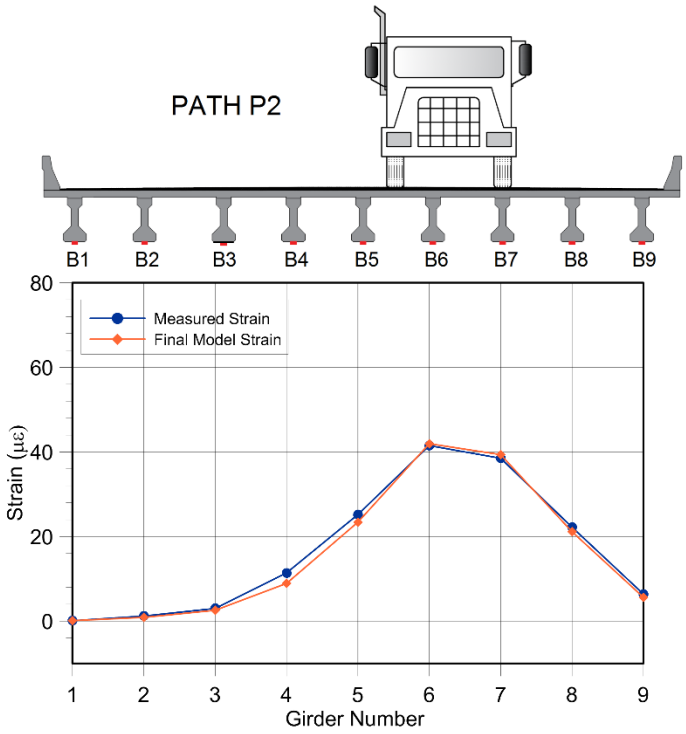

(b) Span 3

Figure 6-41 Measured and modeled strain distribution across all girders for Path P2

The strain response from the calibrated model was used to calculate the distribution factors for girders B4 and B6 based on the modeling results. The results of the distribution factors thus obtained is shown in Table 6-12. The distribution factors obtained from the model was similar to the values obtained from experiment and presented in Table 6-8.

Table 6-12 Distribution Factors from final model

Distribution Factor for moment		
Girders	Span 2	Span 3
B4	0.292	0.289
B6	0.292	0.292

The final calibrated model was loaded with two trucks according to the same configurations as the experiment. The strain distribution of the girders obtained from the model was compared with the strain response of the multiple truck test discussed in Section 6.2.1.5. The results of the comparison for both, Span 2 and span 3 is presented in Figure 6-42. It can be seen that the response of the model was slightly higher than the response obtained from the experiment for Span 2 and the inverse was true for Span 3. Span 2 and Span 3 of the bridge were modeled independently and calibrated separately. Higher consideration was given to calibrate the deflection rather than the strain which could be the reason for the difference in the result.

The distribution factors were calculated from the model results for multiple trucks which are presented in Table 6-13.

Table 6-13 Distribution Factors for multiple trucks

Distribution Factor for moment	
Span 2	0.369
Span 3	0.356

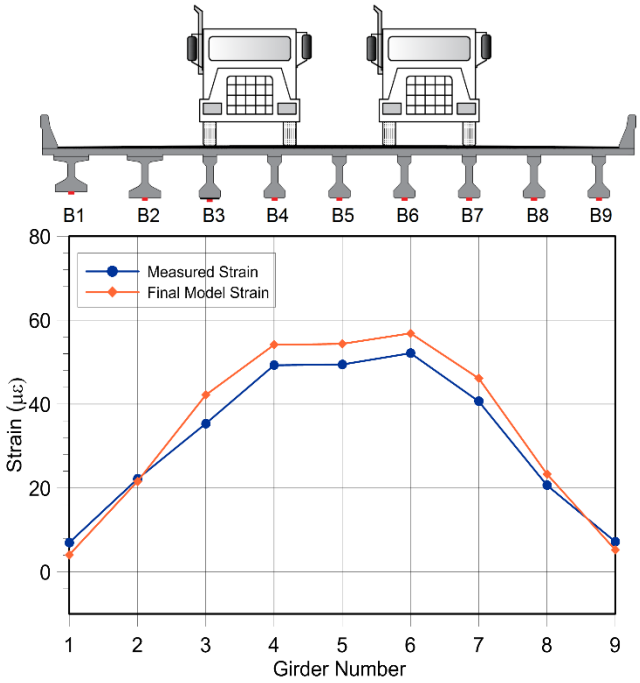

(a) Span 2

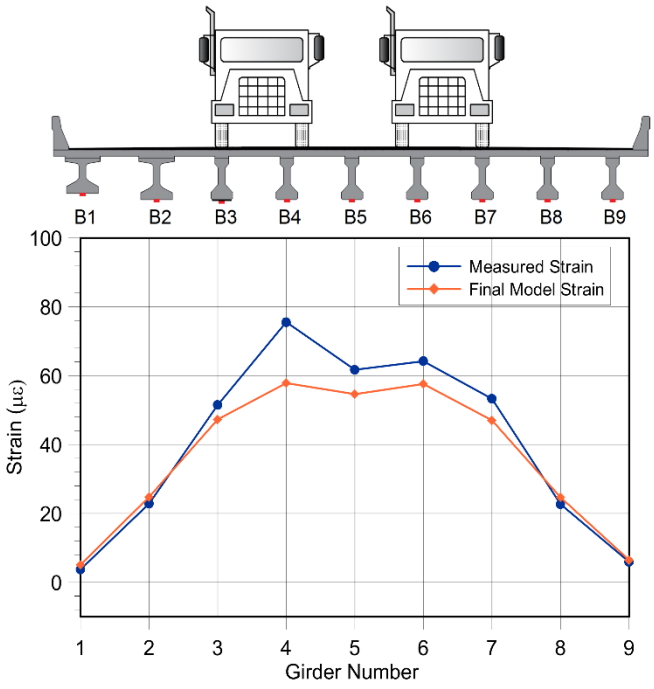

(b) Span 3

Figure 6-42 Measured and modeled strain distribution across all girders for multiple trucks

6.2.4 Distribution Factor comparison

The transverse strain distribution obtained from non-destructive load test was used to calculate the distribution factor for Span 2 and Span 3 of the bridge. Similar calculations were carried out to calculate the Live load DFM based on the modeling results. Figure 6-43 shows the comparison of distribution factors with the AASHTO LRFD distribution factor for girders in both spans of the bridge.

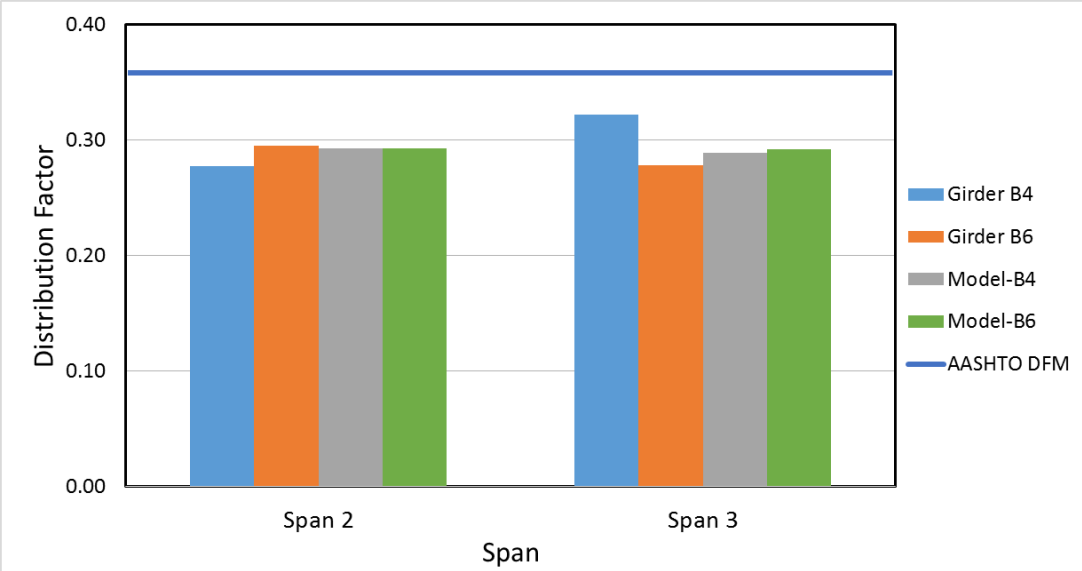

Figure 6-43 Comparison of Distribution Factor with AASHTO for one lane loaded

The distribution factor obtained from the experiment for girder B4 and girder B6 were compared with the distribution factor for interior girders obtained from the AASHTO calculations. The horizontal line shows the value of distribution factor for one lane loaded condition. It can be seen that the distribution factors were all lesser than the values obtained from AASHTO. This reiterates the finding that the distribution factors values based on AASHTO calculations is normally conservative and over estimates the live load applied on the girder. This decrease in experimental DFM can be due to the presence of transverse diaphragms and barrier rails. Girder B4 in Span

2 of the bridge, which was damaged and strengthened with FRP, exhibited a lower distribution factor than the corresponding girder in Span 3.

Similar calculations for distribution factor was carried out when the bridge was loaded with two trucks. The AASHTO distribution factor based on two or more lane loaded was used to analyze and compare the results. Figure 6-44 shows the distribution factor comparison for two lane loaded.

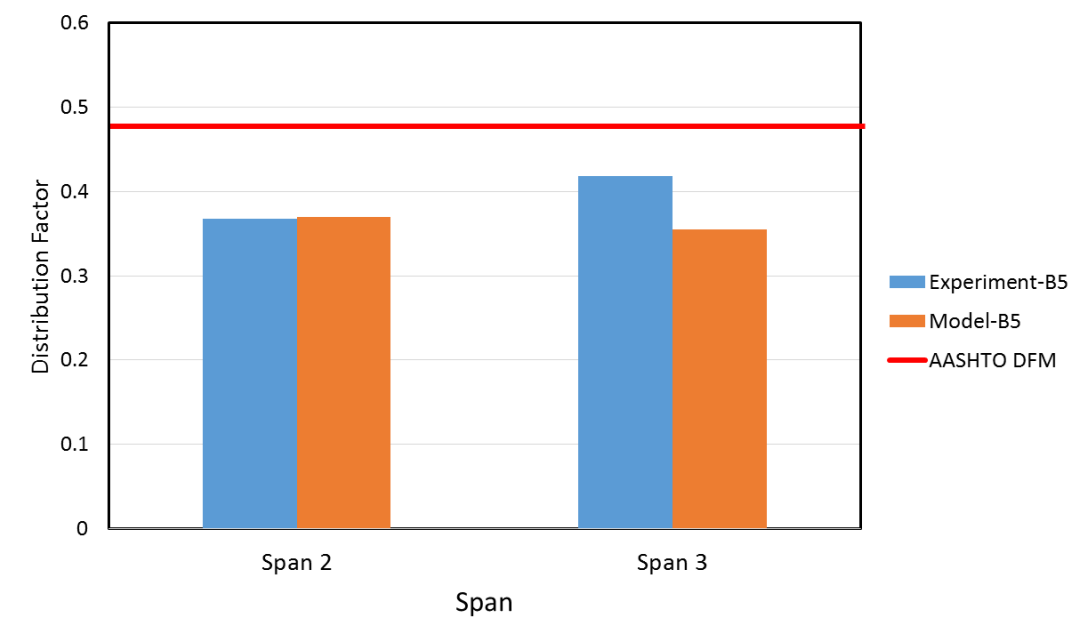

Figure 6-44 Comparison of distribution factors with AASHTO for two lanes loaded

The figure demonstrates that the value of distribution factor for two lane loaded was also conservative than the AASHTO calculations. The distribution factor obtained from the model compared with the experiment was also similar and lesser than the AASHTO distribution factors.

Chapter 7

Conclusion and Recommendations

7.1 Summary

Extreme load hazards is one of the major reasons of damage of bridge infrastructures. Among the extreme hazards, fire hazard is one of the least studied and often difficult to understand. Impact of over height vehicles on bridge structures is another major reasons of damage of bridges. This study aims to perform an in-service performance evaluation of two such bridges, one of which was fire damaged and the other was impact damaged. The main objective of the study was to evaluate the structural performance of bridges which were repaired and strengthened with FRP laminate after an extreme event. A static load test was carried out on the bridges to evaluate the structural performance and to calibrate a finite element model. The main goal of the research was to gain a better understanding of the bridge behavior and repair methodology to assist state DOTs and highway agencies to prepare a reliable and durable method of prolonging the infrastructure design life.

MacArthur bridge was a continuous parabolic reinforced concrete bridge which was fire damaged and repaired with mortar and strengthened with CFRP on two spans. A quasi-static live load test was carried out on the bridge to compare the performance of the FRP strengthened beam with a similar undamaged beam. The results from the load test were used to verify and calibrate a full scale finite element (FE) model which could accurately represent the load distribution and performance characteristics of the in-service bridge. Fire hazard on the bridge was modeled using a computational fluid dynamics (CFD) based software and the temperature values obtained from the heat transfer model were used to modify the material properties of

the bridge. The final calibrated model for fire damaged bridge was found to be reliable with a high degree of accuracy.

Loop 12 bridge selected for the study was impact damaged by an over height vehicle. Two girders suffered severe damage and were replaced and other two girders were cracked and suffered moderate damage. The girders were repaired with epoxy injection and mortar, along with strengthening using FRP laminate. A static load test was carried out on two spans of the bridge to evaluate the performance of the bridge girders to efficiently compare the girder behavior. The load distribution characteristics of two spans, with and without impact damaged girders, were also studied. The results from the experiment was used to verify a FE model to evaluate the bridge performance and in-service behavior. Calibrated FE model was able to accurately represent the bridge behavior.

7.2 Findings and Conclusions

The live load test carried out by varying the transverse position of load vehicle across the bridge yielded enough data to characterize the bridge behavior. The findings and conclusions based on the live load test and FE model calibration are presented in this chapter.

7.2.1 Fire Damaged bridge

The strain distribution behavior of the bridge girders was consistent and found to follow expected trends. Highest strains was observed on the girders directly under the vehicle and strain values decreased further away. This response was consistent for all transverse vehicle positions. Displacement response of the bridge also followed expected trends.

Two separate spans, Span 2 and Span 3 of the MacArthur bridge were selected for the study. Span 3 of the bridge sustained highest level of fire damage and thermal effect during the fire event. As a result, Beam B1 and Beam B2 in Span 3 were repaired and strengthened with FRP. Span 2 of the bridge was exposed to less temperature as it was not exposed to direct fire. The comparison of FRP strengthened Beam B2 in Span 3 and similar undamaged beam in Span 2 showed that the deflection response for strengthened beam was 3% lower and the strain response was 9% lower than the undamaged beam. This shows that mortar repair and CFRP strengthening was able to restore the elastic stiffness and flexural strength of the fire damaged beam. However, a similar beam, which was repaired with mortar but not strengthened with CFRP exhibited strain significantly higher than the strengthened beam.

Fire analysis of the fire hazard on bridge was performed using a Fluid Dynamics Simulator (FDS). The fire model was able to predict the temperature and fire effect on the bridge with acceptable accuracy. Heat transfer analysis using the fire surface temperature showed that the exterior thermal temperature was conducted into the core of the beams and the whole beam cross section was subjected to the same temperature. The effect of fire was maximum on the exterior beams on Span 3 and Span 4.

The fire temperature and load test results was used to calibrate a FE model. It was observed that the beams and deck of the bridge had significantly lost their stiffness especially in Span 3 and Span 4 of the bridge. The stiffness of the bridge in the most severely affected girders was found to be reduced by more than 75%. The stiffness throughout the bridge was reduced significantly ranging from a 20%

reduction to 75% reduction due to the effect of fire. This can be attributed to the induction of microcracks and loss of moisture in the concrete.

The in-service behavior of the FRP sample was evaluated and compared with a similar FRP laminate to see the effect of ageing and service on the FRP sample. It was found that the elastic modulus of the in-service sample was 13% lower than the lab sample and the tensile strength was reduced by 21%.

The calibrated model was able to accurately represent the behavior of the fire damaged bridge. The distribution factors obtained from the live load test and calibrated FE model were compared with the AASHTO LRFD distribution factors for moment (DFM) for slab on beam bridges. It was found that the distribution factors from experiment was almost similar or larger than AASHTO DFM. This shows that the AASHTO LRFD procedures are non-conservative for a fire damaged bridge.

7.2.2 Impact Damaged Bridge

The load distribution characteristics on an impact damaged bridge were studied and compared. The distribution of strain showed expected trends with maximum strain on the girders directly below the load vehicle and the values decreasing further away. Deflection results also showed similar results which showed expected trends and distribution.

Two beams on Span 3 of the bridge were impact damaged and repaired and strengthened with CFRP. The behavior of this strengthened beam was compared with the behavior of an undamaged beam in Span 2 of the bridge. The CFRP strengthened beam exhibited a lower strain of 27% and a lower displacement of 6% under same load conditions. This can be attributed to the increase in stiffness and flexural strength

due to the FRP laminate strengthening. This shows that CFRP laminate strengthening is a viable repair technique for impact damaged girders.

A detailed full-scale 3D FE model was created and shown to be feasible with significant accuracy. Nondestructive load test results were used to calibrate the FE model using manual model updating. The calibrated model showed that the actual stiffness of the bridge was higher than the design stiffness. This could be because of the presence of diaphragms, barriers and unintended composite action between the deck and girder.

The distribution factors calculated using the live load test and calibrated model were compared with the AASHTO LRFD DFM. It was found that the values obtained from experiment were lower than the AASHTO DFM for both one lane loaded and two lane loaded conditions. This result aligns with the established fact that AASHTO DFM are conservative, and found to be true even for impact damaged CFRP laminate strengthened girders. The level of conservativeness was comparable to the undamaged beam.

7.3 Future Research

The following are the recommendations for further research work:

- The effect of different levels of fire and different durations of fire on the performance of fire damaged bridges needs to be studied further.
- The effect of concrete spalling and loss of concrete section due to fire and thermal effects was not evaluated in the numerical model due to lack of specific guidelines. A detailed FE analysis which takes into account the spalling of concrete can be developed.

- A more detailed analyses to determine the specific contribution of different parameters; including repair mortar, wire mesh, strand splicing, epoxy injection, CFRP laminate and U wraps need to be studied to streamline the repair and strengthening procedure. The bond between the repair mortar and existing concrete and the bond between the CFRP and repair mortar need to be studied in more detail.
- The effect of ageing of FRP laminate was studied only on one bridge. More laminate samples from different existing bridges need to be tested. It would be advisable to obtain the FRP coupon samples during strengthening and obtain and test coupon samples every few years of service to see the effect with respect to age of FRP.

Appendix A:

MacArthur Bridge Beam Repair plans

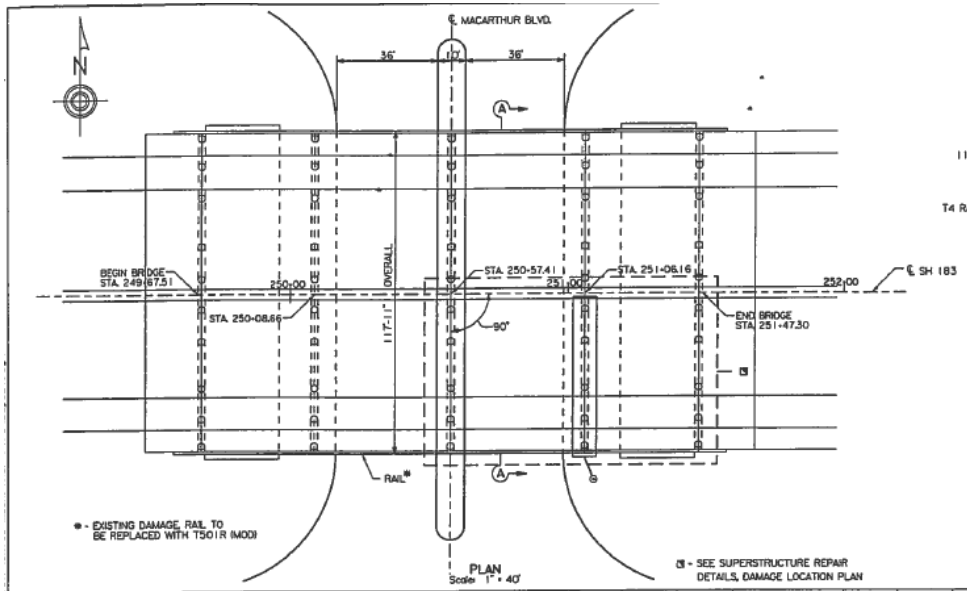

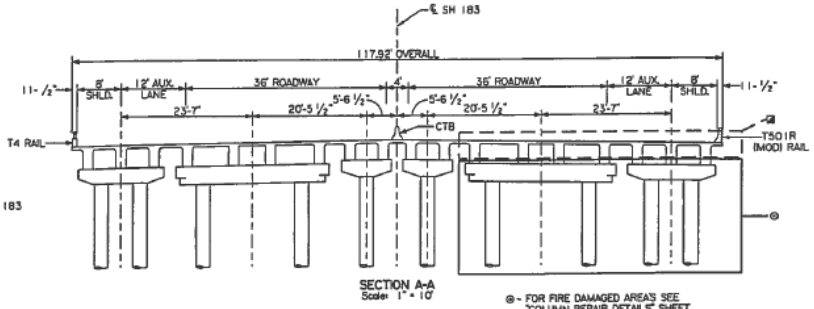

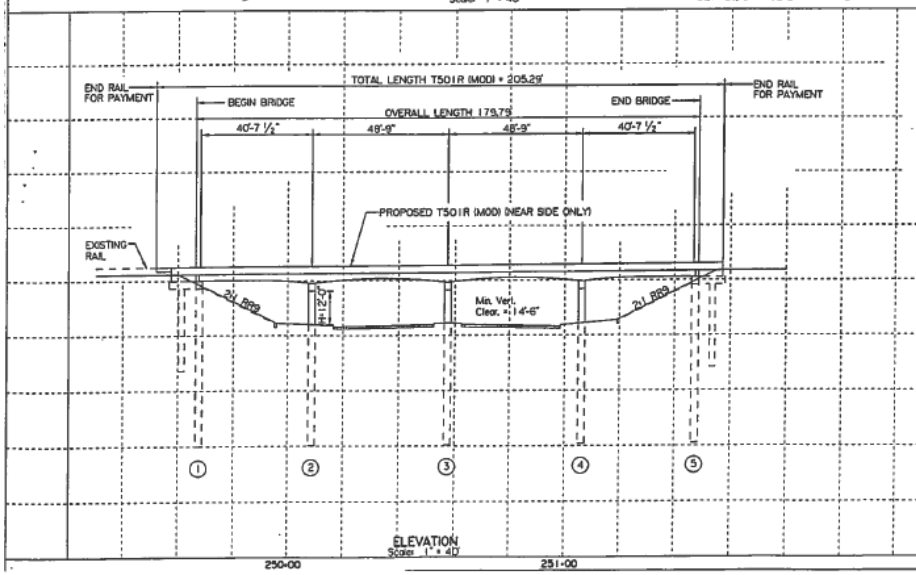

Project General Notes

Damaged areas shown in the superstructure, bent and columns are for information only and are not accurate in size, length, and area.

Remove the loosened concrete only in the damaged areas. Limit the size of the chipping hammers to 15 Lbs. Care must be taken not to cause any further damage. All removal work shall be in accordance with the provisions of Item 429, "Concrete Structure Repair".

Patch material for concrete repair shall be prepacked cementatious mix attaining at least 3000 psi compressive strength in 24 hours and 5000 psi in 28 days following manufacturers recommendation for surface preparation, placing material and curing. Use shrinkage-compensated mixture for shotcrete material approved by the Engineer.

Apply 12 Gauge welded wire mesh in patching area of 1¾" or deeper. Firmly tie the mesh with nails into the properly prepared substrate.

Apply a topcoat matching the existing concrete color to all new concrete, surface repairs and CFRP reinforced areas.

Sequence of Work Requirements:

Place Rail Ty. T501R (MOD) only after all superstructure repairs are complete.

Superstructure repairs may be performed concurrently with bent and column work or at any time before or after.

Repair of Columns 6 and 7 is not subject to the sequence requirements shown below for the Bent and Columns. Work on these columns may be performed at any time.

Bent and Column repair work (Columns 8, 9 & 10) is subject to the following sequence:

1) Remove all loose concrete from the existing bent caps and remove concrete from columns 8, 9 & 10 to the encasement limits shown.
2) Install "Cap Encasement" per details shown.
3) Repair Columns 8, 9 and 10. Repair remainder of bent cap to the limits shown or as directed by the Engineer.

NOTE:
SEE OTHER SHEETS FOR DETAILS NOT SHOWN HERE

Exist. NBI# 18-XXX-0-XXXX-XX-XXX

STATE OF TEXAS
E. A. MERHAM
67081
LICENSED
PROFESSIONAL ENGINEER

6/13/05

Sheet 1 of 22 Sheets

Texas Department of Transportation
© 2005

SH 183

MACARTHUR BLVD. OVERPASS

BRIDGE REPAIR LAYOUT

DESIGN	FED. RD. DIV. NO.	FEDERAL AID PROJECT NO.		HIGHWAY NO.
DESIGN CK	6	(See Title Sheet)		SH 183
	STATE	DISTRICT	COUNTY	SHEET NO.
GRAPHICS RH/WRF	TEXAS	DALLAS	DALLAS	
CORR CHECK KAM	CONTROL 0094	SECTION 03	JOB	

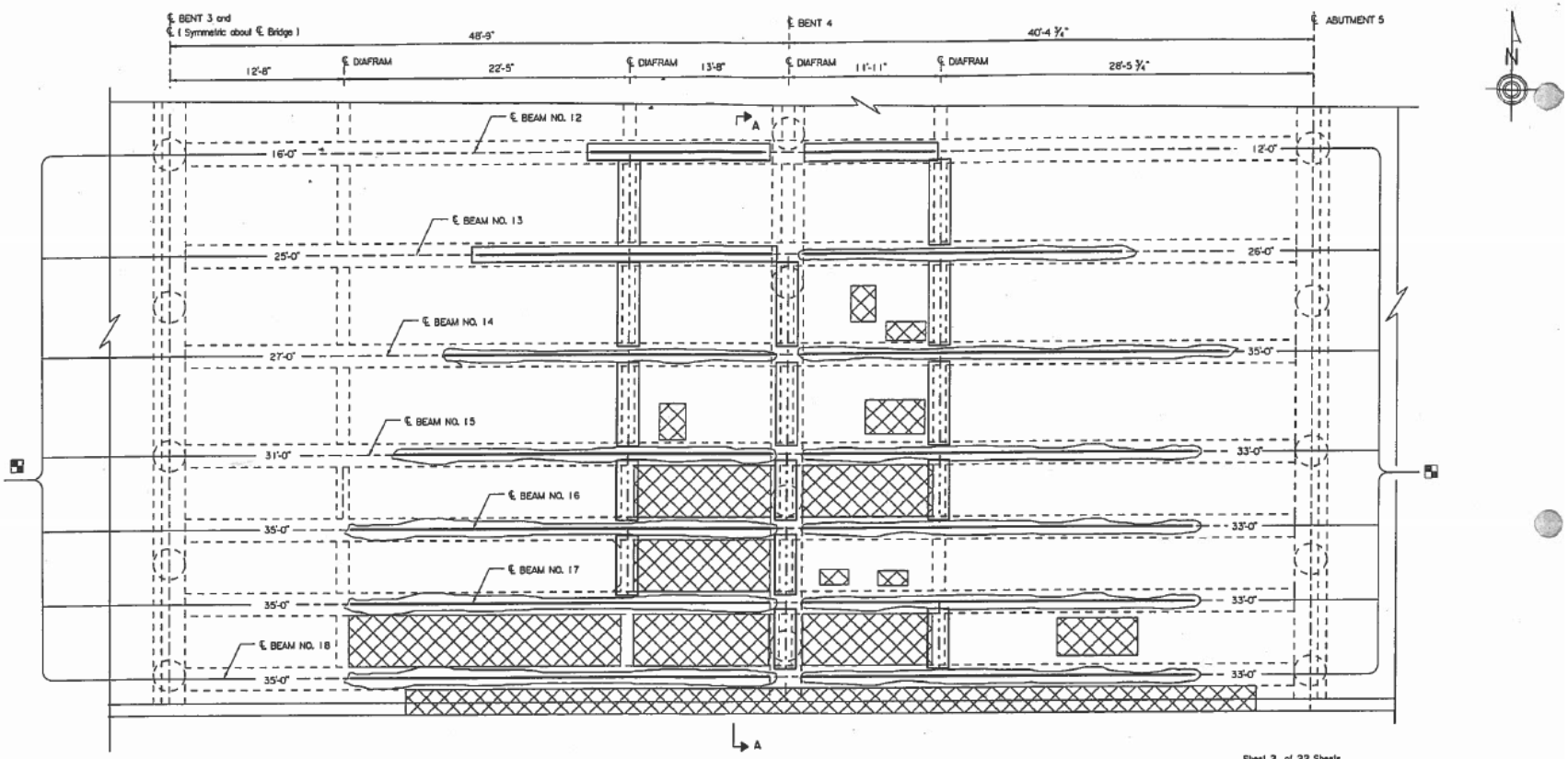

Damaged lengths are Approximate Not able to Measure Exactly

DAMAGE LOCATIONS PLAN

- Indicate approximate limits of slab requiring repair of the bottom surface see details.
- Indicates approximate limits of girder repairs using shotcrete and CFRP in accordance w/details shown
- Indicates approximate limits of girder repairs using shotcrete in accordance w/details shown
- Indicates approximate limits of diaphragm repairs using shotcrete in accordance w/details shown

Superstructure Repair Notes:
Perform superstructure repair work using pneumatically placed concrete in conjunction with the details shown. Perform this work in accordance with Item 429, "Concrete Structure Repair" and Item 431, "Pneumatically Placed Concrete."
Appy CFRP to designated areas of superstructure in accordance with the details shown and "General Notes for CFRP External Strengthening". See "Superstructure Repair Details", Sheet 3.

Notes:
See Layout for "Project General Notes" and "Sequence of Work Requirements".

6-8-05
SUNIL N. PATEL 85345 LICENSED PROFESSIONAL ENGINEER

Sheet 2 of 22 Sheets

Texas Department of Transportation © 2004

S.H.183

MACARTHUR BLVD. OVERPASS

SUPERSTRUCTURE REPAIR DETAILS

SHEET 1 OF 3 SHEETS

DESIGN	FED. RD. DIV. NO.	FEDERAL AID PROJECT NO.		HIGHWAY NO.
SNP	6	(See Title Sheet)		SH183
DESIGN CK	STATE	DISTRICT	COUNTY	SHEET NO.
KAM	TEXAS	DALLAS	DALLAS	
GRAPHICS	CONTROL	SECTION	JOB	
SNP	0094	03		
GRPH CHECK				
KAM				

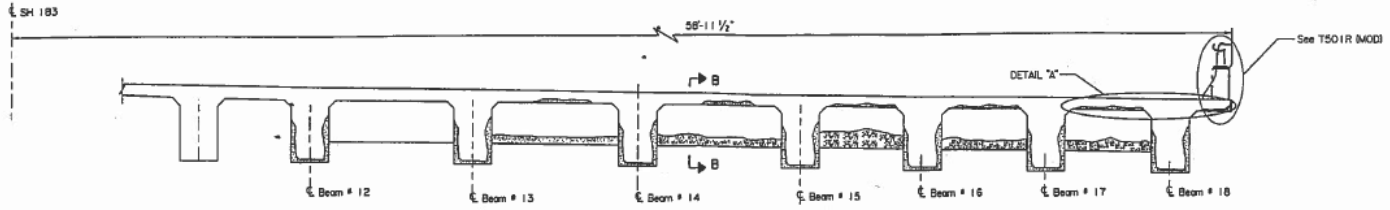

SECTION A-A
Scale : 3/16" = 1'-0"

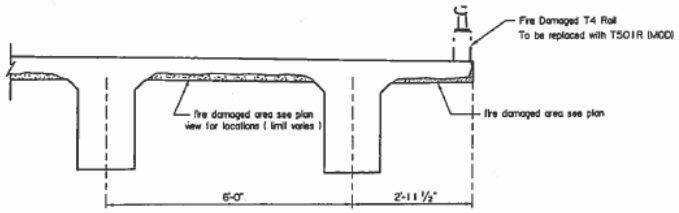

DETAIL "A" (DAMAGED SLAB)

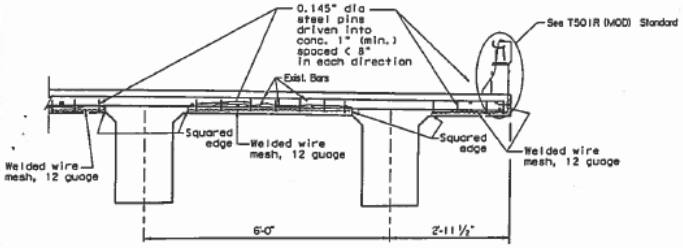

DETAIL "A" (REPAIR SLAB)

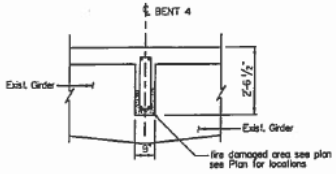

SECTION B-B (DAMAGED DIAFRAM @ BENT 4)

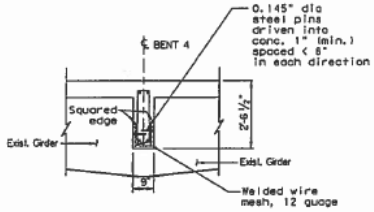

SECTION B-B (REPAIR DIAFRAM @ BENT 4)

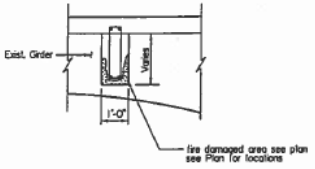

SECTION B-B SIMILAR (DAMAGED DIAFRAM @ INTERIOR BENT)

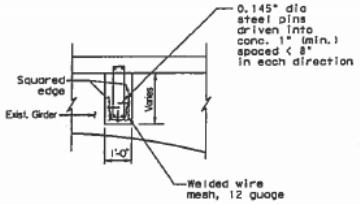

SECTION B-B SIMILAR (REPAIR DIAFRAM @ INTERIOR BENT)

Notes:
See Layout for "Project General Notes" and "Sequence of Work Requirements".

Sheet 3 of 22 Sheets

Texas Department of Transportation
© 2005

S.H. 183

MACARTHUR BLVD. OVERPASS

SUPERSTRUCTURE REPAIR DETAILS

SHHET 2 OF 3 SHEETS

DESIGN	FED. RD. DIV. NO.	FEDERAL AID PROJECT NO.		HIGHWAY NO.
SNP	6	(See Title Sheet)		SH 183
DESIGN CK	STATE	DISTRICT	COUNTY	SHEET NO.
KAM	TEXAS	DALLAS	DALLAS	
GRAPHICS	CONTROL	SECTION	JOB	
SNP	0094	03		
GRAPH CHECK				
KAM				

6-13-05

SUNIL K. PANEL 85345 LICENSED PROFESSIONAL ENGINEER

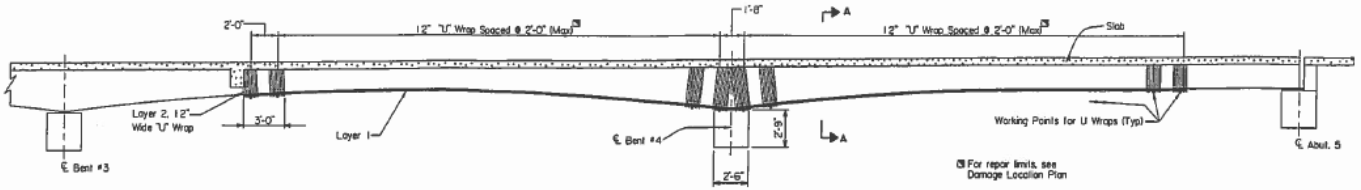

GIRDER REPAIR ELEVATION
Scale: 1/8" = 1'

General Notes for CFRP External Strengthening

1) Carbon fiber reinforced polymer (CFRP) Materials, which are pre-approved for this application, are Wabo MBrace CF 130 High Strength Carbon Fiber Fabric, 9 oz unidirectional, and Sikawrap Hex 117C. Substitutions for the above systems will be allowed providing equivalent strengthening result subject to approval by the Engineer.

2) Perform CFRP work with personal certified or approved by the manufacturer of the system used. Provide documentation to demonstrate a three (3) year track record of successful performance of CFRP concrete repairs on at least four project installations, including the size and location of the projects, and each project's contact person(s) and phone number(s).

3) Provide manufacturer's product data before the beginning of the work indicating product standards, physical and chemical characteristics, environmental durability, technical specifications, limitations, installation instructions, maintenance instructions, and general manufacturer's recommendations regarding each system. The submittals shall include but not limit to: proposed primer, putty, resin saturant, carbon fiber, and the protective topcoat. Provide Health and Safety Sheets and Manufacturer's Specification Data Sheets (MSDS) of each product used on site and certification that the materials conform to local, state and federal environmental and worker's safety laws and regulations.

4) Deliver the CFRP components in original, unopened (except carbon fabric) containers clearly marked with the manufacturer's name, product identification, and batch numbers. Store and handle the various products in conformity with manufacturer's instructions. Do not use components, which have exceeded their shelf life.

5) Do not apply CFRP if raining, or existing concrete surface is wet, or if the ambient or surface temperature is below 45 F. Begin the CFRP work after the concrete is repaired and has attained a minimum 3000 psi compressive strength and is accepted by the Engineer. All substrates shall be clean, dry, sound, and free of surface moisture and frost. Inspect all materials to ensure conformity with the application requirements, and that all materials are new and undamaged. Apply CFRP in accordance with Manufacturer's application specifications and specific Engineer instructions.

6) After 24 hours of initial curing of resin saturant, perform a visual and acoustic tap test inspection on the layered surface. Repair all defective work including voids, bubbles, delamination, and fabric tears, in accordance with manufacturer's recommendations and to the satisfaction of the Engineer. If large defects are found, apply additional layers of CFRP as directed by the Engineer.

7) Perform at least three (3) direct pull-off tests per ASTM D4541 on the project at locations desired by the Engineer. Failure of the bond line at tensile stresses below 200 psi is unacceptable.

8) Apply the topcoat to match the existing concrete color.

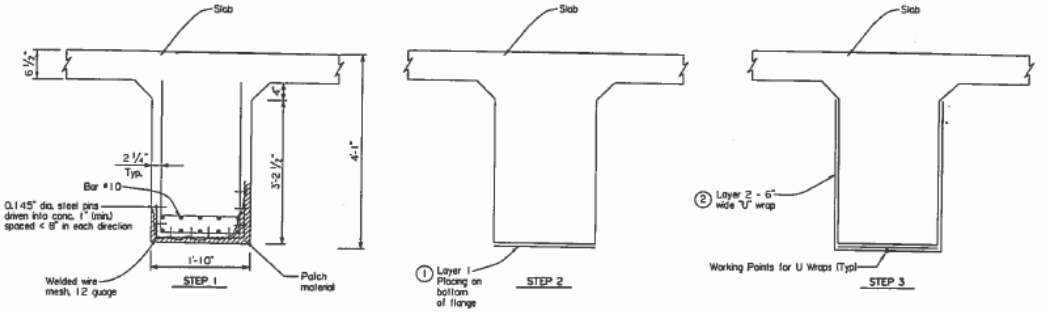

SECTION A-A

1. Layer 1 shall have carbon fiber direction parallel to the axis of the beam.
2. Start "U" wrap at the ends of layer 1. The direction of carbon fiber shall be perpendicular to the axis of the beam.
3. The length of layer 1 may be adjusted in the field by the Engineer.

Notes:
See Layout for "Project General Notes" and "Sequence of Work Requirements".

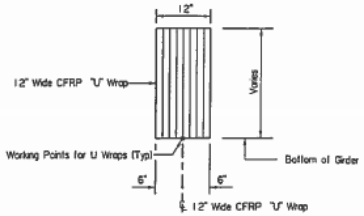

"U" WRAP ELEVATION

STATE OF TEXAS
E. A. HERSH
67081
REGISTERED PROFESSIONAL ENGINEER

6/14/05

Sheet 4 of 22 Sheets

Texas Department of Transportation
© 2005

SH 183

MACARTHUR BLVD. OVERPASS

SUPERSTRUCTURE REPAIR DETAILS

SHEET 3 OF 3 SHEETS

DESIGN	FED.RD. DIV.NO.	FEDERAL AID PROJECT NO.		HIGHWAY NO.
DESIGN CK	6	(See Title Sheet)		SH 183
	STATE	DISTRICT	COUNTY	SHEET NO.
GRAPHICS RH/WRF	TEXAS	DALLAS	DALLAS	
CHKD. CK'D.	CONTROL	SECTION	JOB	
KAM	0094	03		

Appendix B:

Loop 12 Girder Repair Plan

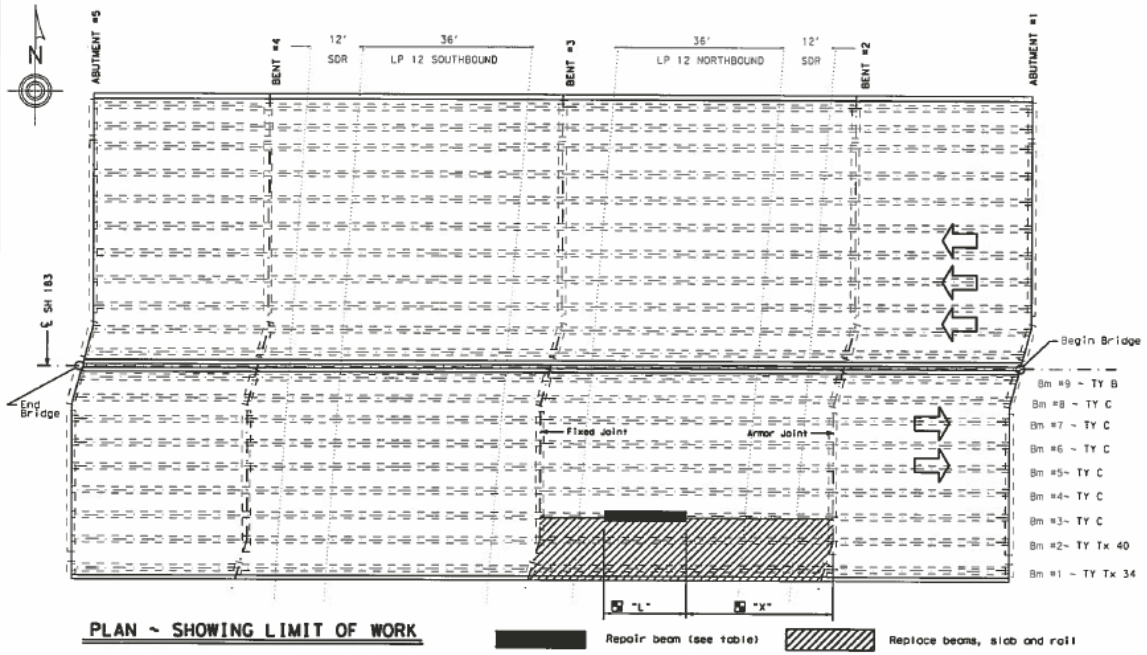

PLAN ~ SHOWING LIMIT OF WORK

Repair beam (see table)

Replace beams, slab and rail

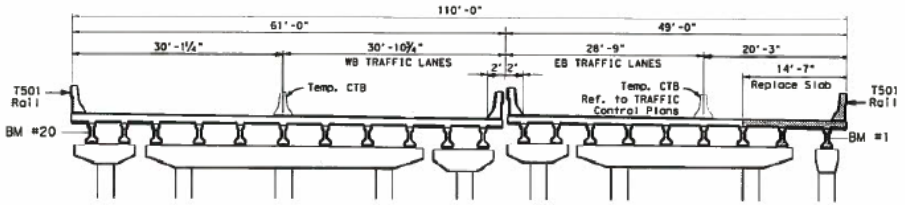

TYPICAL TRANSVERSE SECTION

ITEM	DESCRIPTION OF WORK	UNIT	QTY
0422-6002	REINF CONC SLAB(HPC)	SF	948.5
*0425-6036	PRESTR CONC GIRDER (TX34)	LF	64.67
*0425-6037	PRESTR CONC GIRDER (TX40)	LF	64.67
0450	RAIL (TY T501)	LF	65.00
0454-6004	ARMOR JOINT (SEALED)	LF	30.73
0496-6086	RMV STR (BRDG DEC SLAB BEAM & RAIL)	EA	1
0788-6003	CONCRETE BEAM REP (STRAND SPLICE & CFRP)	EA	1

* Furnished by TxDOT, delivered and erected by contractor.

LIST OF WORK BY BEAM NUMBER

BEAM	"L"	"X"	TYPE OF REPAIR
#1-2	N/A	N/A	REPLACE BEAM, SLAB & RAIL
#3	18'-0"	31'-0"	REPAIR BEAM (INCL. CFRP) & SPLICE FIVE (5) SEVERED STRANDS

~ Approximate dimension field verify.

GENERAL NOTES:

Damaged areas shown are for information only and not accurate in size, length, or area. Refer to original and widening plan sets as required for information pertaining to the existing structural members.

Refer to table: "LIST OF WORK BY BEAM NUMBER." Repair damaged beams where indicated in accordance with Item 788, "Concrete Beam Repair," and the details. Remove beams, slabs, and rail where indicated in accordance with Item 496, "Removing Structures (Bridge slab,beam & rail)" and the details. Replace beams, slab and rail where indicated in accordance with Item 422, "Concrete Structures," Item 425, "Precast Prestressed Concrete Structural Members," Item 450, "Railing," "Cleaning and Sealing Joints and Cracks," Item 454, "Bridge Expansion Joints," and the details.

Patching material for all concrete repairs must be non-shrink cementitious concrete mix capable of attaining at least 3000 psi compressive strength in 2 days and 6000 psi in 28 days.

Repair work for beam 3 will be measured by each beam and paid for under Item 788. Splicing all severed or damaged strands, epoxy injection of all cracks greater than .004" in width, and external strengthening with CFRP where indicated for these beams will be considered susidiary to Item 788.

Removing beams 1 and 2 will be measured by each beam and paid for under Item 496. Removing areas of slab with ACP overlay adjacent to and above these beams, and rail along beam #1 will be considered subsidiary to Item 496. Saw cut through existing ACP overlay (approx. 2" thick) and into top surface of existing deck slab (1" max.) along limit of deck to be removed. Avoid damaging existing top mat of slab reinforcement. Submit a demolition plan for review and approval prior to removing any structure component.

TxDOT will furnish Type Tx 34 and Tx 40 (replacement) beams. Cordinate with designated beam manufacturer, deliver, and erect beams in the locations specified.

Refer to standard Sheets," PRESTRESSED CONCRETE I- GIRDER DESIGNS" (IGND) and "PRESTRESSED CONCRETE I-GIRDER DETAILS" (IGD)
" PERMANENT METAL DECK FORMS" (PMDF),"ARMOR JOINT DETAILS" (AJ)
" THICKENED SLAB END DETAILS" (SBTS), "TRAFFIC RAIL" (TYPE T501)

Use existing bearing pads.

Cut existing dowels as indicated on framing plans.

Furnishing (thickened end) concrete slab w/ACP overlay will be measured by SF and paid for under Item 422. Use Class S concrete and Grade 60 reinforcing steel. Payment for ACP overlay will be subsidiary to Item 422. Refer to Standard Sheet, "THICKENED END SLAB DETAILS (IGTS)." Precast deck panels will not be allowed; PMDF or traditional deck forming may be used.

Furnishing (partial) Type AJ armor joint at bent 2 will be measured by linear foot and paid for under Item 454. Existing armor joint steel may be saved and reused if in acceptable condition. Refer to Standard Sheet, "ARMOR JOINT DETAILS (AJ)

Furnishing Type T501 railing will be measured by linear foot and paid for under Item 450. Refer to Standard Sheet, "TRAFFIC RAIL (TYPE T501)"

STATE OF TEXAS
SUNIL N. PATEL
85345
REGISTERED
PROFESSIONAL ENGINEER
12-09-14

Sheet 1 of 35 Sheets

Texas Department of Transportation
© 2014

SH 183

SH 183 OVERPASS AT LOOP 12

BEAM REPAIR/BEAM & SLAB REPALCEMENT

DESIGN	FED.RD. DIV.NO.	FEDERAL AID PROJECT NO.		HIGHWAY NO.
SNP	6	(See Title Sheet)		SH 183
DESIGN CK	STATE	DISTRICT	COUNTY	SHEET NO.
WRF	TEXAS	DALLAS	DALLAS	
GRAPHICS	CONTROL	SECTION	JOB	
SNP	6282	91	001	
GRPH CHECK				
WRF				

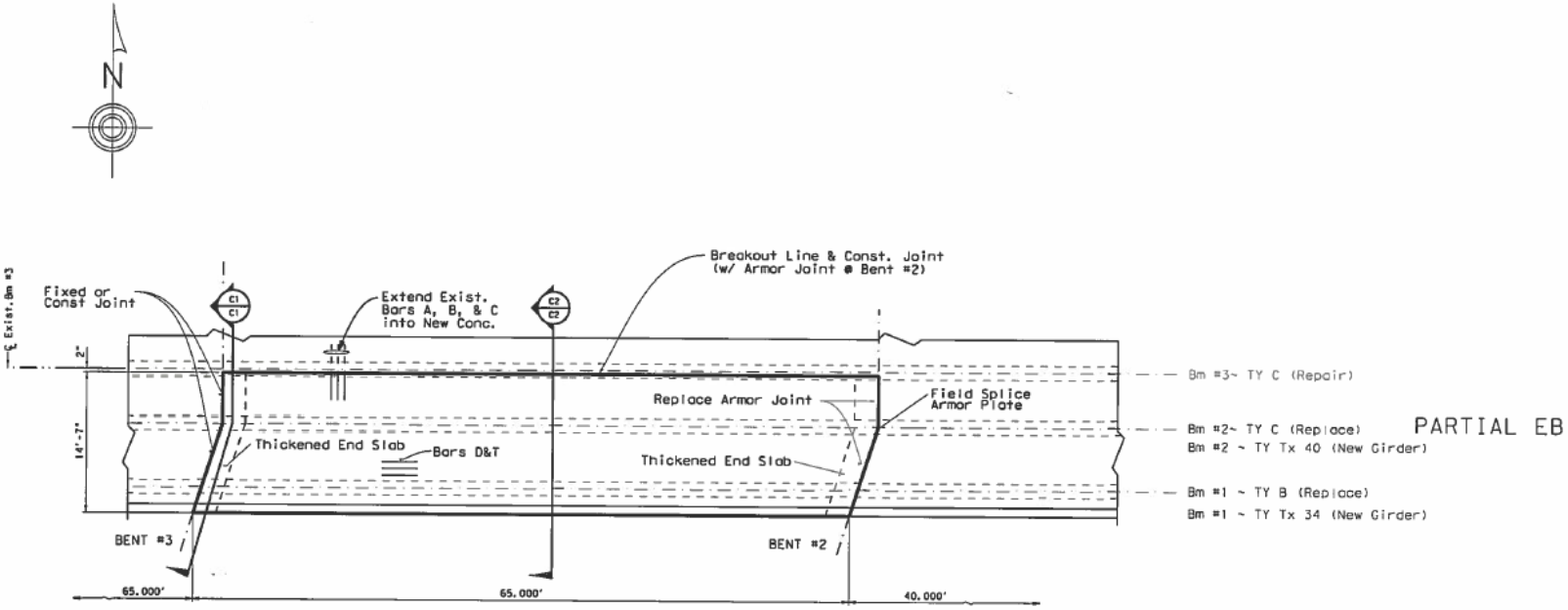

PARTIAL PLANS ~ SHOWING AREA OF DECK & BEAM REMOVAL & REPLACED

SUNIL N. PATEL
85345
12-09-14

Sheet 2 of 35 Sheets

Texas Department of Transportation
© 2014

SH 183

SH 183 OVERPASS AT LOOP 12

BEAM REPAIR/BEAM & SLAB REPALCEMENT

DESIGN	FED. RD. DIV. NO.	FEDERAL AID PROJECT NO.		HIGHWAY NO.
SNP	6	(See Title Sheet)		SH 183
DESIGN CK	STATE	DISTRICT	COUNTY	SHEET NO.
WRF	TEXAS	DALLAS	DALLAS	
GRAPHICS	CONTROL	SECTION	JOB	
SNP	6282	91	001	
DRAFT. CHECK				
WRF				

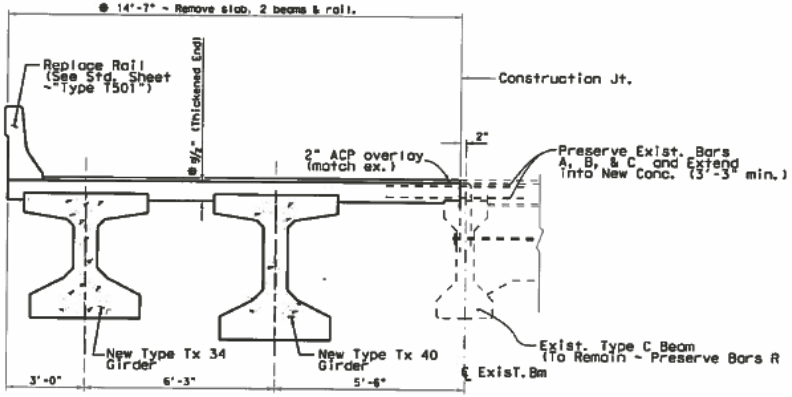

SECTION C1-C1 - (EB) END SECTION

*Reinforcement not shown for clarity. Refer to Std. Sheet - "IBTS" and Section C2-C2 (EB) Interior Section

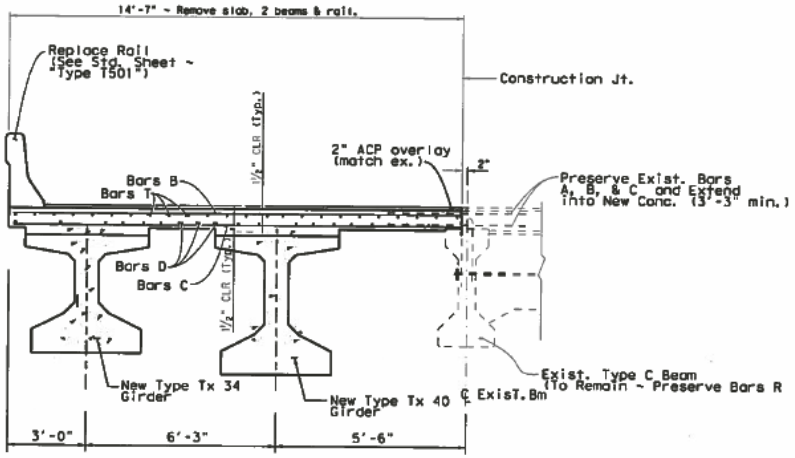

SECTION C2-C2 - (EB) INTERIOR SECTION

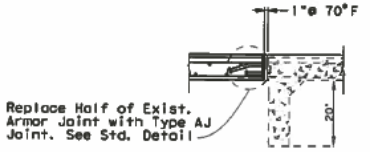

ARMOR JOINT DETAIL - BENT #2

TABLE OF CONSTANT QUANTITIES

Bar	No.	Size	Spac.	Length	Weight
B	156	#5	5"max.	14'-4"	2332
C	130	#5	6"max.	14'-4"	1943
D	20	#5	9"max.	64'-9"	1351
T	20	#5	9"max.	64'-9"	1351

Reinforcing Steel (1)	LB	6977
Class "S" Concrete (2)	CY	22.27
Type Tx 34 Beam	LF	64.66
Type Tx 40 Beam	LF	64.66
Type AJ Armor Joint	LF	14.33
Type T501 Rail	LF	65

(1) Does not include addl. steel required for thickened end slab

(2) Includes addl. concrete required for thickened end slab

STATE OF TEXAS
SUNIL N. PATEL
85345
LICENSED PROFESSIONAL ENGINEER

12-09-14

Sheet 3 of 35 Sheets

Texas Department of Transportation
© 2014

SH 183

SH 183 OVERPASS AT LOOP 12

BEAM REPAIR/BEAM & SLAB REPALCEMENT

DESIGN	FED. RD. DIV. NO.	FEDERAL AID PROJECT NO.		HIGHWAY NO.
SNP	6	(See Title Sheet)		SH 183
DESIGN CK.	STATE	DISTRICT	COUNTY	SHEET NO.
WRF	TEXAS	DALLAS	DALLAS	
GRAPHICS	CONTROL	SECTION	JOB	
SNP	6282	91	001	
QUANTY CHECK				
WRF				

BEAM REPAIR PROCEDURES:

1. Set traffic control.
2. Carefully examine the damaged area and identify extent of cracking in beams. Survey the location, severity, and length of damaged prestressing strand. Thoroughly plan cutting length for each severed strand with the consideration for the location and fit of the splices.
3. Remove loose concrete and prepare the repair area according to Item 788, "Concrete Beam Repair". Care must be taken not to further damage sound concrete or strands along the perimeter of the repair area.
4. Splice all severed strands as shown in the details and in accordance with "Notes for Splicing Strands". Obtain approval of all splice installations prior to retentioning any of the spliced strands.
5. Before retensioning the spliced strands, install anchor studs or steel pins in repair area in accordance with Item 429, "Concrete Structure Repair."
6. After all strands have been spliced and retensioned, place a 40 kip load on the deck above the area to be repaired.
7. Patch the prepared concrete repair area(s) on the beam. After the concrete patches have cured, epoxy inject all cracks greater than .004 inches in width.
8. Prior to the removal of the 40 kip load obtain approval of concrete repairs.
9. After removal of the 40 kip load, begin the application of Carbon Fiber Reinforced Polymer (CFRP) in accordance with Specification Item 786 and the General Notes.
10. Open the bridge to normal traffic once the CFRP has cured as outlined in Item 786 and upon acceptance by the Engineer.

NOTES FOR SPLICING STRANDS:

1. The strand splice system that is pre-approved for the project is GRABB-IT Cable Splice, product of PRESTRESS SUPPLY INC, Florida. The size and grade of the strand to be spliced may vary. Substitutions for the above system that provide equivalent results will be allowed subject to approval by the Engineer.
2. Contact PRESTRESS SUPPLY INC at 1-800-328-8036 (Contact person ~ Mr. Bruce Hartup) for technical support and instruction on the use of the GRABB-IT System. Submit to the Engineer a procedure for installation of the splice system and obtain approval before beginning the work.
3. Deliver all new materials/parts with clear identification of the manufacturer. Handle the devices per the manufacturers instructions.
4. Prior to the actual installation of the splice system, perform a mock up installation with torque wrench by a 3 person crew to demonstrate that the quality installation of the splice system can be achieved. Information about mock-up and mock-up plans are available from the District.
5. Splice and tighten severeved strands (as shown in the details) to have a tension of 24,000 lbs in each 1/2" ϕ LR 270 or 22,000 lbs in each 1/2" ϕ SR 270 strands. Use torque wrench, supplied by a company, Precision Standard, Inc. (1-800-445-7996), or equivalent approved by the engineer to accurately restore the required tensile force in each strand. Provide 2 sets of splices to be used in calibrating the torque wrench and testing the splicing system. Testing will not be scheduled until the splices and the torque wrench are delivered to the job site and examined by the Engineer. Do not reuse the tressed splices to repair project strands. Use a torque wrench with adequate capacity to accurately establish the tension in each strand. Calibrate the torque wrench immediately before installation of the splicing systems. Using an approved bolt calibrator, calibrate the torque wrench to deliver within +5% of the required tensile force. Provide notice to the Engineer so that the calibration can be witnessed by a Bridge Division Structural Steel Inspector and approved by the Engineer.
6. Use saw cut only. Do not use torch to cut strands. Cut damaged and loose ends of strands to leave intact and even whole ends for engagement with the splicing system. If needed, use a new piece of ½"ϕ LR270 strand with additional splice chuck to extend the cut end. Stagger splices as necessary to provide adequate bonding space for patch material around and between system components.
7. Prior to the installation, threads of the splicing system must be thoroughly cleaned and lubricated. Do not lubricate the wedges and splice chucks. Keep strands free of lubricants.
8. Install any required anchor studs or steel pins in the repair area in accordance with Item 429, "Concrete Structure Repair," or as directed by the Engineer before tensioning the spliced strands. Handle and install splicing devices according to manufacturer's instruction. Hand tighten the splicing devices to meet the minimum thread engagement requirement. Install splicing systems on all strands to be spliced as indicated in the plans before tensioning any of the splices.
9. Tension the splice assemblies following a pattern starting from splices at the bottom center of the beam and progressing toward the side edge and upward. Tension all strand splices gradually to 50%, then all to 75%, and then all to 100% of the required tensile force.

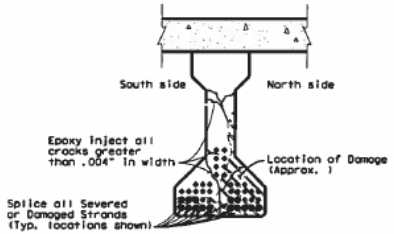

BEAM # 3 CONCRETE & STRAND DAMAGE

(See Table: "LIST OF WORK BY BEAM NUMBER")

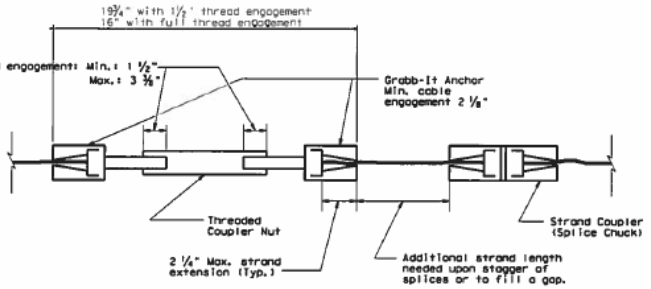

SCHEMATIC OF GRABB-IT SPLICE REPAIR INSTALLATION

(FOR CONTRACTORS INFORMATION)

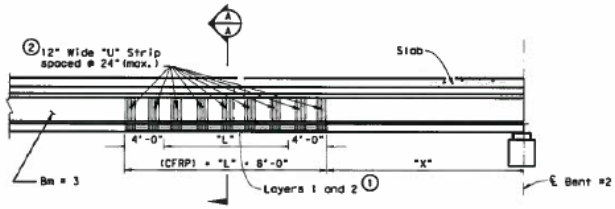

CFRP INSTALLATION AREA ~ NORTH (EXTERIOR) VIEW

Extend CFRP installation area 4'-0" into sound beam on each side of the repaired area. Length of CFRP installation area may increase due to chipping required to expose strand ends.

① The direction of carbon fiber shall be parallel to the beam.

② The direction of carbon fiber shall be perpendicular to the beam.

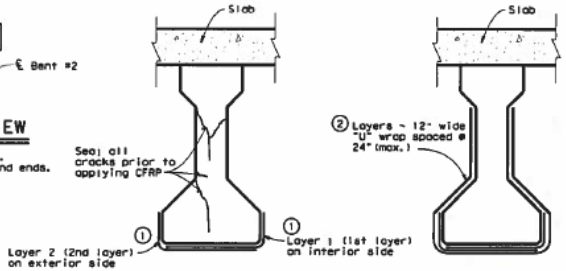

STEP 1 SECTION A-A STEP 2

Fabric width = 24"

PHOTO ~ TYPICAL DAMAGE

SUNIL N. PATEL 85345 REGISTERED PROFESSIONAL ENGINEER

12-09-14

Sheet 4 of 35 Sheets

Texas Department of Transportation © 2014

SH 183

SH 183 OVERPASS AT LOOP 12

BEAM REPAIR/BEAM & SLAB REPALCEMENT

DESIGN	FED.RD. DIV.NO.	FEDERAL AID PROJECT NO.		HIGHWAY NO.
SNP	6	(See Title Sheet)		SH 183
DESIGN CK	STATE	DISTRICT	COUNTY	SHEET NO.
WRF	TEXAS	DALLAS	DALLAS	
GRAPHICS	CONTROL	SECTION	JOB	
SNP	6282	91	001	
CKD CHECK				
WRF				

Appendix C:

Calculations for Live Load Distribution Factors

Appendix C-1: Calculation of Live load Distribution Factors for Moment for Macarthur Bridge

Assumptions

1. The spacing between the beams is assumed to be 8'-0" although the girder spacing varies for some beams.
2. The deck thickness was assumed to uniform across all spans around 6.5 in.
3. The distribution factors were calculated assuming all the girders are of similar cross section and mechanical properties.

From AASHTO (2016b) LRFD Table 4.6.2.2.1-1:

Bridge Type= Type-e (Supporting Components: Cast in place concrete Tee beam and Type of Deck: Monolithic concrete)

Live Load Distribution Factor for Moment in Interior Beams

For type e structure, the distribution factor can be calculated as:

One Design Lane Loaded:

$$D_{1L} = 0.06 + \left(\frac{S}{14}\right)^{0.4} \cdot \left(\frac{S}{L}\right)^{0.3} \cdot \left(\frac{K_g}{12 \cdot L \cdot t_s^{\,3}}\right)^{0.1}$$

where

$$K_g = n \cdot \left(I + A \cdot e_g^{\,2}\right)$$

$E_B := 57000 \cdot \frac{(3255\ psi)^{.5}}{psi^{.5}} \cdot psi = (3.252 \cdot 10^6)\ psi$ Modulus of elasticity of Beam material

$E_D := 57000 \cdot \frac{(3255\ psi)^{.5}}{psi^{.5}} \cdot psi = (3.252 \cdot 10^6)\ psi$ Modulus of elasticity of deck material

$$n := \frac{E_B}{E_D} = 1$$

The distribution factor for moment for the beam is calculated at the mid span of the beam. The section of the beam is parabolic which is why the corresponding cross section of the mid-span beam is considered.

width of beam (b) = 22 in. $b := 22\ in$

Depth of beam at mid span (d) = 2'-1/2" $d := 24.05\ in$

Centroid of the rectangular beam section lies at 12.025 in. from the bottom of the girder.

$I := \frac{b \cdot d^3}{12} = 25502.73\ in^4$ Moment of Inertia about the Centroidal axis

$A := b \cdot d = 529.1\ in^2$ Area of Tx Type C girder

$e_g := 15.275\ in$ distance between the centers of gravity of the basic beam and deck (in.)

$K_g := n \cdot \left(I + A \cdot e_g^{\,2}\right) = 148955.318\ in^4$ 10,000 < Kg <7,000,000

$L := 48.75\ ft$ Length of the span 20< L < 240

$N_b := 6$ Number of beams

$t_s := 6.5\ in$ Thickness of the deck slab 4.5 < ts < 12

$S := 8\ ft$ Spacing between the beams 3.5 < S < 16

$$D_{1L} := 0.06 + \left(\frac{S}{14} \cdot \frac{1}{ft}\right)^{0.4} \cdot \left(\frac{S}{L}\right)^{0.3} \cdot \left(\frac{K_g}{12 \cdot L \cdot t_s^{\,3}}\right)^{0.1} = 0.42$$

Two or More Design Lanes Loaded

$$D_{2L} := 0.075 + \left(\frac{S}{9.5} \cdot \frac{1}{ft}\right)^{0.6} \cdot \left(\frac{S}{L}\right)^{0.2} \cdot \left(\frac{K_g}{12 \cdot L \cdot t_s^{\,3}}\right)^{0.1} = 0.561$$

The controlling distribution factor for moment for interior girders was 0.561

Live Load Distribution Factor for Moment in Exterior Beams

One Lane loaded - Use Lever rule

$$D_{M1} := \frac{8}{8 \cdot 2} = 0.5$$

The distribution factor does not contain the multiple presence factor. Including multiple presence factor in the calculations:

$$g_{M1} := 1.2 \cdot D_{M1} = 0.6$$

Two or more lane loaded

$$D_{M2} = 0.77 + \frac{d_e}{9.1}$$

de is the distance from the centerline of the exterior girder to the inside face of the curb or barrier. The barrier was removed before the test. Hence the outer edge of the deck is considered.

$d_e := 36\ \textit{in} = 3\ \textit{ft}$ -1.0 <de <5.5

$$e := 0.77 + \frac{d_e}{9.1} \cdot \frac{1}{\textit{ft}} = 1.1$$

$$g_{M2} := e \cdot D_{2L} = 0.617$$

The controlling distribution factor for moment for exterior girders was 0.617

Calculation of Live load Distribution Factors for Moment for Loop 12 bridge

Assumptions

1. The spacing between the girders is assumed to be 6'-3" although the girder spacing varies for some beams
2. The thickness of the slab is assumed to be 6.5 in. although there is a thickened slab present above the exterior girders
3. The distribution factors were calculated assuming all the girders are Tx Type C girders although a couple of girders in Span 2 were replaced by a Texas Tx34 and Tx40 girders.

From Table 4.6.2.2.1-1:

Bridge Type= Type-k (Supporting Components: Precast concrete I and Bulb-Tee sections and Type of Deck: Cast in place concrete, precast concrete)

Live Load Distribution Factor for Moment in Interior Beams

From Table: 4.6.2.2.2b-1, for type k:

One Design Lane Loaded:

$$D_{1L} = 0.06 + \left(\frac{S}{14}\right)^{0.4} \cdot \left(\frac{S}{L}\right)^{0.3} \cdot \left(\frac{K_g}{12 \cdot L \cdot t_s^{\,3}}\right)^{0.1}$$

where

$$K_g = n \cdot \left(I + A \cdot e_g^{\,2}\right)$$

$E_B := 57000 \cdot \frac{(3255\ psi)^{.5}}{psi^{.5}} \cdot psi = (3.252 \cdot 10^6)\ psi$ Modulus of elasticity of Beam material

$E_D := 57000 \cdot \frac{(3255\ psi)^{.5}}{psi^{.5}} \cdot psi = (3.252 \cdot 10^6)\ psi$ Modulus of elasticity of deck material

$$n := \frac{E_B}{E_D} = 1$$

Centroid of the I beam section is 17.69 in. from the bottom of the girder.

$I := 82602\ in^4$ Moment of Inertia about the Centroidal axis

$A := 484.9\ in^2$ Area of Tx Type C girder

$e_g := 25.56\ in$ distance between the centers of gravity of the basic beam and deck (in.)

$K_g := n \cdot \left(I + A \cdot e_g^{\ 2}\right) = \left(3.994 \cdot 10^5\right)\ in^4$ 10,000 < Kg <7,000,000

$L := 65\ ft$ Length of the span 20< L < 240

$N_b := 6$ Number of beams

$t_s := 6.5\ in$ Thickness of the deck slab 4.5 < ts < 12

$S := 6.25\ ft$ Spacing between the beams 3.5 < S < 16

$$D_{1L} := 0.06 + \left(\frac{S}{14} \cdot \frac{1}{ft}\right)^{0.4} \cdot \left(\frac{S}{L}\right)^{0.3} \cdot \left(\frac{K_g}{12 \cdot L \cdot t_s^{\ 3}}\right)^{0.1} = 0.358$$

Two or More Design Lanes Loaded

$$D_{2L} := 0.075 + \left(\frac{S}{9.5} \cdot \frac{1}{ft}\right)^{0.6} \cdot \left(\frac{S}{L}\right)^{0.2} \cdot \left(\frac{K_g}{12 \cdot L \cdot t_s^{\ 3}}\right)^{0.1} = 0.479$$

The controlling distribution factor for moment for interior girders was 0.479

Live Load Distribution Factor for Moment in Exterior Beams

One Lane loaded - Use Lever rule

$$D_{M1} := \frac{4.5}{6.25 \cdot 2} = 0.36$$

The distribution factor does not contain the multiple presence factor. Including multiple presence factor in the calculations:

$$g_{M1} := 1.2 \cdot D_{M1} = 0.432$$

Two or more lane loaded

$$D_{M2} = 0.77 + \frac{d_e}{9.1}$$

de is the distance from the centerline of the exterior girder to the inside face of the curb or barrier.

$$d_e := 36\ in - 17\ in = 1.583\ ft$$ -1.0 <de <5.5

$$e := 0.77 + \frac{d_e}{9.1} \cdot \frac{1}{ft} = 0.944$$

$$g_{M2} := e \cdot D_{2L} = 0.452$$

The controlling distribution factor for moment for exterior girders was 0.452

References

1. ABAQUS (2014). “ABAQUS standard user’s manual. Version 6.14, vol. I–III.” Pawtucket (America): Hibbitt, Karlsson & Sorensen, Inc.

2. Abdelatif, A. O., Owen, J. S., & Hussein, M. F. (2015). “Modelling the prestress transfer in pre-tensioned concrete elements.” *Finite Elements in Analysis and Design*, *94*, 47-63.

3. ACI. (2008). “Guide for the design and construction of externally bonded FRP systems for strengthening concrete structures.” ACI 440.2R-08, Farmington Hills, MI.

4. American Association of State Highway and Transportation Officials. (2016a). “Manual for Bridge Evaluation, 2nd Edition, with 2011, 2013, 2014, 2015, and 2016 Interim Revisions.” C3, Washington, DC.

5. American Association of State Highway and Transportation Officials. (2016b). AASHTO LRFD Bridge Design Specifications, Customary U.S. Units, 7th Edition, with 2015 and 2016 Interim Revisions, Farmington Hills, MI.

6. ASCE analysis of U.S. Department of Transportation, Federal Highway Administration. National Bridge Inventory ASCII files.

7. ASCE. (2009). “White paper on bridge inspection and rating.” J. Bridge Eng., 10.1061/(ASCE)1084-0702(2009)14:1(1), 1–5.

8. ASCE. (2013). “2013 report card for America’s infrastructure.” ASCE. (Jul. 3, 2013).

9. ASCE. (2017). ‘2013 report card for America’s infrastructure.’’ ASCE.

10. ASTM A305-49 (1949) “Specification for Minimum Requirements for the Deformations of Deformed Steel Bars for Concrete Reinforcement,’’ Annual Book of ASTM Standards, ASTM International, Vol. 04. 02, West Conshohocken, PA

11. ASTM A370-17 (2017) ‘’Standard Test Methods and Definitions for Mechanical Testing of Steel Products,’’ Annual Book of ASTM Standards, ASTM International, Vol. 04. 02, West Conshohocken, PA

12. ASTM C39/C39M (2014a). “Standard Test Method for Compressive Strength of Cylindrical Concrete Specimens,” Annual Book of ASTM Standards, ASTM International, Vol. 04. 02, West Conshohocken, PA

13. ASTM D3039/D3039M (2014b). “Standard Test Method for Tensile Properties of Polymer Matrix Composite Materials,” Annual Book of ASTM Standards, ASTM International, Vol. 04. 02, West Conshohocken, PA

14. Babrauskas, V. Y. T. E. N. I. S. (1995). SFPE Handbook of fire protection Engineering. National Fire Protection Association, Massachusetts.

15. Bakht, B., & Jaeger, L. G. (1990). “Bridge testing—A surprise every time.” *Journal of Structural Engineering*, *116*(5), 1370-1383.

16. Bakht, B., & Jaeger, L. G. (1992). “Ultimate load test of slab-on-girder bridge.” *Journal of Structural Engineering*, *118*(6), 1608-1624.

17. Barr, P. J., Eberhard, M. O., & Stanton, J. F. (2001). “Live-load distribution factors in prestressed concrete girder bridges.” *Journal of Bridge Engineering*, *6*(5), 298-306.

18. Barr, P. J., Woodward, C. B., Najera, B., & Amin, M. N. (2006). “Long-term structural health monitoring of the San Ysidro Bridge.” *Journal of performance of constructed facilities*, *20*(1), 14-20.

19. Benmokrane, B.; Faza, S.; Gangarao, H. V. S.; Karbhari, V. M.; and Porter, M., “Effects of Alkaline Environment,” Gap Analysis for Durability of Fiber Reinforced Polymer Composites in Civil Infrastructure, ASCE Publications, 2000, pp. 24-28.

20. Bhattacharya, B., Li, D., Chajes, M., and Hastings, J. (2005). “Reliability based load and resistance factor rating using in-service data.” J. Bridge Eng., 10(5), 530–543.

21. Cai, C. S., & Shahawy, M. (2003). “Understanding capacity rating of bridges from load tests.” Practice Periodical on Structural Design and Construction, 8(4), 209-216.

22. Chajes, M. J., Mertz, D. R., & Commander, B. (1997). “Experimental load rating of a posted bridge.” *Journal of Bridge Engineering*, *2*(1), 1-10.

23. Chin, J., Haight, M., Hughes, W., & Nguyen, T. (1998). “Environmental effects on composite matrix resins used in construction.” *Proceedings of CDCC 1998*, 229-242.

24. Chung, W., & Sotelino, E. D. (2006). “Three-dimensional finite element modeling of composite girder bridges.” *Engineering Structures*, *28*(1), 63-71.

25. Cicekli, U., Voyiadjis, G. Z., and Abu Al-Rub, R. K. (2007). “A plasticity and anisotropic damage model for plain concrete.” Int. J. Plast., 23(10–11), 1874–1900.

26. Clark, M. R., McCann, D. M., & Forde, M. C. (2003). “Application of infrared thermography to the non-destructive testing of concrete and masonry bridges.” *Ndt & E International*, *36*(4), 265-275.

27. Committee for European Normalisation (CEN). EN 1993-1-2:2005 “Eurocode 3: Design of steel structures - Part 1-1: General rules and rules for buildings” Brussels, Belgium.

28. D.A. Sack, L.D. Olson, “Advanced NDT methods for evaluating concrete bridges and other structures,” NDT and E Int. 28 (6) (1995) 349–357.

29. DelGrego, M. R., Culmo, M. P., and DeWolf, J. T. (2008). “Performance evaluation through field testing of century-old railroad truss bridge.” J. Bridge Eng., 13(2), 132–138.

30. Dicleli, M. and Erhan, S. (2009). “Live load distribution formulas for single-span prestressed concrete integral abutment bridge girders.” J. Bridge Eng., 14(6), 472–486

31. DOT, U. (1995). “Recording and coding guide for the structure inventory and appraisal of the nation’s bridges.” US Department of Transportation, Bridge Management Branch.

32. El Shahawy, M., and Garcia, A. M. (1989). "Structural research and testing in Florida." Structural Res. Rep. No. SRR-01-89, Fla. Dept. of Transp., Tallahassee, Fla

33. Eng, T. (2011). PyroSim User Manual. The RJA Group Inc, Chicago, USA.

34. FHWA (Federal Highway Administration). (2012). Bridge inspector’s reference manual, Washington, DC.

35. Fu, G., Sardis, P., and Tang, 1. (1992). "Proof testing of highway bridges." Res. Rep. 153, Engineering. Res. and Development Bureau, N.Y. State Dept. of Transp., Albany, N.Y.

36. Gheitasi, A., & Harris, D. K. (2014). “Overload flexural distribution behavior of composite steel girder bridges.” *Journal of Bridge Engineering*, *20*(5), 04014076.

37. Grassl, P., and Jirásek, M. (2006). “Damage-plastic model for concrete failure.” Int. J. Solid. Struct., 43(22–23), 7166–7196.

38. Hag-Elsafi, O., Alampalli, S., & Kunin, J. (2001). “Application of FRP laminates for strengthening of a reinforced-concrete T-beam bridge structure.” Composite structures, 52(3-4), 453-466.

39. Hag-Elsafi, O., Alampalli, S., & Kunin, J. (2004). “In-service evaluation of a reinforced concrete T-beam bridge FRP strengthening system.” Composite Structures, 64(2), 179-188.

40. Heskestad, G. (2016). “Fire plumes, flame height, and air entrainment. In SFPE handbook of fire protection engineering” (pp. 396-428). Springer, New York, NY.

41. Hodson, D., Barr, P., and Halling, M. (2012). “Live-load analysis of posttensioned box girder bridges.” J. Bridge Eng., 17(4), 644–651

42. Huang, D., “Field Test and Rating of Arlington Curved-Steel Box-Girder Bridge, Jacksonville, Florida”, Transportation Research Record, No. 1892, 2004, pp.178-186

43. Hugenschmidt, J., & Mastrangelo, R. (2006). “GPR inspection of concrete bridges.” *Cement and Concrete Composites*, *28*(4), 384-392.

44. IARC Working Group on the Evaluation of Carcinogenic Risks to Humans, & International Agency for Research on Cancer. (1989). “Diesel and gasoline engine exhausts and some nitroarenes” (Vol. 46). World Health Organization.

45. ICRI Technical Guideline No. 310.2R (2013) “Selecting and Specifying Concrete Surface. Preparation for Sealers, Coatings, Polymer Over- lays, and Concrete Repair”

46. Kalayci, E., Civjan, S., Brena, S., and Allen, C. (2011). “Load testing and modeling of two integral abutment bridges in Vermont, US.” Structural Engineering International, 21(2), 181-188.

47. Klaiber, F. W., T. J. Wipf, C. M. Streeter, “Testing of Old Reinforced Concrete Bridges”, Iowa Department of Transportation Project HR-390, Iowa State University, December, 1997.

48. Koskie, J. C. (2008). “Investigation of steel stringer bridge superstructures.” Iowa State University.

49. Lai, L., Baker, G. S., and Dragan, M. S. (2003). “Load testing on two bridge superstructures.” Proc., Structures Congress on Engineering Smarter, ASCE, New York, 1093–1101.

50. Lichtenstein, A. G. (1995). “Bridge rating through nondestructive load testing.” *National Cooperative Highway Research Program Project*, 12-28.

51. Lubliner, J., Oliver, J., Oller, S., & Onate, E. (1989). “A plastic-damage model for concrete.” *International Journal of solids and structures*, *25*(3), 299-326.

52. Lubliner, J., Oliver, J., Oller, S., and O˜nate, E. (1989). “A plastic-damage model for concrete.” Int. J. Solid. Struct., 25(3), 299–326.

53. Mabsout, M. E., Tarhini, K. M., Frederick, G. R., & Tayar, C. (1997). “Finite-element analysis of steel girder highway bridges.” *Journal of Bridge Engineering*, *2*(3), 83-87.

54. Markey, I. (1991). “Load testing of Swiss bridges.” *Steel Construction Today*, *5*(1), 15-20.

55. Mayo, R., Nanni, A., Gold, W., & Barker, M. (1999, November). “Strengthening of bridge G270 with externally-bonded CFRP reinforcement.” In SP-188, American Concrete Institute, Proc., 4th International Symposium on FRP for Reinforcement of Concrete Structures (FRPRCS4), Baltimore, MD, Nov (pp. 429-440).

56. McGrattan, K., Klein, B., Hostikka, S., & Floyd, J. (2010). Fire dynamics simulator (version 5), user’s guide. NIST special publication, 1019(5), 1-186.

57. Miller, T. C., Chajes, M. J., Mertz, D. R., & Hastings, J. N. (2001). “Strengthening of a steel bridge girder using CFRP plates.” Journal of Bridge Engineering, 6(6), 514-522.

58. Moore, M., Phares, B. M., Graybeal, B., Rolander, D., & Washer, G. (2001). “*Reliability of visual inspection for highway bridges,” volume I* (No. FHWA-RD-01-020,).

59. Moses, E, Lebet, J. P., and Bez, R. (1994). "Applications of field testing to bridge evaluation." Journal of Structural Engineering, ASCE, 120(6), 1745-1762.

60. Nutt, R. V., Schamber, R. A., & Zokaie, T. (1988). "*NCHRP 12-26: Distribution of Wheel Loads on Highway Bridges."* Final Report for National Cooperative Highway Research Program

61. Outinen, J., & Mäkeläinen, P. (2004). "Mechanical properties of structural steel at elevated temperatures and after cooling down." Fire and materials, 28(2-4), 237-251.

62. Pallempati, H., Beneberu, E., Yazdani, N., & Patel, S. (2016). "Condition assessment of fiber-reinforced polymer strengthening of concrete bridge components." *Journal of Performance of Constructed Facilities*, *30*(6), 04016052.

63. PCI Industry Handbook Committee. (2004). PCI design handbook: precast and prestressed concrete.

64. Purkiss, J., A. (2007). "Fire safety engineering design of structures." Butterworth-Heinemann, Elsevier, Oxford, UK, 2007.

65. Reed, C. E., & Peterman, R. J. (2004). "Evaluation of prestressed concrete girders strengthened with carbon fiber reinforced polymer sheets." Journal of Bridge Engineering, 9(2), 185-192.

66. Ren, W., Sneed, L. H., Yang, Y., & He, R. (2015). "Numerical simulation of prestressed precast concrete bridge deck panels using damage plasticity model." *International Journal of Concrete Structures and Materials*, *9*(1), 45-54.

67. Sanayei, M., Phelps, J. E., Sipple, J. D., Bell, E. S., & Brenner, B. R. (2011). "Instrumentation, nondestructive testing, and finite-element model updating for bridge evaluation using strain measurements." *Journal of bridge engineering*, *17*(1), 130-138.

68. Saraf, V.K., "Evaluation of Existing RC Slab Bridges", Journal of Performance of Constructed Facilities, Vol.12, No.1, 1998, 20-24

69. Sasher, W. C. (2008). "Testing, assessment and FRP strengthening of concrete T-beam bridges in Pennsylvania." West Virginia University.

70. Schiebel, S., Parretti, R., Nanni, A., & Huck, M. (2002). "Strengthening and load testing of three bridges in Boone County, Missouri." *Practice periodical on structural design and construction*, *7*(4), 156-163.

71. Schlune, H., Plos, M., & Gylltoft, K. (2009). “Improved bridge evaluation through finite element model updating using static and dynamic measurements.” *Engineering structures*, *31*(7), 1477-1485.

72. Schulz, J. L. (1993). “In search of better load ratings.” *Civil Engineering*, *63*(9), 62.

73. Shekar, Y., Azizinamini, A., Barnhill, G., & Boothby, T. E. (1993). PERFORMANCE OF CONCRETE SLAB BRIDGES. FINAL REPORT (No. Proj No. RES1 (0099) P458).

74. Sika Corporation (2006). “State highway 183 MacArthur Boulevard overpass emergency repair” ICRI Concrete Repair Bulletin.

75. Stallings, J. M., Tedesco, J. W., El-Mihilmy, M., & McCauley, M. (2000). “Field performance of FRP bridge repairs.” *Journal of Bridge Engineering*, *5*(2), 107-113.

76. TxDOT (2014). “Item 421.” Texas Department of Transportation.

77. Wright, W., Lattimer, B., Woodworth, M., Nahid, M., and Sotelino, E. (2013), NCHRP 12-85. “Highway bridge fire hazard assessment”, Transportation Research Board, Blacksburg, VA.

78. Yost, J. R., Schulz, J. L., & Commander, B. C. (2005). “Using NDT data for finite element model calibration and load rating of bridges.” In *Structures Congress 2005: Metropolis and Beyond* (pp. 1-9).

79. Yousif, Z., & Hindi, R. (2007). “AASHTO-LRFD live load distribution for beam-and-slab bridges: Limitations and applicability.” *Journal of Bridge Engineering*, *12*(6), 765-773.

80. Zhang, Z., & Aktan, A. E. (1997). “Different levels of modeling for the purpose of bridge evaluation.” *Applied Acoustics*, *50*(3), 189-204.

81. Zheng, Q., and Morgan, R., “Synergistic Thermal-Moisture Mechanics of Epoxies and Their Carbon Fiber Composites,” Journal of Composite Materials, 1993, pp. 1465-1478

Biographical Information

Santosh Timilsina was born in February 1990, in Bhaktapur, Nepal. He competed his Bachelor's in Civil Engineering from Tribhuvan University, Kathmandu, Nepal in December 2011. He has worked as a Site engineer for a Solar Electricity generation project under JICA and as a Design Engineer for various building structures in Nepal. He joined the University of Texas at Arlington for his Ph.D. in January 2015 where he started working under the supervision of Dr. Nur Yazdani. His research interests include Bridge Engineering, Finite Element Analysis, Non-destructive load tests, Fire Analysis and repair and rehabilitation of bridge structures.